

UNIVERSITY OF SURREY

Design and Prototyping of a New Scintillator Array for β -Tagging in GRIFFIN

MPhys Dissertation

M.S.C. Winokan^{a,b}

^a*Department of Physics, University of Surrey, Guildford, Surrey GU2 7XH, United Kingdom*

^b*TRIUMF, 4004 Wesbrook Mall, Vancouver, British Columbia, Canada V6T 2A3*

January 2019



Abstract

The SCintillating Electron-Positron Tagging ARray (SCEPTAR) is an array of twenty plastic scintillators for the detection of β particles originally developed for use with the 8π Spectrometer and now used with the GRIFFIN HPGe array at TRIUMF-ISAC. As a β -tagging array, SCEPTAR's β - γ -coincidence gating greatly reduces the room background and thus improves the signal-to-background ratio of GRIFFIN spectra, while a geometric-vetoing can suppress the background in HPGe spectra from punch-through electrons and removing the need for shielding. SCEPTAR remains GRIFFIN's primary ancillary detector system and together these produce high-precision measurements of complex β -decay schemes near stability and detailed spectroscopic studies of stopped radioactive beams.

The intent for SCEPTAR's replacement is to construct an array of 10mm by 10mm by 1.6mm plastic scintillators (Saint Gobain BC404) arranged in a geometry matching GRIFFIN's Germanium crystals. Contrary to the original SCEPTAR design, SCEPTAR II will employ Silicon Photomultipliers (SiPMs) mounted directly onto the scintillator material.

Informed by a study of the relevant background physics and the state of the field, component choices for the SiPMs were made. Following the acceptance testing, determination of biasing scheme (positive HV reverse biased cathode, anode to ground) and characterisation by IV behaviour of the chosen SensL MicroFC-10035's, two stages of prototypes were constructed. With a single scintillator and SiPM channel prototype the optimal biasing voltage ($\Delta V = 5V$), SiPM positioning (rear corner), pre-amplification (LTC6268-based charge-integrator), and scintillator surface treatments (diffusely reflective TiO) were determined. A four-channel prototype consisting of four scintillators, SiPMs, with independent biasing and ac-coupled signal readout, and a 3D printed holding structure was developed and tested at atmosphere and at high vacuum using two open calibration sources. The energy spectra of ^{90}Sr and ^{207}Bi sources were compared against **GEANT4** simulations and the performance of SCEPTAR I. Finally, recommendations are given for the construction and operation of the final SCEPTAR II detector, and its impact on GRIFFIN's γ -ray detection efficiency was simulated.

Declaration & Copyright

"I hereby declare that the dissertation was composed by myself and has not been presented or accepted in any previous application for a degree. The work, of which this is a record, has been carried out by myself unless otherwise stated. All work of others and all sources of information are indicated and acknowledged by means of explicit references. ***I agree that the University has the right to submit my work for originality checks. I assert my right to be identified as the author of this work and as the copyright owner.***"

Max Winokan

8th January 2019

E-mail address: mw00368@surrey.ac.uk

University Registration Number: 6352420

Acknowledgements

I would like to begin by acknowledging and thanking Dr Adam Garnsworthy, for his supervision, continued support, and for offering this unique opportunity. Adam's expertise in a wide range of fields, and attention to detail helped to achieve the potential of this project in the short duration of the placement.

To Paddy Regan, Paul Stevenson, and the Faculty of Engineering and Physical Sciences I am exceptionally grateful for facilitating this excellent research placement.

While all the staff and students at TRIUMF were extremely helpful and friendly, I would like to highlight the contributions made by Shaun Georges and Daryl Bishop, without whom this project would not be possible.

Other members of the GRSI research group were invaluable in welcoming me and helping me get accustomed to the workplace and facilities. Notably, James Smallcombe, Mike Bowry, and Greg Hackman were of great help.

I would like to thank Mustafa Rajabali, of Tennessee Technical University, Miles Constable, and Giacomo Gallina (TRIUMF) who were resourceful and informative.

Special thanks to Vinzenz Bildstein, and all other members of the GRIFFIN collaboration for their contributions to **detectorSimulations** and helping me solve my **GEANT4** issues.

Finally I would like to thank all the Co-op students who aided in taking measurements, Fletcher Barrett, Alice Murphy, and Aditya Babu, and all those students who did not but nevertheless contributed to my experience. Special thanks to Lewis Sexton for being a good friend and a great table tennis player.

Table of Contents

Abstract	i
Declaration & Copyright	ii
Acknowledgements	iii
List of Acronyms	vii
List of Figures	xiii
List of Tables	xiv
1 Introduction	1
1.1 The Original Scintillator Array for β -Tagging, SCEPTAR	1
1.1.1 Gating on detected β particles	2
1.1.2 Vetoing punch through signals	2
1.2 Motivation and Concept for New Detector, SCEPTAR II	4
1.2.1 Use of New Technologies	4
2 Background Physics and State of the Field	6
2.1 Précis of Literature Review and Interim Report	6
2.1.1 Radioactive Decay	6
2.1.2 Radiation interaction in matter	7
2.1.3 Radiation detectors	9
2.1.4 Quantifying Radiation Detector Performance	12
3 Additional Theory	15
3.1 Further Radiative Decay Processes	15
3.1.1 Internal Conversion Electrons	15
3.1.2 Auger Electrons	15
3.1.3 X-Rays	15
3.2 Calibration source spectra	16
3.2.1 Summed β -decay spectra for a ^{90}Sr source	16
3.2.2 Calculating IC decay spectra for a ^{207}Bi source	16
3.3 Electronics	18
3.3.1 Filter Circuits	18
3.3.2 Transimpedance Amplifiers	20
4 Investigating SiPM's	24
4.1 Component choice	24
4.2 Methodology of Operation	25
4.2.1 Biasing and Readout	25
4.2.2 Amplification	26
4.3 Measured performance	27
4.3.1 Pulse Shapes	28

4.3.2 Breakdown Voltage	28
5 Single scintillator channel prototyping	31
5.1 Experimental Setup	31
5.2 Calibration Source Spectra	31
5.2.1 Comparison to GEANT4 Simulations	32
5.3 Optimising the Prototype Performance	35
5.3.1 Determining SiPM Biasing Voltage	35
5.3.2 Comparing Various Scintillator Surface Treatments	37
5.3.3 Determining Optimal SiPM Positioning	38
6 Four scintillator channel prototype	40
6.1 Experimental Setup	40
6.1.1 Detector Prototype	40
6.1.2 Scintillator Treatment	40
6.1.3 Vacuum Chamber	41
6.1.4 Other Components	41
6.2 Investigations	44
6.2.1 SiPM Characterisation	44
6.2.2 Tweaking Charge Integrating Amplifier Parameters	45
6.2.3 Vacuum Characteristics	46
6.3 Detector Response to Calibration Sources	47
6.3.1 Comparison to GEANT4 Simulations	47
6.3.2 Comparison to Original SCEPTAR Detector	47
7 Proposed Detector Design	51
7.1 Scintillators	51
7.1.1 Surface Treatment	52
7.1.2 Mounting	52
7.2 Scintillation light detection with SiPM's	52
7.2.1 Component choice	53
7.2.2 Biasing	53
7.2.3 Amplification	53
7.2.4 Mounting	53
7.3 Beampipe and Vacuum Chamber	54
7.4 Simulated GRIFFIN Efficiency	55
8 Conclusion & Outlook	57
8.1 Conclusions from Investigations	57
8.2 Recommendations for Proceeding	58
8.3 Final Outlook	59
Bibliography	60
Appendices	65
A Preparing Detector Simulations	65
A.1 GEANT4 Overview	65
A.2 detectorSimulations Overview	66
A.3 Interfacing and Automation	66
A.4 Defining generic targets/detectors	70
A.5 Defining new user interface commands	71

A.6	Adding hit tracking functionality to new detectors	72
A.7	Defining SCEPTAR II detector	73
B	Programs and Scripts	81
B.1	Bash scripts	81
B.2	GEANT4 Macros	82
B.3	ROOT functions	84
C	Circuit Diagrams	88
D	Additional Measurements	89
D.1	Calibration of ORTEC easy-MCA	89
D.2	Saturation Point of Charge Integrating Amplifier	89
D.3	Temperatures Inside GRIFFIN Vacuum Chamber During Operation with PACES	90
E	Literature Review and Interim Report	95

List of Acronyms and Abbreviations

V_{br} Breakdown Voltage. 25, 28

^{207}Bi Bismuth-207. i, iv, ix, x, xii, xiv, 16, 17, 23, 31, 32, 33, 39, 46, 47, 58, 59

^{207}Pb Lead-207. ix, xiv, 16, 17

^{90}Sr Strontium-90. i, iv, ix, x, xi, xii, 16, 23, 27, 30, 31, 32, 33, 34, 35, 37, 38, 39, 44, 45, 46, 47, 48, 47, 58, 59

^{90}Y Yttrium-90. ix, 16

^{90}Zr Zirconium-90. ix, 16

8π 8π Spectrometer. i, ix, 1, 2, 3, 4, 5, 13, 57

AC Alternating Current. 19, 25, 26, 30, 31, 41, 53, 58

ADC Analogue to Digital Converter. 53

APD Avalanche Photodiodes. ix, 10, 13, 24

BGO Bismuth Germanate. 66

CERN European Organization for Nuclear Research. 65

CSDA Continuous Slowing Down Approximation. 8

C-Series SensL C-Series. x, xi, 25, 29, 34, 38, 52, 57

DC Direct Current. 18, 19, 53

DESCANT DEuterated SCintillator Array for Neutron Tagging. 66

FAIR Facility for Antiproton and Ion Research. 65

GRiffin Gamma-Ray Infrastructure For Fundamental Investigations of Nuclei. i, v, vi, ix, xii, 1, 2, 4, 5, 11, 13, 40, 47, 48, 51, 52, 53, 54, 55, 57, 58, 59, 65, 66, 68, 73, 75, 76, 77, 78, 90

GRSI Gamma Ray Spectroscopy at ISAC. iii

GUI Graphical User Interface. 66, 68, 72

HPGe High-Purity Germanium. i, ix, 1, 2, 3, 5, 10, 11, 13, 40, 48, 52, 55, 57

HV High Voltage. 30, 53

ISAC Isotope Separator and Accelerator. i, vii, 5, 57

IV Current-Voltage. i, 28, 57, 58

KEK The High Energy Accelerator Research Organization. 65

LRIR Literature Review and Interim Report. iv, 6, 14, 25

MCA Multi-Channel Analyser. 35, 36

PACES Pentagonal Array of Conversion Electron Spectrometers. vi, 53, 66, 90

PDE Photon Detection Efficiency. 10, 13, 14, 29, 35, 36, 39, 53, 58

PENELOPE A Code System for Monte-Carlo Simulation of Electron and Photon Transport. 65

PMTs Photomultiplier Tubes. 1, 4, 5, 10, 13, 57

RC Resistor Capacitor. 53

RF Radiofrequency. 57

RIBs Rare Isotope Beams. 5, 57

Riken Rikagaku Kenkyjyo. 65

SCEPTAR SCintillating Electron-Positron Tagging ARray. i, iv, v, ix, xii, 1, 2, 3, 4, 5, 14, 31, 35, 47, 51, 55, 57, 65, 66, 68, 70, 73, 76, 79

SCEPTAR I SCintillating Electron-Positron ARray I. i, 1, 48, 57, 58, 59

SCEPTAR II SCintillating Electron-Positron ARray II. i, iv, vi, ix, xi, xii, xiv, 1, 4, 7, 14, 23, 24, 29, 39, 40, 41, 44, 47, 48, 47, 51, 53, 54, 55, 57, 59, 65, 70, 73, 75, 76, 77, 78, 79, 78

SensL MicroFC-10035 SensL C-Series SiPM with 1mm² active area and 35μm microcells. x, xi, xiv, 29, 31, 32, 35, 36, 40, 44, 48, 53, 55, 58

SensL MicroFC-SMTPA-10035 SensL C-Series SiPM with 1mm² active area and 35μm microcells, mounted on a pin adapter board. x, 30, 31, 39, 57

SensL MicroFC-10035's SensL C-Series SiPMs with 1mm² active area and 35μm microcells. i

SiPM Silicon Photomultiplier. i, v, viii, x, xi, xiv, 10, 13, 14, 25, 26, 28, 29, 30, 31, 32, 34, 35, 37, 38, 39, 40, 44, 48, 51, 52, 53, 54, 57, 58, 59, 73

SiPMs Silicon Photomultipliers. i, viii, x, 4, 5, 10, 17, 24, 25, 26, 27, 28, 29, 30, 31, 35, 36, 40, 41, 44, 48, 52, 53, 55, 57, 58

SPICE SPectrometer for Internal Conversion Electrons. 66

TIGRESS TRIUMF ISAC Gamma-Ray Escape Suppressed Spectrometer. 66

TiO titanium oxide. i, xi, 37, 38, 39, 40, 58

UI User Interface. xiv, 66, 71, 72, 73, 75

UVT Ultra-Violet Transmitting. 1, 5, 57

ZDS Zero-Degree Scintillator. 24

List of Figures

Figure 1-1	The upstream half of the original SCEPTAR array (a) In use at GRIFFIN (b) Technical drawing of cross-section. Colourised.	1
Figure 1-2	GRIFFIN HPGe signal versus β -gated HPGe signal for the ^{132}In to ^{132}Sn β^- decay. From experimental data gathered at TRIUMF in July 2016 (S1519). Figure adapted from [5].	2
Figure 1-3	$\gamma\gamma$ (light) and $\beta\text{-}\gamma\gamma$ (dark) coincidence projections from the study of ^{32}Na with 8π . Figure taken from [6].	3
Figure 1-4	Portion of γ -ray spectrum from β -delayed neutron decay of ^{11}Li taken with SCEPTAR, PACES and 8π . This compares well to the previously obtained γ -singles data from [8]. Figure taken from [9].	3
Figure 1-5	(a) Proposed geometry of one SCEPTAR II hemisphere. (b) Prototype of one hemisphere of SCEPTAR II's support structure 3D printed in acrylonitrile butadiene styrene (ABS).	4
Figure 2-1	The decay scheme of ^{36}Cl and the electron resulting energy distribution. Figure taken from [11].	7
Figure 2-2	Exemplar decay schemes of common laboratory β radioisotopes.	7
Figure 2-3	Relative contributions of ionisation and bremsstrahlung energy losses of electrons in lead. Figure taken from [12].	8
Figure 2-4	Stopping powers and ranges of electrons in PVT-based plastic scintillator. Figures produced with data from eSTAR[22].	8
Figure 2-5	Photon interaction cross sections in lead. Figure taken from [12].	9
Figure 2-6	Breakdown, quench, and recharge cycle of an APD operating in Geiger mode. Figure taken from [27].	11
Figure 2-7	A typical γ -ray spectrum in a Germanium detector. Mono-energetic 1.4 MeV γ -rays are simulated in Geant4, passing through absorber materials before detection.	11
Figure 2-8	Gamma-ray interaction mechanisms.	12
Figure 3-1	(a) Decay scheme of ^{90}Sr to ^{90}Zr via ^{90}Y . Adapted from Reference [49] with results from [46, 45]. (b) Beta emission spectra for ^{90}Sr and ^{90}Y beta minus decays, using RADAR[47] data.	16
Figure 3-2	(a) Level scheme of ^{207}Pb following an electron capture decay from ^{207}Bi . Figure adapted from [50]. (b) K and L Internal conversion electrons produced from ^{207}Pb de-excitations following an electron capture decay from ^{207}Bi	17
Figure 3-3	The electron and photon decay spectrum of ^{207}Bi , produced with data from dataset #2 of the NuDat database[48] and [53].	18
Figure 3-4	(a) First-order RC low-pass filter. (b) Second-order RC low-pass filter.	19
Figure 3-5	(a) First-order CR high-pass filter. (b) Second-order CR high-pass filter.	19
Figure 3-6	Transfer functions of first-order passive filter circuits.	20
Figure 3-7	Transimpedance amplifier with equivalent photodiode circuit.	20

Figure 3-8	(a) Uncompensated transimpedance amplifier response. (b) Compensated transimpedance amplifier response ($C_F = 0.5 \text{ pF}$). (c) Compensated transimpedance amplifier response ($C_F = 10 \text{ pF}$)	22
Figure 3-9	Equivalent circuits of amplifier input.	23
Figure 4-1	Comparison of BC404 and BC422Q emission spectra to the sensitivity of SensL C-Series SiPMs. Produced with data from [59, 57, 58].	24
Figure 4-2	Two SensL MicroFC-SMTPA-10035 mounted sensors.	25
Figure 4-3	(a) Negative SiPM biasing configuration. (b) Positive SiPM biasing configuration.	25
Figure 4-4	Biasing and readout circuit for 1mm^2 SensL SiPM.	26
Figure 4-5	Theoretical bias fluctuation attenuation by CRCR filter with resistors of $1.2k\Omega$ and 270nF capacitors. Calculated using Equation 3.4.	26
Figure 4-6	(a) Dual MAR6SM+ based fast amplifier board with built in SiPM bias filter. (b) LTC6268-based charge integrating amplifier.	27
Figure 4-7	Bode plot of the theoretical transfer function, feedback factor and open loop voltage gain of the LTC-6268 amplifier with a feedback loop of $75\text{k}\Omega$ and 10pF . Produced from equations in Section 3.3.2.	27
Figure 4-8	Close up of typical SiPM pulse shapes when exposed to (a) dark noise only (b) scintillation light from a 10mm by 10mm by 1.6mm BC404 scintillator irradiated by a Sr90 source. Time (horizontal) divisions: 400ns. Voltage (vertical) divisions 1mV.	28
Figure 4-9	Charge integrated signals (pink) and input SiPM pulses (blue) when exposed to (a) dark noise only (b) scintillation light from a 10mm by 10mm by 1.6mm BC404 scintillator irradiated by a Sr90 source. Time (horizontal) divisions: 400ns. Voltage (vertical) divisions 5mV (blue) & 50mV (pink).	28
Figure 4-10	An example SiPM pulse with an exponential fit of the pulse's decay. The SiPM was operated at an overvoltage of 4.8 Volts. From this exponential fit, the decay constant is found to be $0.0150(1) \text{ ns}^{-1}$. Hence the half-life is $46.2(4)$ nanoseconds.	29
Figure 4-11	Reverse IV characteristics of three SensL SiPMs with 1mm^2 active area and 504 microcells mounted on pin-adapter boards (MicroFC-SMTPA-10035). (a) Leakage current vs biasing voltage. (b) Square-root of the leakage current vs biasing voltage.	29
Figure 4-12	Reverse IV characteristics of three SensL SiPMs with 1mm^2 active area and 504 microcells of $35\mu\text{m}$ size mounted on pin-adapter boards (MicroFC-SMTPA-10035). (a) Leakage current vs biasing voltage. (b) Square-root of the leakage current vs biasing voltage[59].	30
Figure 5-1	10mm by 10mm by 1.6mm BC404 scintillator held by custom 3D printed holding structure attaching to a SensL C-Series SiPM with 1mm^2 active area and $35\mu\text{m}$ microcells, mounted on a pin adapter board.	31
Figure 5-2	Calibration source spectra taken with a 10mm by 10mm by 1.6mm BC404 scintillator and a SensL MicroFC-10035 SiPM. (a) ^{90}Sr . (b) ^{207}Bi	32
Figure 5-3	GEANT4 visualisation of single scintillator with layer of foil irradiated by fast electrons.	33
Figure 5-4	GEANT4 simulation of energy depositions in a single square of BC404 plastic scintillator when exposed to a calibration source. (a) ^{90}Sr . (b) ^{207}Bi	33

Figure 5-5	Effect of bias voltage on the charge-integrated spectrum produced by a C-Series SiPM coupled to a 1.6mm thick BC404 scintillator exposed to radiation from a ^{90}Sr source.	34
Figure 5-6	Approximated measured gain of a SensL MicroFC-10035 SiPM.	36
Figure 5-7	(a) Scintillator masked for painting. (b) Painted scintillator.	37
Figure 5-8	Comparison of four scintillator surface treatments: (A) Bare BC404 (B) Back and sides painted with TiO paint (thickness $\sim 60\mu\text{m}$), front face bare (C) Back and sides painted with TiO paint (thickness $\sim 60\mu\text{m}$), front face covered with $85\mu\text{m}$ Aluminised Mylar foil (Al. thickness $\sim 500\text{\AA}$) (D) All faces painted with $90\mu\text{m}$ TiO paint.	38
Figure 5-9	Examples of short paths to a point on a scintillator of proportions equal to those studied in this work. See text for details. (a) Point at middle of the large rear face. (b) Off-centre point on the large rear face. (c) Off-centre point on a smaller side face.	38
Figure 5-10	Effect of SiPM position on the charge-integrated spectrum produced by a C-Series SiPM coupled to a 1.6mm thick BC404 scintillator exposed to radiation from a ^{90}Sr source. The scintillator was painted with TiO paint (thickness $\sim 60\mu\text{m}$, diffuse reflection) on all faces except the front and the front face covered with $85\mu\text{m}$ Aluminised Mylar foil (Al. thickness $\sim 500\text{\AA}$, specular reflection)	39
Figure 6-1	(a) Four SensL C-Series SiPM with 1mm^2 active area and $35\mu\text{m}$ microcells prototype board. (b) Four SensL C-Series SiPM with 1mm^2 active area and $35\mu\text{m}$ microcells prototype board with 10mm by 10mm by 1.6mm BC404 scintillators held by a 3D printed structure.	41
Figure 6-2	The four 10mm by 10mm by 1.6mm St. Gobain BC404 polyvinyltoluene-based plastic scintillators and coated with a layer of TiO paint on all surfaces, mounted in the 3D printed prototype mounting structure. A window is left for the paint on one rear corner of each scintillator.	41
Figure 6-3	Measurements of scintillator dimensions before and after painting. (a) Thickness/Depth. (b) Width.	42
Figure 6-4	The prototype vacuum chamber assembled to test the SCEPTAR II prototypes. (a) Visible: various adapters and a Kurt J. Lesker KJL275807LL Convection Enhanced Pirani Vacuum Gauge. (b) Visible: Marmon flange with 34-pin feedthrough.	43
Figure 6-5	IV characteristics of one the SensL MicroFC-10035 channels of the four-scintillator SCEPTAR II prototype. (a) Dark current vs bias voltage. (b) Semi-log plot of dark current vs bias voltage. (c) Square root of dark current vs bias voltage.	44
Figure 6-6	Comparison of the eight SensL C-Series SiPM with 1mm^2 active area and $35\mu\text{m}$ microcells tested in this chapter. Shown with the average and standard-error.	44
Figure 6-7	Comparison of the ^{90}Sr energy spectra taken with the four scintillator channels of the detector prototype B.	45
Figure 6-8	The effect of varying the charge integrating amplifier's input impedance and gain.	45
Figure 6-9	Vacuum pressure inside prototype chamber immediately after powering on the Varian TRISCROLL 300 scrollpump, comparison between different contents.	46

Figure 6-10	Sr90 spectrum at three different vacuum states: at atmosphere (817 Torr), after about 20 minutes of pumping (20 mTorr), and after several hours of pumping (4.2 mTorr).	47
Figure 6-11	Dark noise subtracted calibration source decay spectra produced by four-channel SCEPTAR II prototype in response to (a) ^{90}Sr (b) ^{207}Bi	48
Figure 6-12	Dark noise subtracted calibration source decay spectra produced by four-channel SCEPTAR II prototype in response to (a) ^{90}Sr (b) ^{207}Bi	49
Figure 6-13	Calibration source decay spectra produced by an inner ring SCEPTAR detector operated at a typical bias voltage (1000V) (a) ^{90}Sr (b) ^{207}Bi	50
Figure 7-1	Simulations of electron interactions in BC404 scintillator. (a) Simulated average velocity as a 300 keV electron loses energy. From finite element analysis using eSTAR data. (b) Geant4 simulated energy deposition of fast electrons in 1.6mm of BC404.	51
Figure 7-2	Proposed geometry of one SCEPTAR II hemisphere.	52
Figure 7-3	SCEPTAR II chamber and beampipe concept by Shaun Georges.	54
Figure 7-4	Visualisation of SCEPTAR II detector concept in GRIFFIN.	55
Figure 7-5	GEANT4 simulation of GRIFFIN efficiency with original SCEPTAR and SCEPTAR II design concepts. (a) and (b) are the absolute photopeak efficiencies of GRIFFIN in normal and optimised peak to total (suppressed) modes of operation, respectively. (c) and (d) are the absolute differences in efficiency due to the introduction of various SCEPTAR detector configurations, relative to the efficiency with no ancillary detector (black curve in (a) and (b)). (c) is the difference when GRIFFIN is in normal mode, (d) is the difference for optimised peak to total (suppressed) configuration.	56
Figure 10-1	(a) Single unit of the SCEPTAR II holding geometry. (b) Single unit of the SCEPTAR II holding geometry shown with SiPM and BC404 volumes.	78
Figure 10-2	(a) Prototype of one hemisphere of SCEPTAR II's support structure 3D printed in acrylonitrile butadiene styrene (ABS). (b) 3D model of one hemisphere of SCEPTAR II's support structure as implemented in the new SCEPTAR II class of detectorSimulations and rendered in GEANT4	78
Figure 10-3	Overview of procedure to create the holding structure unit for one SCEPTAR II position in GEANT4 . * denotes that the shape is not shown in its true position in the arithmetic operation.	80
Figure 10-4	Circuit diagram for a fast biasing and readout circuit based on two MAR6SM+ RF amplifiers.	88
Figure 10-5	Circuit diagram for a charge integrating transimpedance amplifier based on a LTC-6268 op-amp.	88
Figure 10-6	Calibrating the pulse-height analysis spectrum of the ORTEC easy-MCA (8k) (a) Discrete spectrum produced from Agilent Function 33522B generator. (b) Obtaining the linear calibration function from recorded channel against known pulse-heights.	89
Figure 10-7	Finding the saturation point of the LTC6268-based charge integrating preamplifier with termination resistance of 82Ω and input resistance 124Ω . (a) Agilent 33522B input pulse and amplifier response (b) Amplifier pulse height against input pulse area.	89
Figure 10-8	LN_2 Dunks	90

Figure 10-9	Positioning of RTD's inside GRIFFIN central vacuum chamber (a) Positioning of POS2 RTD on PACES coldfinger (b) Positioning of POS3 RTD on ZDS	91
Figure 10-10	Overview (a) Temperature overview (b) Pressure overview	92
Figure 10-11	Pumping down PACES (a) Pressure and temperature overview (b) Pressure equilibrium	92
Figure 10-12	Cooling PACES	92
Figure 10-13	Preamp heating	94
Figure 10-14	Return to room temperature	94
Figure 10-15	ZDS Radiative cooling	94

List of Tables

Table 3-1	Properties and probabilities of ^{207}Pb γ -ray transitions following an electron capture decay from ^{207}Bi	17
Table 3-2	Properties and probabilities of ^{207}Pb internal conversion electrons following an electron capture decay from ^{207}Bi	18
Table 5-1	Approximate gain of a SensL C-Series SiPM with 1mm^2 active area and $35\mu\text{m}$ microcells.	36
Table 6-1	Properties of charge-integrating amplifier with various input and termination resistances.	45
Table 6-2	Time until a vacuum pressure below 10 mTorr was achieved with various prototype configurations.	46
Table 10-1	C++ source files in <code>detectorSimulations</code>	67
Table 10-2	Public functions in <code>DetectionSystemSceptar2</code>	74
Table 10-3	New UI commands introduced to determine detector configuration, and to build and place SCEPTAR II.	74

1. Introduction

This thesis documents the research that was undertaken at TRIUMF during 2018, exploring the feasibility and particulars of a replacement to SCintillating Electron-Positron Tagging ARray (SCEPTAR) - an array of plastic scintillators for β -tagging in GRIFFIN.

This work describes the investigations carried out to assess the efficiency of the detector concept through empirical and simulation results, the methods used to operate and characterise the electronics used, and provide a summary of the recommendations and important considerations found in this work for the development of the new detector in the future.

The remainder of this chapter provides an introduction to the original detector, SCEPTAR I, before discussing the motivation for, and details of, the new detector array SCEPTAR II.

1.1. The Original Scintillator Array for β -Tagging, SCEPTAR

The SCintillating Electron-Positron Tagging ARray (SCEPTAR) is a two-part ancillary detector designed for use with the 8π Spectrometer (8π)[1] as shown in Figure 1-1. Each of SCEPTAR's hemispheres contains two rings of plastic scintillators, one with square scintillators, the other with trapezoidal scintillators[2]. The angular positions of the scintillators are determined by the locations of 8π 's High-Purity Germanium (HPGe) detectors, such that each detector position has an associated scintillator paddle with the Germanium crystal. The scintillators are the polyvinyl-toluene based Saint Gobain BC404, have a thickness of 1.6mm, and are covered in a thin reflective aluminised Mylar foil[3, 2]. Scintillation light is carried by Ultra-Violet Transmitting (UVT) acrylic light guides from the scintillators, out of the vacuum chamber through a feedthrough flange, finally to be collected in a set of external 13mm diameter Hamamatsu H3165-10 Photomultiplier Tubes (PMTs). In this arrangement, SCEPTAR's scintillators subtend 80% of the 4π solid angle, facilitating an 80% β -particle detection efficiency[4].

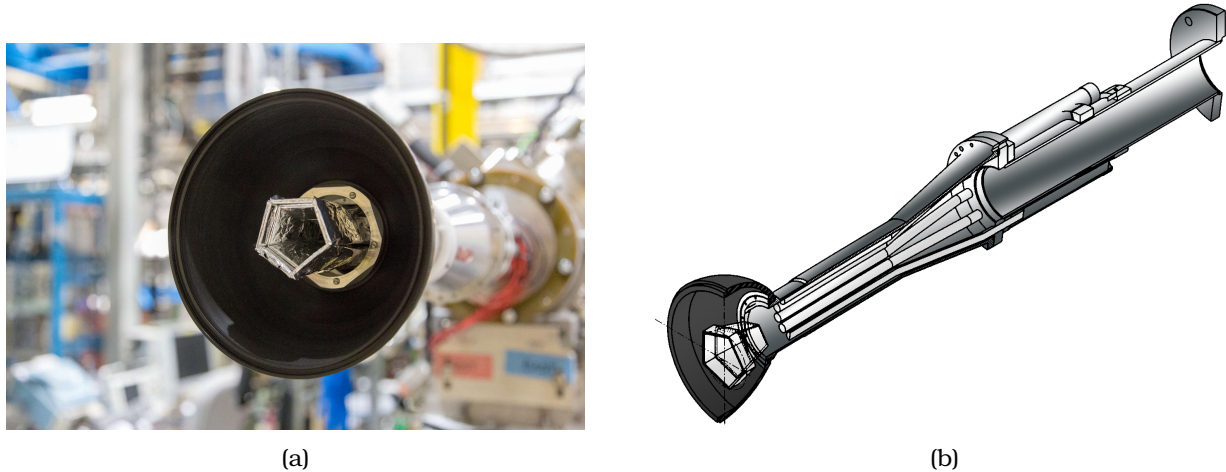


Figure 1-1 The upstream half of the original SCEPTAR array (a) In use at GRIFFIN (b) Technical drawing of cross-section. Colourised.

For nuclear structure research in neutron rich nuclei, demand for high precision branching ratio measurements and super-allowed β -decay transition rates motivated the development of SCEPTAR.

By meeting these aims the 8π spectrometer and SCEPTAR array became the facilities of choice for β -decay and isomer studies at ISAC[3]. As a β -tagging array, SCEPTAR also provides the capability to gate and veto based on detected parent nuclear decays, which can significantly reduce the impact of room background radiation, and suppress unwanted Bremsstrahlung signals[2, 4].

Due to GRIFFIN's backwards compatible design, SCEPTAR can still be used to great effect out of 8π . Far from being decommissioned, SCEPTAR remains the primary ancillary system in use in the GRIFFIN facility[4].

1.1.1. Gating on detected β particles

One of SCEPTAR's most important functions - and indeed its primary function in the GRIFFIN array - is to allow for β - γ coincidence gating[4]. By taking only γ -detection events where a β particle was also detected in SCEPTAR - and hence a β -decay occurred - a large portion of the background spectrum can be removed.

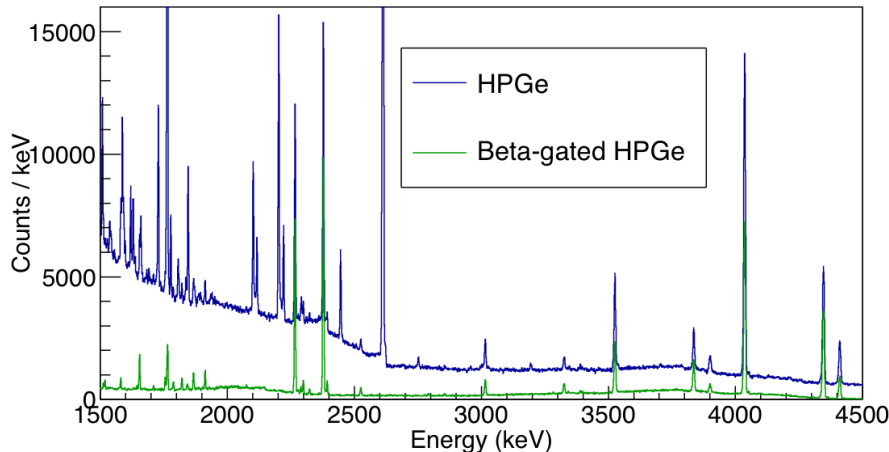


Figure 1-2 GRIFFIN HPGe signal versus β -gated HPGe signal for the ^{132}In to ^{132}Sn β^- decay. From experimental data gathered at TRIUMF in July 2016 (S1519). Figure adapted from [5].

Figure 1-2 provides an example of how effective β -gating with SCEPTAR can be. In this particular case, where SCEPTAR was used in GRIFFIN, many prominent background peaks were removed through the gating method. Notably, the uncorrelated 2614.51 keV peak from the β^- -decay of ^{208}Tl was excluded successfully.

When used in coincidence with 8π , SCEPTAR's gating allowed for such an improvement to the signal-to-background ratio that beams delivered at 2-3 ions/s could be studied[1, 6].

SCEPTAR also considerably improves the signal-to-background ratio in γ - γ coincidence spectra through β - γ - γ coincidence gating, see Figure 1-3.

1.1.2. Vetoing punch through signals

Plastic scintillators are ΔE detectors, this means that at sufficiently high energies, they will only measure a fraction of the electrons energy (See Section 2.1.2.1). Such electrons are said to punch through the scintillator and can prove to be very problematic for the signals from surrounding γ -ray detectors. Fast electrons entering Germanium crystals create unwanted signals, contributing to the noise level and reducing the peak to total ratio. Additionally, during radiative scattering events within the scintillator the fast electrons will produce Bremsstrahlung which further increases background signals in the HPGe detectors located coaxially to the scintillator volume.

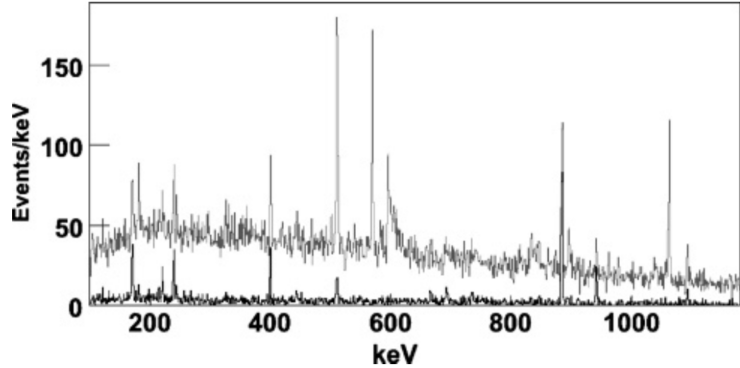


Figure 1-3 $\gamma\text{-}\gamma$ (light) and $\beta\text{-}\gamma\text{-}\gamma$ (dark) coincidence projections from the study of ${}^3\text{Na}$ with 8π . Figure taken from [6].

Hence, the 8π and GRIFFIN facilities include optional Delrin domes (up to 20 mm) that can be placed between the central vacuum chamber and the Germanium crystals[1, 4]. As low-Z absorbers, these do not greatly affect the γ -ray detection efficiency, while slowing down and stopping all but the most energetic β -particles. The issue associated with this method of removing undesired β -signals is that of Bremsstrahlung produced when stopping the electrons. Bremsstrahlung - as electromagnetic radiation - will also interact with the Germanium producing noise[7].

SCEPTAR offers an alternative to low-Z shielding, through vetoing. When a β -particle is detected, the γ -ray signals from the Germanium crystals covered by that scintillator paddle can be ignored (vetoed). SCEPTAR's 1:1 geometry correspondence to the 8π HPGe detectors makes this particularly effective, as only the bare minimum of sensitive volume is ignored. In 8π vetoing $\beta\text{-}\gamma$ coincidence signals in the colinear HPGe detector effectively reduced the background in the spectrum at a small cost of 5% loss in overall coincidence events. β -decays with sufficiently low Q-values can be discriminated against and not excluded, as the electrons are stopped instead of slowed down in SCEPTAR[6].

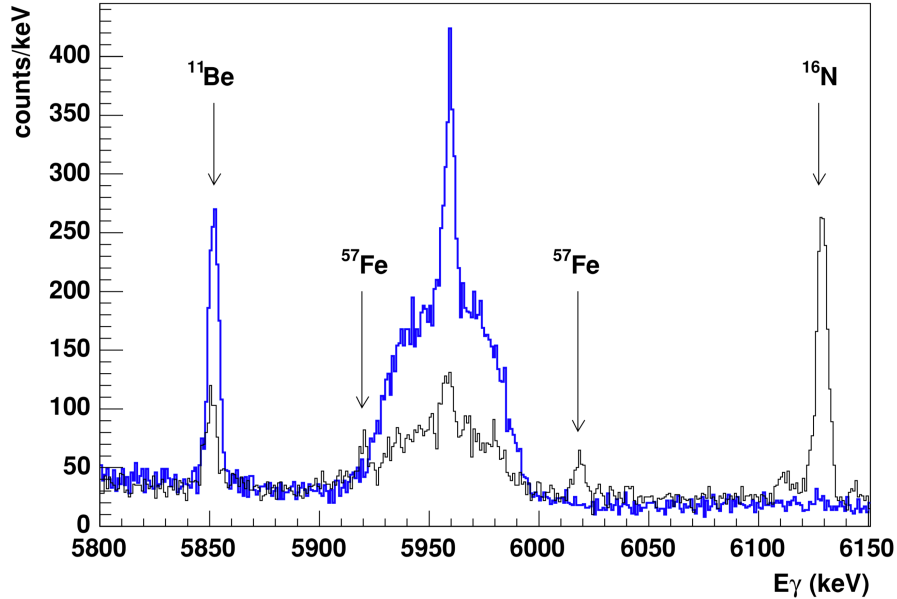


Figure 1-4 Portion of γ -ray spectrum from β -delayed neutron decay of ${}^{11}\text{Li}$ taken with SCEPTAR, PACES and 8π . This compares well to the previously obtained γ -singles data from [8]. Figure taken from [9].

Figure 1-4 shows an example of SCEPTAR's β -tagging and vetoing capabilities when studying β -delayed neutron decay of ${}^{11}\text{Li}$. The improved signal-to-noise ratio of the $\beta\text{-}\gamma$ coincident data more

clearly shows the unresolved 5960 keV doublet in ^{10}Be and 5957 keV narrow peak of the indirect feeding of the 1_1^- level from the ground state of ^{10}Be , as well as removing the iron and nitrogen background peaks[9].

1.2. Motivation and Concept for New Detector, SCEPTAR II

Changing to GRIFFIN's geometry and the resulting one-to-one correspondence to the Germanium crystals will improve the ability to veto signals caused by punch through β particles, which proved to be very useful in the 8π array[1]. As SCEPTAR's scintillator paddles are arranged to match 8π 's geometry, each scintillator has more than one Germanium crystal in its 'shadow' when SCEPTAR is used in GRIFFIN. As a consequence, using SCEPTAR coincidences to reduce punch-through signals in GRIFFIN causes a higher loss in data than necessary. Changing to square scintillator paddles that will match GRIFFIN's rhombicuboctahedral geometry will reinstate one-to-one scintillator to Germanium crystal correspondence.

Figure 1-5a shows the approximate geometry of the scintillator paddles and holding structure in SCEPTAR II. Each square face will be covered by four scintillator volumes in a two by two grid.

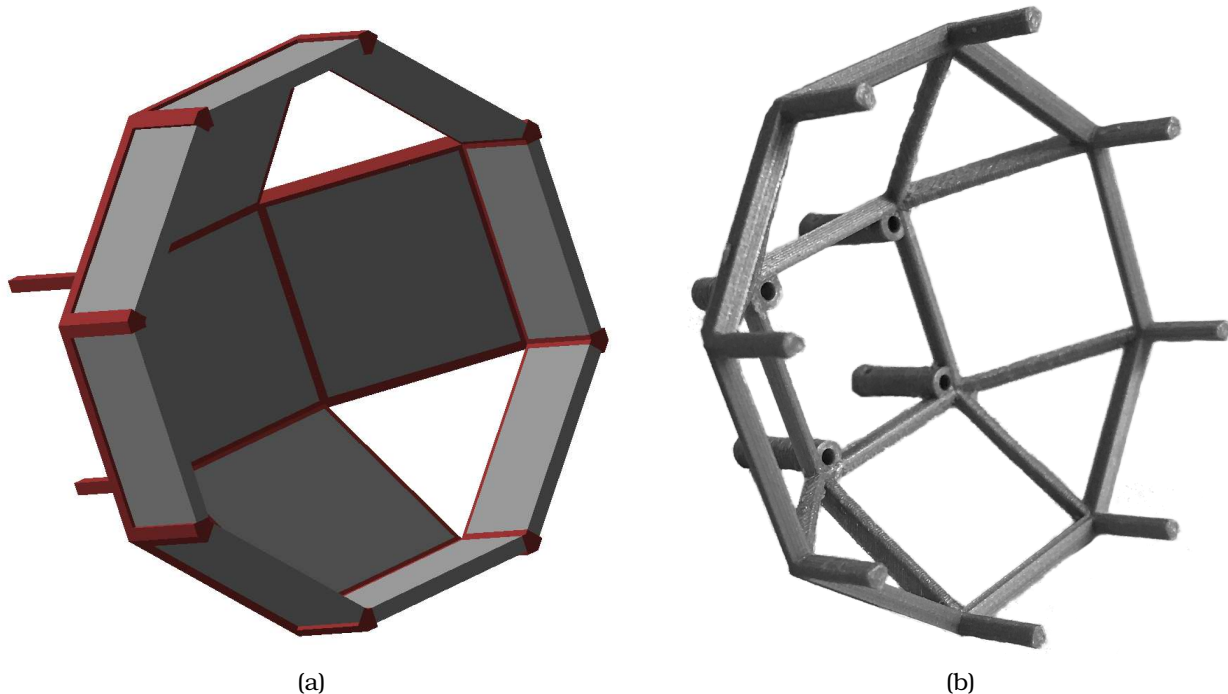


Figure 1-5 (a) Proposed geometry of one SCEPTAR II hemisphere. (b) Prototype of one hemisphere of SCEPTAR II's support structure 3D printed in acrylonitrile butadiene styrene (ABS).

1.2.1. Use of New Technologies

Since the construction of the original SCEPTAR array, technologies that were non-existent or untested for longevity, have since matured and present opportunities to modernise the detector's construction.

Silicon Photomultipliers (SiPMs) are much more compact, inexpensive, and require lower biasing voltage when compared to Photomultiplier Tubes (PMTs). The original SCEPTAR vacuum chamber design is very mechanically challenging due to the light guides, optical feedthrough flange, and PMTs all having to fit within their respective parts of the beampipe and chamber. This is can be seen in the design schematics shown in Figure 1-1b. The smaller dimensions of SiPM's will allow for direct mounting onto the scintillators, removing the need for light-guides and feedthroughs.

The proposed geometry for SCEPTAR II's scintillators will require a support structure that would incur significant cost if machined. The complex structure lends itself very well to 3D printing solutions. Figure 1-5b shows what a low-cost and fast turnover print of the prototype structure looks when printed in ABS.

For additional rigidity, and improved vacuum characteristics (reduction in outgassing) a material such as aluminium would be favourable. Nowadays aluminium 3D printing is available through Direct Metal Laser Sintering (DMLS).

While mounting SiPM's directly onto the scintillators in the vacuum chamber removes the need for optical feedthroughs and light guides, there will be a significant number of signal cables that need to be routed out through a flange and into the data acquisition system. To reduce the number of parts, and improve the easy of construction, flexible printed circuit boards (fPCB's) present an opportunity to combine a part of the support structure with the signal cables. Often manufactured from Kapton, and thin copper sheets these fPCB's cause very little γ -ray attenuation and have excellent vacuum properties.

Use of modern technologies such as compact Silicon PhotoMultipliers (SiPM's), 3D printing, and flexible printed circuit boards, will enable the move to GRIFFIN's geometry.

Conclusion

In this chapter, an introduction to the research project documented by this thesis was presented. SCEPTAR is an ancillary detector composed of two hemispheres and designed for use in 8π Spectrometer, each with two rings of five thin (1.6mm) BC404 plastic scintillators arranged to match the HPGe crystals, and readout through UVT light-guides and external PMTs.

The function and success of SCEPTAR I with the 8π was detailed, where the scintillator array captured energy (ΔE) of incident β -particles and provided the means for $\beta - \gamma$ and $\beta - \gamma - \gamma$ coincidences. This β -gating functionality was discussed in Section 1.1.1 and example spectra are provided in Figures 1-2 and 1-3. Additionally, SCEPTAR allows for vetoing against high-energy electrons that are not fully captured in the thin scintillator. Discussed in Section 1.1.2 this functionality discards HPGe signals in the crystal(s) directly behind the scintillator where an electron has punched through. Without producing further Bremsstrahlung radiation, this technique improves the background signals of the 8π as seen in Figure 1-4.

The two hemispheres of SCEPTAR have been used for over a decade as the first choice experimental facilities in the study of β -decay and isomer studies with RIBs at TRIUMF's ISAC. The detector's performance has begun to decrease as the detector ages, and technological advances in the fields of 3D printing and Silicon Photomultipliers allows for a new detector to be built that will match GRIFFIN's HPGe crystal geometry. This change will reinstate the quality of vetoing when used with GRIFFIN and will improve the directional resolution of tagging measurements. The details of this possibility were initially discussed in Section 1.2.

The following two chapters discuss the relevant theory and work of others that were considered before investigations commenced.

2. Background Physics and State of the Field

A study of the background physics and a review of relevant literature to support this research project were performed and documented as part of the “Literature Review and Interim Report” module (PHY3058). The key details of chapters 2-4 are summarised and reflected upon in this chapter, while the entirety of the interim report is included in Appendix E of this thesis.

2.1. Précis of Literature Review and Interim Report

This Section provides a summary of the most important topics discussed in the Literature Review and Interim Report.

2.1.1. Radioactive Decay

Radioactive decays occur in unstable nuclei. In the case of α and β -decays, the parent nuclei emit particles in order to approach a more stable isobar for their given mass number. In γ -decay the nuclear species remains unchanged[10].

2.1.1.1. Beta Decay

Fast electrons in radiation measurement most frequently come from a radioisotope that decays through β -minus emission[11]. β -minus decay “provides a convenient way for an unstable nucleus to ‘slide down’ the mass parabola[10]”.



Equation 2.1 shows the process for β -minus decay schematically. X and Y are the parent and daughter nuclei, β^- denotes an electron, and $\bar{\nu}$ is an anti-neutrino[12, 11, 13].

The neutrinos produced by β -decay go mostly undetected due to their remarkably small interaction probability with matter[14, 13]. The recoil nucleus Y while carrying little kinetic energy, is in most cases in an excited state, releasing γ -rays during its relaxation to the ground state.

Properties of produced radiation

β -decays can be characterised by an invariant decay energy known as the Q-value. This energy value is equal to the difference in binding energy that can be released in the decay[10, 15].

The β -particles are produced with a bell-shaped continuous energy distribution[10, 11, 16]. The endpoint energy describes the maximally possible energy of the β -radiation, when the energy carried by the neutrino approaches zero[11, 17, 18].

2.1.1.2. Gamma-ray producing processes

This Subsection describes the various processes that can result in the emission of high-energy electromagnetic photons, γ -rays.

Gamma-rays following β -decay

Non-pure β -decays produce daughter nuclei which are in an excited nuclear state. Similar to optical transitions in atoms, the excited nucleons will reconfigure to reduce the overall energy of the quantum state[11].

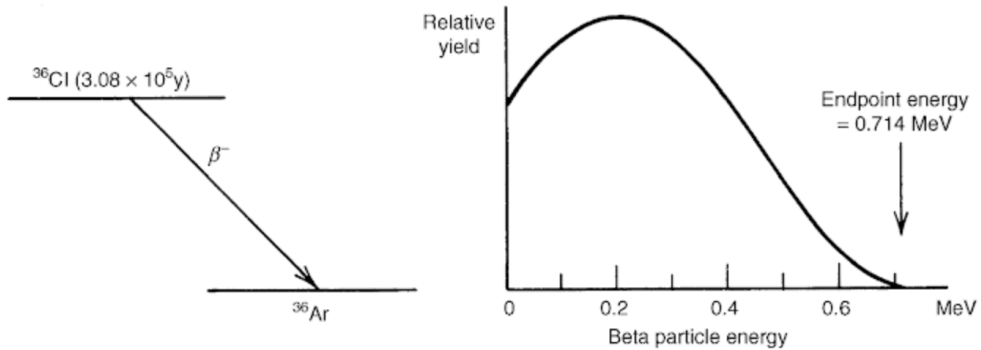


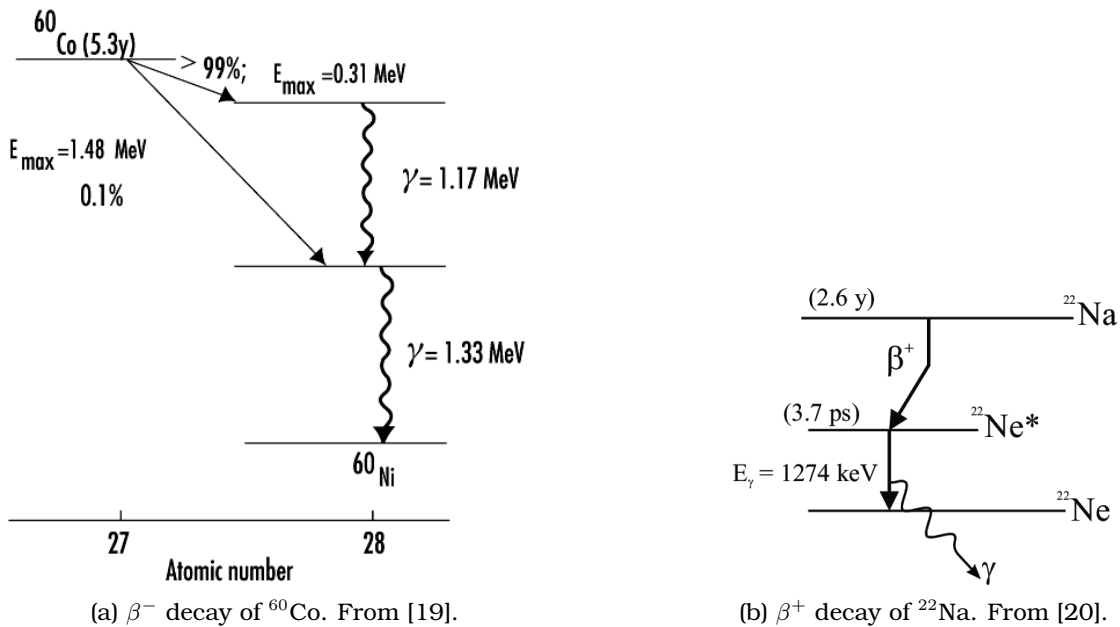
Figure 2-1 The decay scheme of ^{36}Cl and the electron resulting energy distribution. Figure taken from [11].

When this occurs, γ -rays carry off the excess energy. The de-excitation can be directly to the ground state or to an intermediate state which will also decay by γ -emission.

In the absence of Doppler shifting, the produced photons are nearly mono-energetic, with state-to-state transitions having very specific energies, a decay's γ spectrum can be used to make deductions about the level and decay schemes involved[11].

Annihilation radiation

Decays through β^+ -emission, produce annihilation photons when the positron encounters an electron. Two electromagnetic annihilation photons are produced, each at 511 keV and travelling in opposite directions due to momentum conservation.



(a) β^- decay of ^{60}Co . From [19].

(b) β^+ decay of ^{22}Na . From [20].

Figure 2-2 Exemplar decay schemes of common laboratory β radioisotopes.

2.1.2. Radiation interaction in matter

When radiation passes through matter it transfers some of its energy to the molecules of the material. This results in excitations and/or ionisations that can be experimentally observed[12, 11]. The relevant particles and materials for the development of the SCEPTAR II array are electrons in scintillator materials, photons in silicon photodiodes and Germanium detectors.

2.1.2.1. Interaction of fast electrons in matter

Electrons can lose energy through Coulomb interactions also known as “collisional” interactions (excitation, ionisation) as well as through radiative processes (Bremsstrahlung)[11, 12].

“Collisional” losses occur when a fast electron interacts with and transfers energy to an orbital electron. Either exciting it or ionising it, depending on the energy deposited. When a fast electron interacts with an orbital electron, due to their equal masses very large angle deviations are possible[11, 21].

Radiative energy losses can occur at any point of an electron’s passage through matter and can take the form of “Bremsstrahlung” or electromagnetic radiation[11, 21]. Bremsstrahlung is a result of an interaction with the nuclear Coulomb field as shown in 2.2 which is a process forbidden in vacuum.

$$e^- + N \rightarrow e^- + N + \gamma \quad (2.2)$$

Through quantum mechanics, the probability of emitting radiation in the form of a photon is proportional to acceleration squared. As a result, it is much more likely to occur close to a nucleus than an atomic electron, as the nuclear forces are greater and hence contribute to the particle’s acceleration more at closer distances[12].

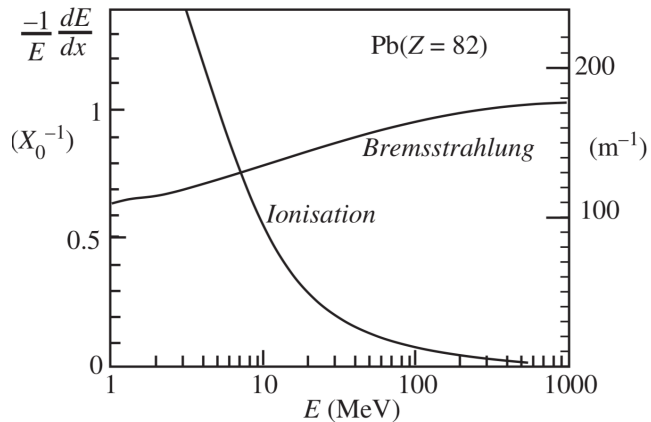


Figure 2-3 Relative contributions of ionisation and bremsstrahlung energy losses of electrons in lead. Figure taken from [12].

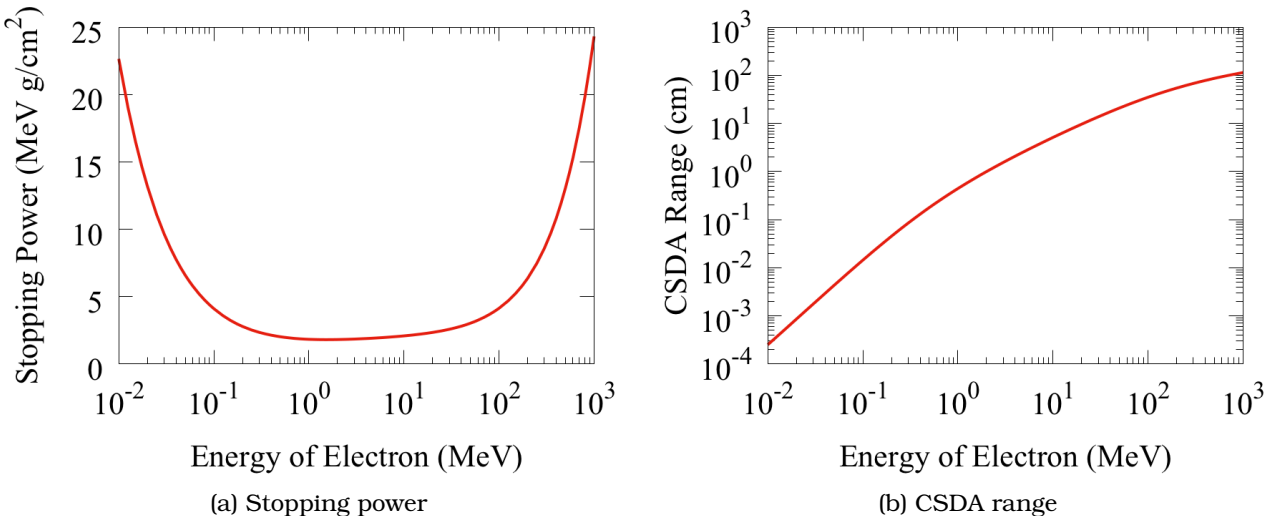


Figure 2-4 Stopping powers and ranges of electrons in PVT-based plastic scintillator. Figures produced with data from eSTAR[22].

The average fraction of energy that a fast electron will deposit in a given physical volume is dependent on its initial velocity. The main categories of behaviours are; electrons which lose all their energy within a material are known as ‘captured’; those which leave through the other side of the material with non-zero energy are known as having *punched-through* the material; and electrons which scatter within the material and eventually leave through the front face of the scintillator are known as *backscattered*.

2.1.2.2. Interactions of photons in matter

Of the large variety of mechanisms through which γ -rays interact in matter, only three prove to be relevant for radiation detection. These are photoelectric absorption, Compton scattering, and pair production[12]. Unlike the interaction of charged particles, γ -rays typically deposit almost all their energy in single “catastrophic” events. In such an event, a sudden and abrupt change occurs in the incident photon.

As energy increases the interaction probabilities (cross sections) vary between the three main interaction mechanisms. The relative contributions of the photoelectric effect, Compton scattering and pair production are shown in Figure 2-5.

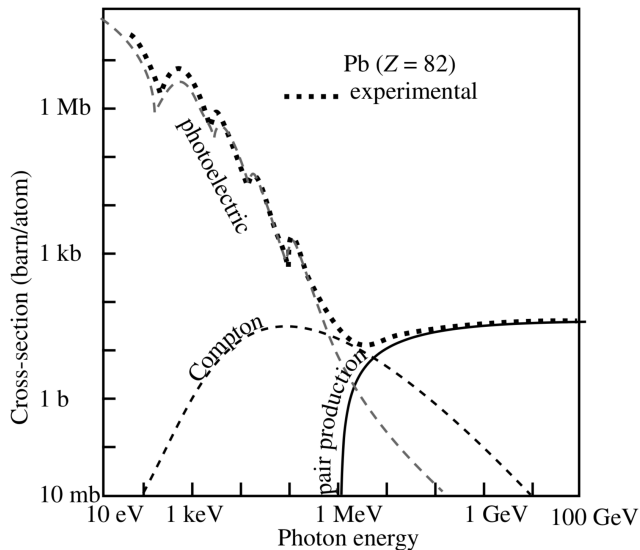


Figure 2-5 Photon interaction cross sections in lead. Figure taken from [12].

At energies below 1 MeV, the photoelectric effect is the most probable mechanism of interaction for γ -rays[12]. High Z absorber materials also enhance the probability of this process[7]. In the photoelectric absorption, the γ -photon's energy is completely deposited into the absorber atom. This is facilitated by an electron which is released from the bulk material. These energetic electrons are known as “photoelectrons” and can only occur with whole atom interactions (not with free electrons).

Compton scattering is frequently the dominant process in γ -ray energies ordinarily produced from radioactive decay. Compton scattering involves the deflection of a photon by an angle θ relative to its incident direction. The electron, assumed to be initially at rest, absorbs some of the photon's energy and becomes known as a *recoil electron*. The fraction of energy transferred in the interaction depends on the recoil angle, producing a continuous spectrum of deposited energies[11, 7, 12].

If the energy of the γ -ray is greater than the rest-mass of two electrons, then the photon may spontaneously produce a matter-antimatter pair in an electron and positron[11].

2.1.3. Radiation detectors

This Subsection describes the mechanisms and details of radiation detectors that are involved in this work.

2.1.3.1. Scintillation detectors

Detection of scintillation light has been one of the oldest methods for ionising radiation detection. Energy deposition (dE/dx) through radiation interactions discussed in Section 2.1.2 cause transitions to excited states of the detector molecules, that emit light when they decay. When combined with a photoreceptor, scintillators can be used for a variety of purposes such as calorimetry, time-of-flight measurement, tracking, tagging and vetoing. Scintillators remain an integral detector type in the fields of nuclear, particle, and medical physics[11, 23, 24].

The fluorescence from organic scintillation materials occurs through transitions of individual molecules (as opposed to crystalline excitations in inorganic scintillators). Prompt fluorescence is the de-excitation mode

relied on for radiation detection, due to its relatively fast decay times. Prompt fluorescence is also referred to as *principal scintillation light*. A property of the π electron structure that makes it especially useful as a scintillator material is its transparency to its own fluorescence.

Plastic scintillators are formed by taking a polymer (e.g. polystyrene, lucite/plexiglass, polyvinyltoluene) and doping with a scintillator (e.g. p-Terphenyl, PDB)[23]. Plastic scintillators also have a far lower 'retro-diffusion'¹ rate of the order 8% compared to 80-90% of sodium iodide[25].

2.1.3.2. Silicon photodiodes and photomultipliers

Photodiodes are solid-state semiconductor photon detectors. When operated in Geiger-mode and configured into large arrays, they are known as Silicon Photomultipliers (SiPMs) and are capable of amplifying single-photon energy depositions into detectable electronic pulses.

Silicon photodiodes

In order to work as a photodiode, Silicon must be doped to create regions with unbalanced negative (electrons) and positive (holes) charge-carriers. Intrinsic silicon crystal's resistance is high, and a *pn*-junction must be formed for efficient charge collection. By doping a region with atoms of group V elements (electron donors such as phosphorous or arsenic) and an adjacent region with group III elements (electron acceptors such as boron or aluminium). These *extrinsic* regions are known as *n*-doped and *p*-doped, respectively, and allow either negatively-charged electrons or positively-charged holes to become the majority charge carriers. As the conduction and valence band energy levels are shared by all atoms in the lattice, an electric field can easily cause the charge-carrier to drift through the crystal. At the *pn*-junction a depletion layer is formed, which is free of mobile charge carriers, as these are attracted across the junction to recombine with their opposite charge partners. It is in this region that an incident photon will create an electron-hole pair that can be accelerated by a reverse-bias to produce a current[26, 27, 28, 16].

The Avalanche Photodiodes

Avalanche Photodiodes (APD) exploit the photoelectric effect to convert light to electricity. Increasing the bias voltage across a *pn*-junction increases the acceleration of charge-carriers, meaning that they gain more kinetic energy in between scattering events[27, 26].

Usually such collisions produce *phonon vibrations*, however above a bias known as the *breakdown voltage* the mean energy of the carriers will be sufficient to exceed the silicon band gap energy[26]. This results in *impact ionisations* producing further electron-hole pairs and thus carrier multiplication. This rapid increase in charge-carriers is known as an avalanche.

This process is called Geiger discharge, and allows for a single allowed photon to trigger a self-perpetuating cascade of ionisation through the silicon which has now broken down and become conductive. The current flow created must be halted by means of a quenching resistor, which effectively lowers the voltage and stops the avalanche. Following a recharge period, the diode is once again susceptible to a photon-induced breakdown. This cycle can be seen in Figure 2-6.

Silicon Photomultiplier

A Silicon Photomultiplier (SiPM) is an array of avalanche photodiodes connected in parallel. Each microcell is operated in Geiger mode and can produce gains of the order of 10^5 to 10^6 charge-carriers per signal[26, 29, 27]. These signals last up to tens of nanoseconds.

While a mere decade ago SiPM performance was less favourable compared to vacuum PMTs[30, 31] the technology has come a long way, and now silicon photomultipliers are in routine operation for many of the world's greatest detector facilities, for fast-timing, and single-photon counting purposes[29].

The lower cost, reliability of solid-state components, insensitivity to magnetic fields, and far smaller footprints make SiPM's excellent alternatives to vacuum PMTs[23]. Additionally, modern silicon photomultipliers have high Photon Detection Efficiency (PDE), are mechanically and electrically robust, and require far less power and lower bias voltages during operation[29].

¹the rate of *retro-diffusion* is the probability that incident radiation will scatter back out through the front face of a thin detector

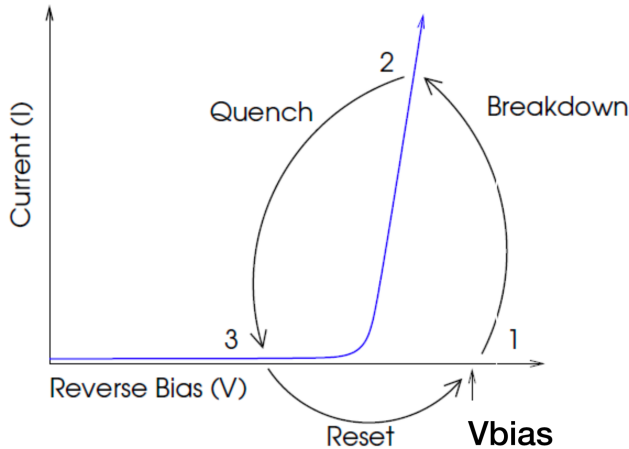


Figure 2-6 Breakdown, quench, and recharge cycle of an APD operating in Geiger mode. Figure taken from [27].

2.1.3.3. Germanium γ -ray detectors

For over 30 years the state of the art for γ -ray spectroscopy relies on high-purity Germanium crystals. The reason for this is that in order to capture γ -rays large detector active areas are required. HPGe detectors have very small bandgaps (around 0.7 eV). At room temperature the dominance of thermally-induced leakage current makes it impossible to use germanium detectors. By cooling with liquid nitrogen to temperatures below 130 K (which are deemed acceptable for spectroscopy performance[32, 33, 34]) the detectors can be operated to achieve the gold standard in γ -ray spectroscopy[11].

Features of a γ -ray energy spectrum

Figure 2-7 shows a typical γ -ray spectrum detected in a simulated GRIFFIN HPGe detector.

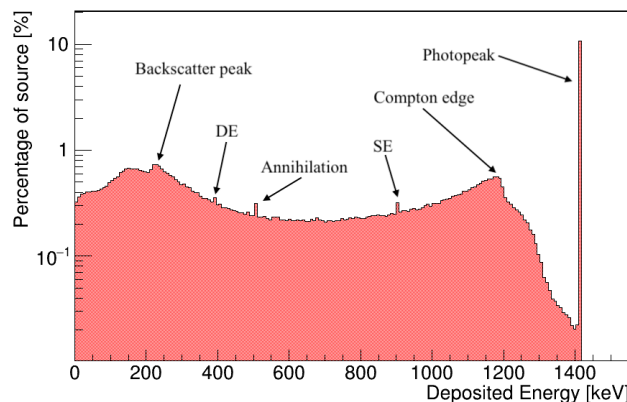


Figure 2-7 A typical γ -ray spectrum in a Germanium detector. Mono-energetic 1.4 MeV γ -rays are simulated in Geant4, passing through absorber materials before detection.

The most prominent feature is the photopeak in the highest energy occupied histogram bin. The photopeak is a result of a photoelectric absorption event, by which all the photon's energy is deposited in the active area of the detector. This can be formed through a single photoelectric absorption or by a series of scattering events within the depletion region of the **same** crystal and concluded with a photoelectric absorption[7, 11].

Compton scattering is responsible for the continuum of energies below the photopeak, where the γ -ray only loses part of its energy in the active volume of the detector[7]. The Compton edge is found at the maximum possible energy deposition through a *single* scattering event.

The backscatter peak is formed when the photon undergoes a large angle ($\theta = 180^\circ$) backscatter in surrounding material *before* the secondary photon is absorbed in the detector. The energy of the photopeak and hence the energy of the incident γ -ray is given by the sum of the backscatter and Compton edge energies[7, 11].

In addition to the features of the continuous spectrum, there are three peaks attributed to pair production.

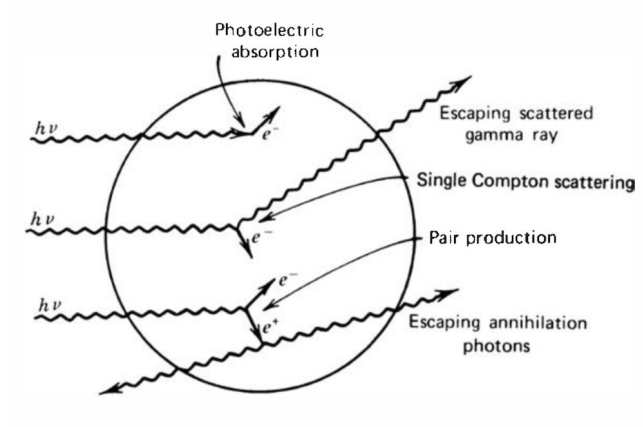


Figure 2-8 Gamma-ray interaction mechanisms.

2.1.4. Quantifying Radiation Detector Performance

This Subsection describes the methods and metrics by which radiation detectors can be quantified.

2.1.4.1. Scintillation detectors

Scintillation detectors can be characterised by their light output and detection efficiency.

Scintillator light output

Organic scintillation light output is often quantified relative to the output of Anthracene, one of the oldest organic scintillators in use. Anthracene also has the highest light output in its class[11].

Anthracene has been widely studied for its β -particle detection capabilities (see references [35, 36, 37]) and its light output is dependent on electron energy and detector geometry. The electron to photon energy conversion efficiency is of the order of one or two percent, and the amount of energy deposited per produced photon is of the order of several keV[36].

The collection of scintillation light is also of significant importance when designing detectors. With modern scintillation materials (except for very large scintillator volumes) self-absorption light losses are negligible, and the main difficulties arise from the scintillator's interfaces. Standard practice in scintillation arrays is to use light guides to direct the scintillation light to photodetectors[11].

Detection efficiency

Any radiation detector can be characterised by the efficiency at which it detects radiation. For scintillation detectors not only are there geometrical factors, limitations in physical material, but also considerations must be made into light detection.

The main geometric factor involved in a β -tagging array such as SCEPTAR is the solid angle coverage. Solid angle is a measure of the surface area of a unit sphere covered by a projection of a certain object and can be calculated by performing a surface integral projection onto a unit sphere for every surface:

$$\Omega = \iint_S \frac{\hat{n} \cdot d\mathbf{a}}{r^2} \quad (2.3)$$

Where \hat{n} is a unit vector from the origin, $d\mathbf{a}$ is the differential patch of area, r is the distance from the origin to the patch.

Another factor determining overall detection efficiency in scintillation detectors will arise through the light detection mechanisms. Photons can be lost at interfaces, in light guides, and are not guaranteed to be detected in the photodetectors.

Theoretically, any energy deposition above the 3-4 keV spacing between the fluorescent and ground state of the scintillator will result in the emission of scintillation light. At this minimum energy, however, single photons will be produced which may not be detected in the photosensors. In reality this leads to higher minimum energy thresholds for electron detection in scintillators.

Other considerations are aspects such as the electronic noise level in the circuit, and the dark current of the photodetector (which may not be distinguishable from low amplitude pulses generated by low energy electrons).

2.1.4.2. γ -ray spectrometers

γ -ray spectrometers can be characterised by their detection efficiency, energy resolution, and photopeak to total ratios.

γ -ray spectrometer detection efficiency

The efficiency of Germanium detectors for use in spectrometers can be defined relative to a standard detector, or absolutely. The relative efficiency for the HPGe in use at 8π and GRIFFIN are given relative to the efficiency of a 3-inch square sodium iodide scintillator at a 25 cm source-to-detector distance.

The absolute γ -ray detection efficiency for a large γ -ray spectrometer is the probability that a γ -ray emitted from the origin of the vacuum chamber has its energy fully captured in a Germanium crystal. This is calculated by taking the ratio of photons in the photopeak to the total emitted photons. The absolute γ -ray efficiency will include the intrinsic efficiency of the Germanium detectors (measured also by the relative efficiency) and include geometric factors such as the solid angle coverage of the crystals.

An effective way to obtain this absolute efficiency is to run simulations in Geant4[38]. Geant4 simulations include definitions of the HPGe detectors, that have been validated against experimental results[39].

γ -ray spectrometer energy resolution

The energy resolution of a γ -ray spectrometer is given through the combination of several factors: the statistical spread in the number of charge carriers, electronic noise and variations in the charge collection efficiency. The energy resolution is measured by the full width at half maximum (FWHM) of a Dirac delta-function, such as an ideal measurement of a monoenergetic γ -ray from a nuclear level transition[11].

Photopeak to total ratio

A measure of γ -ray spectrometer's performance that is not greatly affected by geometric factors is the photopeak to total ratio. This ratio is calculated by comparing the population of the full-energy/photopeak and the total captured energy spectrum.

2.1.4.3. Photomultipliers and photodiodes

A large proportion of the investigations presented in this work involve understanding the behaviour of the SiPM which are used to generate the scintillation energy spectrum. Hence, this section describes their characteristics and behaviours in detail.

Breakdown voltage and overvoltage

The breakdown voltage is the bias potential at which the APD's in the SiPM array operate in Geiger-mode. The breakdown voltage can be measured by observing the sudden increase in current in an IV plot (see ??), or for more precise determination by taking a linear fit to the voltage intercept of a \sqrt{I} versus V plot (see ??[27]).

Many, if not all other parameters of a SiPM are determined by the overvoltage. Defined as the difference between the biasing voltage and the breakdown voltage ($\Delta V = V_{bias} - V_{br}$), the overvoltage affects gain, PDE, dark performance, crosstalk, and afterpulsing[28].

Gain

The gain can be measured by finding the distance between adjacent photoelectron peaks in a SiPM photo-electron spectrum. Such a spectrum is generated by performing charge integration on a signal produced by a SiPM while being exposed to low-level pulses[40].

Photon Detection Efficiency and Responsivity

The Photon Detection Efficiency (PDE) while slightly different from the quantum efficiency often quoted for PMTs and APDs, is a measure of the sensitivity of a SiPM. The PDE is a function of wavelength, overvoltage and microcell fill factor[27, 29].

Rigorously, the PDE is the statistical probability that an incident photon interacts with a microcell producing an avalanche and is defined in equation 2.4.

$$PDE(\lambda, V) = \nu(\lambda) \cdot \epsilon(V) \cdot F \quad (2.4)$$

Where ν is the quantum efficiency of silicon, ϵ is the avalanche initiation probability, and F is the fill factor of the device. To calculate the PDE the responsivity R of the sensor is used. Defined as the average photocurrent per incident optical power, $R = I_p/P_{op}$. The PDE can now be written as follows:

$$PDE = \frac{R \cdot hc}{\lambda Ge(1 + P_{AP})(1 + P_{XT})} \cdot 100\% \quad (2.5)$$

where h is the Planck constant, c is the speed of light, λ is the wavelength of incident light, G is the gain and e is the elementary charge. P_{AP} and P_{XT} are the afterpulsing and crosstalk probabilities, respectively[27].

Dark Count Rate / Dark Current

The main source of noise in a silicon photomultiplier is the dark count rate (DCR) which primarily originates from thermal electrons generated in the active volume. These electrons initiate an avalanche producing breakdown signals that are identical to photon-generated signals[27]. Thermally-generated electrons form noise at single-photon amplitudes, which can be reduced by setting a sufficiently large threshold. Often quoted in kHz as the dark count rate is comprised of a series of pulses, for continuous applications the dark count rate is often considered as a *dark current*.

The DCR can be measured using a counting system with a threshold set at the half-photon level. The DCR increases with bias and temperature and scales with the size of the active area[28].

Optical Crosstalk

Optical crosstalk is an additional component of SiPM noise that is a result of Bremsstrahlung photons that initiate secondary avalanches in adjacent microcells. Crosstalk is defined as the probability that an avalanching microcell will cause an avalanche in a second microcell. The process happens instantaneously and thus single-photons can generate signals equivalent to multiple photons[27, 41].

The optical crosstalk can be estimated by taking the ratio of the dark count rates for thresholds where single-photon events are excluded against all higher than half-photon events[42]. Crosstalk increases with overvoltage.

Afterpulsing

Due to defects in the silicon, charge carriers can become trapped during a breakdown. These are released with a delay up to several nanoseconds, potentially triggering another avalanche known as an afterpulse[27]. Afterpulsing is negligible if the delay is short (and the microcell has not recharged yet)[41]. The afterpulse probability can be determined by measuring the statistical distribution of consecutive pairs of dark counts[42].

Temperature Dependency

The breakdown voltage of a SiPM varies linearly with temperature. Increases in temperature result in a higher breakdown voltage, which in turn determines many of the important characteristics of a photomultiplier such as the gain and PDE[27]. SensL C-Series SiPM's are notably stable in response to temperature changes with a breakdown voltage temperature dependency of $dV_{br}/dT \approx 20mV/K$ [28]. The dark count rate - resulting from thermal electrons - is also affected by temperature fluctuations, such that higher temperatures produce more frequent dark signals (higher DCR).

Conclusion

In this chapter, a summary of the key theoretical considerations presented in the Literature Review and Interim Report are given. Detailing the theory behind the radioactive processes which are the source of radiation studied with SCEPTAR and in future SCEPTAR II, the means by which these particles interact with detector materials, and finally the metrics and methods by which the relevant detector types can be characterised.

Sections 2.1.1 and 2.1.2 described the theory behind β -decay, and γ -ray producing processes, while the latter introduced and described the mechanisms by which particles interact with matter. Sections 2.1.3 and 2.1.4 moved onto describing the radiation detectors relevant to this work, including their mechanisms of radiation detection, important performance metrics, and methods of characterisation.

The next chapter introduces additional theory not presented in the LRIR, that are however of significant importance to the investigations documented later in the thesis.

3. Additional Theory

Additional theoretical considerations are included in this chapter. These can broadly be grouped into radioactive decay, with a focus on the calibration sources used in investigations to follow in later chapters, and some basic theory of electronics.

3.1. Further Radiative Decay Processes

In addition to the radioactive decay processes presented in ??, this section outlines two means by which electrons can be produced from a radioisotope, as well as another classification of electromagnetic radiation, in x-rays.

3.1.1. Internal Conversion Electrons

It has previously been described that a nucleus in an excited radioactive state, such as the daughter nucleus from a non-pure β -decay de-excites to its ground state via the emission of a γ -ray photon. While this is the most frequently observed behaviour, these photons have a finite probability of interacting electromagnetically with an atomic electron. If released, the energy of the electron which is ejected from the atom is the energy of the transition minus the binding energy of the electron[11, 43, 21]. This is seen below in Equation 3.1:

$$E_{e^-} = E_{ex} - E_b \quad (3.1)$$

As the electrons may be situated in one of a number of different shells, a single γ -ray transition creates a spectrum of several monoenergetic electron lines[11].

3.1.2. Auger Electrons

Many processes, nuclear or otherwise, may leave a vacancy in the electron shells of the atom. In this case an electron from a higher shell may fill it, releasing a characteristic x-ray or transferring this energy to another electron - ionising it. Such a freed electron is known as an Auger electron, and its monoenergetic energy is determined by the initial and final states of the transition producing it. Auger electrons typically have much lower energies than those produced by β -decay or internal conversion[11].

3.1.3. X-Rays

As touched upon in the previous subsection, if an atom finds itself in a state of deviation from its normal electronic configuration, the electrons will rearrange themselves to return to the lowest-possible energy arrangement. These transitions release energy in the form of photons known as x-rays. These photons have characteristic energies, as their energy is determined solely by the atomic states involved in the transition[11].

3.2. Calibration source spectra

In order to simulate the calibration source spectra produced from electrons in scintillation detectors the energy spectra of the radioactive decay must be known. Where available, empirical data sets remove the need for substantial theoretical calculations.

3.2.1. Summed β -decay spectra for a ^{90}Sr source

^{90}Sr undergoes β^- decay (with 100% intensity) to produce ^{90}Y with half-life 28.79(6) years, which also a β^- decay emitter with the dominant decay (99.984% intensity) having a half-life of 64.1 hours[44, 45, 46]. As the daughter half-life is significantly shorter than the parent, these two decays are in equilibrium. The nuclear states involved in this decay can be seen in the level scheme in Figure 3-1a. For the case of β decay the RADAR[47] provides reliable and validated sources for many popular β emitters. Compiled using NNDC[48] decay datasets the decay spectra for ^{90}Sr and ^{90}Y are shown in Figure 3-1b.

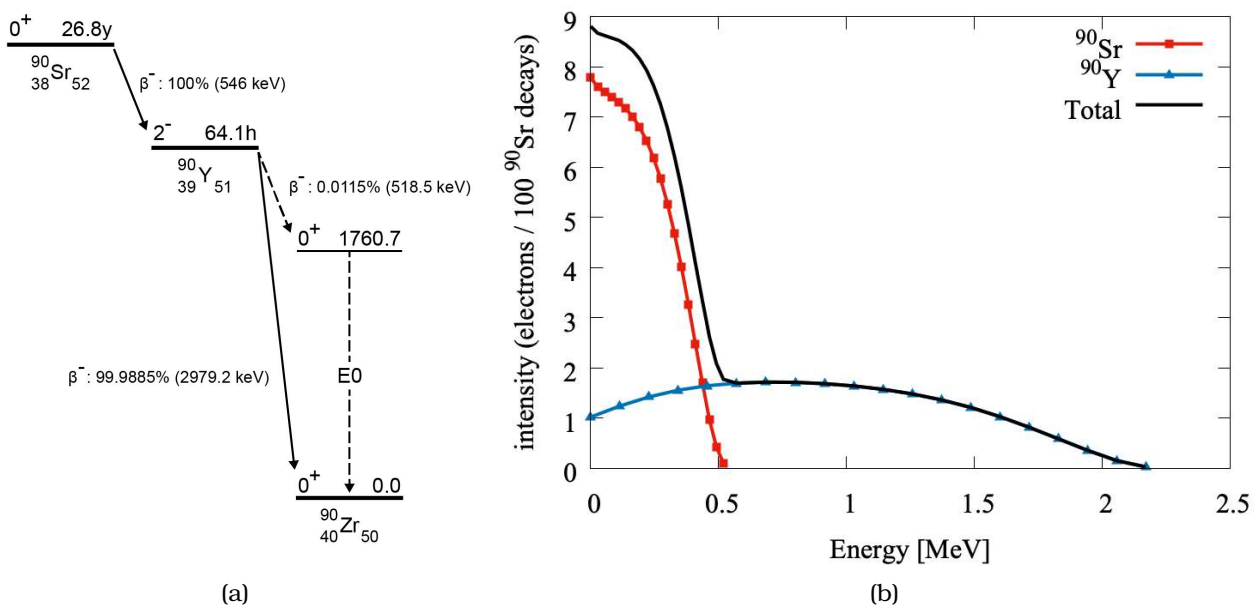


Figure 3-1 (a) Decay scheme of ^{90}Sr to ^{90}Zr via ^{90}Y . Adapted from Reference [49] with results from [46, 45]. (b) Beta emission spectra for ^{90}Sr and ^{90}Y beta minus decays, using RADAR[47] data.

The individual emission spectra from ^{90}Sr and ^{90}Y were normalised to an integral of 1 beta-ray/decay, effectively scaling the emission probabilities by the ratio of their end-point energies. Since each ^{90}Sr β^- decay results in a β^- of the daughter nucleus ^{90}Y , the individual spectra of the parent and daughter decays can be combined through simple addition. The discretised spectra were added using a linear interpolation function written in C++¹ and shown as the “Total” spectrum in Figure 3-1b.

3.2.2. Calculating IC decay spectra for a ^{207}Bi source

^{207}Bi decays by electron capture to one of three excited states in ^{207}Pb , which decay to its stable ($1/2^-$) ground state by means of electromagnetic transitions[50]. These photons have a finite probability of interacting electromagnetically with an atomic electron, which is subsequently released with a fixed energy determined by the energy of the incident photon and the binding energy of the

¹The function `MSpecManip::Add()` is part of `MTools` and can be found at <https://github.com/mwinojan/MTools>.

electron. This produces an electron spectrum composed of the combination of many monoenergetic emissions.

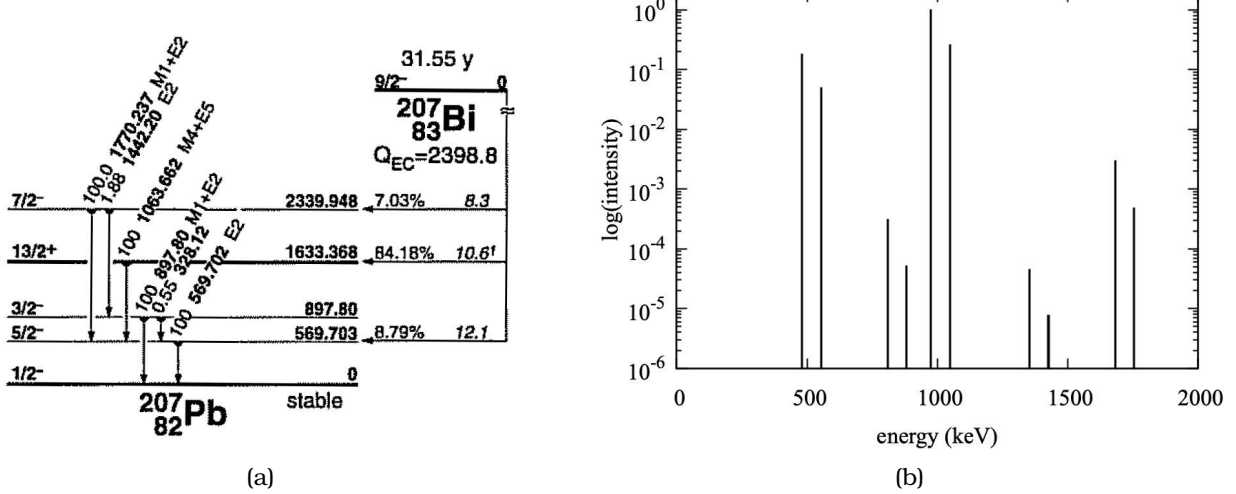


Figure 3-2 (a) Level scheme of ^{207}Pb following an electron capture decay from ^{207}Bi . Figure adapted from [50]. (b) K and L Internal conversion electrons produced from ^{207}Pb de-excitations following an electron capture decay from ^{207}Bi .

In order to determine this emission spectrum the probabilities of the γ -ray transitions involved in the decay of ^{207}Bi to ^{207}Pb must be evaluated. Books tabulating known isotopes and their properties such as [50] provide energy level and decay data, including a level scheme in Figure 3-2a. The transition probabilities as well as beta branching ratios from the ^{207}Bi decay can be combined to evaluate the probability of the gamma-ray decay given that an electron capture decay occurred. These are shown in the rightmost column of Table 3-1

Table 3-1 Properties and probabilities of ^{207}Pb γ -ray transitions following an electron capture decay from ^{207}Bi .

γ_i	Transition (keV)	Transition	Energy (keV)	$p(\gamma_i)$
γ_1	$2339.948 \rightarrow 569.703$	$7/2^- \rightarrow 5/2^-$	1770.237	6.869845×10^2
γ_2	$2339.948 \rightarrow 897.800$	$7/2^- \rightarrow 3/2^-$	1442.200	1.292880×10^3
γ_3	$1633.368 \rightarrow 569.703$	$13/2^+ \rightarrow 5/2^-$	1063.662	7.359857×10^1
γ_4	$897.800 \rightarrow 0.000$	$3/2^- \rightarrow 1/2^-$	897.800	1.255849×10^3
γ_5	$897.800 \rightarrow 569.703$	$3/2^- \rightarrow 5/2^-$	328.120	7.071944×10^6
γ_6	$569.703 \rightarrow 0.000$	$5/2^- \rightarrow 1/2^-$	569.703	8.733113×10^1

The information in Table 3-1 can be entered into an Internal Conversion Coefficient database such as Reference [51], which “integrates a number of tabulations on internal conversion electron (ICC) and electron-positron pair conversion coefficients (IPC), as well as $\Omega(E0)$ electronic factors”[52]. The coefficients returned are the probability with which the associated gamma ray produces a conversion electron. Taking into account the probability of the gamma-ray transitions from Table 3-1, Table 3-2 lists the energies and probabilities of the produced conversion electrons for K and L shells. The resultant spectrum is shown in Figure 3-2b.

3.2.2.1. Additional radiation from a ^{207}Bi source

In addition to the conversion electrons produced from the γ -ray transitions of the daughter nucleus in the decay of ^{207}Bi to ^{207}Pb , Auger electrons, X rays and γ rays are produced. Together these form the complete decay spectrum of ^{207}Bi as seen in Figure 3-3

Table 3-2 Properties and probabilities of ^{207}Pb internal conversion electrons following an electron capture decay from ^{207}Bi .

γ_i	Transition (keV)	Shell	Energy (keV)	$p(e_{ci} {}^{207}\text{Bi} \rightarrow {}^{207}\text{Pb})$
γ_1	2339.948 \rightarrow 569.703	K	1682.23	2.352994e-04
		L	1754.44	3.822752e-05
γ_2	2339.948 \rightarrow 897.800	K	1354.20	3.515552e-06
		L	1426.52	6.071138e-07
γ_3	1633.368 \rightarrow 569.703	K	975.66	7.929756e-02
		L	1048.10	2.003484e-02
γ_4	897.800 \rightarrow 0.000	K	809.80	2.468751e-05
		L	882.01	4.088869e-06
γ_6	569.703 \rightarrow 0.000	K	481.70	1.412972e-02
		L	554.42	3.918476e-03

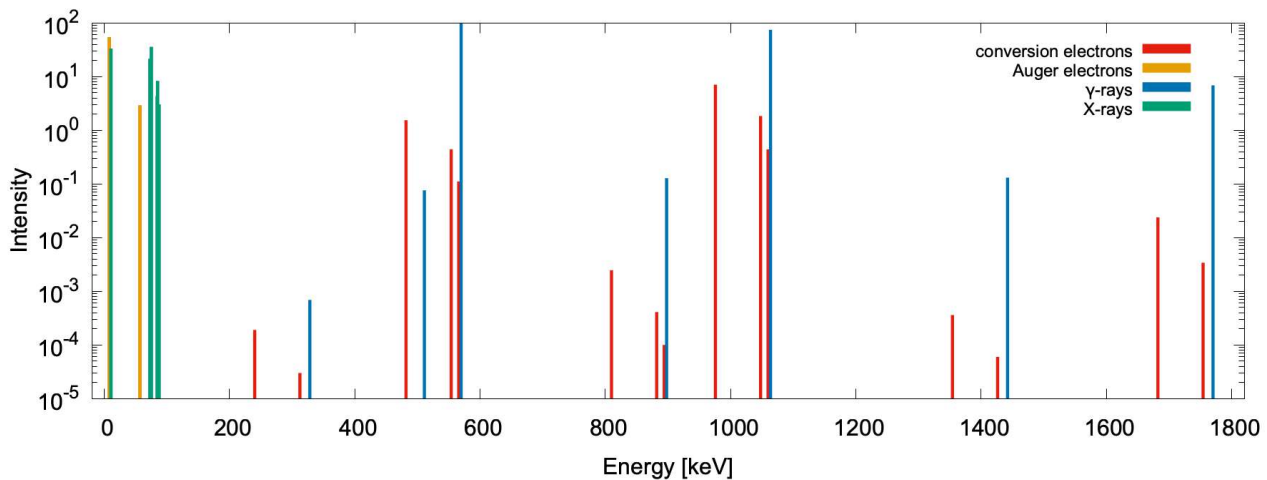


Figure 3-3 The electron and photon decay spectrum of ^{207}Bi , produced with data from dataset #2 of the NuDat database[48] and [53].

3.3. Electronics

Later chapters will detail the investigations performed with SiPMs and their use in detection of the scintillation light from electronic energy depositions. The relevant electronic theory for both the passive filter, and active amplification circuits will be discussed in this chapter.

3.3.1. Filter Circuits

Passive filter circuits are among the simplest electronic devices that attenuate signals which have a frequency outside of the frequency band that is allowed to pass. The filters we are considering in this work are approximately linear in their response and are time-invariant.

Filters are characterised by their cut-off frequency at which the input power is attenuated to half or 3 dB. For a first-order filter consisting of a single resistor and capacitor, the cutoff frequency is given by the reciprocal of the time constant:

$$\omega_c = 1/\tau = 1/RC \quad (3.2)$$

Where ω_c is the cutoff frequency, τ is the time constant which is equivalent to the product of the resistance R and capacitance C .

3.3.1.1. Low-pass filter

In applications where high-frequency fluctuations are not desired, such as in the removal of noise from a DC bias, a low-pass filter is employed. Such a filter consists simply of a resistor in series and a capacitor coupling to ground. This first-order filter is shown along with its second order variant in Figure 3-4 and attenuates frequencies above a certain cut-off[54, 27].

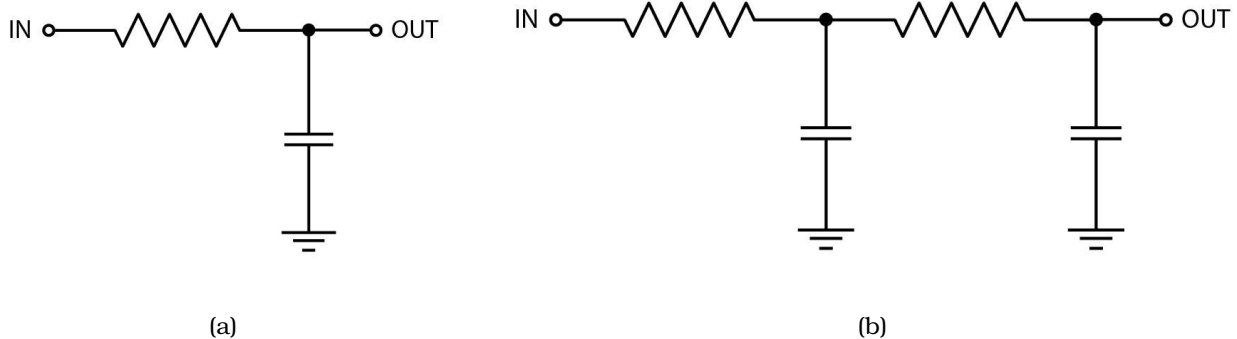


Figure 3-4 (a) First-order RC low-pass filter. (b) Second-order RC low-pass filter.

In such a circuit, Direct Current cannot pass through the capacitor, but Alternating Current can, effectively short circuiting the high-frequency band to ground[54]. The transfer function of the first-order RC filter, which described the attenuation is shown in Equation 3.3[54].

$$V_{out}(f) = V_{in} \frac{1}{\sqrt{(2\pi f RC)^2 + 1}} \quad (3.3)$$

Where V_{out} is the voltage output of the amplifier as a function of the frequency f , R and C are the resistance and capacitance as before.

For a second-order RC low-pass filter, such as the one shown in Figure 3-4b, the transfer function is the square of Equation 3.3, which evaluates to Equation 3.4[54].

$$V_{out}(f) = V_{in} \frac{1}{(2\pi f RC)^2 + 1} \quad (3.4)$$

Where V_{out} is the voltage output of the amplifier as a function of the frequency f , R and C are the resistance and capacitance

3.3.1.2. High-pass filter

A high-pass filter, such as those seen in Figure 3-5 produces an opposite transfer function, as low-frequency/Direct Current signals cannot pass through the capacitor[54].

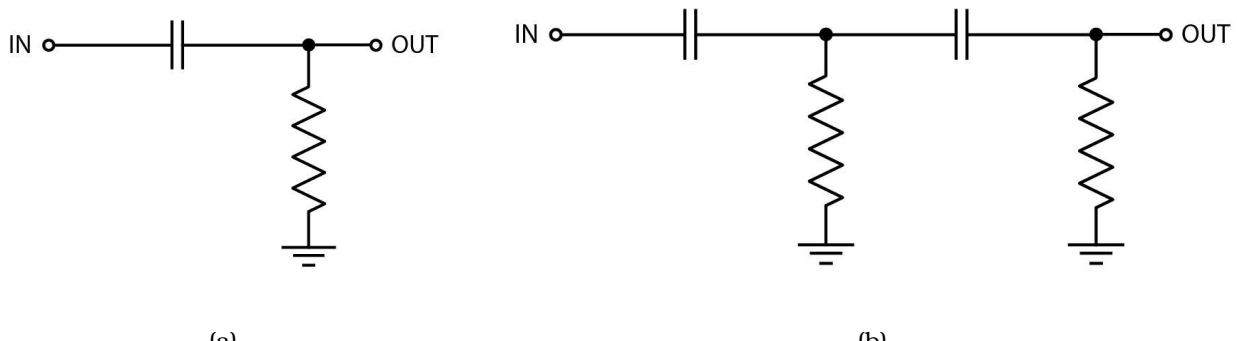


Figure 3-5 (a) First-order CR high-pass filter. (b) Second-order CR high-pass filter.

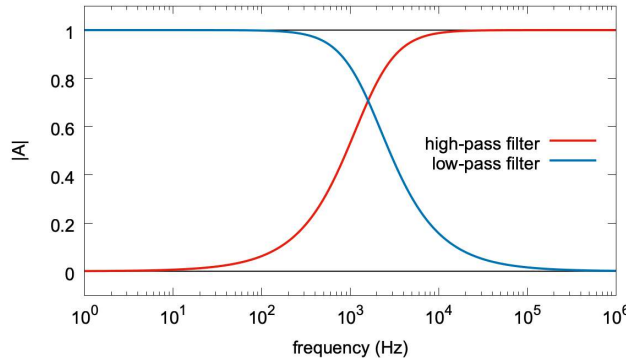


Figure 3-6 Transfer functions of first-order passive filter circuits.

The transfer function is given algebraically in Equation 3.5 for a first-order CR high-pass filter.

$$V_{out}(f) = V_{in} \frac{2\pi f RC}{2\pi f RC + 1} \quad (3.5)$$

Where V_{out} is the voltage output of the amplifier as a function of the frequency f , R and C are the resistance and capacitance

Its second-order counter part is again given by the square of the first[54]:

$$V_{out}(f) = V_{in} \left(\frac{2\pi f RC}{2\pi f RC + 1} \right)^2 \quad (3.6)$$

Where V_{out} is the voltage output of the amplifier as a function of the frequency f , R and C are the resistance and capacitance

An exemplar transfer function for both a first-order low-pass and high-pass filter is shown on a Bode plot in Figure 3-6.

3.3.2. Transimpedance Amplifiers

A transimpedance amplifier (TIA) is an op-amp configuration that acts as a current to voltage converter. Often used to amplify the current output of photo-multiplier tubes and photo diodes with a more linear current response than their voltage response, to a usable voltage[55]. A simplified circuit for a TIA is shown in Figure 3-7.

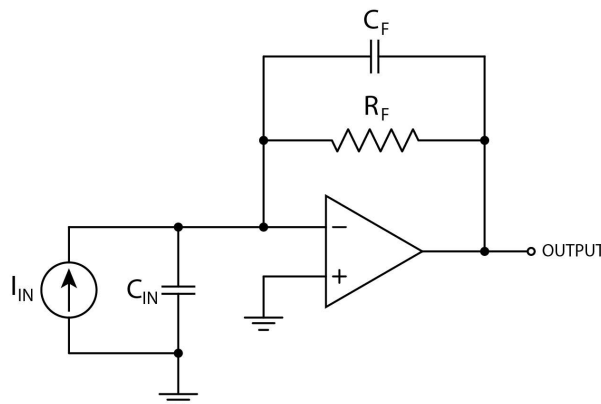


Figure 3-7 Transimpedance amplifier with equivalent photodiode circuit.

When an op-amp is configured with a negative feedback loop containing a resistor and a capacitor, it can be referred to as a transimpedance amplifier[54]. A photodiode can be represented by an

equivalent circuit in the form of a current source and a capacitor[56]. The response of the amplifier is given by Equation 3.7[54, 56]:

$$V_{OUT} = I_{IN} \frac{-R_F}{1 + \frac{1}{A_{OL}(\omega)\beta(\omega)}} \quad (3.7)$$

Where the A_{OL} is the open loop voltage gain given by Equation 3.8, β is the feedback factor given by Equation 3.9, ω is the angular frequency ($\omega = 2\pi f$), and the other values are taken from the circuit configuration as labelled in Figure 3-7.

$$A_{OL}(\omega) = \frac{A_{OL}}{1 + i(\frac{\omega}{\omega_{PD}})} \quad (3.8)$$

$$\beta(i\omega) = \frac{1 + R_F C_F i\omega}{1 + R_F(C_{IN} + C_F)i\omega} \quad (3.9)$$

Where terms are as in Equation 3.7, with the addition of the imaginary number i , the dominant pole frequency ω_{PD} , and the introduction of subscripts to distinguish between different passive electronic components. The capacitors and resistors have the same naming scheme as used in Figure 3-7.

In order to evaluate β the natural or dominant pole frequency of the circuit is required. Denoted by ω_{PD} it is given by Equation 3.10:

$$\omega_{PD} = \sqrt{\frac{2\pi GBW}{R_F(C_{IN} + C_F)}} \quad (3.10)$$

Where the new term GBW denotes the gain bandwidth of the op-amp.

The frequency response of such an amplifier is best understood by considering the response on a Bode plot, as seen in Figure 3-8. The introduction a feedback capacitor C_F reduces the peaking of the gain.

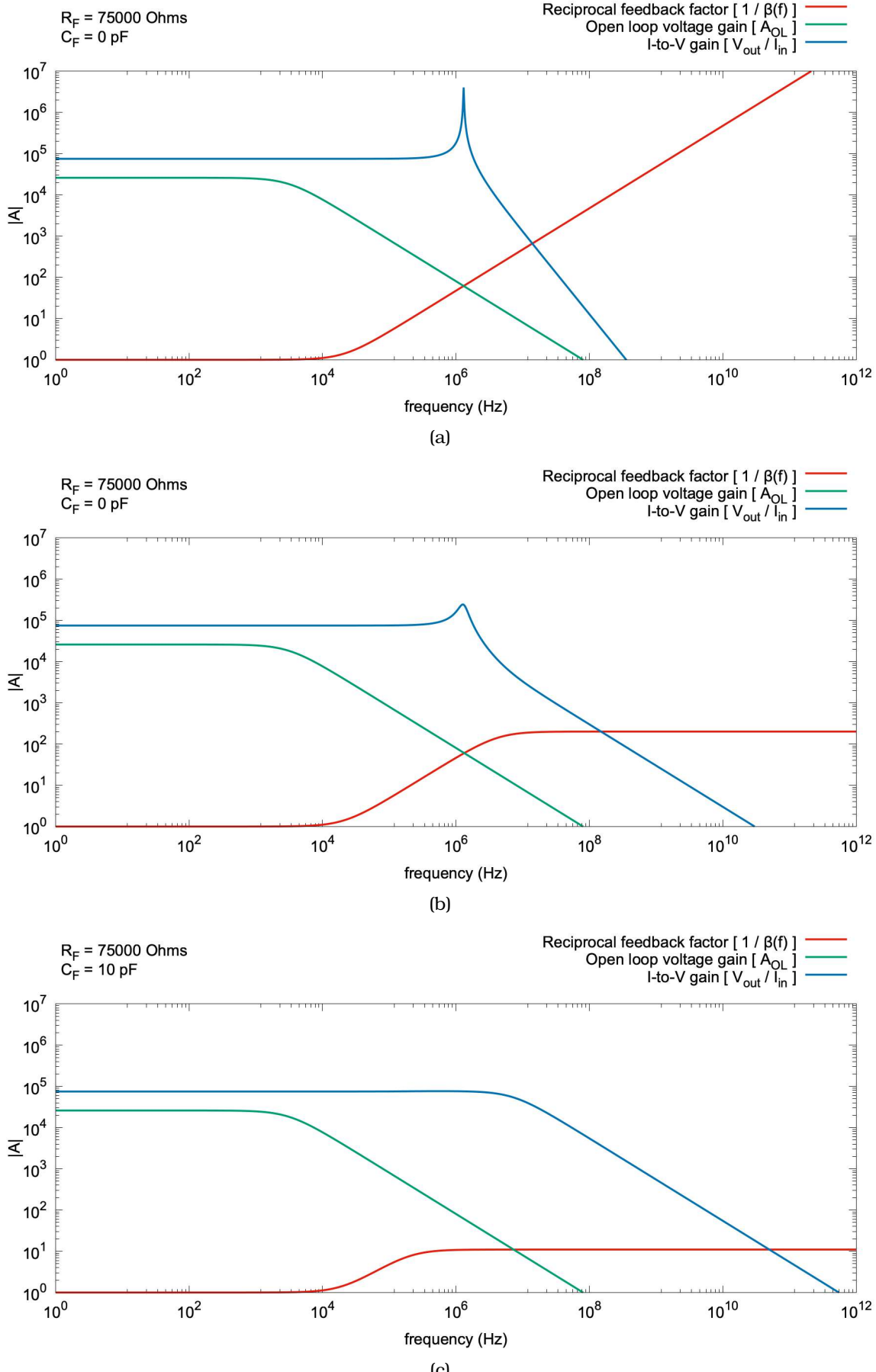


Figure 3-8 (a) Uncompensated transimpedance amplifier response. (b) Compensated transimpedance amplifier response ($C_F = 0.5$ pF). (c) Compensated transimpedance amplifier response ($C_F = 10$ pF).

3.3.2.1. Input Impedance and Current

To maintain a 50Ω input impedance and to estimate the amount of current flowing into the amplifier, the input of the amplifier can be considered as a closed-loop with a voltage source[54, 56]. This is illustrated in Figure 3-9.

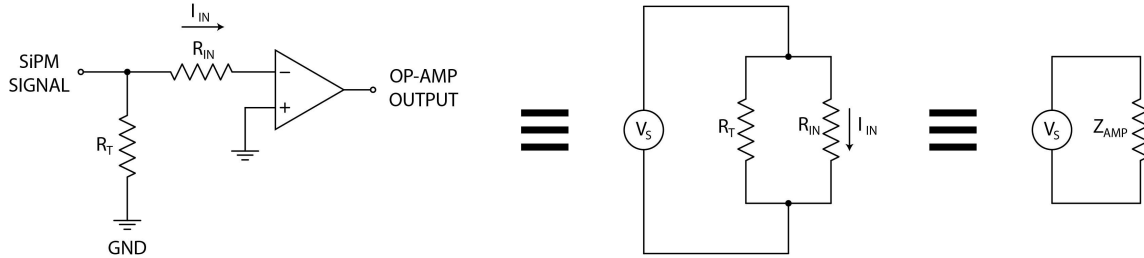


Figure 3-9 Equivalent circuits of amplifier input.

The impedance of the amplifier is equal to the total resistance of the two parallel resistances R_T and R_{IN} , which is equal to Equation 3.11[55].

$$Z_{AMP} = \frac{1}{\frac{1}{R_T} + \frac{1}{R_{IN}}} \quad (3.11)$$

Where Z_{AMP} is the amplifier's input impedance, R_T and R_{IN} are the termination and input resistor values as seen in Figure 3-9.

The current that flows through the input resistor and hence into the amplifier is calculated via Equation 3.12[54].

$$\frac{I_{IN}}{I_{SiPM}} = \frac{Z_{AMP}}{R_{IN}} \quad (3.12)$$

Where the terms are as described before in Equation 3.12.

Conclusion

In this chapter, additional theoretical considerations which were not discussed in the Literature Review or Interim Report have been presented. The decay processes resulting in Auger electrons, internal conversion electrons and x-rays were described in Section 3.1. These were included due to the specific decays of ^{90}Sr and ^{207}Bi sources which are described in Sections 3.2.1 and 3.2.2, respectively. These two calibration sources were used extensively to test SCEPTAR II detector prototypes. These investigations will be detailed in the following chapters. The final section (3.3) in this chapter introduces some minimal electronics theory which is relevant to the work discussed in this thesis. Specifically, the transfer functions of passive filter circuits, and transimpedance amplifiers were discussed.

4. Investigating SiPM's

This chapter outlines the factors informing the component choice of the Silicon Photomultipliers (SiPMs) for use in the new SCEPTAR II array, and the characterisation of said devices.

4.1. Component choice

The scintillator material for the new SCEPTAR II array was to be the same as its predecessor's. St. Gobain's BC404 is a proven and reliable, polyvinyltoluene-based, plastic scintillator with high light output and a broad emission spectrum, peaking at 408 nm[57, 58]. The chosen light detector should have excellent sensitivity to most if not all of the BC404 prompt fluorescence spectrum. SensL's C-Series of SiPMs was soon identified as a suitable candidate, due to its good agreement with the BC404 response, high gain, relative inexpensive, and robustness[27, 28, 59].

The C-Series' spectral response domain ranges from 300 to 950 nanometres with a peak sensitivity at 420 nm[59]. This spectral range compares very well to the candidate BC404 plastic scintillator emission spectrum, as seen in Figure 4-1. The lower-wavelength light output from BC422Q, the scintillator used in the ZDS detector, is also shown[60, 61]. The BC422Q material is used for the ZDS for its extremely good timing properties.

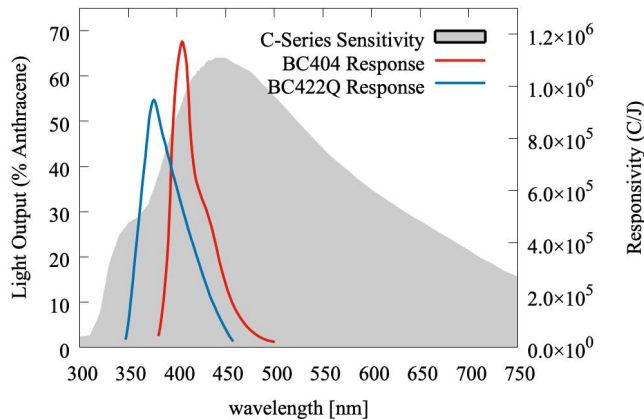


Figure 4-1 Comparison of BC404 and BC422Q emission spectra to the sensitivity of SensL C-Series SiPMs. Produced with data from [59, 57, 58].

C-Series SiPMs are available in three sizes, with active areas of 1mm by 1mm, 3mm by 3mm and 6mm by 6mm[59]. Due to there being less restrictions in sensor placement, reduced attenuation of γ rays and increased simplicity of the biasing and readout circuits, the 1mm^2 sensor size was chosen. As detailed in Section 2.1.4 and the interim report, the microcell size greatly affects the performance of SiPMs[27, 26, 29, 31]. SensL produces 1mm^2 C-series SiPMs with four microcell sizes: $10\mu\text{m}$, $20\mu\text{m}$, $35\mu\text{m}$, and $50\mu\text{m}$ [59]. These sensors have 2880, 1296, 504, and 282 microcells respectively[59].

While performance is generally quite excellent across the range of sensors, there are some differences. Due to the nature of APD arrays, crosstalk, dark current and count rate, gain, photon detection efficiency, pulse width, and recharge times increase with microcell size[27, 26]. While it is favourable to increase gain, and photon detection efficiency, the increase in crosstalk, dark noise,

and microcell recharge times is not. Due to the relative low-energy of dark noise (up to several p.e. events) compared to scintillation light (many tens of microcells firing simultaneously) the increased efficiency of larger microcells outweighs the noise considerations. However, due to a three fold increase in afterpulsing probability in the $50\mu\text{m}$ microcell size sensors the $35\mu\text{m}$ size was chosen after weighing all the above factors[59].

Thus the 1mm² with 504 microcells of $35\mu\text{m}$ size were chosen, and three SensL MicroFC-SMTPA-10035 pin-adapter board mounted sensors were ordered for testing. Two of which are shown in Figure 4-2.

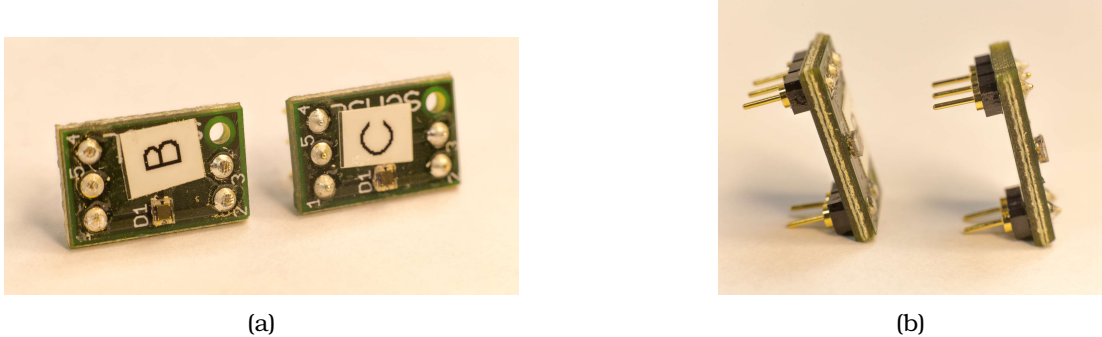


Figure 4-2 Two SensL MicroFC-SMTPA-10035 mounted sensors.

4.2. Methodology of Operation

In this Section the operation of the SensL C-Series SiPMs is discussed, including recommendations for biasing and readout of the sensors, and amplification of the fast signals they produce.

4.2.1. Biasing and Readout

In order for a SiPM to operate in Geiger mode (see Section 2.1.3.2 and LRIR) it must be reverse biased above its Breakdown Voltage (V_{br}). Labelled with respect to the terminals on a C-Series SiPM Figure 4-3 shows how a SiPM is biased by holding one of either the anode or cathode to ground and the other to the bias voltage of chosen polarity.

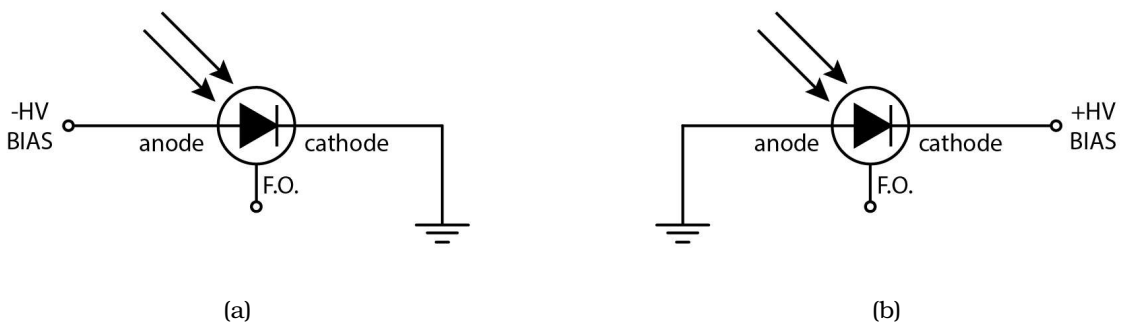


Figure 4-3 (a) Negative SiPM biasing configuration. (b) Positive SiPM biasing configuration.

As timing is not of the highest priority in the design of this detector[5], the standard output provides a cleaner unipolar pulse shape (see Section 4.3.1) and is thus used in this work and the fast output terminal (F.O.) is left floating as recommended by SensL[62]. SensL further recommends that the bias supply is filtered through a second-order passive low-pass filter (see Section 3.3.1). In both biasing schemes the signal can be taken through an AC coupling capacitor at either terminal of the diode[62, 63]. The chosen mode of SiPM operation using a positive bias and an AC coupled

readout at the cathode is shown in Figure 4-4. The theoretical attenuation of this filter configuration is shown in Figure 4-5 (see Section 3.3.1).

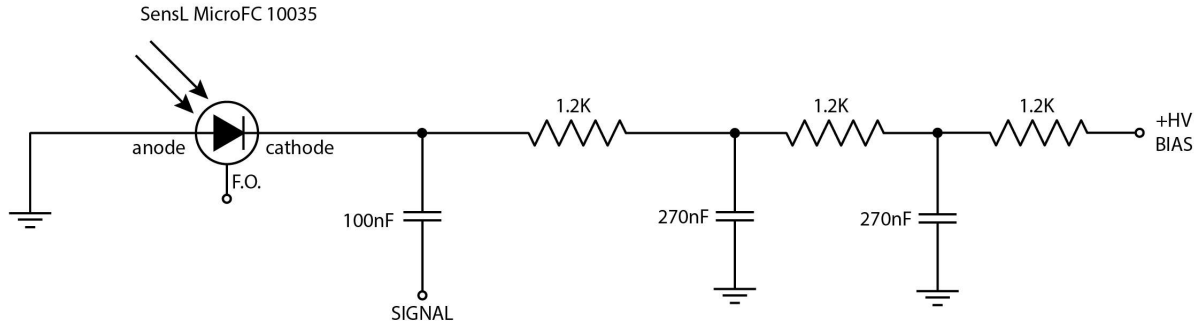


Figure 4-4 Biasing and readout circuit for 1mm² SensL SiPM.

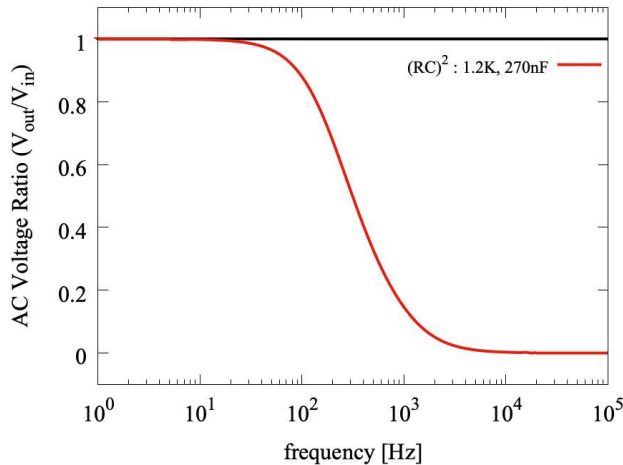


Figure 4-5 Theoretical bias fluctuation attenuation by CRCR filter with resistors of 1.2kΩ and 270nF capacitors. Calculated using Equation 3.4.

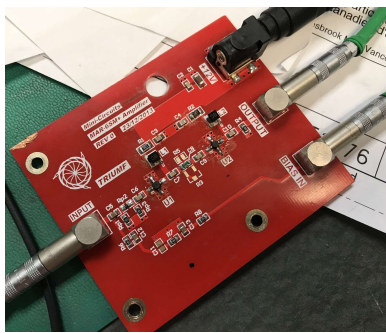
4.2.2. Amplification

The signals produced by a SiPM range from single millivolts to several volts, depending on the quantity of microcells that are firing in response to the detection of light[59, 62]. Additionally these signals are very fast, lasting tens of nanoseconds[62]. Together this presents a formidable amplification problem, requiring very high slew rates, a large bandwidth, and good linearity over a large domain of input current without reaching saturation.

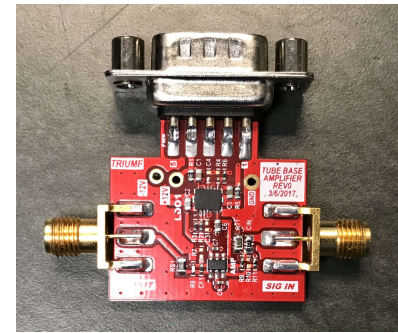
Initially investigations were performed using a fast radiofrequency amplifier before moving on to a charge integrating transimpedance amplifier design for ease of digitisation and the improved linearity of a SiPM's current response. Both are detailed in this subsection.

4.2.2.1. Fast amplification

For fast amplification of the SiPM signals a previously made in-house amplifier design was employed, shown in Figure 4-6a. Based on dual MAR6SM+ monolithic amplifiers from Mini-Circuits, the circuit provides a filtered bias to the SiPM and amplifies an AC-coupled signal by roughly 100 times. The circuit for this fast amplifier is shown in Figure 10-4 of Appendix C.



(a)



(b)

Figure 4-6 (a) Dual MAR6SM+ based fast amplifier board with built in SiPM bias filter. (b) LTC6268-based charge integrating amplifier.

4.2.2.2. Charge integration

To capitalise on the excellent linearity of the current output of SiPMs, a charge integrating amplifier design was developed, based on the Linear Technology LTC6268 500 MHz operational amplifier. This amplifier, shown in Figure 4-6b, achieves a high gain up to 1 MHz, with minimal peaking when operated with a feedback loop of $75\text{k}\Omega$ and 10pF . This is illustrated by the Bode plot of the amplifier's transfer function in Figure 4-7. The circuit for this charge integrating amplifier is shown in Figure 10-4 of Appendix C.

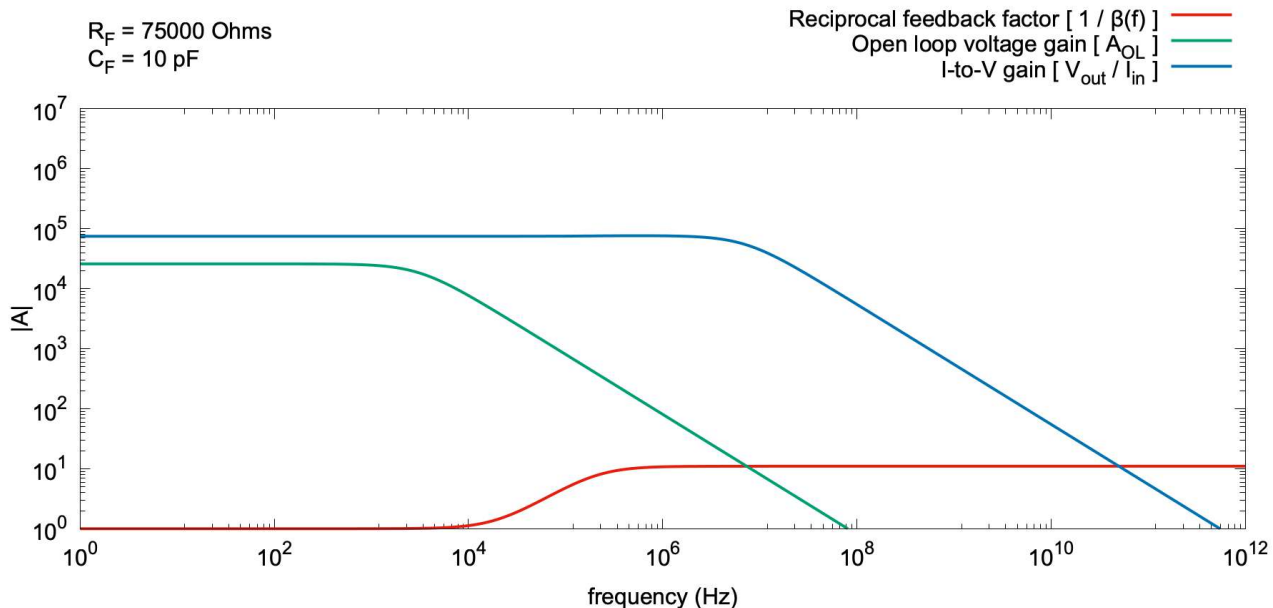


Figure 4-7 Bode plot of the theoretical transfer function, feedback factor and open loop voltage gain of the LTC-6268 amplifier with a feedback loop of $75\text{k}\Omega$ and 10pF . Produced from equations in Section 3.3.2.

4.3. Measured performance

This Section discusses the preliminary acceptance testing of the three MicroFC-SMTPA-10035 mounted SiPMs. The pulse shapes were observed, and dark performance was used to determine their breakdown voltage.

4.3.1. Pulse Shapes

The pulses observed from one of the mounted SiPMs are shown in Figures 4-8 and 4-9. These were taken at 29V which is just under 5 volts of overvoltage according to the manufacturer [59]. There is a clear increase in the rate and magnitude of the produced pulses when the sensor is coupled to a square of BC404 scintillator and exposed to a source of ionising radiation (^{90}Sr).

As expected, the pulses produced by the SiPMs are very fast in both their rise and fall times, and range greatly in their magnitude, especially when coupled to a scintillator and irradiated with a calibration source. The decay constant, which is the product of the quenching resistance and capacitance of the microcells in the SiPM array, can be approximately determined with an exponential fit to the pulse as seen in Figure 4-10. The decay constant of these SiPMs is measured to be 0.0150(1) per nanosecond at an overvoltage of 4.8 Volts. Note that the time constant is dependent on overvoltage, thus not a fundamental property of the SiPM.

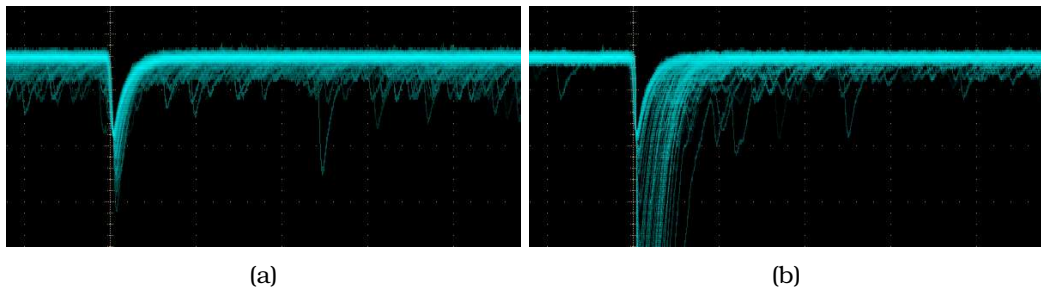


Figure 4-8 Close up of typical SiPM pulse shapes when exposed to (a) dark noise only (b) scintillation light from a 10mm by 10mm by 1.6mm BC404 scintillator irradiated by a Sr90 source. Time (horizontal) divisions: 400ns. Voltage (vertical) divisions 1mV.

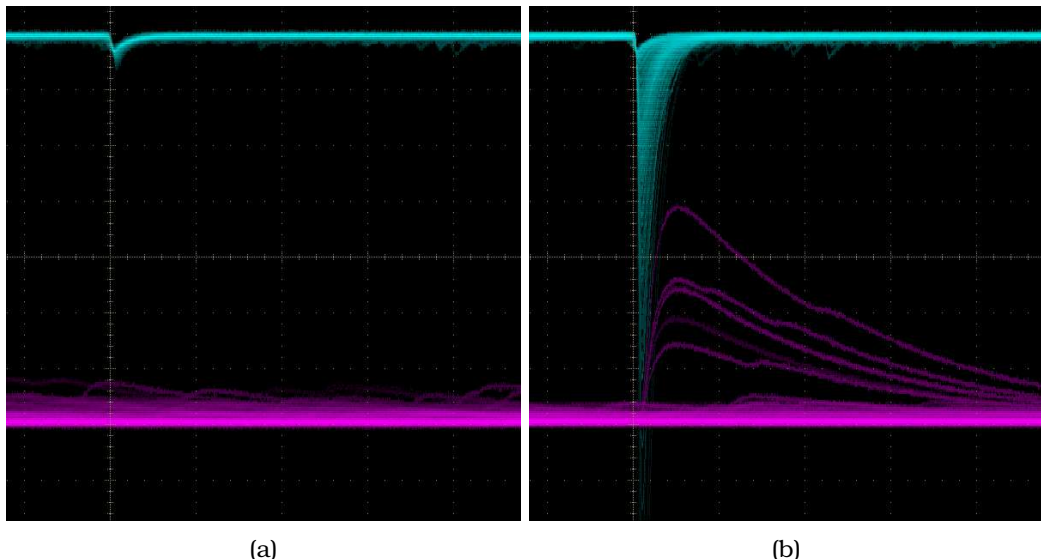


Figure 4-9 Charge integrated signals (pink) and input SiPM pulses (blue) when exposed to (a) dark noise only (b) scintillation light from a 10mm by 10mm by 1.6mm BC404 scintillator irradiated by a Sr90 source. Time (horizontal) divisions: 400ns. Voltage (vertical) divisions 5mV (blue) & 50mV (pink).

4.3.2. Breakdown Voltage

As described in Section 2.1.4.3 and the interim report, the breakdown voltage of a SiPM can be determined by considering its Current-Voltage (IV) characteristics. These are observed by reverse biasing the sensor across its anode and cathode, and observing the current drawn. The current is

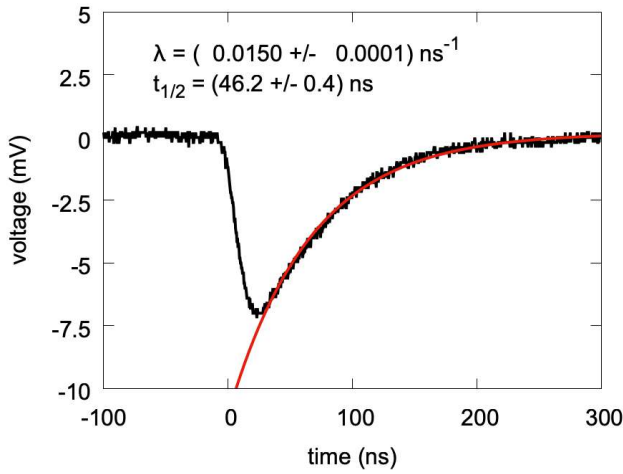


Figure 4-10 An example SiPM pulse with an exponential fit of the pulse's decay. The SiPM was operated at an overvoltage of 4.8 Volts. From this exponential fit, the decay constant is found to be $0.0150(1) \text{ ns}^{-1}$. Hence the half-life is 46.2(4) nanoseconds.

proportional to the square of the overvoltage, until it is out of the recommended operating voltage. A linear fit can be taken of the square root of the current against voltage across the recommended operating range, and the x-intercept will be equal to the Breakdown Voltage (V_{br}). This can be seen in Figure 4-11.

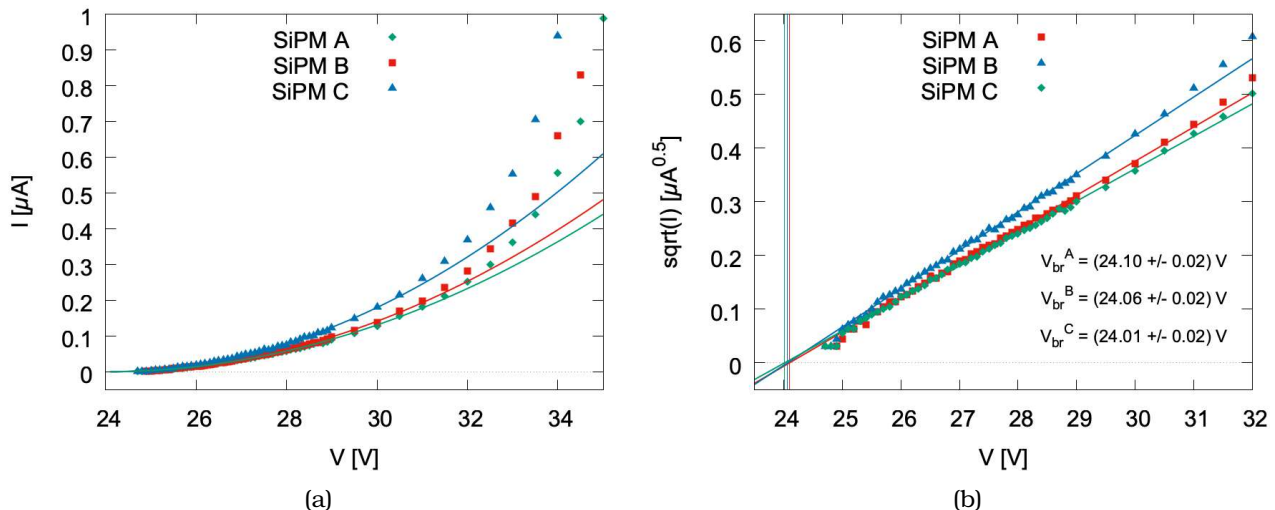


Figure 4-11 Reverse IV characteristics of three SensL SiPMs with 1mm^2 active area and 504 microcells mounted on pin-adapter boards (MicroFC-SMTPA-10035). (a) Leakage current vs biasing voltage. (b) Square-root of the leakage current vs biasing voltage.

Evidently the SiPMs are behaving as expected, and their performance reproduces the manufacturer's behaviour well, as seen in Figure 4-12. This technique has been validated to determine the breakdown voltage with acceptable certainty, and will be used for future sensors as well.

Conclusion

This chapter has outlined the factors informing the component choice of the Silicon Photomultipliers (SiPMs) for use in detecting the scintillation light from the new SCEPTAR II detector array, as well as the methods involved in characterisation of these devices.

In Section 4.1 the reasoning behind the selection of the SensL C-Series SiPM with 1mm^2 active area and $35\mu\text{m}$ microcells (SensL MicroFC-10035) were given. In short, the sensitivity of the SensL

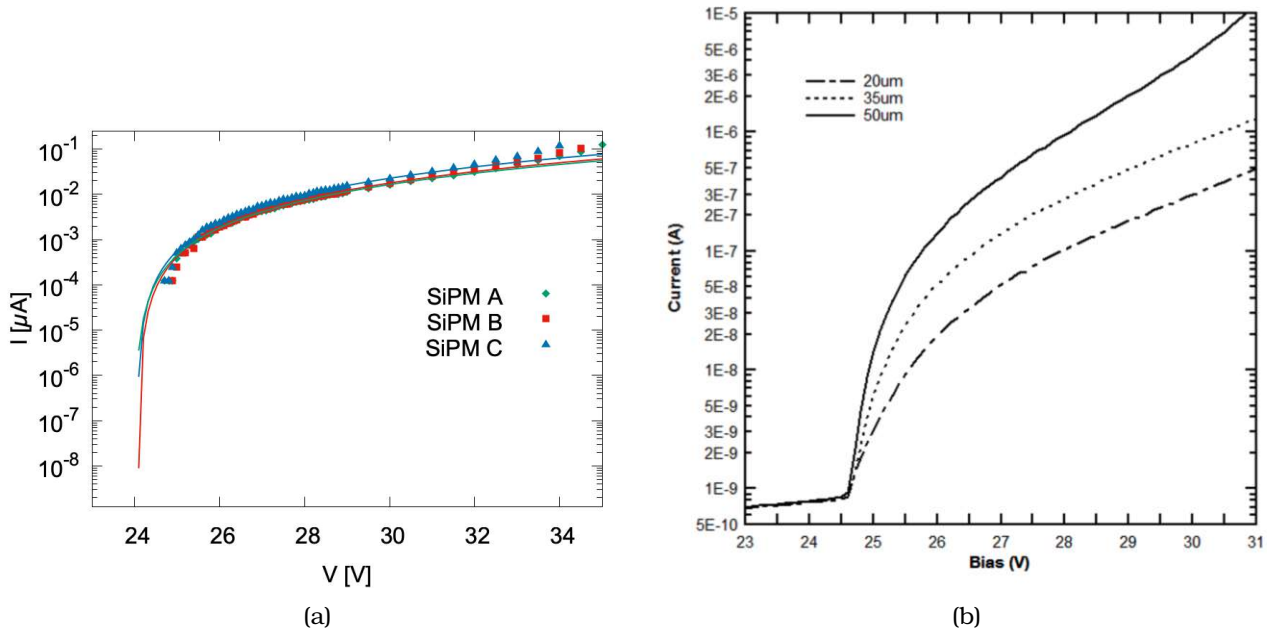


Figure 4-12 Reverse IV characteristics of three SensL SiPMs with 1mm^2 active area and 504 microcells of $35\mu\text{m}$ size mounted on pin-adapter boards (MicroFC-SMTPA-10035). (a) Leakage current vs biasing voltage. (b) Square-root of the leakage current vs biasing voltage[59].

C-Series sensors is highly compatible with the emission spectrum of the Saint Gobain BC404 plastic scintillator, and boasts excellent performance with high gain and PDE even with SensL's smallest sensor size (1mm by 1mm active area).

In the next Section 4.2, various biasing schemes have been presented. The reverse positive HV biasing and AC coupled cathode readout circuit that were employed for all SiPM investigations described in this work was shown in Figure 4-4. Additionally, two amplification schemes are described - one fast radiofrequency amplifier - and one transimpedance (charge-integrating) amplifier.

Section 4.3 applies the characterisation methods described in Section 2.1.4.3 to the three SensL MicroFC-SMTPA-10035 mounted SiPMs ahead of testing with a single scintillator channel in the following chapter. The pulse shapes of the SiPMs with and without charge integration in response to the room background and ^{90}Sr calibration source was observed in Section 4.3.1. The characteristic breakdown voltage of the three sensors was also measured.

5. Single scintillator channel prototyping

Following the investigations into the performance of the SiPMs, their efficiency in detecting scintillation light was explored. For satisfactory performance, the SiPMs should detect the prompt fluorescence from BC404 plastic scintillator with near perfect efficiency, reproduce the calibration source decay spectra obtained with those produced by the original SCEPTAR array and those predicted by **GEANT4** simulations. Factors analysed in this chapter include the effect of varying SiPM biasing voltage, the effect of varying the scintillator surface coating, and the effect of varying the position of the SiPM on the surface of the scintillator.

5.1. Experimental Setup

The investigations documented in this chapter were performed using one of three SensL MicroFC-SMTPA-10035 mounted SiPMs. A 3D printed holding structure, holds a 10mm square BC404 scintillator of 1.6mm thickness so that one surface is almost flush to the front window of the SiPM and can be coupled using optical couplant/grease. Such an arrangement is shown in fig. 5-1 where the SiPM is coupled to the corner of one of the narrow edges.

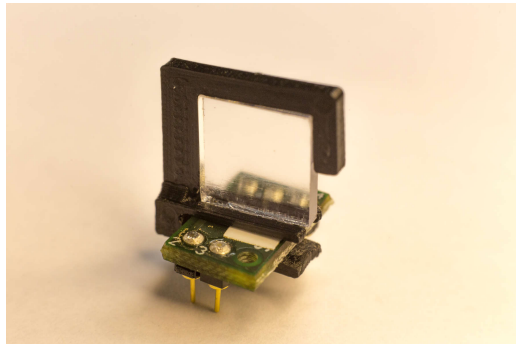


Figure 5-1 10mm by 10mm by 1.6mm BC404 scintillator held by custom 3D printed holding structure attaching to a SensL C-Series SiPM with 1mm^2 active area and $35\mu\text{m}$ micro-cells, mounted on a pin adapter board.

This pin-adapter board was then attached to a prototype board which holds the SiPM anode to ground and the cathode to a filtered and positive HV bias. Signals were taken from the cathode via a 300pF AC-coupling capacitor and integrated using a pre-amplifier. The pre-amplifier was the same design as the charge-integrating transimpedance amplifier detailed in section 4.2.2.2 and given schematically in fig. 10-5 of Appendix C. The 50Ω input termination was achieved via a 51Ω termination resistor and 499Ω input resistance.

5.2. Calibration Source Spectra

To evaluate the effectiveness of the SensL MicroFC-10035 coupled to a 1.6mm thick BC404 scintillator, two calibration sources were used. Both sources ^{90}Sr and ^{207}Bi produce well known electron spectra, and the expected energy deposition in scintillators can be estimated via **GEANT4** simulations. The empirically known decay spectra of these isotopes are described in Section 3.2. Two MCA

spectra are shown in Figure 5-2, one for each of the calibration sources. The SiPMs were biased to 29V which is the maximum SiPM overvoltage recommended by SensL for sensors with a 24V breakdown.

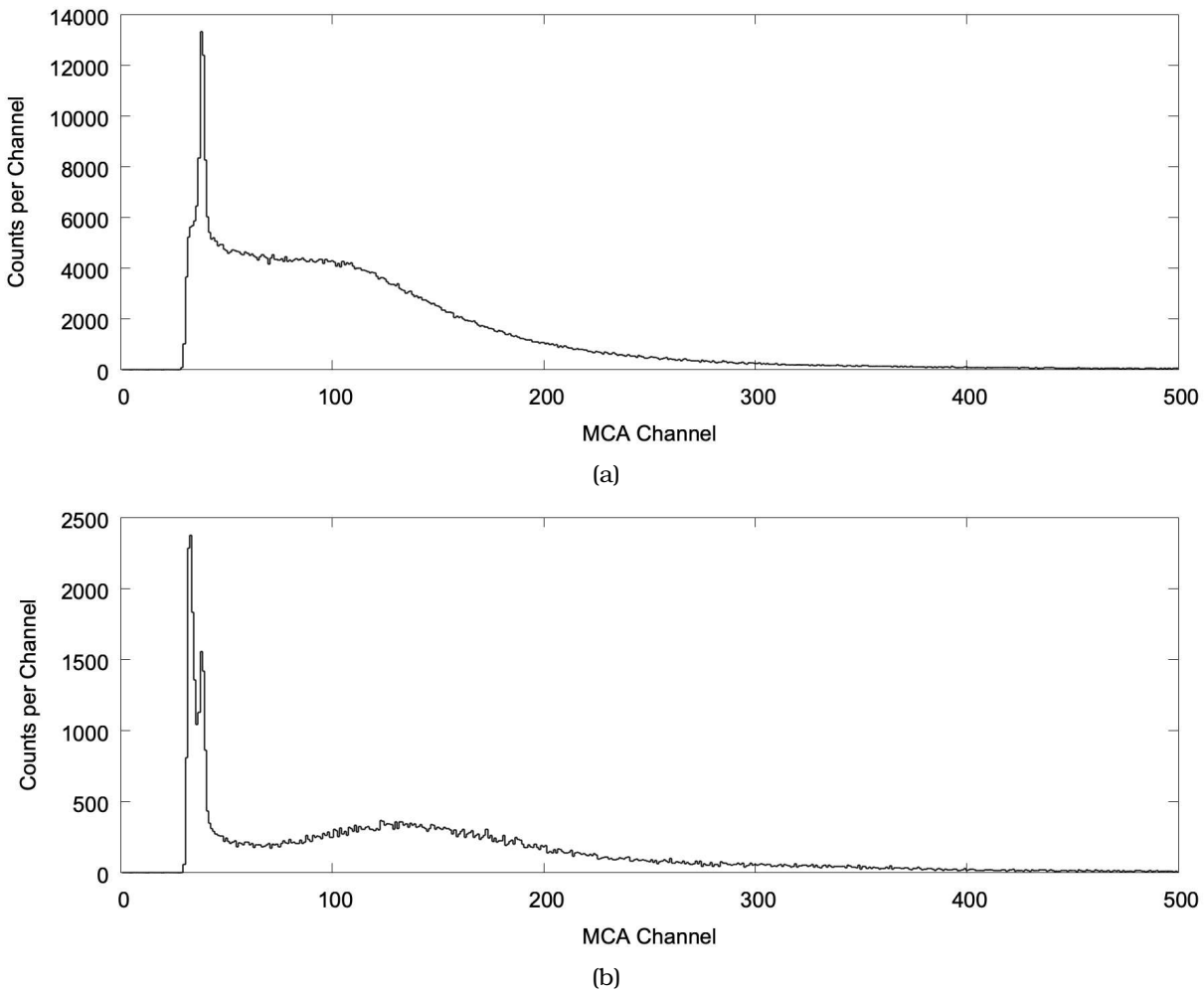


Figure 5-2 Calibration source spectra taken with a 10mm by 10mm by 1.6mm BC404 scintillator and a SensL MicroFC-10035 SiPM. (a) ^{90}Sr . (b) ^{207}Bi .

5.2.1. Comparison to GEANT4 Simulations

Monte Carlo simulations of the experimental circumstances can be used to great effect in understanding the empirical results and verifying the behaviour of the prototype detectors. In this work the `detectorSimulations` application based on the `GEANT4` framework was used. The `detectorSimulations` application has been validated to high accuracy and was used to simulate the single scintillator detector prototypes discussed in this chapter. An introduction to this simulation suite is provided in Appendix A which also gives an exhaustive description of the simulation methodology.

To verify that the spectra produced by the single scintillator prototype are valid, the experimental configuration was simulated in `detectorSimulations`. The plastic scintillator detector volume and the simulated particles by which it is irradiated is shown in Figure 5-3.

Figure 5-4 shows the results of such a simulation. These simulations differ from the known decay spectra discussed in Section 3.2 as the thin scintillator is a ΔE detector. Such a thin scintillator does not capture all the energy of incident electrons. Known as punch-through electrons, these are the cause of the disappearance of high-energy peaks such as the 1682 keV internal conversion decay of ^{207}Bi .

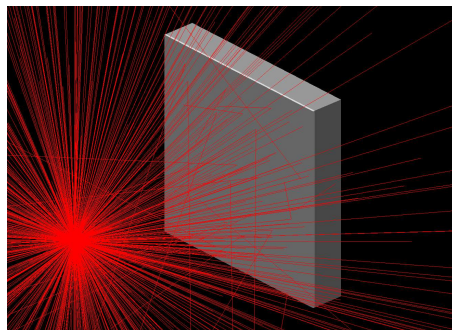


Figure 5-3 **GEANT4** visualisation of single scintillator with layer of foil irradiated by fast electrons.

While certain features of the simulated spectra can be recognised in the prototype's response, further differences arise due to the finite and poor energy resolution of the detector. This adds an uncertainty to the energy value of every captured event, and can be approximated by adding a Gaussian "smear" to simulated spectra. The plots shown in Section 3.2 have **not** been smeared. The non-zero energy resolution of the real detector obscures or modifies features present in the simulation results. For instance, for ^{90}Sr the ~ 400 keV peak in Figure 5-4a is not visible in Figure 5-2a. In the ^{207}Bi spectra, all the discrete internal conversion peaks shown in Section 5.2.1 have been "smeared out" to form the continuum seen in Figure 5-2b.

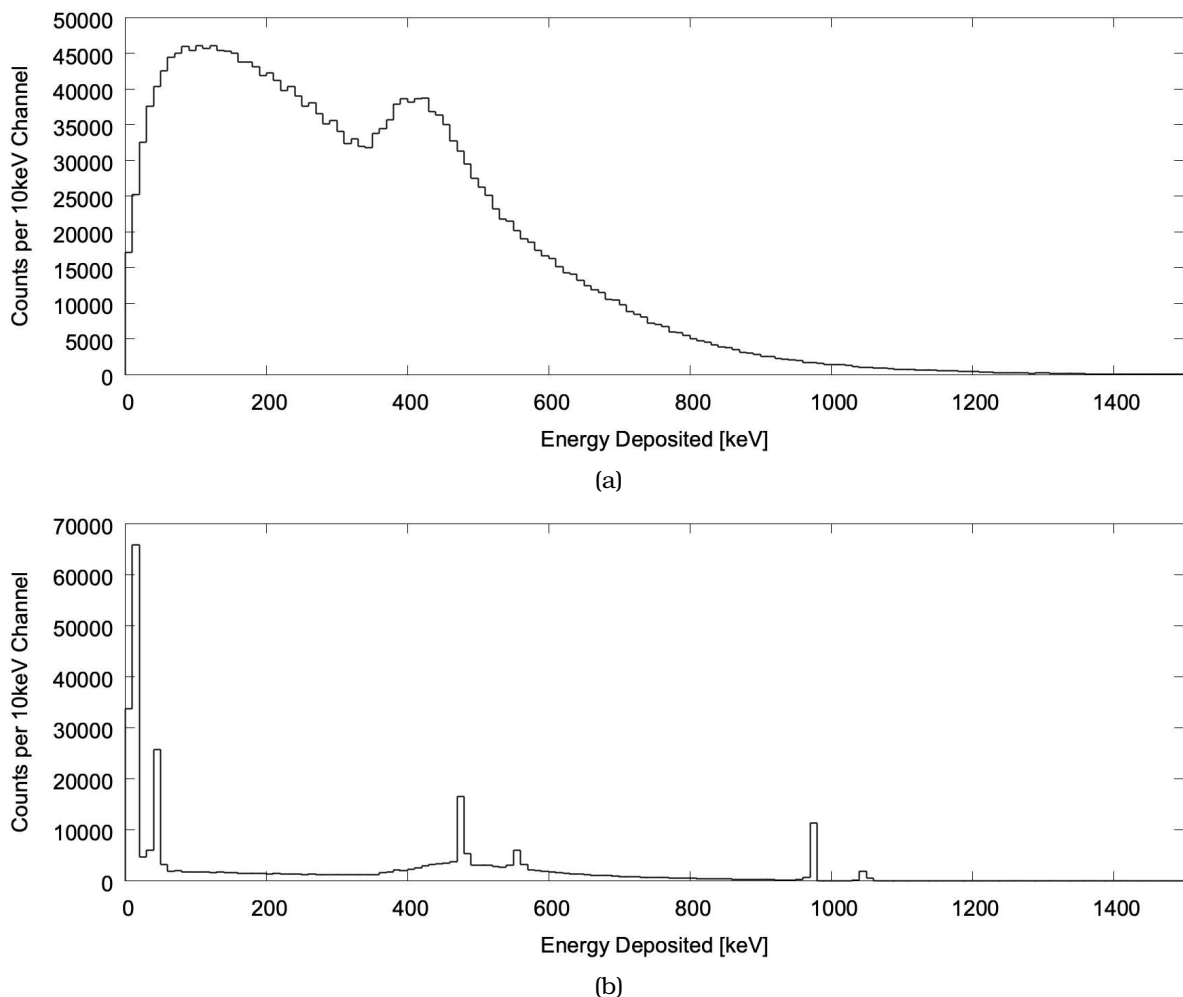


Figure 5-4 **GEANT4** simulation of energy depositions in a single square of BC404 plastic scintillator when exposed to a calibration source. (a) ^{90}Sr . (b) ^{207}Bi .

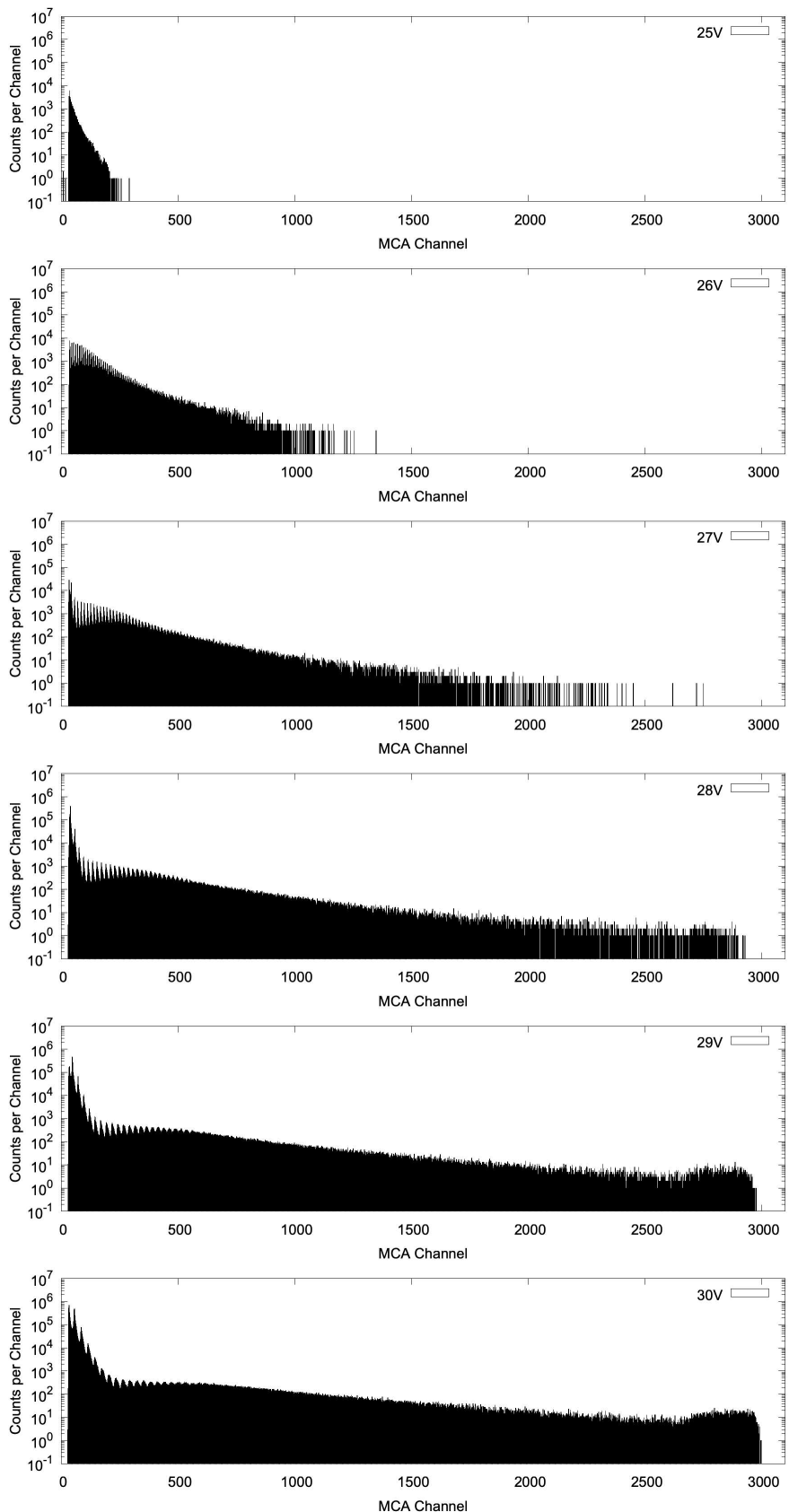


Figure 5-5 Effect of bias voltage on the charge-integrated spectrum produced by a C-Series SiPM coupled to a 1.6mm thick BC404 scintillator exposed to radiation from a ^{90}Sr source.

5.3. Optimising the Prototype Performance

The use of thin scintillators to tag β particles in rare isotope beam spectroscopy, has been proven through studies with the original SCEPTAR system[3, 2, 9], and the use of SiPMs to detect prompt fluorescence from said scintillators is widely accepted in several fields[64, 65, 66, 67]. However, the optimal operating parameters and hardware setup must be determined to make full use of the equipment and produce the best possible results. In this section, work is detailed which investigates several factors affecting performance of the prototype detector. Results from this work were used to inform decisions about the four-channel prototype discussed in the immediately following chapter.

5.3.1. Determining SiPM Biasing Voltage

The first parameter to study is that of the SiPM bias. As almost all of a SiPM's behaviour is determined by its overvoltage and hence bias voltage, it is of high priority to choose the overvoltage early. This ensures a consistent behaviour for the rest of the investigations.

A ^{90}Sr calibration was used in combination with the single scintillator detector arrangement discussed earlier. In one volt increments, data was collected for 5 minutes using an ORTEC easy-MCA which illustrates the effects of different bias potentials. These are seen in Figure 5-5.

As theory and literature suggests, increasing overvoltage increases the gain, noise, and photon detection efficiency of the sensors. This manifests itself in the resultant spectra as follows:

The increasing gain can be observed in the stretching of the ^{90}Sr energy deposition spectrum. As the overvoltage increases, the gain of the sensor increases, this results in an increase in the number of charge carriers per avalanche, and hence pulses of larger magnitude are produced by each microcell. This results in a larger output pulse of the charge-integrating amplifier which will be registered in a higher channel of the ORTEC easy-MCA (pulse height analyser). A calculation of the gain is performed in Section 5.3.1.1.

The increasing contribution of dark noise, i.e. microcell discharges due to thermally excited electrons and not incident photons, can be seen in the emergence and increasing magnitude of the low-channel/low-energy peaks. As the overvoltage increases the acceleration of charge carriers in the SiPM's active area also increases. This increases the probability that thermal electrons will be accelerated above the work function of the Silicon creating a greater number of dark noise counts. The charge of this dark noise is proportional to the number of microcells firing in the SiPM, creating the discrete set of peaks in the low energy region of the spectra.

The increased overvoltage also increases the Photon Detection Efficiency (PDE) of the SiPM. We can see this in the reduced drop in counts which would be expected from increasing the overvoltage. This is elaborated upon in Section 5.3.1.2.

As the gain increases, one can see the amplifier begin to saturate. This is evidenced by a peak beginning to emerge above MCA channel 2500. This is not a concern at this stage of the investigation as the gain of the amplifier can be adjusted once the operating parameters have been determined.

5.3.1.1. Approximating SiPM Gain

By scaling spectra of adjacent overvoltage by a factor k in x and a factor $1/k$ in y until they have approximately constant relative difference across the energy range, the relative gain caused by the one volt increase for each of the studied overvoltages was determined. Then the relative gain between any pair of these voltages can be calculated along with an uncertainty due to the original fitting. Adjusted in absolute magnitude to match the gain curve given by the manufacturer SensL approximate absolute gain of the sensor was obtained. This can be seen in Figure 5-6 and Table 5-1.

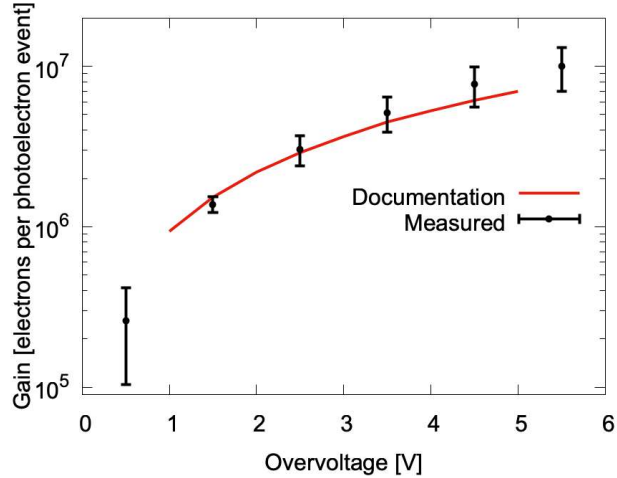


Figure 5-6 Approximated measured gain of a SensL MicroFC-10035 SiPM.

Table 5-1 Approximate gain of a SensL C-Series SiPM with 1mm² active area and 35μm microcells.

O vervoltage	Approximate Gain
1.0	$2.6(1.6) \times 10^5$
2.0	$1.4(0.2) \times 10^6$
3.0	$3.0(0.7) \times 10^6$
4.0	$5.2(1.3) \times 10^6$
5.0	$7.7(2.2) \times 10^6$
6.0	$1.0(0.3) \times 10^7$

5.3.1.2. Evaluating Photon Detection Efficiency of the SiPMs

The increasing gain observed in the previous section results in the general increase in the number of counts in the spectra as biasing voltage is increased. To estimate the Photon Detection Efficiency (PDE), the relative difference in the number of counts in spectra of different voltages can be compared to the expected increase due to gain alone.

For an electron of energy E , its detection creates a count which occupies channel n in the MCA's histogram. Supposing that increasing the overvoltage by one Volt increases the gain by a factor k , the energy E now corresponds to some channel kn . However, as the spacing of the histogram bins increases one would expect that the number of counts in bin kn at voltage $V + 1$, N_{kn}^{V+1} is equal to $\frac{1}{k}N_n^V$.

For the spectra presented in Figure 5-5 and by considering the approximate gain determined in Section 5.3.1.1 it is clear that the PDE must be increasing. Considering for example channel 1000 in the 28V spectrum. Increasing the overvoltage to 29V produces a 50% increase in the gain. Now we compare the counts in channel 1500 of the 29V spectrum and see that it less than 10% lower in population, far lower than the one third decrease expected if PDE remains unchanged. Ergo, the PDE must be increasing. Thus we have verified the manufacturer's claims that PDE increases with overvoltage.

5.3.1.3. Recommendation for SensL MicroFC-10035 Operating Bias

As the overvoltage increases, diminishing returns start to appear in the gain and PDE. Above the maximum recommended overvoltage (5V) the dark count rate rapidly increases with voltage (see Section 4.3.2)[27, 28, 59]. For these reasons, operating the SensL MicroFC-10035 SiPMs at five volts of overvoltage is recommended. As seen in Figure 5-5, a satisfactory calibration source spectrum

can be obtained with this biasing scheme.

5.3.2. Comparing Various Scintillator Surface Treatments

An important consideration in optimising the detector performance is maximising the light collection. Scintillation light is released isotropically in all directions from the point of interaction[68]. To ensure that as much of the scintillation light as possible reaches the photodetector, the surfaces of the scintillator can be coated, leaving a window for the SiPM. One option is to paint the scintillator with a white reflective paint. Produced by the same manufacturer as the scintillator itself, the BC620 diffuse reflector paint contains titanium oxide (TiO) as a pigment offers excellent reflectivity over the range of emission of the BC404 plastic scintillator. Figure 5-7 shows how such a scintillator is masked and the result of using an airbrush to apply the TiO paint. An alternative is to use a reflective aluminium coated Mylar foil, which would provide specular reflection at the expense that some photons may be lost due to the unavoidable gap at the scintillator interface. In addition, an option for the final detector is to use an evaporator to coat the scintillator surface directly with a thin layer of Al.

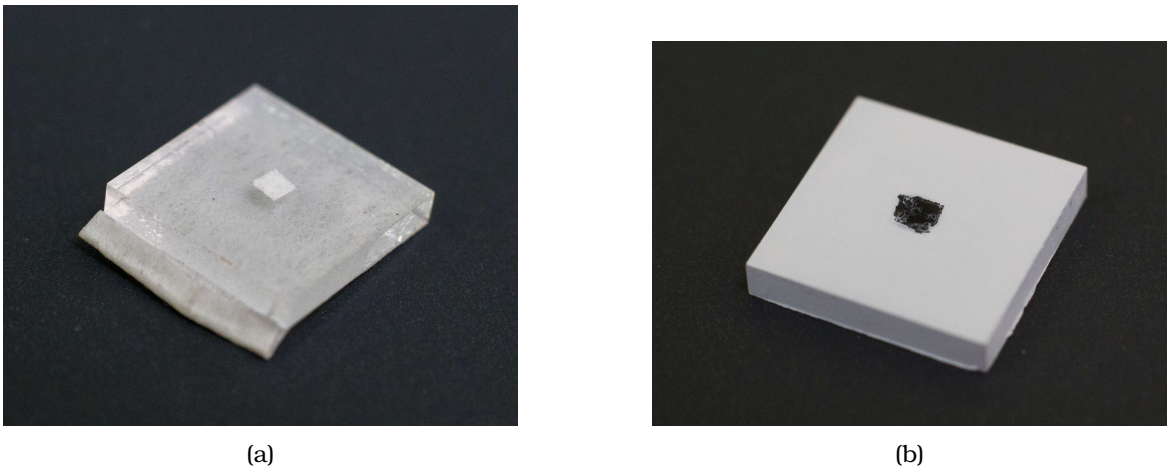


Figure 5-7 (a) Scintillator masked for painting. (b) Painted scintillator.

The introduction of any material in front of the scintillator however will result in the attenuation of incoming radiation. Therefore, it is favourable to introduce the minimum amount of material while maintaining the desired performance.

The four configurations investigated are listed below:

- Bare BC404
- Painted with TiO paint (thickness $\sim 60\mu m$, diffuse reflection) on all faces except the front.
- Painted with TiO paint (thickness $\sim 60\mu m$, diffuse reflection) on all faces except the front and the front face covered with $85\mu m$ Aluminised Mylar foil (Al. thickness $\sim 500\text{\AA}$, specular reflection)
- All faces painted with $90\mu m$ TiO paint (diffuse reflection)

The bare scintillator is used as a control. The fully painted configuration should be ideal in terms of light collection, but may result in more attenuation than desired and may have unfavourable timing performance.

Figure 5-8 shows four ^{90}Sr energy spectra, one for each of the configurations listed above. Taken at 29V with the same SiPM mounted on a corner of the large rear face of the scintillator.

The results in Figure 5-8 show a clear improvement to the detection efficiency due to the introduction of any reflective material on the scintillator's interfaces. Painting the back and sides with TiO provides a marginal improvement to the number of detected counts in the lower-half of the

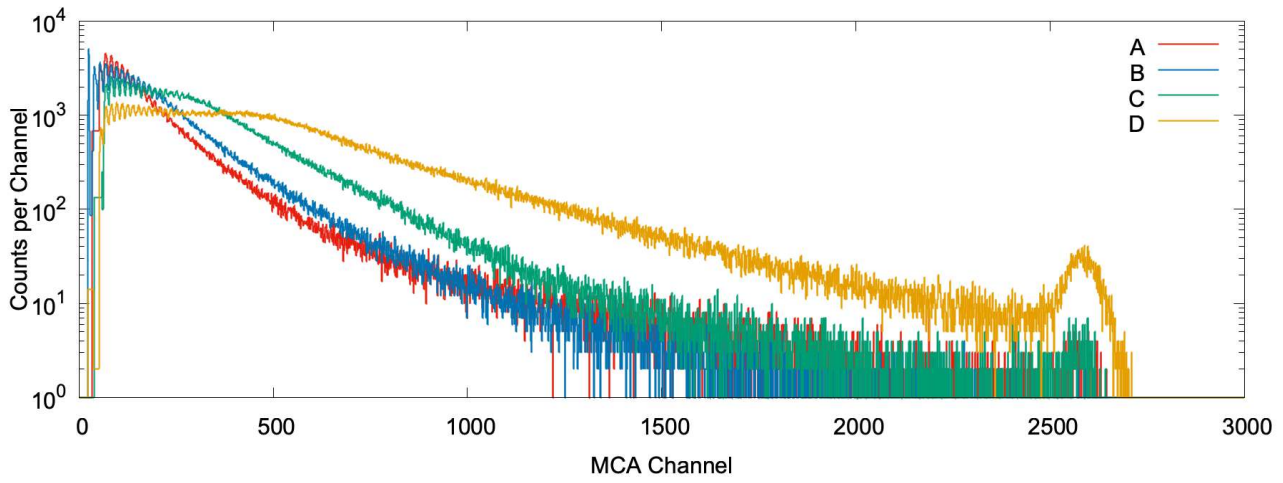


Figure 5-8 Comparison of four scintillator surface treatments: (A) Bare BC404 (B) Back and sides painted with TiO paint (thickness $\sim 60\mu\text{m}$), front face bare (C) Back and sides painted with TiO paint (thickness $\sim 60\mu\text{m}$), front face covered with $85\mu\text{m}$ Aluminised Mylar foil (Al. thickness $\sim 500\text{\AA}$) (D) All faces painted with $90\mu\text{m}$ TiO paint.

spectrum. Covering the front face with the Aluminised foil provides another improvement over a similar energy domain. The greatest improvement over the entire energy spectrum is obtained by covering all faces with the diffuse white TiO paint. The latter two configurations, however, also exhibit signs of attenuation due to the metal in the foil and paint. This deforms the shape of the spectrum at the lower energy ranges by attenuating the least energetic electrons.

5.3.3. Determining Optimal SiPM Positioning

Another factor involved in the efficient collection of scintillation light, is the size and position of the photodetector. The origin of the scintillation light can be assumed to be evenly distributed in the volume. The density of photon strikes on one of the scintillators interfaces is higher at its boundaries, resulting in the highest density at the corners of the surfaces[68].

One can explain this behaviour by considering short paths to various points along the scintillator. Figure 5-9a shows a point in the middle of the rear face of the scintillator. The simplest path requiring only one reflection is path **1**, possible with specular and diffuse reflection, this path is possible for any point on the rear face. Path **2** involves a reflection from one of the side surfaces and is also possible with both specular and diffuse reflection. Conversely, path **2** does benefit from a shorter path and hence larger solid angle of the virtual image of the sensor, from being closer to the side of the scintillator as seen in Figure 5-9b. The third path, which requires diffuse reflection also increases in probability with proximity to the sides. Since each point in the scintillator is initially reached with equal probability to any other, the increased probability of reflected rays reaching the same position at the corners results in a higher density known as edge enhancement. This is true also by extension for the side faces although all paths are on average longer, see Figure 5-9c.

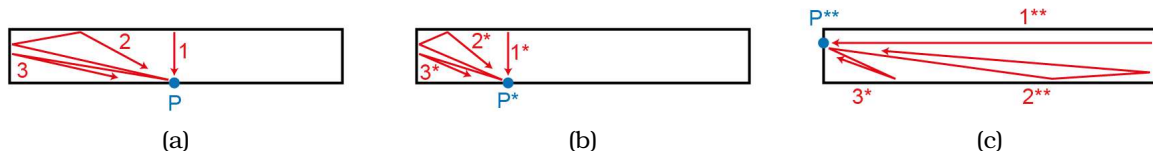


Figure 5-9 Examples of short paths to a point on a scintillator of proportions equal to those studied in this work. See text for details. (a) Point at middle of the large rear face. (b) Off-centre point on the large rear face. (c) Off-centre point on a smaller side face.

Figure 5-10 shows ^{90}Sr energy spectra taken with different SiPM placements on the scintillator.

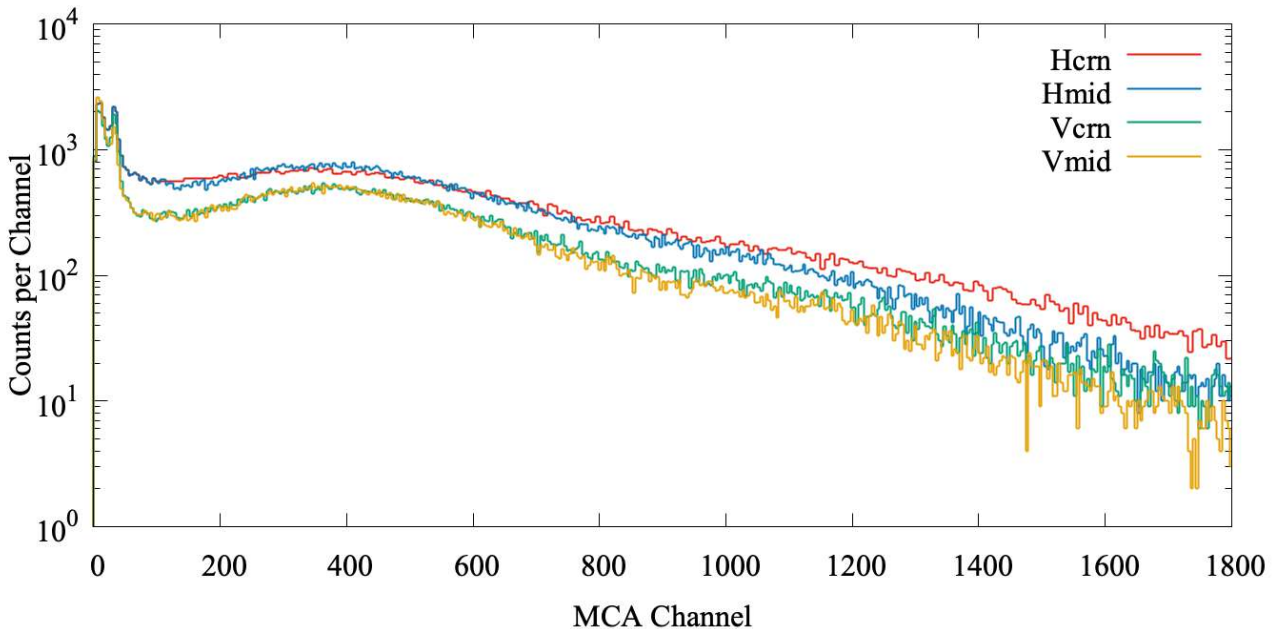


Figure 5-10 Effect of SiPM position on the charge-integrated spectrum produced by a C-Series SiPM coupled to a 1.6mm thick BC404 scintillator exposed to radiation from a ^{90}Sr source. The scintillator was painted with TiO paint (thickness $\sim 60\mu\text{m}$, diffuse reflection) on all faces except the front and the front face covered with $85\mu\text{m}$ Aluminised Mylar foil (Al. thickness $\sim 500\text{\AA}$, specular reflection)

As suggested by theory, for either face an improvement is seen when moving the sensor to the corner of the face. A more significant decrease in performance is seen when the SiPM is moved to the side face.

Conclusion

This Chapter has detailed the investigations with the first SCEPTAR II prototype, made up of a single 10mm by 10mm by 1.6mm BC404 scintillator coupled to a SensL MicroFC-SMTPA-10035 SiPM by means of a 3D printed holding structure.

Investigations into the effects of physical parameters such as the surface treatment and SiPM positioning on the detector performance were carried out. It was determined that the maximum overvoltage recommended by SensL produced the most satisfactory calibration source spectra in response to ^{90}Sr and ^{207}Bi (See Section 5.3.1). These results were further validated by comparison to **GEANT4** simulation results which, while not identical, had characteristic features recognisable in the empirical data. The gain and PDE of the sensors was also estimated (See Section 5.3.1).

As for the scintillator treatment, a coating all over the scintillator with diffusely reflective titanium oxide (TiO) paint, provided the most efficient capture of scintillation light (See Section 5.3.2). The optimal SiPM position was found to be on the rear of the scintillator, with the corner offering a narrow improvement to other locations on the rear face (See Section 5.3.3).

The next Chapter builds upon the findings with a four-channel prototype which allows for the investigations into multi-channel operation, as well as measure the improvements due to more robust production, and the deterioration due to longer signal pathways that would be more applicable to the final detector design.

6. Four scintillator channel prototype

In the previous chapter we have determined that the combination of the SensL C-Series SiPM with 1mm^2 active area and $35\mu\text{m}$ microcells with 10mm by 10mm by 1.6mm BC404 plastic scintillator worked satisfactorily for the purposes of the SCEPTAR II detector. The optimal biasing voltage, surface coating, and SiPM position were also determined. In this chapter, a further prototype was developed to investigate the performance of several SiPM channels operated simultaneously. The purpose of this prototype was to take the conclusions from the previous investigations and to develop a mock detector which more closely resembled the design of the final SCEPTAR II array. The four scintillators each with SiPM light detection resembles the design of the SCEPTAR II array, but reduced to one GRIFFIN HPGe clover-type detector with four crystals. A vacuum chamber was also assembled with a section of beampipe which emulated the $\sim 53\text{ cm}$ distance between the feedthrough flange and detector. The vacuum characteristics of the chamber were also investigated.

6.1. Experimental Setup

This section describes the experimental setup used to take the measurements in the remainder of this chapter.

6.1.1. Detector Prototype

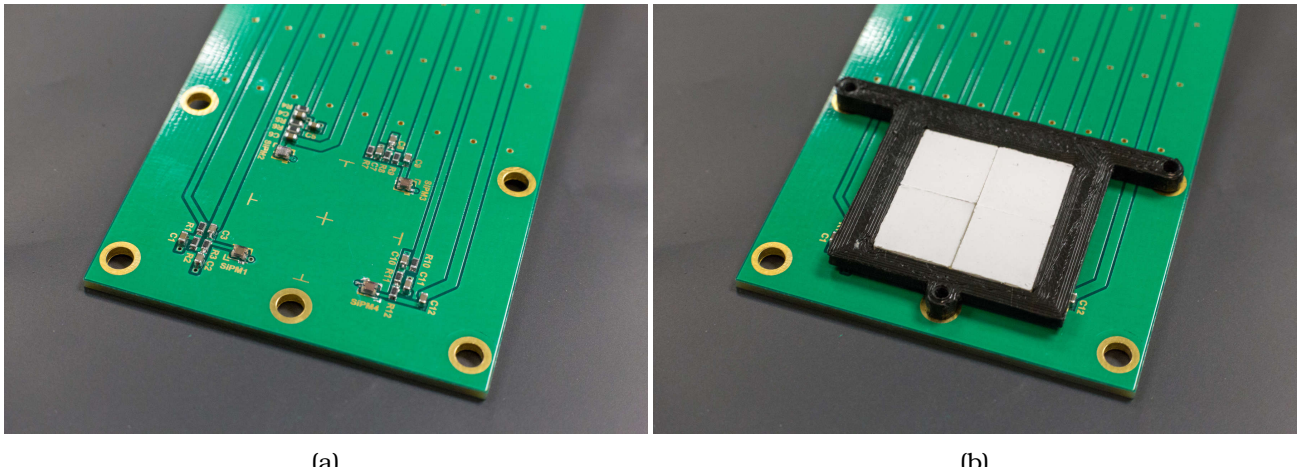
Two populated prototype boards were constructed, each with the following properties: Four of the previously investigated SensL MicroFC-10035 1mm^2 SiPMs were mounted on a long custom printed circuit board along with a low-pass filter circuit for the SiPM bias and ac coupling capacitor for the SiPM readout for each of the sensors. The prototype board is shown in Figure 6-1 with and without the scintillators. The scintillators in question were once again 10mm by 10mm by 1.6mm St. Gobain BC404 polyvinyltoluene-based plastic scintillators and coated with a layer of TiO paint on all surfaces.

The circuitry for a single SiPM channel is shown in Figure 4-4. All of these components are at the detector end of the prototype board (see Figure 6-1a).

6.1.2. Scintillator Treatment

As determined in the previous investigations, the use of St. Gobain BC620 reflective (TiO-based) paint on all surfaces results in efficient scintillation light-collection in the SiPM. A small opening was left on the corner of the rear scintillator face for the SensL MicroFC-10035 (see Figure 6-2).

To increase the accuracy of the **GEANT4** simulations, the titanium metal in the paint should be included in the detector definition. The thickness of the paint was calculated from precise measurements of the width and depth of the scintillator before and after painting. Each measurement after painting represents two paint layers on each side of the scintillator. The single paint layers on the top and bottom of the scintillator were found to be 98(1) microns thick on average. The results are shown graphically in Figure 6-3.



(a)

(b)

Figure 6-1 (a) Four SensL C-Series SiPM with 1mm^2 active area and $35\mu\text{m}$ microcells prototype board. (b) Four SensL C-Series SiPM with 1mm^2 active area and $35\mu\text{m}$ microcells prototype board with 10mm by 10mm by 1.6mm BC404 scintillators held by a 3D printed structure.

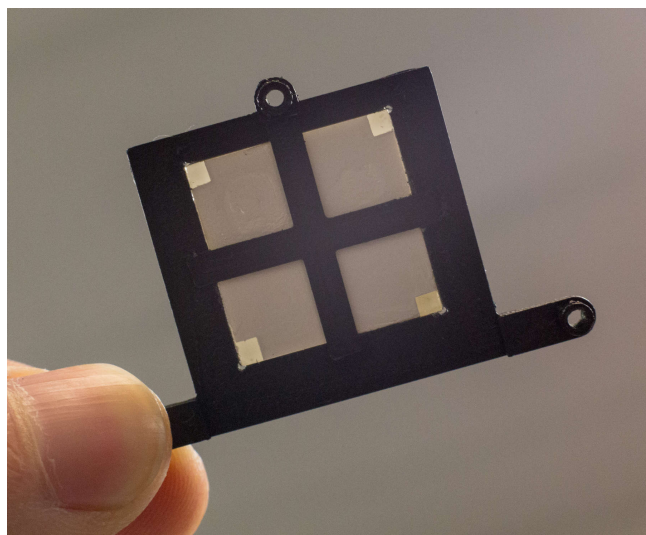


Figure 6-2 The four 10mm by 10mm by 1.6mm St. Gobain BC404 polyvinyltoluene-based plastic scintillators and coated with a layer of TiO paint on all surfaces, mounted in the 3D printed prototype mounting structure. A window is left for the paint on one rear corner of each scintillator.

6.1.3. Vacuum Chamber

The vacuum chamber, is centred around a large cubic chamber made with inch-thick steel with internal dimensions roughly 8" cubed. The chamber has two Marmon openings. On one end a Kurt J. Lesker KJL275807LL Convection Enhanced Pirani vacuum gauge and Varian TRISROLL 300 scrollpump are attached via various adaptors. On the other side a 17" section of spare beampipe was connected, ending in a custom Marmon feedthrough flange with a 34-pin connector. The chamber can be seen in Figure 6-4.

6.1.4. Other Components

Not shown in the figures above, are the biasing and readout electronics. A pigtail with 16 BNC connectors was used to pass bias and receive signals from the detector prototype via the 34-pin connector. A mesytec MHV-4 4-channel high precision bias supply was used to supply the positive $<30\text{V}$ bias to the SiPMs.

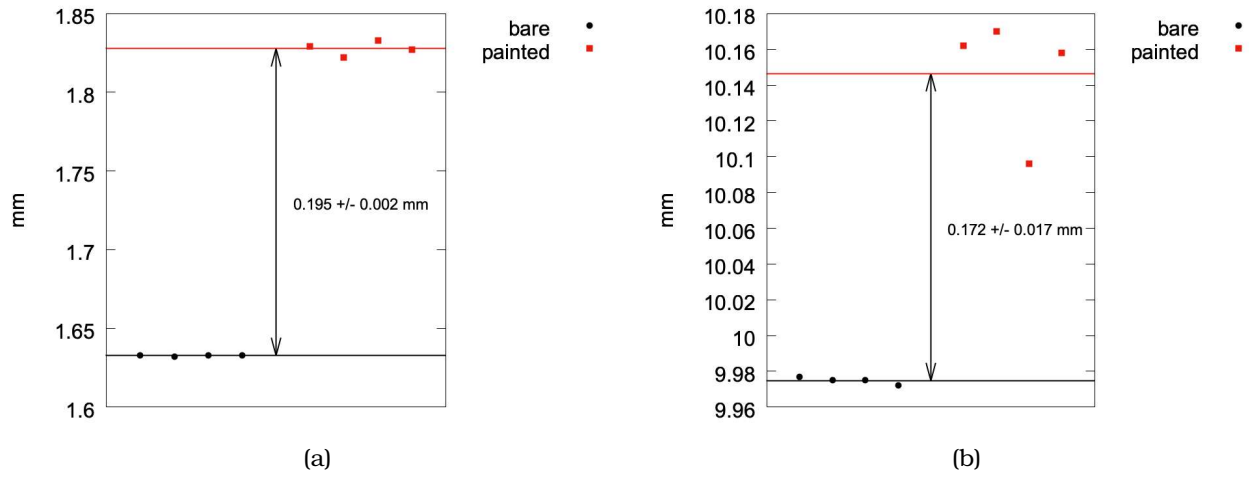
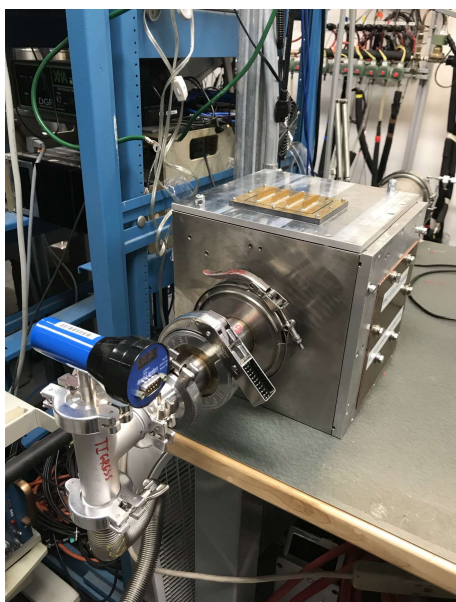


Figure 6-3 Measurements of scintillator dimensions before and after painting. (a) Thickness/Depth. (b) Width.

The signals read from the cathode of the SiPMs by an AC coupling capacitor were integrated and amplified by a pre-amplifier. The pre-amplifier was the same design as the charge-integrating transimpedance amplifier detailed in section 4.2.2.2 and given schematically in fig. 10-5 of Appendix C. Various input and termination resistances were investigated, all of which maintained an approximate 50Ω amplifier input impedance. The output from the pre-amplifier were digitised using an ORTEC easy-MCA with 8192 channels.



(a)



(b)

Figure 6-4 The prototype vacuum chamber assembled to test the SCEPTAR II prototypes. (a) Visible: various adapters and a Kurt J. Lesker KJL275807LL Convection Enhanced Pirani Vacuum Gauge. (b) Visible: Marmon flange with 34-pin feedthrough.

6.2. Investigations

This section details the SiPM characterisation, determination of pre-amplifier input and termination resistances, and the vacuum characteristics of the four-channel prototype.

6.2.1. SiPM Characterisation

The SiPMs on the two prototype boards were characterised by the determination of their breakdown voltage as described in Section 4.3.2.

The results from such an investigation are shown in Figure 6-5, where “B1” denotes the first SiPM on the second prototype board. The approximately quadratic dark current above the breakdown voltage and deviation above an overvoltage of ~ 6 V is consistent with the behaviour of the other seven SiPMs and matches earlier results and manufacturer’s specifications.

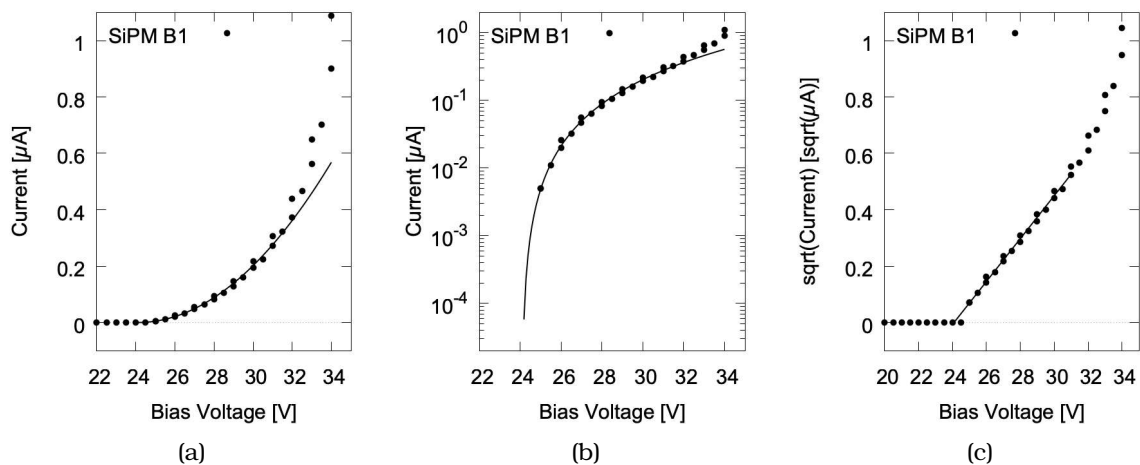


Figure 6-5 IV characteristics of one the SensL MicroFC-10035 channels of the four-scintillator SCEPTAR II prototype. (a) Dark current vs bias voltage. (b) Semi-log plot of dark current vs bias voltage. (c) Square root of dark current vs bias voltage.

The breakdown voltage for all eight SensL MicroFC-10035s is shown in Figure 6-6.

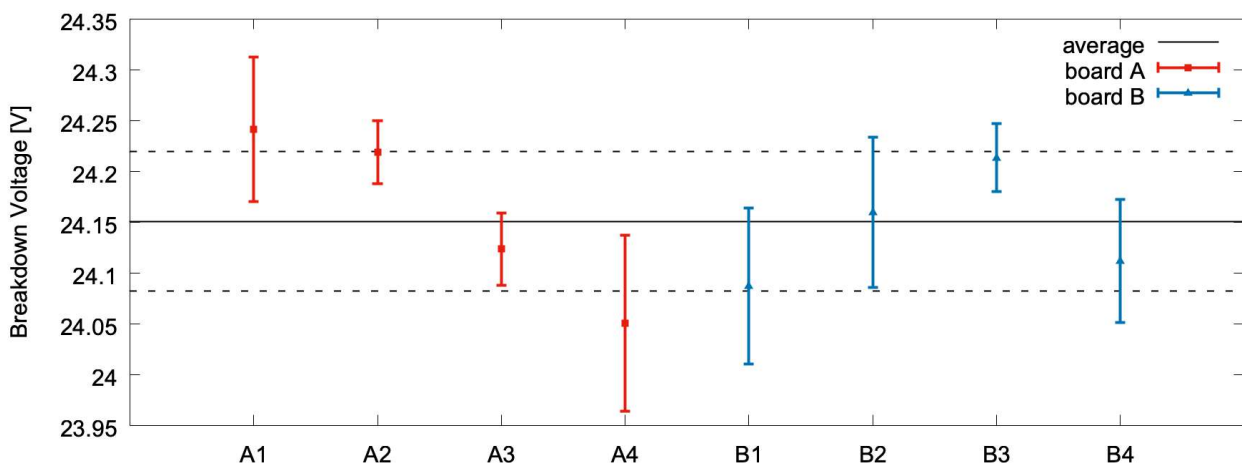


Figure 6-6 Comparison of the eight SensL C-Series SiPM with 1mm^2 active area and $35\mu\text{m}$ micro-cells tested in this chapter. Shown with the average and standard-error.

The spectra obtained from the prototype board B, when exposed to a ^{90}Sr source in air are shown in Figure 6-7. It can be seen that while the spectra are similar, the slightly increased breakdown voltage of SiPMs B2 and B3 results in a reduction in gain.

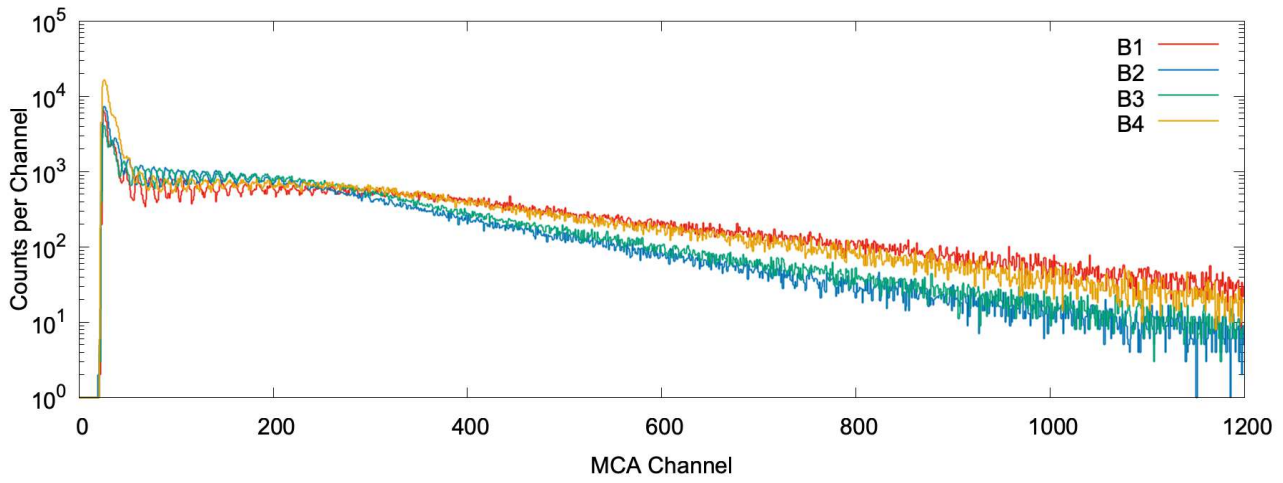


Figure 6-7 Comparison of the ^{90}Sr energy spectra taken with the four scintillator channels of the detector prototype B.

6.2.2. Tweaking Charge Integrating Amplifier Parameters

In previous investigations, SiPM signals corresponding to particularly energetic electrons have saturated the charge-integrating pre-amplifier input. To alleviate this, the input and terminator resistors can be modified, resulting in a change to the fraction of the signal's current being integrated. See Section 3.3.2.1 for this calculation. The optimal resistor values will reveal more of the low-energy behaviour while avoiding saturation of the preamp. In Figure 6-8 several terminator and input resistor values are compared. The effective input impedance and input current ratio are shown in Table 6-1.

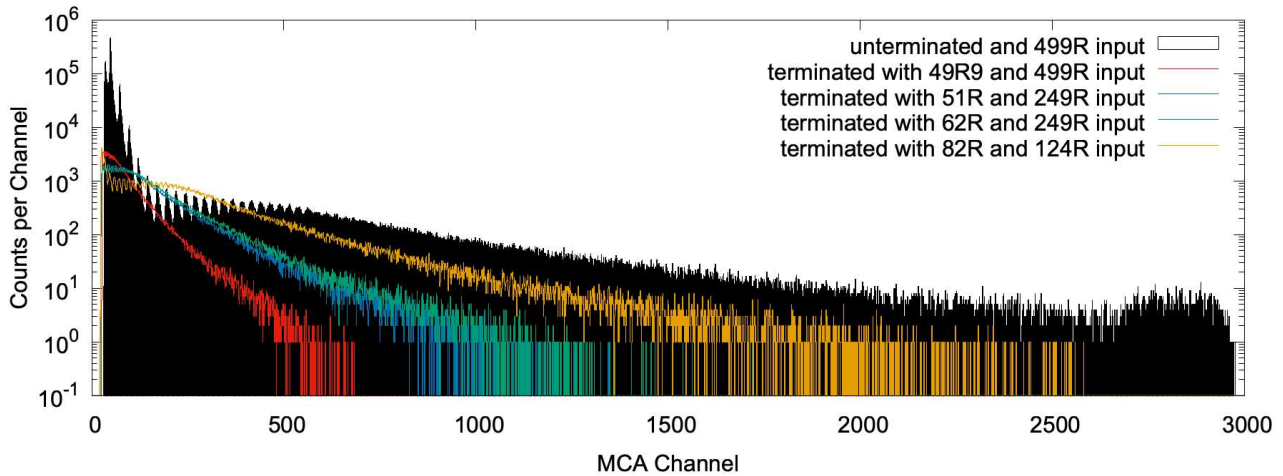


Figure 6-8 The effect of varying the charge integrating amplifier's input impedance and gain.

Table 6-1 Properties of charge-integrating amplifier with various input and termination resistances.

Input Resistance (Ω)	Termination Resistance (Ω)	Input Impedance (Ω)	Input Current (I_{IN}/I_{SiPM})
499	∞	∞	1.00
499	49.9	45.4	0.10
249	51.0	42.3	0.20
249	62.0	49.6	0.25
124	82.0	49.4	0.66

The final configuration, with an input resistance of 124Ω and an effective input impedance of 49.4Ω produces a ${}^{90}\text{Sr}$ spectrum that occupies a large range of the pre-amplifier's input without reaching saturation.

6.2.3. Vacuum Characteristics

The vacuum chamber was initially pumped down with no contents, in order to confirm that the chamber was sufficiently sealed. The pressure during this pumping can be seen in the black curve of Figure 6-9.

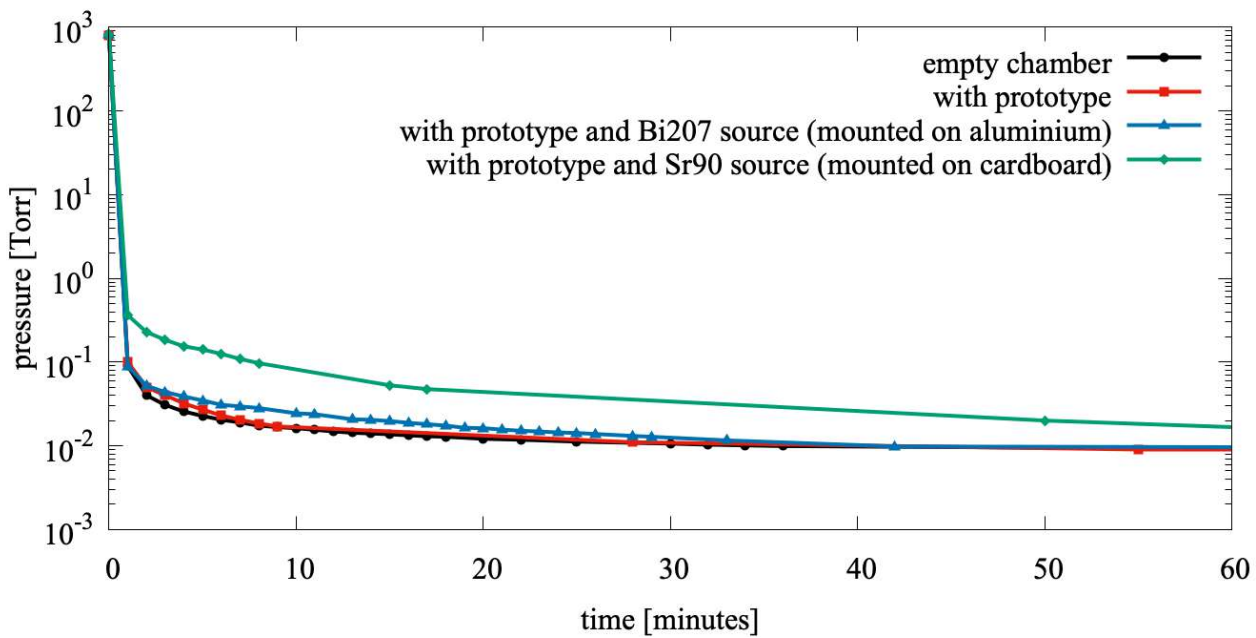


Figure 6-9 Vacuum pressure inside prototype chamber immediately after powering on the Varian TRISCROLL 300 scrollpump, comparison between different contents.

The prototype was then placed in the vacuum chamber and the Varian TRISCROLL 300 scrollpump was again powered on. The red curve in Figure 6-9 shows that the introduction of the prototype board, steel stand-offs, 3D printed scintillator holding structure (PLA), and painted scintillators did not exhibit a significant amount of outgassing. The chamber reached pressure equilibrium at a similar rate with the prototype, as it did empty. The introduction of the calibration sources did, however, increase the time until equilibrium, but only by up to two hours, with the ${}^{90}\text{Sr}$ source taking the longest (due to it being mounted on a strip of cardboard). A qualitative comparison between the outgassing and time until pressure equilibrium can be obtained from the time taken to reach a given pressure. Table 6-2 shows the time since the scroll pump's activation until a pressure below 10 mTorr is achieved. Increasing uncertainties are due to linear interpolation between data points.

Table 6-2 Time until a vacuum pressure below 10 mTorr was achieved with various prototype configurations.

Configuration	Time since pump activation [minutes]
Empty Chamber	37(1)
With Prototype	41(2)
With Prototype and ${}^{207}\text{Bi}$	78(6)
With Prototype and ${}^{90}\text{Sr}$	94(10)

Figure 6-10 shows ${}^{90}\text{Sr}$ calibration source spectra taken at different pressures. The calibration

source was kept at \sim 15 mm distance from the front face of the scintillators. As expected, the removal of air from the chamber reduces the attenuation of the electrons, increasing the counts in each MCA channel. The spectrum is otherwise very similar.

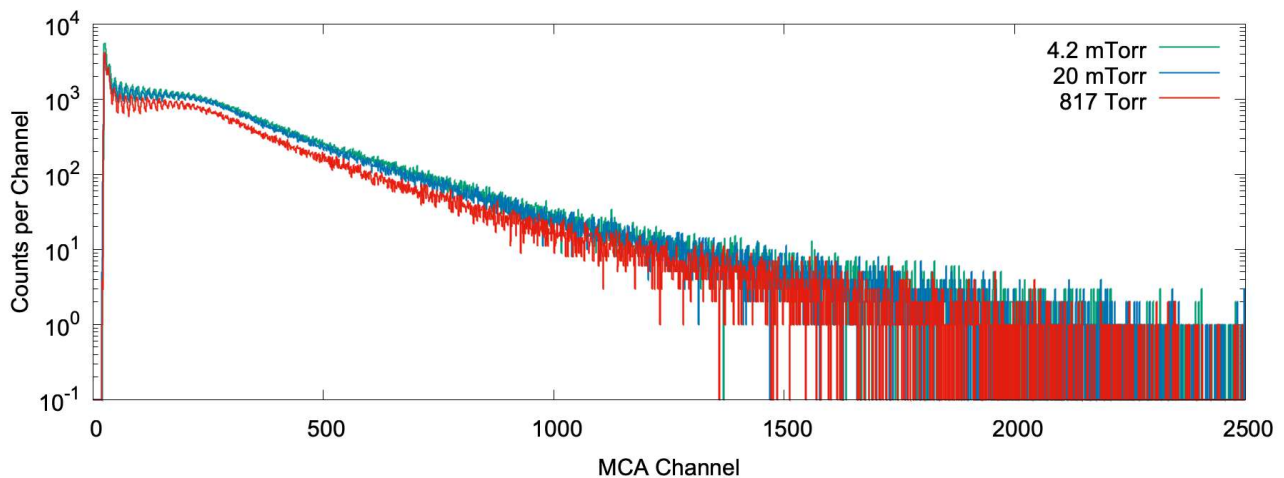


Figure 6-10 Sr90 spectrum at three different vacuum states: at atmosphere (817 Torr), after about 20 minutes of pumping (20 mTorr), and after several hours of pumping (4.2 mTorr).

6.3. Detector Response to Calibration Sources

Figure 6-11 shows the response of one of the prototype detector channels to ^{90}Sr and ^{207}Bi calibration sources, and taken with a positive bias of 29V and at a vacuum pressure of 4 mTorr. Additionally, a spectrum taken with this channel with no source was used to determine the impact of dark noise and room background radiation. Taken for the same duration as the measurements with a source present, these backgrounds were subtracted from the calibration source spectra spectra.

6.3.1. Comparison to GEANT4 Simulations

The prototype detector was simulated in `detectorSimulations` (a `GEANT4` simulation program, see Appendix A). Following this, an energy smearing was applied using `NTuple2EventTree` (see Appendix A) which emulates the non-ideal energy resolution that is typical of plastic scintillators. The polynomial smearing curve is given in Equation 6.1.

$$s(E) = 400 + 0.0005 \cdot E^3 \quad (6.1)$$

Where E is the energy deposited in the scintillator in units of keV.

Comparing the MCA spectra to the simulation results, it is possible to obtain an energy calibration. To this end, the spectra were matched in energy by applying a linear calibration to the MCA channels ($E(c) = 1.65 \cdot (c - 20)$) and scaling the counts by a constant factor unique to the source and duration of the measurement. The comparisons between the simulation and the prototype's response are shown in Figure 6-12.

6.3.2. Comparison to Original SCEPTAR Detector

For reference the spectra produced by an inner ring channel from the upstream hemisphere of the original SCEPTAR detector is shown in Figure 6-13. This data was taken by applying a 1000V bias to the SCEPTAR channel 14, amplifying the pulses using a charge-integrating pre-amplifier,

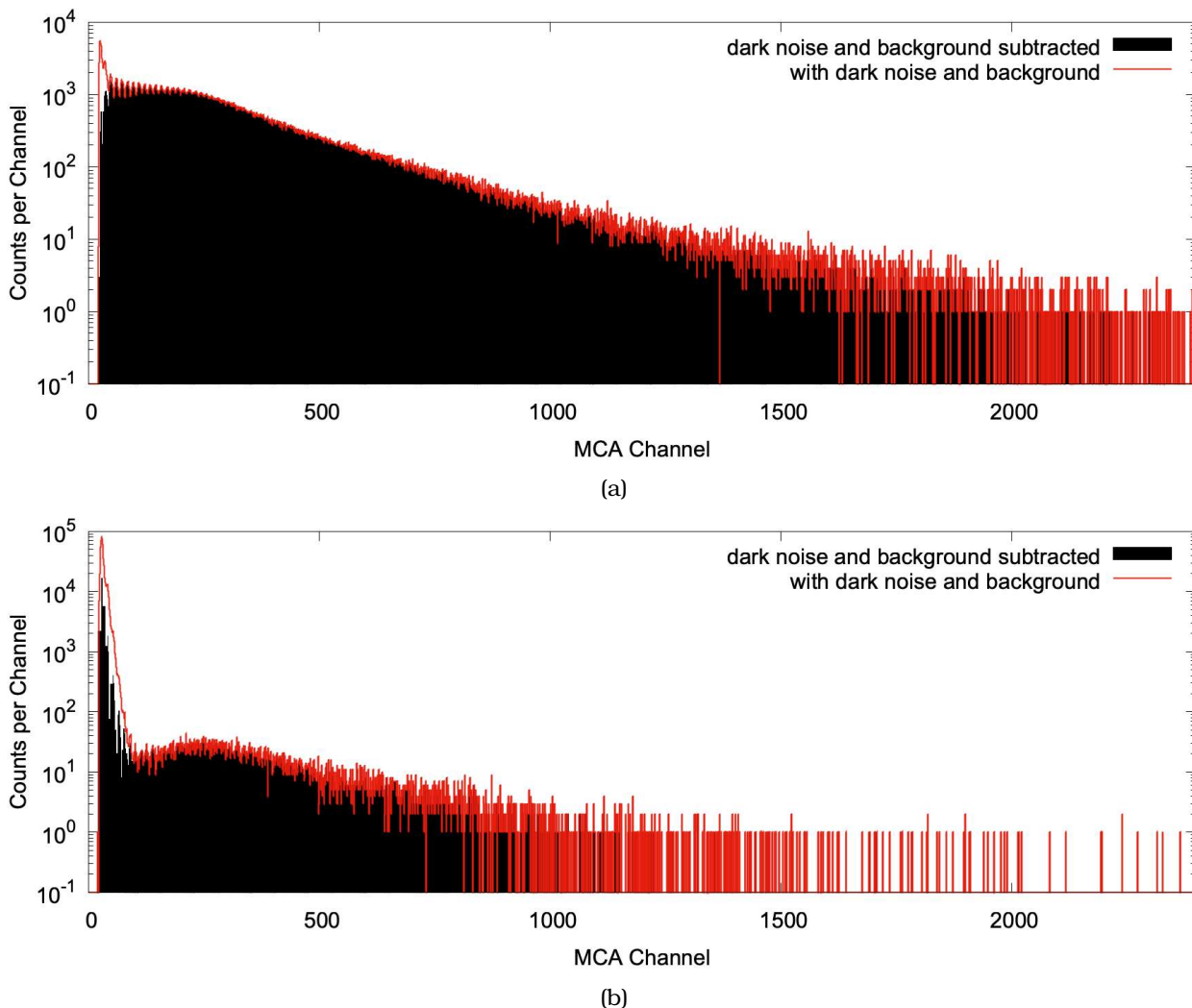


Figure 6-11 Dark noise subtracted calibration source decay spectra produced by four-channel SCEPTAR II prototype in response to (a) ^{90}Sr (b) ^{207}Bi .

and digitising using an ORTEC easy-MCA (8k). The spectra were taken with SCEPTAR at GRIFFIN (beamline ILE1B) and at high vacuum.

Conclusion

In this chapter, a further prototype was developed to investigate the performance of several SiPM channels operated simultaneously. The purpose of this prototype was to take the conclusions from the previous investigations and to develop a mock detector which more closely resembled the design of the final SCEPTAR II array. The four scintillators each with SiPM light detection resembles the design of the SCEPTAR II array, but reduced to one GRIFFIN HPGe clover-type detector with four crystals. A vacuum chamber was also assembled with a section of beampipe which emulated the $\sim 53\text{ cm}$ distance between the feedthrough flange and detector.

The investigations with the four channel prototype commenced with the acceptance and characterisation of each SiPM channel. The pulse shapes were observed and the breakdown voltage was determined for each channel. Following this, ^{90}Sr source energy spectra were taken with each channel, at atmosphere. Amplification with the Linear Technologies LTC6268-based charge-integrating pre-amplifier was optimised to occupy the full input current domain while avoiding saturation. For SensL MicroFC-10035 SiPMs operated at an overvoltage of 5 V, a suitable input current fraction is two-thirds of the total SiPM current. This is achieved by using an input resistance of 124Ω

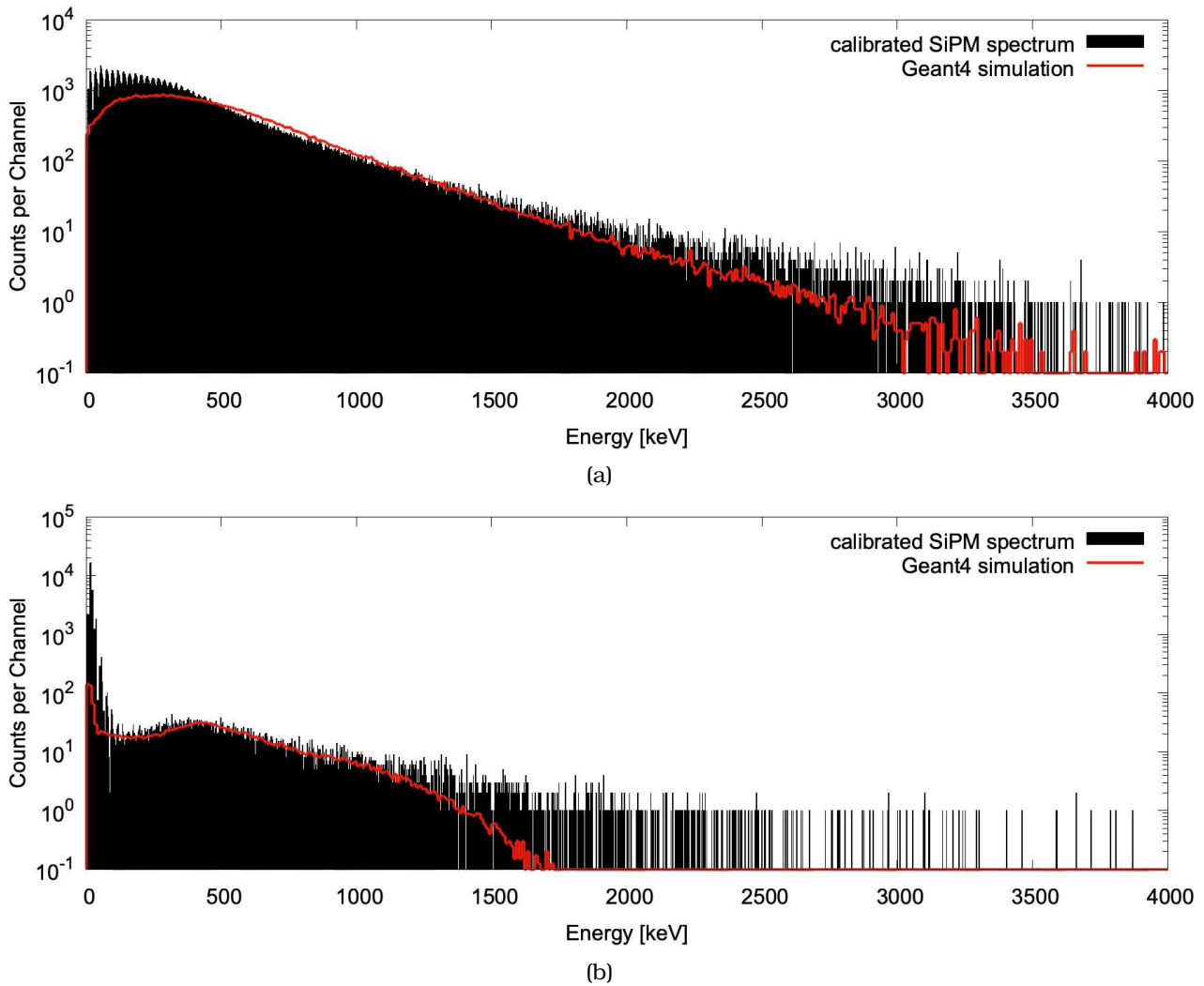
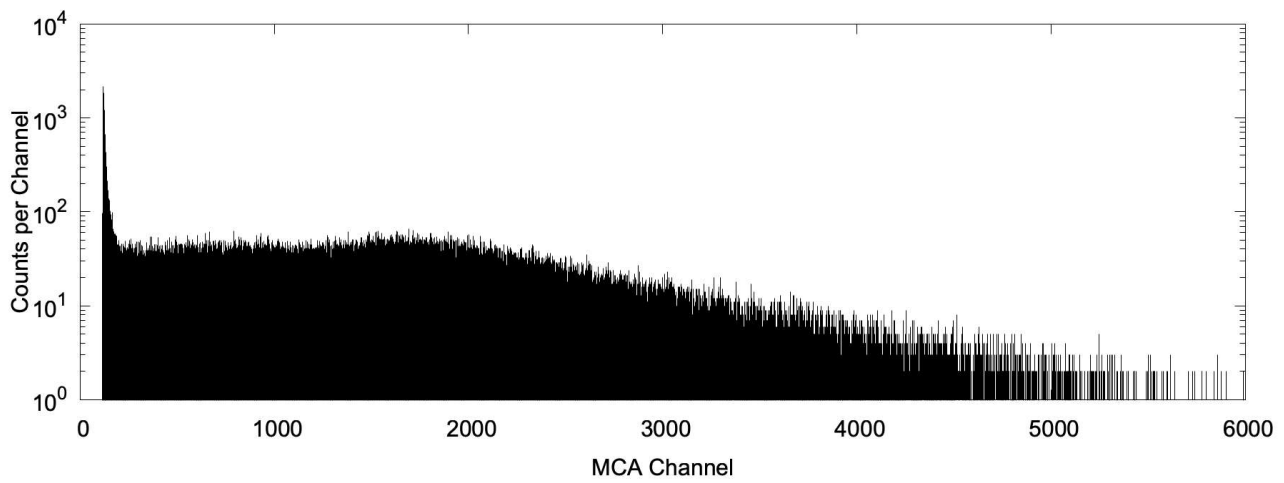


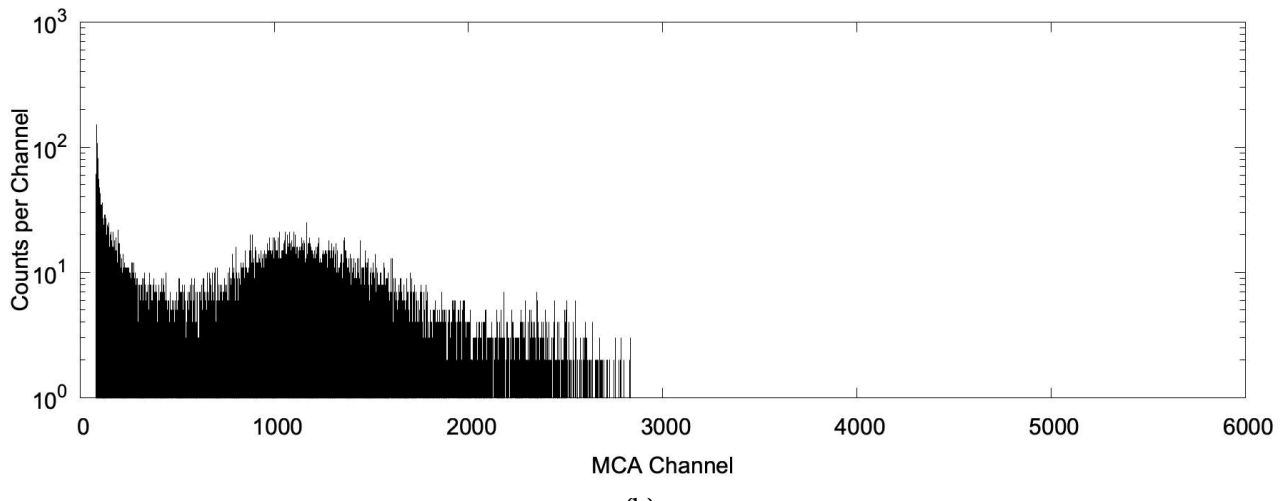
Figure 6-12 Dark noise subtracted calibration source decay spectra produced by four-channel SCEPTAR II prototype in response to (a) ^{90}Sr (b) ^{207}Bi .

and an input termination of 82Ω . For further details see Sections 4.2.2.2 and 6.2.2. The vacuum characteristics were as expected, the removal of air from the chamber reduces the attenuation of the electrons, increasing the counts in each MCA channel. The prototype exhibited minimal outgassing, taking 10% longer to reach 10 mTorr compared to the empty chamber (See Section 6.2.3). The low-energy region of the energy spectra was improved by taking a background subtraction. Following this, the measured energy spectra were in good agreement to simulation spectra obtained from `detectorSimulations` (with a significant but not unexpectedly large energy smearing applied) (See Section 6.3.1). The prototype's energy spectra, while not identical, were recognisably similar to SCEPTAR I's response (See Section 6.3.2).

This concludes the empirical investigations carried out in this work. The following Chapter details the proposed detector design with recommendations for construction, and operation informed by the results included in this and previous Chapters.



(a)



(b)

Figure 6-13 Calibration source decay spectra produced by an inner ring SCEPTAR detector operated at a typical bias voltage (1000V) (a) ^{90}Sr (b) ^{207}Bi .

7. Proposed Detector Design

From the investigations in the previous chapters, a range of conclusions can be drawn regarding the feasibility and specifics of the SCEPTAR II design concept presented in Section 1.2. This chapter outlines all the key recommendations that can be informed by this research regarding the design, construction, and operation of the new detector array.

7.1. Scintillators

Without further investigation, it was decided that the same plastic scintillator material would be used as with the original SCEPTAR array. Saint Gobain's BC404 is a polyvinyl-toluene based organic scintillator and exhibits excellent light output (68% of Anthracene), fast counting properties, and may be used in vacuum[57, 58]. Used to great success in SCEPTAR, BC404 has heritage at TRIUMF and its properties are more than suitable for continued use in β -particle tagging.

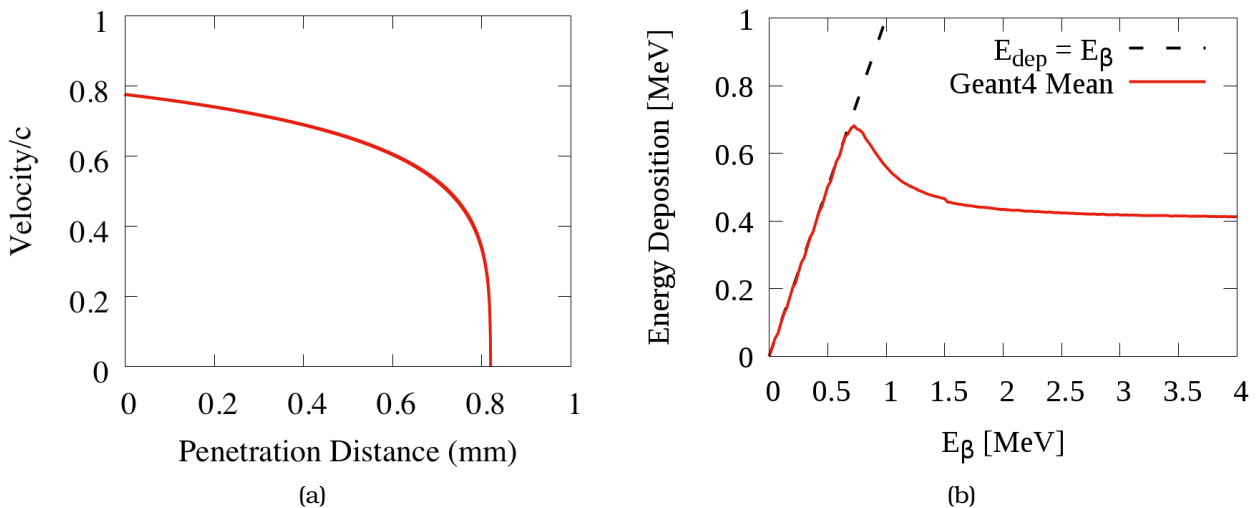


Figure 7-1 Simulations of electron interactions in BC404 scintillator. (a) Simulated average velocity as a 300 keV electron loses energy. From finite element analysis using eSTAR data. (b) Geant4 simulated energy deposition of fast electrons in 1.6mm of BC404.

The BC404 scintillators in SCEPTAR I are of 1.6mm thickness. These thin scintillators fully stop electrons up to energies of \sim 700 keV. Above this electron energy, a sufficient amount of energy, \sim 400 keV on average, is deposited in the scintillator for the tagging of high-energy electrons and positrons. Monte Carlo simulations, such as those shown in Figure 7-1 as well as results from SCEPTAR I's experimental career confirm the suitability of this thickness for β -particle tagging in GRIFFIN. The other two dimensions of the scintillator were chosen to be 10mm by 10mm, resulting in an approximately 2" diameter as with SCEPTAR I. The resulting geometry, as well as a conceptual holding structure are shown in Figure 7-2. An important consideration is minimizing the material in the chamber so that the HPGe low-energy efficiency is not significantly affected.

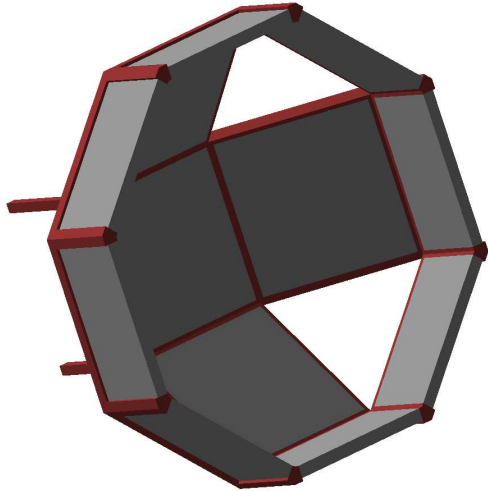


Figure 7-2 Proposed geometry of one SCEPTAR II hemisphere.

7.1.1. Surface Treatment

During investigations with a single scintillator, it was found that the surface treatment of the scintillators had a large influence on the spectrum of fluorescence produced in response to a calibration source. The Saint Gobain white reflective BC620 paint on all sides produced the most favourable results. The white TiO molecules form a diffuse reflective coating which is highly reflective especially around the 408nm peak emission wavelength of BC404[57]. The paint was thinned using water and applied with a simple airbrush. Several layers were applied creating a relatively thick ($\sim 100\mu\text{m}$) coating. The scintillator was masked with a small amount of tape to leave a window for the SiPM on the corner of the rear face. The thick layer of titanium oxide proved to have a non-negligible attenuation of electrons, and hence for the final detector a thinner yet equally uniform layer is recommended.

Alternatively, an option for the final detector is to use an evaporator to coat the scintillator surface directly with a thin layer of Al. This would create a coating with specular reflective properties, and would allow for extremely uniform and carefully controllable thickness. Further investigation would be required to determine if the specular coating across all scintillator faces is as efficient as the diffuse coating studied in this work.

7.1.2. Mounting

Investigations described previously in this work have involved holding the scintillators in place with a 3D printed structure. A simple pressure/friction fit sufficed for the purposes in this work, although the application of Kapton-tape (suitable for vacuum) was also used to secure the scintillators. Care should be taken that the coating of paint on the scintillators is not damaged during assembly or disassembly of the detector. Figure 7-2 shows a conceptual holding structure that does not place any additional material in the path to GRIFFIN's HPGe detectors. As 3D printing processes improve, it is becoming more prevalent to print in metallic compounds and to use these methods for production as well as prototyping[69, 70]. Aluminium is a more robust alternative to the PLA filament used in this work, and would improve the already satisfactory vacuum characteristics.

7.2. Scintillation light detection with SiPM's

While SiPMs have been used extensively to measure scintillation light[30, 68, 65, 66], a significant amount of work was required to verify and optimise the SiPM detectors for the fluorescence photons.

The SensL C-Series SiPMs are robust due to their plastic shrouding and exhibit excellent gain and detection efficiency and are a good match for the emission spectrum of BC404.

7.2.1. Component choice

In Section 4.1, the reasons for the selection of the SensL MicroFC-10035 were detailed. In short, the 1mm sensor with $35\mu\text{m}$ microcells has a high gain, and Photon Detection Efficiency (PDE) while maintaining a small and versatile package. The SensL Micro-FC-30035 and 60035 are alternatives with larger sensor arrays, and could be considered should a greater surface covering be desired.

7.2.2. Biasing

In this work the SensL MicroFC-10035 SiPMs were operated in a positive reverse bias configuration with the anode held to ground. Such a scheme is shown in Figure 4-4 where a second-order RC low-pass filter is used to clean up the HV bias, and an AC coupling capacitor is used to take the DC independent signal.

As discussed at the end of Section 5.3.1, an overvoltage of five volts is recommended for the SensL MicroFC-10035 SiPMs. Satisfactory gain, Photon Detection Efficiency, and dark count rates are observed at this bias. As Silicon devices, SiPMs are also affected by temperature fluctuations, reducing dark noise count rates, and decreasing the breakdown voltage[71, 72]. During operation at GRIFFIN, the simultaneous use of other ancillary detectors such as PACES may decrease the temperature in the vacuum chamber by up to 15 degrees Celsius in the downstream ancillary detector, see Appendix D.3. In this case the breakdown voltage would decrease by around 300mV[27, 59]. This will change the behaviour of the sensors in exactly the same way as increasing the bias voltage, and in extreme cases should be compensated for to keep the results consistent. Hence it is recommended to include a temperature sensor in the detector array and compensate the HV bias accordingly. Many modern power supplies include built-in functionality for temperature dependent biasing.

7.2.3. Amplification

During the course of the investigations discussed in this work, two amplifier types were investigated, fast amplification of the SiPM voltage signals, and a charge integration using a transimpedance amplifier that produced longer pulses with heights proportional to the charge in the SiPM pulse.

The charge-integrating amplification scheme using a Linear Technologies LTC6268 exhibited improved linearity compared to the fast radiofrequency amplifier. In addition, the “slower” charge integrated pulses are more suitable for digitisation with the 100MHz GRIF-16 ADC[73]. For SensL MicroFC-10035 SiPMs operated at an overvoltage of 5V, a suitable input current fraction is two-thirds of the total SiPM current. This is achieved by using an input resistance of 124Ω and an input termination of 82Ω . For further details see Section 4.2.2.2. The circuit for the charge integrating pre-amplifier is shown in Figure 10-4 of Appendix C.

7.2.4. Mounting

In this work the SensL C-Series SiPM with 1mm^2 active area and $35\mu\text{m}$ microcells were mounted manually using regular soldering techniques onto a fibreglass prototype board, see Section 6.1.1. While the SiPMs were operational and produced satisfactory energy spectra in response to scintillation light, a small amount of additional leakage current was present due to the imperfect soldering. For the final detector design reflow soldering is recommended as this would drastically reduce the workload for mounting many SiPMs, improve the quality of the soldering connections, and follows

the manufacturers specifications[62]. For the final detector, the option of producing a fully or partially flexible printed circuit board is available. These flexible circuit boards replace the standard fibre-glass with vacuum-suitable Kapton[74], and would allow for a single large board to be produced that can “wrap” around the SCEPTAR II detector.

In order to increase the efficiency at which photons travel from the scintillator to the SiPM shroud and then active area, optical coupling grease are used to optically unify the two materials at their common interface. Products such as the Saint Gobain BC-630 Silicone Grease have similar refractive indices to the transparent plastics and a small amount can be used to join two surfaces which otherwise are not unified[57, 75].

7.3. Beampipe and Vacuum Chamber

Shaun Georges, a mechanical technician in the Gamma-Ray Spectroscopy at ISAC group of TRI-UMF, has designed a concept for a new ancillary detector template for GRIFFIN. Using a square beampipe, and the familiar Delrin vacuum chamber, this design allows for feedthrough flanges anywhere along the beampipe and allows electrical wires to be mounted easily along the flat sides of the interior. A render of such a design is shown in Figure 7-3.

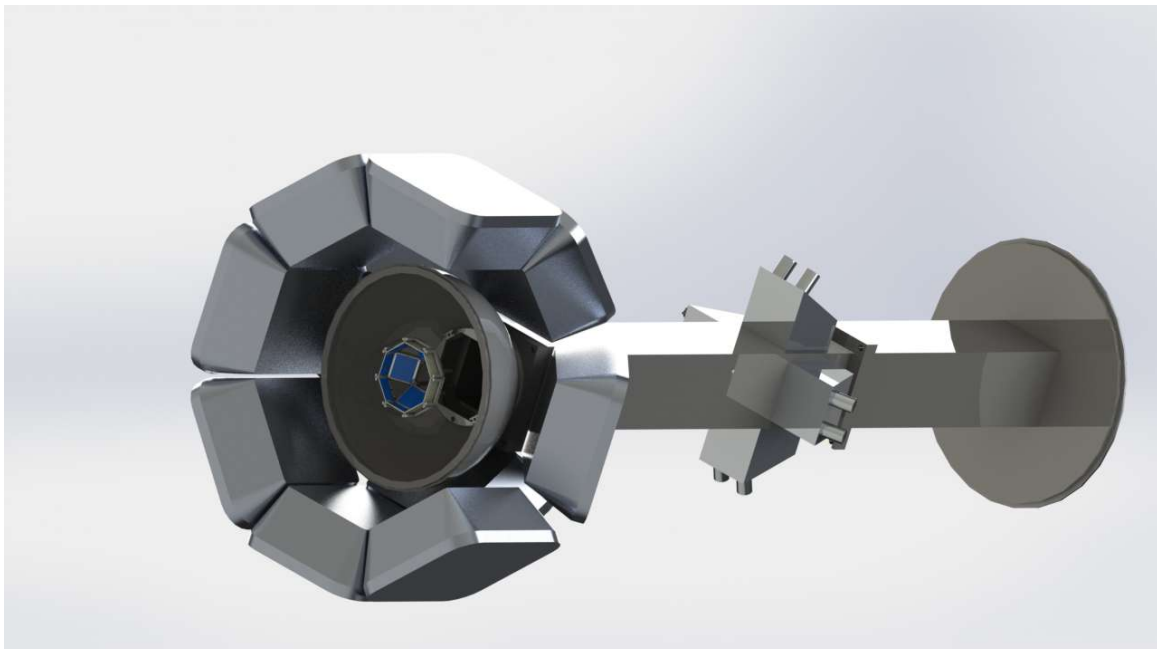


Figure 7-3 SCEPTAR II chamber and beampipe concept by Shaun Georges.

7.4. Simulated GRIFFIN Efficiency

To ensure that GRIFFIN will retain its exceptional γ -ray detection efficiency when operated with SCEPTAR II, minimal material is placed between the beam implantation point and the germanium crystals. The design concept has strategically placed the 3D printed holding structure at the borders of the GRIFFIN HPGe crystals, where the BGO Compton Suppression shields are positioned, so that minimal γ -ray attenuation occurs. At the distance of approximately 27mm, the 2.7mm² front surface area SensL MicroFC-10035 occupy a very small surface area, and placed at the corners of the scintillator they obscure only a small portion of GRIFFIN's active area. The rounded corners of GRIFFIN's clover-type detectors further reduces this effect, see Figure 7-4. Apart from the scintillators, and the thin flexible printed circuit board holding the SiPMs in place, the SCEPTAR II design concept maintains GRIFFIN's excellent efficiency. This is confirmed by **GEANT4** simulations with **detectorSimulations**, as seen in Figure 7-5.

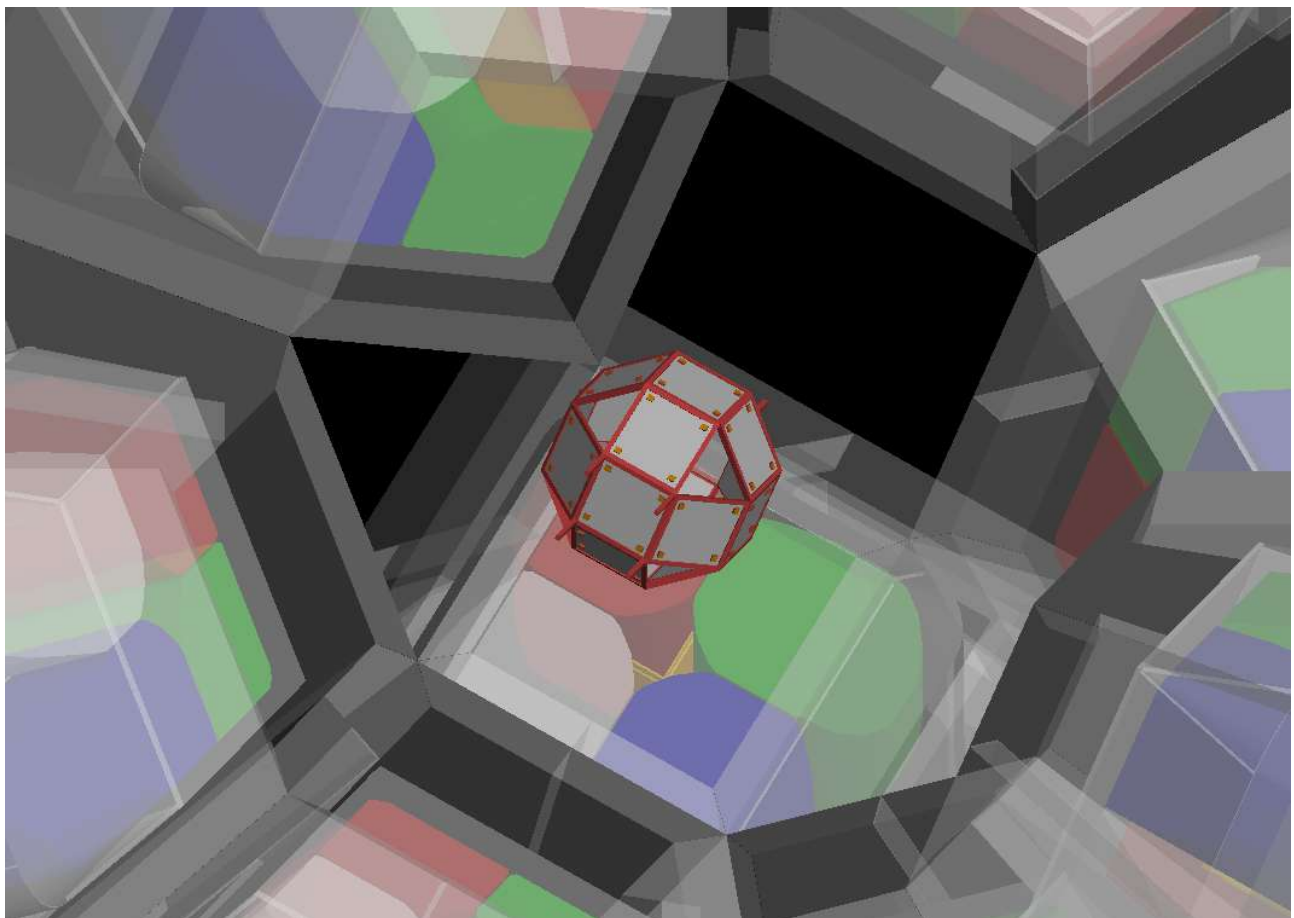


Figure 7-4 Visualisation of SCEPTAR II detector concept in GRIFFIN.

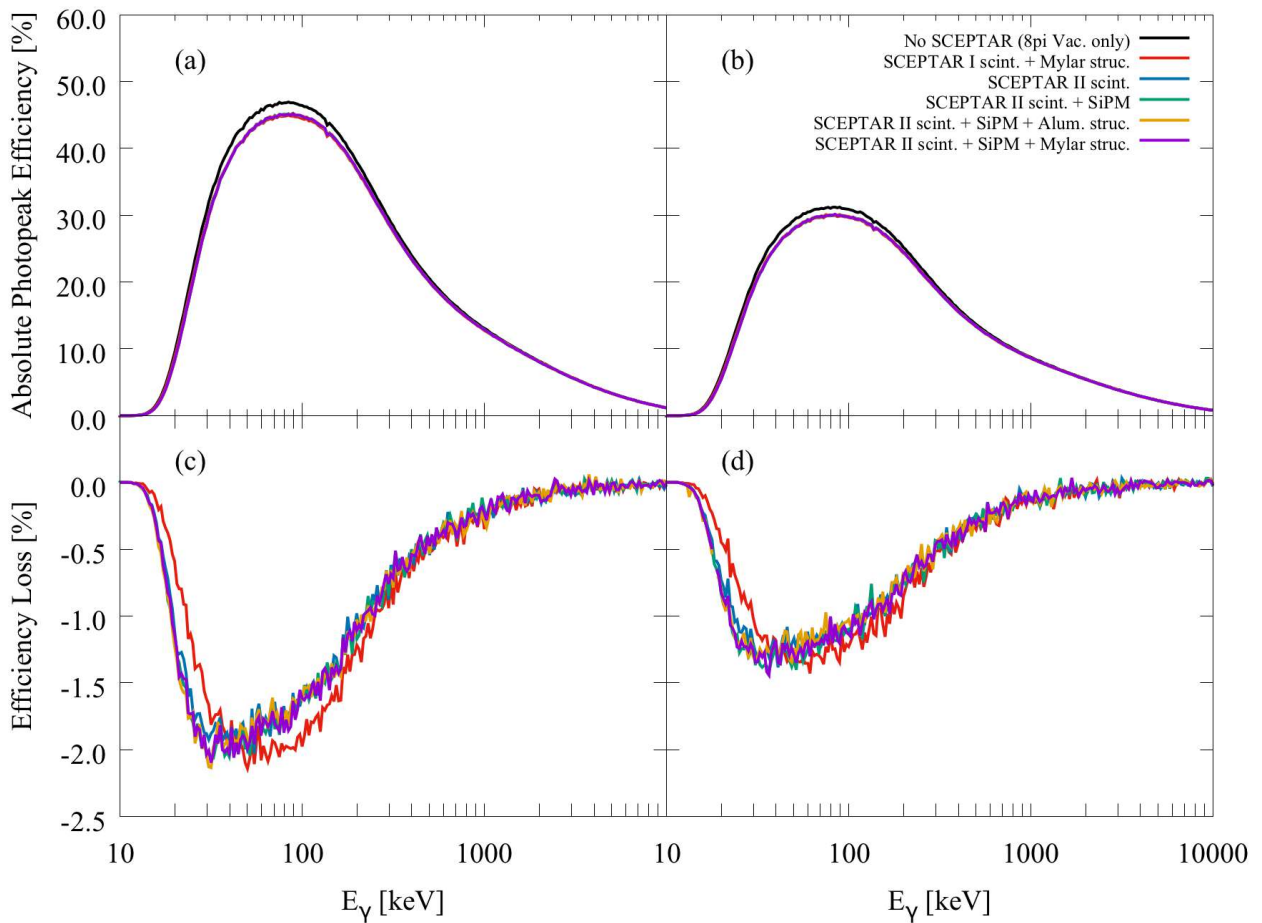


Figure 7-5 **GEANT4** simulation of GRIFFIN efficiency with original SCEPTAR and SCEPTAR II design concepts. (a) and (b) are the absolute photopeak efficiencies of GRIFFIN in normal and optimised peak to total (suppressed) modes of operation, respectively. (c) and (d) are the absolute differences in efficiency due to the introduction of various SCEPTAR detector configurations, relative to the efficiency with no ancillary detector (black curve in (a) and (b)). (c) is the difference when GRIFFIN is in normal mode, (d) is the difference for optimised peak to total (suppressed) configuration.

8. Conclusion & Outlook

This final chapter, serves to summarise the key considerations and results of the work documented in this thesis.

The work documented by this thesis, was undertaken in order to determine the best course of action towards building a replacement for SCintillating Electron-Positron Tagging ARray (SCEPTAR). SCEPTAR is an ancillary detector composed of two hemispheres and designed for use in 8π Spectrometer, each with two rings of five thin (1.6mm) BC404 plastic scintillators arranged to match the HPGe crystals, and readout through UVT light-guides and external PMTs. SCEPTAR I proved to be a vital part of TRIUMF's nuclear structure program and together with the 8π Spectrometer supported a wide range of β -decay and isomer studies with RIBs at TRIUMF-ISAC. Providing the means for β - γ and β - γ - γ coincidences and vetoing of punch-through electron signals SCEPTAR I greatly increased the quality of research possible with the 8π facility (See Sections 1.1.1 and 1.1.2).

The components of SCEPTAR are beginning to exhibit signs of ageing and SCEPTAR's the non-matching positioning between the scintillators and GRIFFIN's HPGe crystals reduces the efficiency at which punch-through electron signals can be vetoed. The research conducted in this work serves to determine the feasibility of a new detector design where 10mm by 10mm by 1.6mm BC404 scintillators are arranged matching GRIFFIN's geometry and are read out by SensL C-Series Silicon Photomultipliers (SiPMs). Additionally, recommended construction and operating methodologies were determined.

This thesis began with an introduction to relevant theory including radioactive decay (Section 2.1.1), interaction processes between particles and matter (Section 2.1.2), radiation detectors and their characterisation (Sections 2.1.3, 2.1.4, 3.1 and 3.2), and finally passive filter circuits and transimpedance amplifiers (Section 3.3). Taking into consideration the findings of this background study, the investigations and prototyping of the SCEPTAR II detector were completed, as described in the following Section.

8.1. Conclusions from Investigations

This section provides a brief summary of the investigations performed in this work.

Investigations began with three SensL C-Series SiPM with 1mm^2 active area and $35\mu\text{m}$ micro-cells, mounted on a pin adapter board, a sensor chosen for its compatibility with the Saint Gobain BC404 plastic scintillator's emission spectrum, favourable performance characteristics, and robust yet small form factor (See Section 4.1). A reverse biasing scheme with a positive bias on the cathode of the SiPM and the anode held to ground (OV) was chosen and satisfactory pulse shapes were observed when coupled to a prototype scintillator. The pulses were also amplified using first a fast RF amplifier and a charge-integrating transimpedance amplifier. The latter, based on the Linear Technologies LTC6268 op-amp was chosen as the SiPMs current response exhibits improved linearity and the amplifier's longer pulses are more suitable for digitisation. The methodology for obtaining the breakdown voltage of a SiPM from its Current-Voltage characteristics was applied to the sensors with promising results, obtaining sensible values with $<0.01\%$ relative uncertainty even with manually taken data.

Following the successful operation and characterisation of the three SensL MicroFC-SMTPA-10035 sensors, a prototype set-up with single 10mm by 10mm by 1.6mm BC404 scintillators was

assembled. The scintillators were mounted using a 3D printed holding structure and coupled to the SiPM using Saint Gobain BC630 Silicone grease.

A suite of prototype scintillators with varying surface treatments was prepared. These allowed for the investigation of the effect physical parameters such as the surface treatment and SiPM positioning on the detector performance. It was determined that the maximum overvoltage recommended by SensL produced the most satisfactory calibration source spectra in response to ^{90}Sr and ^{207}Bi sources (See Section 5.3.1). These results were further validated by comparison to **GEANT4** simulation results which while not identical, had characteristic features recognisable in the empirical data. The gain and PDE of the sensors was also estimated (See Section 5.3.1). As for the scintillator treatment, a coating all over the scintillator with diffusely reflective titanium oxide (TiO) paint, provided the most efficient capture of scintillation light (See Section 5.3.2). The optimal SiPM position was found to be on the rear of the scintillator, with the corner offering a narrow improvement to other locations on the rear face (See Section 5.3.3).

The next, and final set of prototypes produced entailed four detector channels, each with a scintillator, SensL MicroFC-10035 SiPM, and independent biasing and readout circuitry for the sensors. The prototype boards have a length of $\sim 53\text{ cm}$ which is approximately equal to distance between the centre of the detector array and the feedthrough flanges once the detector is in GRIFFIN. The four scintillators were painted on all sides using TiO (Saint Gobain BC620) diffusely reflective paint, were mounted to a 3D printed prototype holding structure, and coupled to the SiPMs using optical coupling grease (Saint Gobain BC630) (See Section 6.1). A prototype vacuum chamber was assembled which approximated the geometry of a GRIFFIN ancillary detector and allowed for testing of the prototype in vacuum (See Section 6.1.3).

The investigations with the four channel prototype commenced with the acceptance and characterisation of each SiPM channel. The pulse shapes were observed and the breakdown voltage was determined for each channel. Following this ^{90}Sr energy spectra were collected with each channel, at atmosphere. Amplification with the Linear Technologies LTC6268-based charge-integrating pre-amplifier was optimised to occupy the full input current domain while avoiding saturation. For SensL MicroFC-10035 SiPMs operated at an overvoltage of 5V, a suitable input current fraction is two-thirds of the total SiPM current. This is achieved by using an input resistance of 124Ω and an input termination of 82Ω . For further details see Sections 4.2.2.2 and 6.2.2. The vacuum characteristics were as expected, the removal of air from the chamber reduces the attenuation of the electrons, increasing the counts in each MCA channel. The prototype exhibited minimal outgassing, taking 10% longer to reach 10 mTorr compared to the empty chamber (See Section 6.2.3). The low-energy region of the energy spectra was improved by taking a background subtraction. Following this, the measured energy spectra were in good agreement to simulation spectra obtained from **detectorSimulations** (with a significant but not unexpectedly large energy smearing applied) (See Section 6.3.1). The prototype's energy spectra, while not identical, were recognisably similar to SCEPTAR I's response (See Section 6.3.2).

8.2. Recommendations for Proceeding

In Chapter 7 all the findings from the prototype investigations were presented. In summary:

- The prototype investigations validate the concept of using 10mm by 10mm by 1.6mm Saint Gobain BC404 plastic scintillator with SensL MicroFC-10035 SiPM fluorescence detection.
- The results indicate an optimal over-voltage is five volts above the breakdown (determined via Current-Voltage investigations) and the readout via an AC coupling capacitor and charge-integrating amplifier offered excellent linearity.
- It was found that a thin layer of diffusely reflective TiO paint (Saint Gobain BC620), with a

window for the SiPM at a rear corner, and coupling via Saint Gobain BC630 Silicone grease resulted in satisfactory collection of scintillation light.

- The SiPM signals did not interfere in the multi-channel configuration, did not show significant signal degradation over the \sim 50 cm distance, and operated well at high vacuum.
- It is predicted by **GEANT4** simulations that the SCEPTAR II design concept will not significantly reduce GRIFFIN's excellent γ -ray detection efficiency.

8.3. Final Outlook

The results presented in this work have informed a set of recommendations for the final design, construction and operation of SCEPTAR II. The investigations with calibration sources (^{90}Sr and ^{207}Bi) and a four-channel prototype are satisfactory and sufficiently similar to both SCEPTAR I's response and **GEANT4** simulations to instil confidence in the SCEPTAR II design concept which is an extension of the prototype's design.

Bibliography

- [1] A. B. Garnsworthy and P. E. Garrett. "The 8π spectrometer". In: *Hyperfine Interactions* 225.1 (Jan. 2014), pp. 121–125. ISSN: 1572-9540. DOI: 10.1007/s10751-013-0888-4. URL: <https://doi.org/10.1007/s10751-013-0888-4>.
- [2] AB Garnsworthy. "Exotic nuclei studied with the 8pi spectrometer at TRIUMF". In: *EPJ Web of Conferences*. Vol. 93. EDP Sciences. 2015, p. 01032.
- [3] Elizabeth Cunningham. "SCEPTAR: The New Scintillator Array for the 8pi Spectrometer". In: *APS Division of Nuclear Physics Meeting Abstracts*. 2003.
- [4] AB Garnsworthy. "Exploring Exotic Nuclei with the GRIFFIN Spectrometer at TRIUMF-ISAC". In: *Acta Physica Polonica B* 47 (2016), p. 713.
- [5] Adam Garnsworthy. *Experience with GRIFFIN*. TRIUMF FRIB Decay Station Workshop. Jan. 2018.
- [6] CM Mattoon et al. " β decay of Na 32". In: *Physical Review C* 75.1 (2007), p. 017302.
- [7] G Nelson and D Reilly. "Gamma-ray interactions with matter". In: *Passive nondestructive analysis of nuclear materials* (1991), pp. 27–42.
- [8] F. Sarazin et al. "Halo neutrons and the β decay of ^{11}Li ". In: *Physical Review C: Nuclear Physics* 70 (3 Sept. 2004), p. 031302. DOI: 10.1103/PhysRevC.70.031302. URL: <https://link.aps.org/doi/10.1103/PhysRevC.70.031302>.
- [9] Gordon C Ball, 8 π /TIGRESS collaboration, et al. "Gamma-ray spectroscopy at TRIUMF-ISAC: recent highlights and future plans". In: *Journal of Physics: Conference Series*. Vol. 387. IOP Publishing. 2012, p. 012014.
- [10] Kenneth S Krane and David Halliday. *Introductory nuclear physics*. Vol. 465. Wiley New York, 1988.
- [11] Glenn F Knoll. *Radiation detection and measurement*. John Wiley & Sons, 2010.
- [12] Alessandro Bettini. *Introduction to Elementary Particle Physics*. Cambridge University Press, 2008.
- [13] Luca Nanni. "Fermi theory of beta decay: A first attempt at electroweak unification". In: *arXiv preprint arXiv:1803.07147* (2018).
- [14] Enrico Fermi. "Tentativo di una teoria dei raggi β ". In: *Il Nuovo Cimento* 11.1 (1934), p. 1.
- [15] Ernst Roeckl and Ivan Mukha. "Q values of radioactive decay: Examples from nuclear physics and related fields". In: *International Journal of Mass Spectrometry* 349-350 (2013). 100 years of Mass Spectrometry, pp. 47–56. ISSN: 1387-3806. DOI: <https://doi.org/10.1016/j.ijms.2013.03.021>. URL: <http://www.sciencedirect.com/science/article/pii/S1387380613001127>.
- [16] Kenneth S. Krane. *Modern Physics*. 3rd ed. Wiley, 2012.
- [17] Wilton N Catford. *Lectures in Nuclear and Particle Physics*. Faculty of Engineering and Physical Sciences, University of Surrey. 2017.
- [18] Alex F Bielajew. *Elements of Nuclear Engineering and Radiological Sciences II, β decay*. Nuclear Engineering and Radiological Sciences, The University of Michigan. 2012.

- [19] Jeanne Mager Stellman. *Encyclopaedia of occupational health and safety*. Vol. 1. International Labour Organization, 1998.
- [20] Carlos Palacio. “Some effects on polymers of low-energy implanted positrons”. Jan. 2008.
- [21] Emilio Segrè. *Nuclei And Particles An Introduction To Nuclear And Subnuclear Physics 2nd.Ed.* W. A. Benjamin, 1977.
- [22] National Institute of Standards and Technology. *ESTAR: Stopping Powers and Ranges of Electrons*. (Available at: <https://physics.nist.gov/PhysRefData/Star/Text/method.html>).
- [23] Johanna Stachel. *Detectors in Nuclear and Particle Physics, Scintillation counters*. Department of Physics and Astronomy, University of Heidelberg. June 2015.
- [24] Yuhong Yu et al. “The plastic scintillator detector for DAMPE”. In: *Astroparticle Physics* 94 (2017), pp. 1–10. ISSN: 0927-6505. DOI: <https://doi.org/10.1016/j.astropartphys.2017.06.004>. URL: <http://www.sciencedirect.com/science/article/pii/S0927650516302031>.
- [25] Lino Miramonti. “A plastic scintillator detector for beta particles”. In: *Radiation Measurements* 35.4 (2002), pp. 347–354. ISSN: 1350-4487. DOI: [https://doi.org/10.1016/S1350-4487\(02\)00051-3](https://doi.org/10.1016/S1350-4487(02)00051-3). URL: <http://www.sciencedirect.com/science/article/pii/S1350448702000513>.
- [26] A Ghassemi and K Sata and K Kobayashi. “Multi-Pixel Photon Counter”. Hamamatsu technical note. Mar. 2016.
- [27] SensL. “An Introduction to the Silicon Photomultiplier”. Manufacturer’s technical note. 2011.
- [28] SensL. “How to Evaluate and Compare Silicon Photomultiplier Sensors”. Manufacturer’s technical note. Oct. 2015.
- [29] Adam Nepomuk Otte et al. “Characterization of three high efficiency and blue sensitive silicon photomultipliers”. In: *Nuclear Instruments and Methods in Physics Research Section A: Accelerators, Spectrometers, Detectors and Associated Equipment* 846 (2017), pp. 106–125.
- [30] B. Dolgoshein et al. “Status report on silicon photomultiplier development and its applications”. In: *Nuclear Instruments and Methods in Physics Research Section A: Accelerators, Spectrometers, Detectors and Associated Equipment* 563.2 (2006). TRDs for the Third Millennium, pp. 368–376.
- [31] D Renker and E Lorenz. “Advances in solid state photon detectors”. In: *Journal of Instrumentation* 4.04 (2009), P04004.
- [32] Guy A Armantrout. “High operating temperature limitations for germanium detectors”. In: *IEEE Transactions on Nuclear Science* 19.3 (1972), pp. 289–298.
- [33] GH Nakano, DA Simpson, and WL Imhof. “Characteristics of large intrinsic germanium detectors operated at elevated temperatures”. In: *IEEE Transactions on Nuclear Science* 24.1 (1977), pp. 68–72.
- [34] Richard H Pehl, Eugene E Haller, and Richard C Cordi. “Operational characteristics of germanium detectors at higher temperatures”. In: *IEEE Transactions on Nuclear Science* 20.1 (1973), pp. 494–499.
- [35] E Gatti and F De Martini. “A new linear method of discrimination between elementary particles in scintillation counters”. In: *Nuclear Electronics II. Proceedings of the Conference on Nuclear Electronics. V. II.* 1962.
- [36] JI Hopkins. “Electron energy studies with the anthracene scintillation counter”. In: *Review of Scientific Instruments* 22.1 (1951), pp. 29–33.
- [37] L. W. Johnston et al. “Response of an Anthracene Scintillation Counter to 10 to 120 keV Electrons”. In: *Review of Scientific Instruments* 28.10 (1957), pp. 765–767.

- [38] Sea Agostinelli et al. "GEANT4 - a simulation toolkit". In: *Nuclear instruments and methods in physics research section A: Accelerators, Spectrometers, Detectors and Associated Equipment* 506.3 (2003), pp. 250–303.
- [39] MA Schumaker et al. "Measured and simulated performance of Compton-suppressed Ti-GRESS HPGe clover detectors". In: *Nuclear Instruments and Methods in Physics Research Section A: Accelerators, Spectrometers, Detectors and Associated Equipment* 570.3 (2007), pp. 437–445.
- [40] V. Chmilla et al. "On the characterisation of SiPMs from pulse-height spectra". In: *Nuclear Instruments and Methods in Physics Research Section A: Accelerators, Spectrometers, Detectors and Associated Equipment* 854 (2017), pp. 70–81.
- [41] Y. Du and F. Retière. "After-pulsing and cross-talk in multi-pixel photon counters". In: *Nuclear Instruments and Methods in Physics Research Section A: Accelerators, Spectrometers, Detectors and Associated Equipment* 596.3 (2008), pp. 396–401.
- [42] Patrick Eckert et al. "Characterisation studies of silicon photomultipliers". In: *Nuclear Instruments and Methods in Physics Research Section A: Accelerators, Spectrometers, Detectors and Associated Equipment* 620.2 (2010), pp. 217–226.
- [43] Kai Siegbahn. *Alpha-, Beta-, and Gamma-Ray Spectroscopy*. 2nd ed. Vol. 1. North-Holland Publishing Company, 1966.
- [44] International Network of Nuclear Structure and Decay Data Evaluators. *Evaluated Nuclear Structure Data File Search and Retrieval*. (Available at: <http://www.nndc.bnl.gov/ensdf/>).
- [45] H.H. Hansen. "Measurement of the beta-ray spectra of 90Sr-90Y". In: *The International Journal of Applied Radiation and Isotopes* 34.8 (1983), pp. 1241–1247.
- [46] M.J. Woods and S.E.M. Lucas. "Half-life of 90Sr: measurement and critical review". In: *Nuclear Instruments and Methods in Physics Research Section A: Accelerators, Spectrometers, Detectors and Associated Equipment* 369.2 (1996), pp. 534–538.
- [47] *the RADiation Dose Assessment Resource: On-Line Decay Data*. (Available at: <https://www.doseinfo-radar.com/RADAROver.html>).
- [48] Brookhaven National Laboratory. *National Nuclear Data Center*. (Available at: <http://www.nndc.bnl.gov>).
- [49] D.C. Kocher. "Nuclear Data Sheets for A = 90". In: *Nuclear Data Sheets* 16.1 (1975), pp. 55–105.
- [50] Richard B Firestone and Virginia S Shirley. "Table of isotopes, 2 volume set". In: *Table of Isotopes, 2 Volume Set, by Richard B. Firestone, Virginia S. Shirley (Editor)*, pp. 3168. ISBN 0-471-33056-6. Wiley-VCH, December 1998. (1998), p. 3168.
- [51] Department of Nuclear Physics, The Australian National University. *BrIcc v2.3S: Conversion Coefficient Calculator*. (Available at: <http://bricc.anu.edu.au>).
- [52] T. Kibédi et al. "Evaluation of theoretical conversion coefficients using BrIcc". In: *Nuclear Instruments and Methods in Physics Research Section A: Accelerators, Spectrometers, Detectors and Associated Equipment* 589.2 (2008), pp. 202–229.
- [53] F.G. Kondev and S. Lalkovski. "Nuclear Data Sheets for A = 207". In: *Nuclear Data Sheets* 112.3 (2011), pp. 707–853. URL: <http://www.sciencedirect.com/science/article/pii/S0090375211000111>.
- [54] Robert L Boylestad, Louis Nashelsky, and Lihua Li. *Electronic devices and circuit theory*. Vol. 11. Prentice Hall Englewood Cliffs, NJ, 2002.

- [55] Paul E Gray, Campbell T Searle, and William D Gill. "Electronic Principles: Physics, Models, and Circuits". In: *American Journal of Physics* 39 (1971), pp. 126–126.
- [56] Jerald G Graeme. *Photodiode amplifiers: op amp solutions*. McGraw-Hill New York, 1996.
- [57] Saint-Gobain Ceramics and Inc. Plastics. "Organic Scintillation Materials and Assemblies". July 2018.
- [58] Saint-Gobain. <https://www.crystals.saint-gobain.com/>.
- [59] SensL. "C-Series: Low Noise, Blue-Sensitive Silicon Photomultipliers". Manufacturer's datasheet. 2017.
- [60] A.B. Garnsworthy, et al. "The GRIFFIN Facility for Decay-Spectroscopy Studies at TRIUMF-ISAC". In: *Nuclear Instruments and Methods in Physics Research Section A: Accelerators, Spectrometers, Detectors and Associated Equipment* 918.9 (2019).
- [61] CE Svensson and AB Garnsworthy. "The GRIFFIN spectrometer". In: *Hyperfine Interactions* 225.1-3 (2014), pp. 127–132.
- [62] SensL. "C-Series: Low Noise, Blue-Sensitive Silicon Photomultipliers". Manufacturer's user manual. 2017.
- [63] Han Gyu Kang et al. "A dual-ended readout detector using a meantime method for SiPM TOF-DOI PET". In: *IEEE Transactions on Nuclear Science* 62.5 (2015), pp. 1935–1943.
- [64] P Buzhan et al. "The advanced study of silicon photomultiplier". In: *Advanced Technology And Particle Physics*. World Scientific, 2002, pp. 717–728.
- [65] Daniel Krons. "Developement of a portable β -spectrometer for in situ measurements of Sr-90 and Y-90 using a plastic scintillator and a silicon photomultipler (SiPM)." In: (2015).
- [66] M Grodzicka et al. "Performance of FBK high-density SiPMs in scintillation spectrometry". In: *Journal of Instrumentation* 9.08 (2014), P08004.
- [67] Slawomir Piatek. "Silicon Photomultiplier: Operation, Performance & Possible Applications". Hamamatsu webinar.
- [68] Menge, P R and Yang, K and McLaughlin, M and Bacon, B. "Efficient Positioning of SiPMs on Large Scintillation Crystals". In: *NSS/MIC*. Saint-Gobain Crystals. IEEE. 2016.
- [69] Collin Ladd et al. "3D printing of free standing liquid metal microstructures". In: *Advanced Materials* 25.36 (2013), pp. 5081–5085.
- [70] David Bak. "Rapid prototyping or rapid production? 3D printing processes move industry towards the latter". In: *Assembly Automation* 23.4 (2003), pp. 340–345.
- [71] A Falcone et al. "Vacuum ultra-violet and ultra-violet scintillation light detection by means of silicon photomultipliers at cryogenic temperature". In: *Nuclear Instruments and Methods in Physics Research Section A: Accelerators, Spectrometers, Detectors and Associated Equipment* 787 (2015), pp. 216–219.
- [72] Nicola Serra et al. "Experimental and TCAD study of breakdown voltage temperature behavior in $n\{+\}/p$ SiPMs". In: *IEEE Transactions on Nuclear Science* 58.3 (2011), pp. 1233–1240.
- [73] AB Garnsworthy et al. "The GRIFFIN data acquisition system". In: *Nuclear Instruments and Methods in Physics Research Section A: Accelerators, Spectrometers, Detectors and Associated Equipment* 853 (2017), pp. 85–104.
- [74] H Isaacson. *Electronic module using flexible printed circuit board with heat sink means*. US Patent 3,766,439. Oct. 1973.
- [75] Saint-Gobain Ceramics and Inc. Plastics. "BC-630 Safety Data Sheet". May 2017.

- [76] Geant4 Collaboration. *Geant4, a simulation toolkit: Overview*. (Available at: <http://geant4.web.cern.ch>).
- [77] Geant4 Collaboration. *Geant4 Scope of Application*. (Available at: <http://geant4-userdoc.web.cern.ch/geant4-userdoc/UsersGuides/IntroductionToGeant4/html/IntroductionToG4.html>). 2017.
- [78] V N Ivanchenko et al. “Geant4 Electromagnetic Physics for LHC Upgrade”. In: *Journal of Physics: Conference Series* 513.2 (2014), p. 022015.
- [79] E. Casarejos et al. “Design of iTof: A ToF-wall detector to identify relativistic ions in R3B-FAIR”. In: *Nuclear Instruments and Methods in Physics Research Section A: Accelerators, Spectrometers, Detectors and Associated Equipment* 661 (2012). X. Workshop on Resistive Plate Chambers and Related Detectors (RPC 2010), S137–S140.
- [80] A Tarifeno-Saldivia et al. “Conceptual Design of a Hybrid Neutron-gamma Detector for Study of -delayed Neutrons at the RIB Facility of RIKEN.” In: (2017).
- [81] E T Rand et al. “Geant4 Developments for the Radon Electric Dipole Moment Search at TRI-UMF”. In: *Journal of Physics: Conference Series* 312.10 (2011), p. 102013.
- [82] James E. Gentle. *Random Number Generation and Monte Carlo Methods*. 2nd ed. Statistics and computing. Springer, 2003.
- [83] J. Allison et al. “Recent developments in Geant4”. In: *Nuclear Instruments and Methods in Physics Research Section A: Accelerators, Spectrometers, Detectors and Associated Equipment* 835 (2016), pp. 186–225.
- [84] Francesc Salvat, Jose M Fernandez-Varea, and Josep Sempau. *PENELOPE. A code system for Monte Carlo simulation of electron and photon transport*. (Available at: <http://www.mcnpvised.com/visedtraining/penelope/penelope0.pdf>).
- [85] Lawrence Livermore National Laboratory. *Nuclear and Atomic Data - Electrons*. (Available at: <https://wci.llnl.gov/codes/tart/electrons.html>).
- [86] J. Allison et al. “Geant4 developments and applications”. In: *IEEE Transactions on Nuclear Science* 53.1 (Feb. 2006), pp. 270–278.
- [87] GRIFFIN Collaboration. *detectorSimulations_v10*. (Available at: https://github.com/GRIFFINCollaboration/detectorSimulations_v10).
- [88] MA Schumaker et al. “Measured and simulated performance of Compton-suppressed Ti-GRESS HPGe clover detectors”. In: *Nuclear Instruments and Methods in Physics Research Section A: Accelerators, Spectrometers, Detectors and Associated Equipment* 570.3 (2007), pp. 437–445.
- [89] Tatsumi Koi. *GEANT4: EM Physics*. SLAC National accelerator Laboratory.

Appendices

A. Preparing Detector Simulations

Simulations form an important part of modern physics, as they can be used to predict behaviour of complex detector systems. For systems that already exist, simulations allow for the determination of characteristics that are difficult or impossible to measure empirically. In the case of new detector designs, simulations aid in the decision making and establish the feasibility of the design. In this work individual scintillators, as well as the larger systems of Gamma-Ray Infrastructure For Fundamental Investigations of Nuclei (GRIFFIN), SCintillating Electron-Positron Tagging ARray (SCEPTAR) and its replacement SCintillating Electron-Positron ARray II (SCEPTAR II) are simulated in **GEANT4**.

A.1. GEANT4 Overview

GEANT4 is a toolkit for simulating the passage of particles through matter developed in response to the increase in demand for accurate and thorough simulations of particle detectors used in modern nuclear and particle physics[76]. **GEANT4** was created out of two studies performed independently at CERN and KEK in 1993[38]. The objective was to develop an entirely new program based on object-oriented programming to allow for the functionality and flexibility required for simulating subatomic, nuclear, accelerator, space and medical physics[77].

One of the largest non-corporate object-oriented software collaborations of its kind, **GEANT4** is the state of the art toolkit for physical Monte Carlo simulations[76]. It has been used to inform detector development in some of the world's greatest nuclear physics labs, including CERN, Riken, FAIR, and TRIUMF[78, 79, 80, 81].

A.1.1. Monte Carlo Simulation Mechanisms

At its core, **GEANT4** is a Monte Carlo simulation package where particles are simulated by calculating the random path they take through various materials. Monte Carlo is the name given to stochastic computational methods that use high-statistics repeated random sampling to glean information about a system where no analytical method is available, and/or where a more structured discretisation of the problem space is inefficient[82].

Each particle, following production, has a partly-randomly determined step length that determines how long the particle will exist before the next interaction or decay event[38]. The particulars of how these individual steps are evaluated can be found in the **GEANT4** documentation available at Reference [77].

For electronic energy losses the physics considered by **GEANT4** is broken down into two main processes, ionisation and bremsstrahlung. The former simulates Møller and Bhabha scattering¹ as well as δ -ray (high-energy secondary electron) production[38, 11]. Additionally use of the PENELOPE and Livermore Monte Carlo models is available through G4PenelopeIonisationModel and G4LivermoreIonisationModel[83, 84, 85].

¹Møller and Bhabha scattering is the scattering of electrons by γ -ray exchange with electrons and positrons respectively

GEANT4 owes its high-adoption rate in fields of physical simulation to continued efforts to verify and improve the accuracy of the toolkit's capabilities. The incorporation of new physics is compared to experimental data as well as previous versions of **GEANT4** to ensure validity and accuracy[86].

A.2. **detectorSimulations** Overview

detectorSimulations is a **GEANT4** application developed by the GRIFFIN collaboration. Available at [87], **detectorSimulations** provides simulation code for the GRIFFIN array and it's suite of ancillary detection systems. Based on the reputable and experimentally validated **GEANT4** software, **detectorSimulations** has also been corroborated against the performance of real TIGRESS detectors in [88].

A.2.1. File structure

As a relatively large C++ project, **detectorSimulations** makes use of over 30 C++ source files included in the `$detSim/src` directory, and their associated headers in the `$detSim/include` directory. Where `$detSim` denotes the path to the **detectorSimulations** directory cloned via `git`.

The different source files in **detectorSimulations** and their functions are summarised in Table 10-1.

Each of the above has an associated header file.

A.3. Interfacing and Automation

Firstly, to begin simulations **detectorSimulations** needs to be compiled by using `cmake` and `make` from within a build directory:

```
1 cd $pathToBuildDir
2 cmake $pathToDetSimSrcDir
3 make
```

The `cmake` command generates a makefile that compiles all .cc files included in the .hh headers within `$pathToDetSimSrcDir/include/`. Subsequent re-compilations without new source files only require `make` to rebuild. Then the **detectorSimulations** GUI can be launched via `./GRIFFINV10`.

A.3.1. Using **GEANT4** macros

GEANT4 macros have extension `.mac` and contain a series of UI commands that are used to set up and run simulations. From within the **detectorSimulations** UI macros are executed as follows:

```
1 /control/macroPath pathToMacroDirectory
2 /control/execute macro.mac
```

Where the first line is only necessary if the macro is **not** in the same directory as the `GRIFFINV10` executable.

To run **detectorSimulations** from within a terminal with a macro:

```
1 ./\acrshort{grif}v10 macro.mac
```

Basic macro template

This section contains all the necessary information to write **GEANT4** macros for basic detector simulations using **detectorSimulations**. The following sections are all necessary for a successful simulation, and should be included in this order. Example macros are provided in Appendix B.2.

Table 10-1 C++ source files in **detectorSimulations**

File (.cc)	Function
ActionInitialization	Initialisation for detectors and generators
Apparatus*	Classes to define logical volumes that do not have detection functionality. Including GRIFFIN and DESCANT support structures, generic and layered targets, vacuum chamber shells for 8pi/GRIFFIN ancillary detectors and the SPICE target chamber.
BeamDistribution	Class to load an energy spectrum from a file
DetectionSystem*	Classes to define logical volumes for detectors. Including; real detectors 8π , ancillary BGO, DESCANT, GRIFFIN, LaBr, PACES, S3, SCEPTAR, NaI, and SPICE; as well as generic detectors Box, Grid and Testcan.
DetectorConstruction	The main detector class of detectorSimulations which interfaces with the various Apparatus and DetectionSystem classes to define detectors.
DetectorConstructionSuppressed	Sensitive information counterpart of DetectorConstruction , this class defines materials used in the various detector systems.
DetectorMessenger	Class that defines GEANT4 UI commands.
EventAction	Run at the start of every beam event (particle). Includes functions for clearing variables, processing hit trackers and step actions.
HistoManager	Manages the ROOT output and fills the NTuples.
NonUniformMagneticField	Defines magnetic field with TabulatedMagneticField
PhysicsList	Loads physics lists for hadrons and particles.
PhysicsListMessenger	Defines UI commands for interfacing with PhysicsList and PhysList*
PrimaryGeneratorAction	Class create particle guns and radiation sources.
PrimaryGeneratorMessenger	UI commands for PrimaryGeneratorAction .
RunAction	Initialisation and destruction of HistoManager class during a simulation run.
SteppingAction	Hit tracking and energy deposition definitions.
TabulatedMagneticField	Loads magnetic field data from a file.

Selecting Physics Lists and Initialisation

At the beginning of every macro the physics lists and interaction processes are loaded, and the run must be initialised.

```

1 /DetSys/phys>SelectPhysics emlivermore
2 /run/initialize
3 /process/em/fluo true
4 /process/em/auger true
5 /process/em/pixe true

```

The first line in the macro snippet above selects the PEID/Livermore Monte Carlo models (**G4LivermoreIonisationModel**), these were used for all simulations described in this work[85]. Line 2 initialises the **GEANT4** run. The remaining lines activate the fluorescence, Auger, and particle-induced x-ray emission (PIXE) interactions[89].

Console verbosities

The console output verbosities are controlled with various `*/verbose` commands where 0 is the minimum:

```
1 /control/verbose 0
2 /run/verbose 0
3 /event/verbose 0
4 /tracking/verbose 0
```

Within the source code, information is written to the **GEANT4** log via **G4cout**.

Selecting world material

The default world material is controlled with:

```
1 /DetSys/world/material Material
```

Commonly **Material** is either **Vacuum** or **Air**.

Detector placement commands

In order to place detectors already defined in the standard **detectorSimulations** distribution the following commands can be used:

```
1 # \acrshort{grif} detector properties for normal/unsuppressed mode:
2 /DetSys/det/SetCustomShieldsPresent 0
3 /DetSys/det/SetCustomRadialDistance 11 cm
4 /DetSys/det/SetCustomExtensionSuppressorLocation 0
5 /DetSys/det/include\acrshort{grif}Hevimet 0
6
7 # Place normal mode \acrshort{grif} detector N:
8 /DetSys/det/SetCustomDeadLayer N N 0
9 /DetSys/det/add\acrshort{grif}CustomDetector N
10
11 # Place optimised peak to total mode \acrshort{grif} detector N:
12 /DetSys/det/add\acrshort{grif}BackDetector N
13
14 # Place all 20 Sceptar paddles:
15 /DetSys/det/addSceptar 20
16
17 # Place Delrin vacuum chamber:
18 /DetSys/app/add8piVacuumChamber
```

All the simulations discussed in this work that use unmodified **detectorSimulations** detector classes are placed with the above commands. The 8π vacuum chamber, SCEPTAR, and optimised peak to total mode GRIFFIN detectors can simply be placed with the appropriate `/DetSys/det/add*` command. However, for unsuppressed/normal mode GRIFFIN detectors the `/DetSys/det/addGRIFFINCUSTOMDetector` command is used which requires its dead layer to be set (line 8) and the overall shield and positioning parameters to be set (lines 2-5). Normal mode operation uses no suppression shields (lines 2,4), positioning with the detector front at 11 cm, and no Hevimet (line 5). While the generic (cuboid) target class is often used to define basic detector geometries in this work, these require modifications to the source for optimal usage, see Section A.4.

Visualisation

When running from within the **detectorSimulations** GUI the current simulation environment can be rendered in a 3D visualiser using the following commands:

```
1 /vis/open OGL
2 /vis/viewer/set/viewpointThetaPhi 70 20 deg
3 /vis/viewer/zoomTo 0.5
```

```
4 /vis/viewer/set/style surface
5 /vis/drawVolume
6 /vis/scene/add/trajectories smooth
7 /vis/scene/endOfEventAction accumulate 100
```

The first line selects the OGL (Open Graphics Library) as the renderer. Lines 2-3 determine the initial camera direction and field of view, respectively. Line 4 determines the rendering style for all objects, available styles are: (**wireframe** and **surface**). Line 5 renders all defined logical volumes. Lines 6-7 enable particle trajectory plotting and select the maximum number of trajectories displayed. Visualisation is **not** recommended when operating in batch.

Particle and Events

The **/gun/** class is used for linear beam simulations. The following commands run a simulation with an idealistic beam of **N Particles** with energy **E keV** in the direction $(v_x, v_y, v_z) = (0, 0, v_z)$ from the origin:

```
1 /gun/particle Particles
2 /gun/energy E keV
3 /run/beamOn N
```

The **/DetSys/gun** class is used for simulations with particles emitted with a uniform radial direction distribution. The following commands run a simulation with **N Particles** with uniformly random radial directions originating from the origin:

```
1 /DetSys/gun/particle Particles
2 /DetSys/gun/efficiencyEnergy E keV
3 /run/beamOn N
```

Available particle types are **e-**, **e+**, **gamma**, **proton**, and **alpha**.

A.3.2. Automatic macro generation

Natively, **detectorSimulations** does not provide functionality to run simulations with a range of particle beam energies. To evaluate characteristics such as γ -ray detection efficiencies and to reproduce detector responses to β -decay sources **Bash** scripts are used to generate the **GEANT4** scripts and execute it within a new instance of **detectorSimulations**.

An example script which runs **detectorSimulations** with using a source spectrum given in an input file is shown below:

```
1 if [[ $# -eq 0 ]] ; then
2   echo 'No arguments passed to script'
3   echo 'Usage: ./macro_gen directory macro spectrum'
4   exit 0
5 fi
6
7 dir=$1
8 mac=$2
9 specfile=$3
10
11 mkdir $dir
12
13 logfile="macro_gen_log.txt"
14
15 while read line; do
16
17   E=$(echo $line | cut -d " " -f 1) # first column, space separator
18   N=$(echo $line | cut -d " " -f 2) # second column, space separator
```

```

19
20  if [ ! -f ./"$dir"/max_"$E".root ]; then # if file does not exist
21      # copy macro and append beam commands:
22      cp $mac auto.mac
23      echo "/DetSys/gun/particle e-" >> auto.mac
24      echo "/DetSys/gun/efficiencyEnergy" "$E"" MeV" >> auto.mac
25      echo "/run/beamOn ""$N" >> auto.mac
26
27      start='date +%s'
28
29      ../../acrshort{grif}v10 auto.mac # execute detectorSimulations with generated macro
30
31      end='date +%s'
32      end2='date'
33      runtime=$((end-start)) # determine runtime of the simulation
34
35      # move the root output and macro
36      mv g4out.root "$dir"/max_"$E".root
37      mv auto.mac "$dir"/max_"$E".mac
38
39      echo $dir", \"$E\" MeV completed in \"$runtime\" seconds, at \"$end2 >> $logfile
40  else
41      echo $dir", \"$E\" MeV skipped" >> $logfile
42      echo "File \"$dir"/max_"$E".root already present. Skipped."
43  fi
44
45 done < $specfile

```

The bash script given above takes arguments for the directory within which the output **ROOT** files will be stored, the macro used for simulation², and a two-column text file containing information about the source spectrum. For every line present in the spectrum file, it is parsed for the energy (**E**) and number of particles in the beam (**N**). This information is appended to the macro run in **detectorSimulations**.

A.4. Defining generic targets/detectors

In order to simulate the response of a scintillation detector, the quantity of energy deposited by incident radiation must be determined. In ?? the mechanisms by which β -particles can interact and deposit energy in matter were presented. These interactions are included in the physics of **GEANT4**. Both **SCEPTAR I** and the proposed **SCEPTAR II** design uses 1.6 mm thick BC404 scintillator manufactured by St. Gobain[58]. Initial investigations into electron energy depositions in BC404 were performed by defining a square of BC404 scintillator in vacuum, and then introducing a beam of monoenergetic electrons normally.

A.4.1. Generic target macro commands

Within the **detectorSimulations** application the *Generic Target* detector class is used to define the scintillator volume. In the unmodified **detectorSimulations** version (as of October 2018) the scintillator targets are defined as follows:

```

1 /DetSys/app/genericTarget BC404
2 /DetSys/app/genericTargetDimensions 1.0 1.0 0.16 cm
3 /DetSys/app/genericTargetPosition 0 0 5.08 cm

```

²The macro should contain all the necessary simulation setup as given in Section A.3.1, excluding the visualisation **and** particle and events functionality. A blank line at the end of the blank macro is also necessary.

This defines a scintillator square with a 10 mm by 10 mm front face and a thickness of 1.6 mm, positioned on the positive z-axis so that the front face is at 5cm from the beam origin.

A.4.2. Modifications to detectorSimulations to allow for multiple generic targets

In `detectorSimulations` the UI commands `/DetSys/app/genericTarget`, `/DetSys/app/genericTargetDimensions`, and `/DetSys/app/genericTargetPosition` call functions within the `DetectorConstruction` class. For example `/DetSys/app/genericTargetDimensions` calls `SetGenericTargetDimensions()` which is shown below:

```
1 void DetectorConstruction::SetGenericTargetDimensions( G4ThreeVector vec ) {
2   DetectorConstruction::fGenericTargetDimensions = vec;
3   DetectorConstruction::fSetGenericTargetDimensions = true;
4   DetectorConstruction::SetGenericTarget();
5 }
```

This function takes the input vector for the target dimensions and stores it in a private variable within `DetectorConstruction`, sets a boolean flag to true saying that generic target dimensions have been defined, and finally calls another function which then actually creates the new detector. The function for the position command is identical in its functionality, and the material function simply replaces the vector argument for a string.

The `SetGenericTarget()` function checks if all the boolean flags for the material, position and dimension parameters. If they are all true then a new instance of the `ApparatusGenericTarget()` is created. Every new call to one of the three generic target commands results in a call to `SetGenericTarget()`. This results in an issue when multiple parameters need to be changed between successive detectors, as changing one parameter also creates an additional target volume.

To rectify this issue the calls to `SetGenericTarget()` within `SetGenericTargetMaterial()`, `SetGenericTargetDimensions()` and `SetGenericTargetPosition()` were removed. Instead, a new UI command was defined that calls `SetGenericTarget()` directly, the function of which remained largely unchanged. The method for defining a new UI command can be seen in Section A.5.

With the changes described above a generic target is now created with the following macro commands:

```
1 /DetSys/app/genericTarget material
2 /DetSys/app/genericTargetDimensions a b c unit
3 /DetSys/app/genericTargetPosition x y z unit
4 /DetSys/app/genericTargetConstructor
```

A.5. Defining new user interface commands

In `detectorSimulations` the user interface commands are handled by the `G4UIMessenger` class `DetectorMessenger` in `DetectorMessenger.cc`. To set up a new UI command the following needs to be performed:

A.5.1. Declaring a new user interface command

A new command pointer is privately declared in the `DetectorMessenger` class contained in the header file (`DetectorMessenger.hh`):

```
1 G4UIcmdWithAString* fNewStringCmd;
```

The available UI command types are: `G4UIcmdWithoutParameter`, `G4UIcmdWithABool`, `G4UIcmdWithAnInteger`, `G4UIcmdWithADouble`, `G4UIcmdWithADoubleAndUnit`, `G4UIcmdWithAString`, `G4UIcmdWith3Vector`, and `G4UIcmdWith3VectorAndUnit`.

Following this the new command instance must be created and a UI command phrase defined in the `DetectorMessenger` class in the source file (`DetectorMessenger.cc`):

```
1 fNewStringCmd = new G4UIcmdWithAString("/DetSys/example/stringCommand", this);
```

Now the UI command phrase “/DetSys/example/stringCommand” creates a new instance of the `fNewStringCmd` command object. Then guidance is added to the command (which can be accessed in the help menu of the GUI), and declare which states the command should be available in:

```
1 fNewStringCmd->SetGuidance("Some int.");
2 fNewStringCmd->AvailableForStates(G4State_PreInit, G4State_Idle);
```

Practically all UI commands in `detectorSimulations` are available only in the pre-initialisation and idle stages of execution.

It is good practice to delete the pointer to the command object instance in the `DetectorMessenger` class destruction function:

```
1 delete fNewStringCmd;
```

A.5.2. Adding functionality to a user interface command

Every time a UI command is called in the `GEANT4` UI the `DetectorMessenger::SetNewValue()` function is called. Within this function calls are made to various functions of the current instance of the `DetectorConstruction` class. For the `fNewStringCmd` example from above, the string argument is passed to the example function `DetectorConstruction::SomeDetectorFunction()` in the following way:

```
1 if( command == fNewStringCmd ) {
2   fDetector->SomeDetectorFunction(fNewStringCmd->GetNewStringValue(newValue));
3 }
```

Where “String” in `GetNewStringValue(newValue)` is replaced with the appropriate variable from: `Bool`, `Integer`, `Double`, or `3Vector`.

A.6. Adding hit tracking functionality to new detectors

In `SteppingAction.cc` of `detectorSimulations` every step within a user-defined logical volume triggers `UserSteppingAction(const G4Step* aStep)` within the `SteppingAction` class. The pointer to the `G4VPhysicalVolume`, its name and the energy deposited in the step are retrieved as follows:

```
1 G4VPhysicalVolume* volume =
  aStep->GetPreStepPoint()->GetTouchableHandle()->GetVolume();
2 G4String volname = volume->GetName();
3 G4double edep = aStep->GetTotalEnergyDeposit();
```

Other hit parameters such as the kinetic energy, step number, particle name, process type are accessed in a similar fashion. Once all the current parameters are loaded detector specific hit registration is performed:

Generally, to add energy deposition hit tracking to a new detector type one must:

- Search for the desired detector string within the volume name
- If non-energy energy deposition
 - Define hit parameters/identifiers
 - Add a new hit and pass this to an `EventAction` object pointer from the `EventAction.cc`.

A.6.1. Example for generic target

Energy deposition hit tracking to the generic target detector type is added as follows:

```
1 found = volname.find("target");                                // find position substring
2 if (edep != 0 && found !=G4String::npos) {                      // non-zero energy and found
```

```

3 G4Material *material = aStep->GetTrack()->GetMaterial(); // get pointer to material
4 G4String matName = material->GetName(); // get material name
5
6 int volNum, matNum;
7 std::istringstream iss(volname.substr(3,1)); // make stream from string
8 iss >> volNum; // get volume number
9 matNum = 0; // default material number
10 if (matName == "Silicon") matNum = 1; // set material numbers
11 if (matName == "G4_KAPTON") matNum = 2; // ''
12 if (matName == "Copper") matNum = 3; // ''
13 if (matName == "BC404") matNum = 4; // ''
14 fDet = volNum; // set fDet
15 fCry = matNum; // set fCry
16 systemID = 9900 + 10*matNum + volNum; // set systemID
17 mnemonic = "Tgt__"; // set mnemonic
18 mnemonic.replace(3,1,G4intToG4String(volNum)); // ''
19 mnemonic.replace(5,1,G4intToG4String(matNum)); // ''
20 // add a hit tracker with parameters defined above:
21 fEventAction->AddHitTracker(mnemonic, evntNb, trackID, parentID, fStepNumber,
   particleType, processType, systemID, fCry-1, fDet-1, edep, pos2.x(), pos2.y(),
   pos2.z(), time2, targetZ);
22 }

```

These parameters can be used to identify the hit by their entries in the respective NTuple.

A.7. Defining SCEPTAR II detector

The SCEPTAR II scintillator array is similar to its predecessor, in that the BC404 scintillator volumes are arranged to match the angular positions of detectors in the large γ -ray spectrometer array it sits within. Therefore it is efficient to define the new SCEPTAR II detector class in a similar fashion to the original SCEPTAR class (`DetectionSystemSceptar`).

A.7.1. Overview of new class structure

To recreate the SCEPTAR II detector within `detectorSimulations`, the original SCEPTAR classes were used as a template. In `DetectionSystemSceptar2.hh` a new class `DetectionSystemSceptar2` is defined. The new detector class contains code to:

- Choose a detector configuration
- Place scintillator volumes at GRIFFIN crystal angular positions
- Place approximate SiPM volumes on the back of the scintillators
- Choose the thickness and material for the SCEPTAR II holding structure
- Place the SCEPTAR II holding structure with given parameters

In terms of the public functions of `DetectionSystemSceptar2` this functionality is provided as seen in Table 10-2.

A.7.2. New UI commands

Several new UI commands have been defined for the new SCEPTAR II detector system. The general methodology to define new `GEANT4` UI commands are seen in Section A.5. These determine detector configuration, and then to build and place said detector. Their functions are outlined in Table 10-3.

The details of the implementation and functionality of the command in Table 10-3 are given in the following sections.

UI Commands to set boolean flags for SiPMs and holding structure

Table 10-2 Public functions in `DetectionSystemSceptar2`

Function	Description
<code>DetectionSystemSceptar2()</code>	Class constructor
<code>~DetectionSystemSceptar2()</code>	Class destructor
<code>SetConfig(G4int configuration, G4bool buildStruc, G4bool buildSipm)</code>	Set detector configuration
<code>SetStructureMaterial(G4String material)</code>	Set structure material
<code>SetStructureThickness(G4double thickness)</code>	Set structure thickness
<code>BuildDetector()</code>	Create the necessary detector volumes
<code>PlaceDetector(G4LogicalVolume* expHallLog)</code>	Place the necessary detector volumes in the given volume
<code>Debrief()</code>	Write a summary to the console

Table 10-3 New UI commands introduced to determine detector configuration, and to build and place SCEPTAR II.

UI Command & Variable in <code>DetectorMessenger</code>	Description
<code>"/DetSys/det/Sceptar2BuildSipm"</code> <code>fSceptar2BuildSipm</code>	<code>G4UIcmdWithABool</code> to set whether to build SCEPTAR II SiPM array
<code>"/DetSys/det/Sceptar2BuildStruc"</code> <code>fSceptar2BuildStruc</code>	<code>G4UIcmdWithABool</code> to set whether to build SCEPTAR II holding structure
<code>"/DetSys/det/Sceptar2StructureMaterial"</code> <code>fSceptar2StructureMaterialCmd</code>	<code>G4UIcmdWithAString</code> to set SCEPTAR II holding structure material
<code>"/DetSys/det/Sceptar2StructureThickness"</code> <code>fSceptar2StructureThicknessCmd</code>	<code>G4UIcmdWithADoubleAndUnit</code> to set SCEPTAR II holding structure thickness
<code>"/DetSys/det/addSCEPTAR II2"</code> <code>fAddDetectionSystemSceptar2Cmd</code>	<code>G4UIcmdWithAnInteger</code> to build and place SCEPTAR II detector in given configuration

In `DetectorMessenger` the UI commands `fSceptar2BuildSipm` and `fSceptar2BuildStruc` extract the value of the boolean argument passed during the call, and execute corresponding functions in the `DetectorConstruction` class object `fDetector`:

```
1 if (command == fSceptar2BuildStrucCmd) {  
2   fDetector->SetSceptar2BuildStructure(fSceptar2BuildStrucCmd->GetNewBoolValue(newValue));  
3 }  
4 if (command == fSceptar2BuildSipmCmd) {  
5   fDetector->SetSceptar2BuildSipm(fSceptar2BuildSipmCmd->GetNewBoolValue(newValue));  
6 }
```

Within `DetectorConstruction()` of `DetectorConstruction.cc` these passed values are simply stored in two `G4bool` private variables:

```
1 void DetectorConstruction::SetSceptar2BuildStructure(G4bool build) {  
2   fSceptar2BuildStruc = build;  
3 }  
4 void DetectorConstruction::SetSceptar2BuildSipm(G4bool build) {  
5   fSceptar2BuildSipm = build;  
6 }
```

UI Commands to set holding structure parameters

Similarly to the commands for the boolean flags in Section A.7.2, SCEPTAR II's holding structure parameters are passed to **fDetector** as follows:

```
1 if (command == fSceptar2StructureMaterialCmd) {
2   fDetector->SetSceptar2StructureMaterial(newValue);
3 }
4 if (command == fSceptar2StructureThicknessCmd) {
5   fDetector->SetSceptar2StructureThickness(fSceptar2StructureThicknessCmd->
6     GetNewDoubleValue(newValue));
7 }
```

Following this, the values are stored privately in appropriate variables:

```
1 void DetectorConstruction::SetSceptar2StructureMaterial(G4String material) {
2   fSceptar2StructureMaterial = material;
3 }
4 void DetectorConstruction::SetSceptar2StructureThickness(G4double thickness) {
5   fSceptar2StructureThickness = thickness;
6 }
```

Building and placing the SCEPTAR II detector

As with other UI commands, `/DetSys/det/addSceptar2` followed by an integer configuration calls a function in **DetectorConstruction()** and passes its argument:

```
1 if(command == fAddDetectionSystemSceptar2Cmd) {
2   fDetector->AddDetectionSystemSceptar2(fAddDetectionSystemSceptar2Cmd->
3     GetNewIntValue(newValue));
4 }
```

Where the implementation of the command **fAddDetectionSystemSceptar2Cmd** differs to the UI commands described earlier, is that the function **AddDetectionSystemSceptar2()** (of **DetectorConstruction**) now creates a new **DetectionSystemSceptar2** object:

```
1 void DetectorConstruction::AddDetectionSystemSceptar2(G4int config) {
2   if(fLogicWorld == NULL) Construct();
3
4   DetectionSystemSceptar2* pSceptar2 = new DetectionSystemSceptar2();
5   pSceptar2->SetConfig(config, fSceptar2BuildStruc, fSceptar2BuildSipm);
6   pSceptar2->SetStructureMaterial(fSceptar2StructureMaterial);
7   pSceptar2->SetStructureThickness(fSceptar2StructureThickness);
8   pSceptar2->BuildDetector();
9   pSceptar2->PlaceDetector(fLogicWorld);
10  pSceptar2->Debrief();
11 }
```

The above function, when called, constructs the logic world, and then proceeds to define the new detection system on line 4. Lines 5-7 pass the newly defined detector parameters or their default values. Lines 8-9 call functions which build and place the detector system in the logic world respectively. **Debrief()** provides the user with information about the placed detector and errors through the **GEANT4** console.

A.7.3. Using GRIFFIN coordinates

In **GEANT4** volumes are positioned within the world volume using a position vector (**G4ThreeVector**) and an orientation matrix (**G4RotationMatrix**). For a given GRIFFIN position number and crystal number, and a

cartesian position given in the variables **x**, **y**, and **z** - the position vector and rotation matrix are defined as follows:

```
1 theta = fCoords[positionNumber][0]*deg;
2 phi = fCoords[positionNumber][1]*deg;
3 alpha = fCoords[positionNumber][2]*deg; // yaw
4 beta = fCoords[positionNumber][3]*deg; // pitch
5 gamma = fCoords[positionNumber][4]*deg; // roll
6
7 rotate = new G4RotationMatrix;
8 rotate->rotateX(M_PI/2.0);
9 rotate->rotateX(alpha);
10 rotate->rotateY(beta);
11 rotate->rotateZ(gamma);
12
13 move = G4ThreeVector(TransX(x,y,z,theta,phi), TransY(x,y,z,theta,phi),
   TransZ(x,z,theta));
```

Where the **fCoords** array contains the GRIFFIN angular coordinates, and the functions **TransX()**, **TransY()**, and **TransZ()** return position components in the GRIFFIN coordinate space.

A.7.4. Creating new detector volumes

The detector geometry of SCEPTAR II, like the original SCEPTAR, can be broken down into repetitions of smaller units. To reduce the amount of redundant code these repetitive units are defined in a **G4AssemblyVolume** of which repeated imprints can be made to produce the full detector.

The scintillators are defined as a **G4Box** in the private function **SquareScintillator()**:

```
1 G4Box* DetectionSystemSceptar2::SquareScintillator() {
2   G4Box* squareScintillator = new G4Box("squareScintillator", scintThick/2,
   scintWidth/2, scintWidth/2);
3   return squareScintillator;
4 }
```

This scintillator is then placed within the **G4AssemblyVolume** in **ConstructScintillator()**:

```
1 void DetectionSystemSceptar2::ConstructScintillator() {
2
3   // Visualisation attributes:
4   G4VisAttributes* scintillatorVisAtt = new G4VisAttributes(G4Colour(0.6, 0.6, 0.6));
5   scintillatorVisAtt->SetVisibility(true);
6
7   // Check if the material has been defined:
8   fMaterialScint = G4Material::GetMaterial("BC404");
9   if( !fMaterialScint ) {
10     G4cout << " ----> Material " << "BC404" << " not found, cannot build the
11       scintillator! " << G4endl;
12     errors++;
13   }
14
15   // Physical volume:
16   G4Box* scintillator = SquareScintillator();
17   // Logical volume:
18   fScintillatorLog = new G4LogicalVolume(scintillator, fMaterialScint,
```

```

    "Sceptar2ScintillatorLog", 0, 0, 0);
19 // Apply visualisation attributes:
20 fScintillatorLog->SetVisAttributes(scintillatorVisAtt);
21 // Add logical volume to the assembly volume:
22 fAssembly->AddPlacedVolume(fScintillatorLog, moveNull, rotateNull);
23 }

```

Once **fAssembly** contains all the required logical volumes, **PlaceDetector()** creates “imprints” for all the required GRIFFIN positions. Once the GRIFFIN coordinates for the given position are stored in the **move** position vector and **rotate** rotation matrix the imprint is created in the **expHallLog** world volume as follows:

```
1 fStructureAssembly->MakeImprint(expHallLog, move, rotate, 0);
```

A.7.5. Holding structure geometry

The holding structure for SCEPTAR II’s scintillators was implemented in **GEANT4** in a similar fashion to the scintillator volumes - a symmetric unit was defined in a **G4AssemblyVolume** and imprints are made at all required GRIFFIN positions. These units are defined in **SquareStructure()**:

```

1 G4VSolid* strucPlane = new G4Box("strucPlane", strucThick/2, scintWidth*4/3,
      scintWidth*4/3);
2 G4VSolid* scintHole = new G4Box("scintHole", strucThick, scintWidth, scintWidth);
3 G4VSolid* struc1 = new G4SubtractionSolid("struc1", scintPlane, scintHole, 0,
      moveNull);
4 G4VSolid* strucCut = new G4Box("strucCut", cutWidth, cutWidth, scintWidth*2);
5
6 rotate = new G4RotationMatrix;
7 rotate->rotateX(90.*deg);
8 rotate->rotateZ(2*M_PI/16);
9 move = G4ThreeVector(0.0,0.0,cutDist);
10 G4VSolid* struc2 = new G4SubtractionSolid("struc2", struc1, strucCut, rotate, move);
11
12 rotate = new G4RotationMatrix;
13 rotate->rotateX(90.*deg);
14 rotate->rotateZ(-2*M_PI/16);
15 move = G4ThreeVector(0.0,0.0,-cutDist);
16 G4VSolid* struc3 = new G4SubtractionSolid("struc3", struc2, strucCut, rotate, move);
17
18 rotate = new G4RotationMatrix;
19 rotate->rotateZ(-2*M_PI/16);
20 move = G4ThreeVector(0.0,cutDist,0.0);
21 G4VSolid* struc4 = new G4SubtractionSolid("struc4", struc3, strucCut, rotate, move);
22
23 rotate = new G4RotationMatrix;
24 rotate->rotateZ(2*M_PI/16);
25 move = G4ThreeVector(0.0,-cutDist,0.0);
26 G4VSolid* struc5 = new G4SubtractionSolid("struc5", struc4, strucCut, rotate, move);
27
28 return struc5;

```

The above code returns a pointer to a **G4VSolid** which contains a single unit which can be repeated to create the full holding structure. The finished volume is shown in Figure 10-1

This result is achieved through a series of arithmetic operations with **G4VSolid**’s. The series of subtraction steps are shown in Figure 10-3, and the completely defined holding structure and a 3D printed prototype are

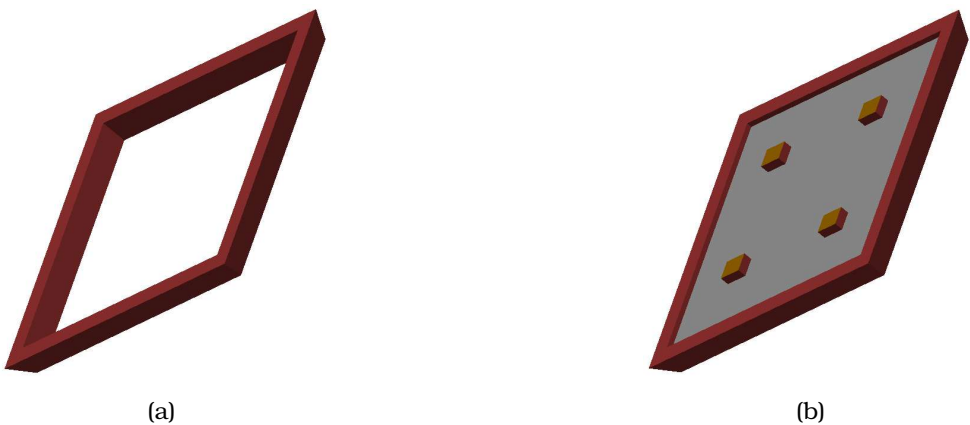


Figure 10-1 (a) Single unit of the SCEPTAR II holding geometry. (b) Single unit of the SCEPTAR II holding geometry shown with SiPM and BC404 volumes.

shown in Figure 10-2.

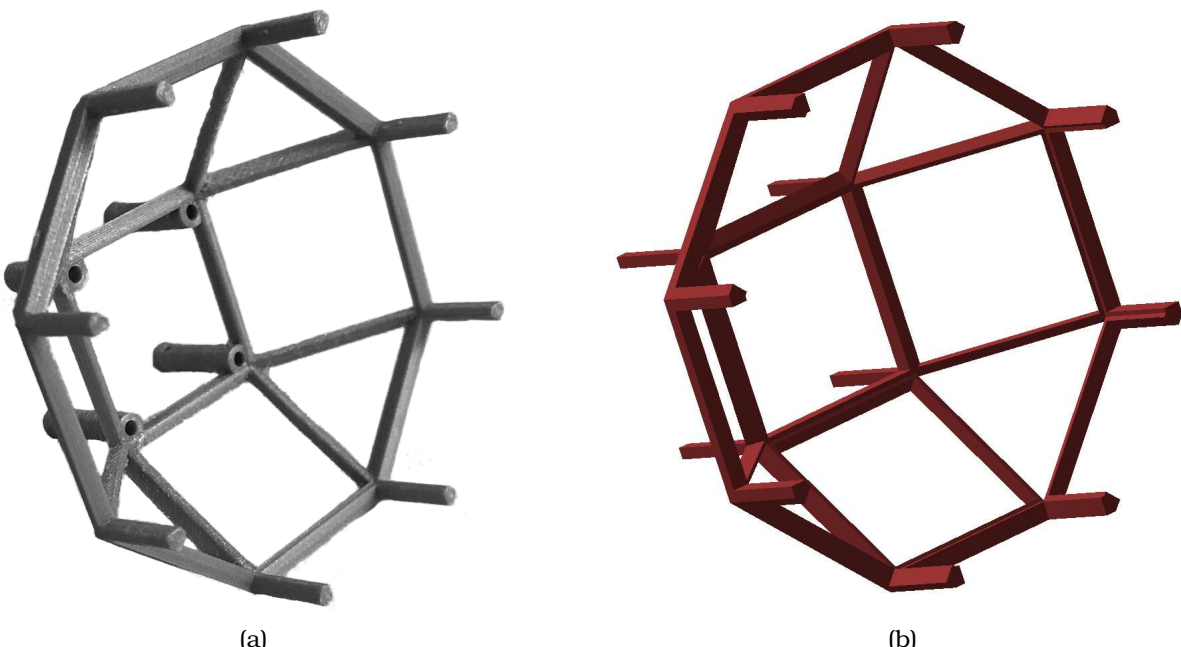


Figure 10-2 (a) Prototype of one hemisphere of SCEPTAR II's support structure 3D printed in acrylonitrile butadiene styrene (ABS). (b) 3D model of one hemisphere of SCEPTAR II's support structure as implemented in the new SCEPTAR II class of `detectorSimulations` and rendered in `Geant4`.

A.7.6. Adding SiPM volumes

Approximations for the SiPM volumes are defined with `G4Box` and `G4SubtractionSolid` and added to `fAssembly` in `ConstructSiPM()`. Silicon is used for the active material, copper for the conductive layer, and Mylar for the plastic shroud.

A.7.7. Adding hit tracking

While the method by which hit tracking is added for the SCEPTAR II scintillators is similar to that of the Generic Target class described in Section A.6, there are some key differences. As SCEPTAR II contains many scintillator volumes, which correspond to GRIFFIN Germanium crystals, the variables `fDet` and `fCry` must be set to the correct position. The imprint number of the assembly volume is used to find the position during hit tracking through the function `SetDetNumberForSceptar2()` in `SteppingAction.cc`:

```
1 found = volname.find("Sceptar2Scintillator");
2 if (edep != 0 && found!=G4String::npos) {
3     SetDetNumberForSceptar2(volname);
4     mnemonic.replace(0,3,"S2_");
5     mnemonic.replace(3,2,G4intToG4String(fDet));
6     mnemonic.replace(5,1,G4intToG4String(fCry));
7     systemID = 5000;
8     fEventAction->AddHitTracker(mnemonic, evntNb, trackID, parentID, fStepNumber,
9                                   particleType, processType, systemID, fCry, fDet, edep, pos2.x(), pos2.y(),
9                                   pos2.z(), time2, targetZ);
9 }
```

The mnemonic detector and crystal numbers are added to the mnemonic. The `systemID` used for SCEPTAR II is the same as for the original SCEPTAR class - this ensures that processing workflows for the original SCEPTAR with `NTuple2EventTree` can continue to work with SCEPTAR II simulations.

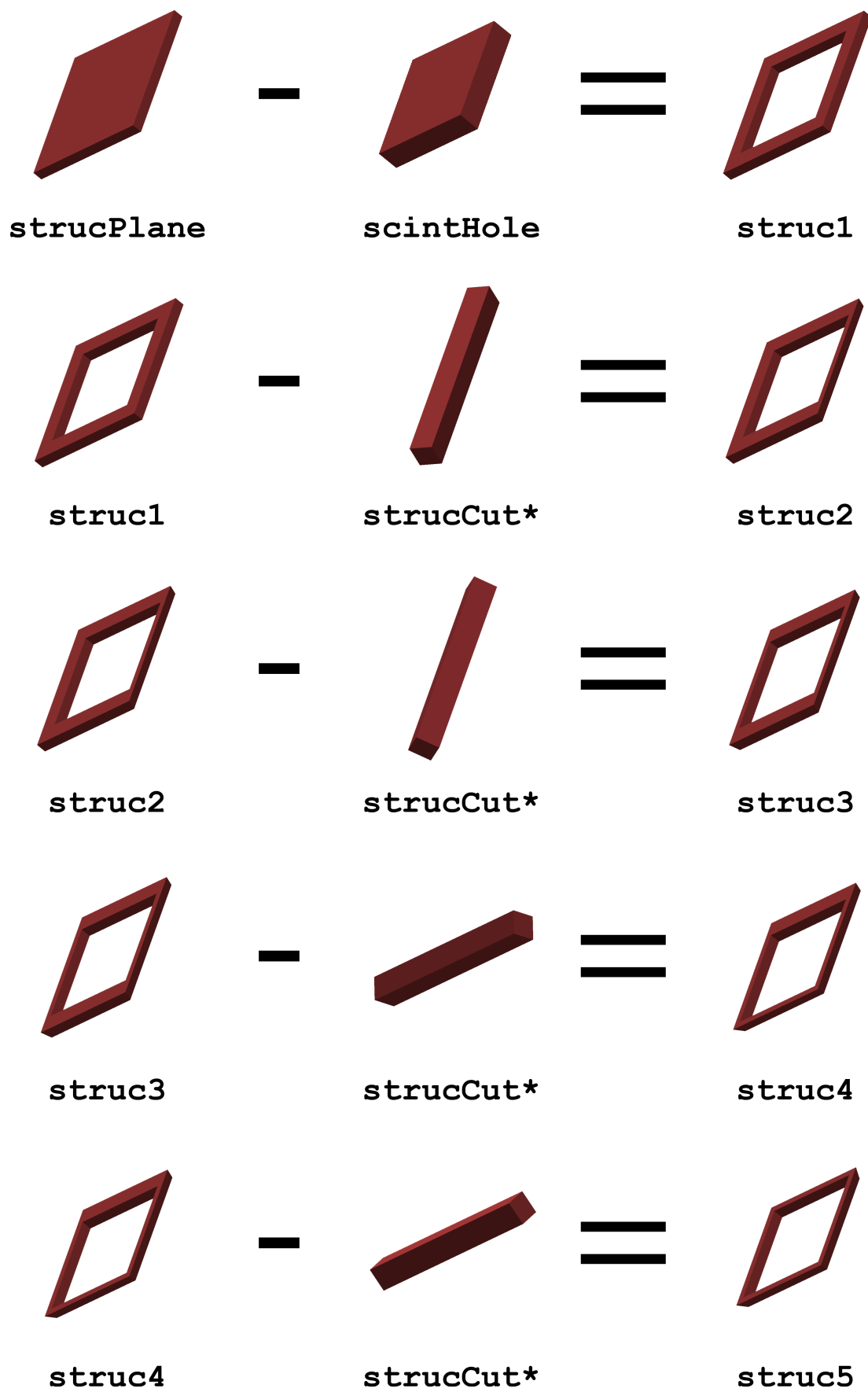


Figure 10-3 Overview of procedure to create the holding structure unit for one SCEPTAR II position in **GEANT4**. * denotes that the shape is not shown in its true position in the arithmetic operation.

B. Programs and Scripts

B.1. Bash scripts

B.1.1. NTuple2EventTree smearing automation

Generates `NTuple2EventTree` settings file and executes to smear all `.root` files in the given directory.

Listing 1 `NTuple_smear.sh`

```
1 #####%
2 # ~~~~ Max Winokan ~ NTuple_smear.sh ~ SCEPTAR smearing automation ~~~~ %
3 #####
4
5 # Execute as: ./NTuple_smear.sh $inDir $outDir $resolution
6
7 #      $indir      : directory with input ROOT files
8 #      $outdir      : output directory
9 #      $resolution : energy resolution for smearing
10
11 # Tested with NTuple2EventTree in November 2018.
12 # (c) November 2018, Max Winokan. TRIUMF, Vancouver BC, Canada.
13
14 if [[ $# -eq 0 ]]; then
15   echo 'No arguments passed to script'
16   echo 'Usage: ./NTuple_smear.sh $inDir $outDir $resolution'
17   exit 0
18 fi
19
20 inDir=$1
21 outDir=$2
22 mkdir $outDir
23 resolution=$3
24
25 echo "----SMEARING-----"
26 echo "in = $inDir"
27 echo "out = $outDir"
28 echo "res = $resolution"
29 echo "-----"
30
31 cp ntSet_blnk.dat ntSet.dat          # copy blank settings file
32
33 # append resolution settings:
34 for i in `seq 0 19`; do             # loop over all SCEPTAR detectors
35   echo "Sceptar.\"$i\".Resolution.Linear: \"$resolution >> ntSet.dat
36 done
37
38 cd $inDir                          # change to input directory
39 cp ~/NTuple/NTupleDictionary_rdict.pcm . # copy NTuple dictionary
40
41 # run NTuple
42 for filename in *.root; do         # loop over all .root files
43   echo "Smearing: " $filename
44   NTuple -sf ../ntSet.dat -if $filename -of ../$outDir/$filename -vl 1
```

```

45 done
46
47 rm NTupleDictionary_rdict.pcm           # remove the dictionary

```

B.2. GEANT4 Macros

Template **GEANT4** macro to run simulations with any of the **detectorSimulations** systems required to reproduce simulations described in this work.

Listing 2 *template.mac*

```

1 #####%
2 # ~~~~ Max Winokan ~ template.mac ~ detectorSimulations Geant4 Macro template ~~~~ %
3 #####%
4
5 # Execute as: root ./Griffinv10 template.mac
6 # Uncomment commands in sections as needed.
7 # Tested with geant4-10-02 & detectorSimulations Nov2018 mwinokan fork.
8 # (c) November 2018, Max Winokan. TRIUMF, Vancouver BC, Canada.
9
10 ##### Physics and interaction processes #####
11
12 /DetSys/phys>SelectPhysics emlivermore
13 /run/initialize
14 /process/em/fluo true
15 /process/em/auger true
16 /process/em/pixe true
17
18 ##### World properties #####
19
20 # /DetSys/world/material G4_AIR
21 /DetSys/world/material Vacuum
22
23 ##### GRIFFIN normal mode #####
24
25 # /DetSys/det/SetCustomShieldsPresent 0
26 # /DetSys/det/SetCustomRadialDistance 11 cm
27 # /DetSys/det/SetCustomExtensionSuppressorLocation 0
28 # /DetSys/det/includeGriffinHevimet 0
29
30 # /DetSys/det/SetCustomDeadLayer 1 1 0
31 # /DetSys/det/addGriffinCustomDetector 1
32 # /DetSys/det/SetCustomDeadLayer 2 2 0
33 # /DetSys/det/addGriffinCustomDetector 2
34 # /DetSys/det/SetCustomDeadLayer 3 3 0
35 # /DetSys/det/addGriffinCustomDetector 3
36 # /DetSys/det/SetCustomDeadLayer 4 4 0
37 # /DetSys/det/addGriffinCustomDetector 4
38 # /DetSys/det/SetCustomDeadLayer 5 5 0
39 # /DetSys/det/addGriffinCustomDetector 5
40 # /DetSys/det/SetCustomDeadLayer 6 6 0
41 # /DetSys/det/addGriffinCustomDetector 6
42 # /DetSys/det/SetCustomDeadLayer 7 7 0
43 # /DetSys/det/addGriffinCustomDetector 7

```

```

44 # /DetSys/det/SetCustomDeadLayer 8 8 0
45 # /DetSys/det/addGriffinCustomDetector 8
46 # /DetSys/det/SetCustomDeadLayer 9 9 0
47 # /DetSys/det/addGriffinCustomDetector 9
48 # /DetSys/det/SetCustomDeadLayer 10 10 0
49 # /DetSys/det/addGriffinCustomDetector 10
50 # /DetSys/det/SetCustomDeadLayer 11 11 0
51 # /DetSys/det/addGriffinCustomDetector 11
52 # /DetSys/det/SetCustomDeadLayer 12 12 0
53 # /DetSys/det/addGriffinCustomDetector 12
54 # /DetSys/det/SetCustomDeadLayer 13 13 0
55 # /DetSys/det/addGriffinCustomDetector 13
56 # /DetSys/det/SetCustomDeadLayer 14 14 0
57 # /DetSys/det/addGriffinCustomDetector 14
58 # /DetSys/det/SetCustomDeadLayer 15 15 0
59 # /DetSys/det/addGriffinCustomDetector 15
60 # /DetSys/det/SetCustomDeadLayer 16 16 0
61 # /DetSys/det/addGriffinCustomDetector 16
62
63 ##### GRIFFIN optimised peak to total mode #####
64
65 # /DetSys/det/addGriffinBackDetector 1
66 # /DetSys/det/addGriffinBackDetector 2
67 # /DetSys/det/addGriffinBackDetector 3
68 # /DetSys/det/addGriffinBackDetector 4
69 # /DetSys/det/addGriffinBackDetector 5
70 # /DetSys/det/addGriffinBackDetector 6
71 # /DetSys/det/addGriffinBackDetector 7
72 # /DetSys/det/addGriffinBackDetector 8
73 # /DetSys/det/addGriffinBackDetector 9
74 # /DetSys/det/addGriffinBackDetector 10
75 # /DetSys/det/addGriffinBackDetector 11
76 # /DetSys/det/addGriffinBackDetector 12
77 # /DetSys/det/addGriffinBackDetector 13
78 # /DetSys/det/addGriffinBackDetector 14
79 # /DetSys/det/addGriffinBackDetector 15
80 # /DetSys/det/addGriffinBackDetector 16
81
82 ##### Griffin Structure #####
83
84 # /DetSys/app/addGriffinStructure 0          # both up- and down-stream halves
85 # /DetSys/app/addGriffinStructure 1          # upstream half
86 # /DetSys/app/addGriffinStructure 2          # downstream half
87
88 ##### SCEPTAR I #####
89
90 # /DetSys/det/addSceptar 20                 # whole SCEPTAR
91 # /DetSys/app/add8piVacuumChamber           # vacuum chamber
92 # /DetSys/app/add8piVacuumChamberAuxMatShell 20 mm # Delrin shell
93
94 ##### SCEPTAR II #####
95
96 # /DetSys/det/sceptar2BuildSipm 1          # build SiPM volumes
97 # /DetSys/det/sceptar2BuildStruc 1          # build holding structure

```

```

98 # /DetSys/det/sceptar2StructureMaterial Aluminum          # holding structure material
99 # /DetSys/det/sceptar2StructureThickness 2.0 mm          # holding structure thickness
100 # /DetSys/det/addSceptar2 3                            # place and build SCEPTAR II
101                                         #   1 - downstream
102                                         #   2 - upstream
103                                         #   3 - upstream & downstream
104
105 ##### Generic Cuboid Target #####
106
107 # /DetSys/app/genericTargetMaterial BC404             # material
108 # /DetSys/app/genericTargetDimensions a b c mm        # dimensions
109 # /DetSys/app/genericTargetPosition x y z mm         # position
110 # /DetSys/app/genericTargetColour 1.0 1.0 1.0          # RGB colour
111 # /DetSys/app/genericTargetConstructor                # build and place
112
113 ##### Verbosities #####
114
115 /control/verbose 0
116 /run/verbose 0
117 /event/verbose 0
118 /tracking/verbose 0
119
120 ##### Visualisation #####
121
122 # /vis/open OGL                                     # renderer
123 # /vis/viewer/set/viewpointThetaPhi 30 -50 deg      # camera direction of view
124 # /vis/viewer/zoomTo 1.0                           # camera field of view
125 # /vis/viewer/set/style surface                   # volume rendering style
126 # /vis/drawVolume                                # draw volumes
127 # /vis/scene/endOfEventAction accumulate 100       # accumulate 100 events
128 # /vis/scene/add/trajectories smooth            # include trajectories
129
130 ##### Particle generator #####
131
132                                         # uniform radial source
133 # /DetSys/gun/particle e-                         # particle: {e-,e+,gamma...}
134 # /DetSys/gun/efficiencyEnergy 1000 keV           # energy
135
136                                         # ideal linear beam from origin
137 # /gun/particle e-                               # particle: {e-,e+,gamma...}
138 # /gun/energy 1000 keV                          # energy
139
140 ##### Run #####
141
142 # /run/beamOn 100000

```

B.3. ROOT functions

B.3.1. `loopsum_smear()`

Used to sum and plot all the `.root` files produced by `NTuple2EventTree`.

Listing 3 `loopsum_smear.c`

```

1 /*%%%%%%%%%%%%%%%
2 % ~~~~ Max Winokan ~ loopsum_smear.c ~ NTuple plotting and summing ~~~~ %
3 %%%%%%%%%%%%%%%%
4
5 Execute as: root ./loopsum_smear.c(nD)
6
7 ... Where nD is the detector number that is filtered for.
8      nD = -1, is a null-filter
9
10 Tested with ROOT 6.08/02.
11
12 (c) November 2018, Max Winokan. TRIUMF, Vancouver BC, Canada.      */
13
14 #include "TSystem.h"
15 #include <iostream>
16 #include <fstream>
17 using namespace std;
18
19 // parameters:
20 int numBins = 2000; // number of bins in plotted histograms
21 int start = 0; // energy of first bin
22 int stop = 2000; // energy of last bin
23
24 void loopsum_smear(int thisDet) {
25
26 // declare functions:
27 void h12ascii (TH1* h, string outputFile); // export histogram as text data
28 TString plotString(string hName); // generate plotting string
29
30 // generate the filter string:
31 TString filtString;
32 if (thisDet == -1) filtString = "";
33 else filtString = "SceptarDetector.fDetectorId==" + to_string(thisDet);
34
35 // Get all .root files in current directory:
36 const char* inDir = ".";
37 const char* ext = ".root";
38 char* dir = gSystem->ExpandPathName(inDir);
39 void* dirp = gSystem->OpenDirectory(dir);
40 const char* entry;
41 const char* filename[1000];
42 Int_t n = 0;
43 TString str;
44 while ((entry = (char*)gSystem->GetDirEntry(dirp))) {
45     str = entry;
46     if(str.EndsWith(ext)) filename[n++] = gSystem->ConcatFileName(dir, entry);
47 }
48
49 // file and tree arrays:
50 TFile * file[1000];
51 TTree * tree[1000];
52
53 // loop over all files:
54 for (Int_t i = 0; i < n; i++) {

```

```

55
56 // load file and tree:
57 file[i] = new TFile(filename[i]);
58 tree[i] = (TTree*)file[i]->Get("tree");
59
60 // skip if tree has no entries:
61 int entries = tree[i]->GetEntries();
62 if (entries == 0) {
63     cout << "\033[31m" << "Tree in " << filename[i] << " has no entries!" <<
64         "\033[0m" << endl;
65     continue;
66 }
67
68 // draw the individual tree in histogram, plot and save:
69 tree[i]->Draw(plotString("hProj")); // draw tree to histogram
70 TCanvas * c1 = new TCanvas("c1", "canvas c1", 900, 600); // plot histogram on
71     canvas
72 TH2 * hProj = (TH2*)gDirectory->Get("hProj"); // get pointer to
73     histogram
74 hProj->SetXTitle("Deposited Energy");
75 hProj->SetYTitle("Counts");
76 hProj->SetAxisRange(1, 1000000., "Y");
77 gPad->SetLogy();
78 hProj->SetTitle("E = " +
79     ((TString)filename[i])(4, ((TString)filename[i]).Length()-9) + ", " +
80     filtString);
81 hProj->SetFillStyle(3001);
82 hProj->SetFillColor(kRed);
83 hProj->Draw("hist same"); // redraw with new style
84     settings
85 c1->SaveAs("proj_" + ((TString)filename[i])(4, ((TString)filename[i]).Length()-9) +
86     "_d" + (TString)to_string(thisDet) + ".png");
87 c1->Close();
88 }
89
90 // loop over all files:
91 for (Int_t i = 0; i < n; i++) {
92
93 // skip if tree has no entries:
94 int entries = tree[i]->GetEntries();
95 if (entries == 0) {
96     cout << "\033[31m" << "Tree in " << filename[i] << " has no entries!" <<
97         "\033[0m" << endl;
98     continue;
99 }
100
101 // console output:
102 if ( i == 0 ) cout << "Summing files:" << endl;
103 cout << filename[i] << " [ " << i+1 << " / " << n << " ]" << endl;
104
105 if ( i == 0 ) { // if first file
106     tree[i]->Draw(plotString("hSum"), filtString); // draw first tree to hSum
107 } else {
108 }
```

```

101     tree[i]->Draw(plotString("hNew"), filtString); // draw tree[i] to hNew
102
103     TH2 * hSum = (TH2F*)gDirectory->Get("hSum"); // pointer to hSum
104     TH2 * hNew = (TH2F*)gDirectory->Get("hNew"); // pointer to hNew
105     hSum->Add(hNew); // add hNew to hSum
106
107     if (i == n-1) { // if last file
108         // plot the summed histogram:
109         TCanvas *c2 = new TCanvas("c2", "canvas c2", 900, 600);
110         hSum->SetXTitle("Deposited Energy");
111         hSum->SetYTitle("Counts");
112         hSum->SetTitle(filtString);
113         hSum->SetFillStyle(3001);
114         hSum->SetFillColor(kRed);
115         hSum->Draw("hist same");
116         c2->SaveAs("sum_d"+(TString)to_string(thisDet)+".png"); // linear y-axis
117         gPad->SetLogy();
118         hSum->Draw("hist same");
119         c2->SaveAs("sum_log_d"+(TString)to_string(thisDet)+".png"); // logscale y-axis
120
121         // export text data
122         h12ascii(hSum, "sum_d"+to_string(thisDet)+".dat");
123     }
124 }
125 }
126 }
127
128 void h12ascii (TH1* h, string outputfile) {
129     Int_t n = h->GetNbinsX();
130     ofstream output(outputfile, ios::app);
131
132     for (Int_t i=1; i<=n; i++) {
133         output << h->GetBinLowEdge(i)+h->GetBinWidth(i)/2 << " " << h->GetBinContent(i)
134             << endl;
135     }
136 }
137 TString plotString(string hName) {
138
139     TString varStr = "SceptarDetector.fEnergy"; // for NTuple data
140     // TString varStr = "depEnergy"; // for raw sim data
141
142     TString rangeStr = "(" + to_string(numBins) + "," + to_string(start) + "," +
143         to_string(stop) + ")";
144     TString plotStr = varStr + ">>" + hName + rangeStr;
145
146     return plotStr;
147 }
```

C. Circuit Diagrams

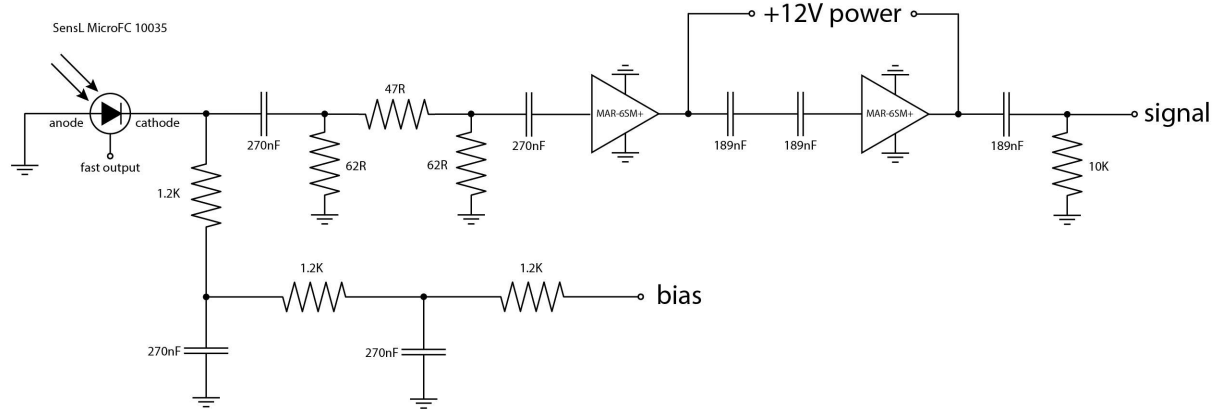


Figure 10-4 Circuit diagram for a fast biasing and readout circuit based on two MAR6SM+ RF amplifiers.

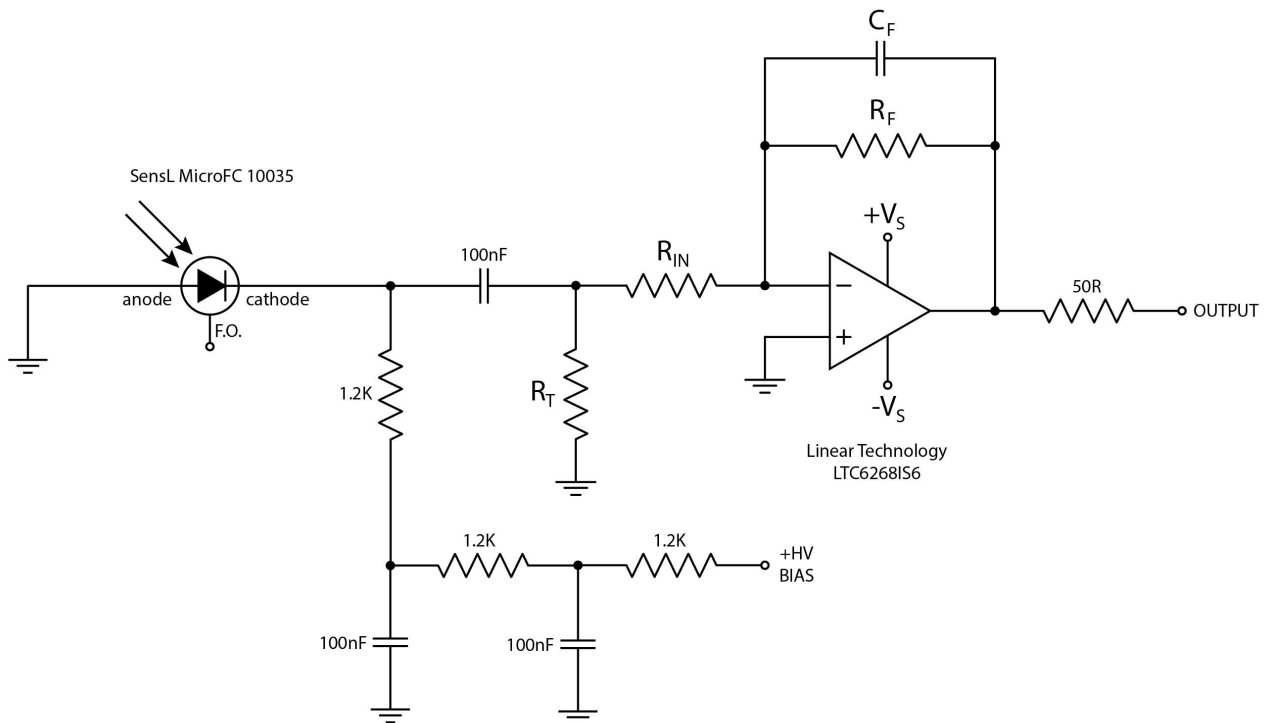


Figure 10-5 Circuit diagram for a charge integrating transimpedance amplifier based on a LTC-6268 op-amp.

D. Additional Measurements

D.1. Calibration of ORTEC easy-MCA

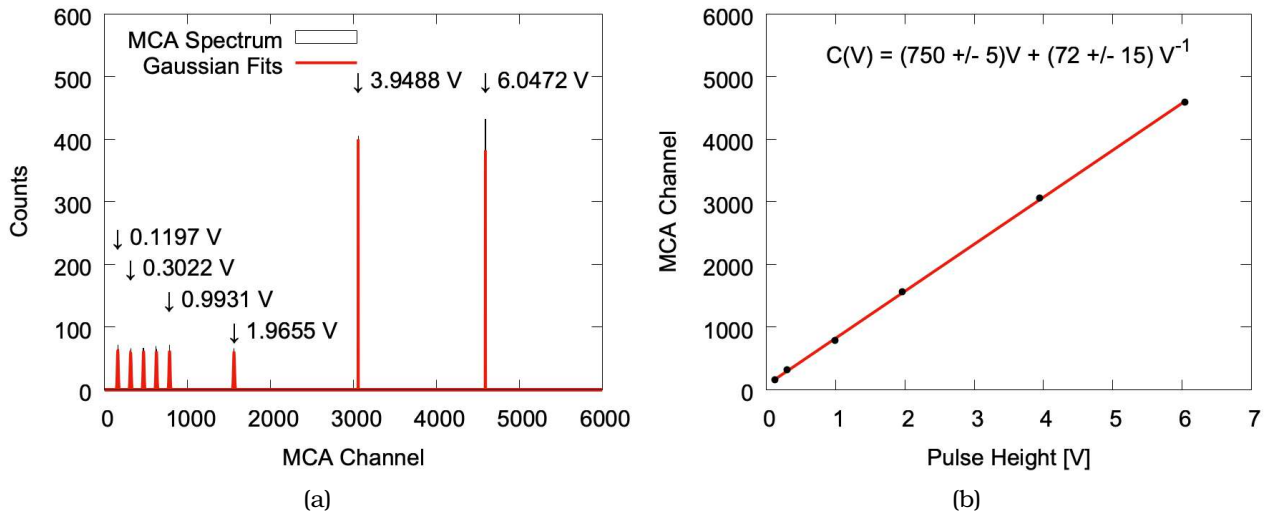


Figure 10-6 Calibrating the pulse-height analysis spectrum of the ORTEC easy-MCA (8k) (a) Discrete spectrum produced from Agilent Function 33522B generator. (b) Obtaining the linear calibration function from recorded channel against known pulse-heights.

D.2. Saturation Point of Charge Integrating Amplifier

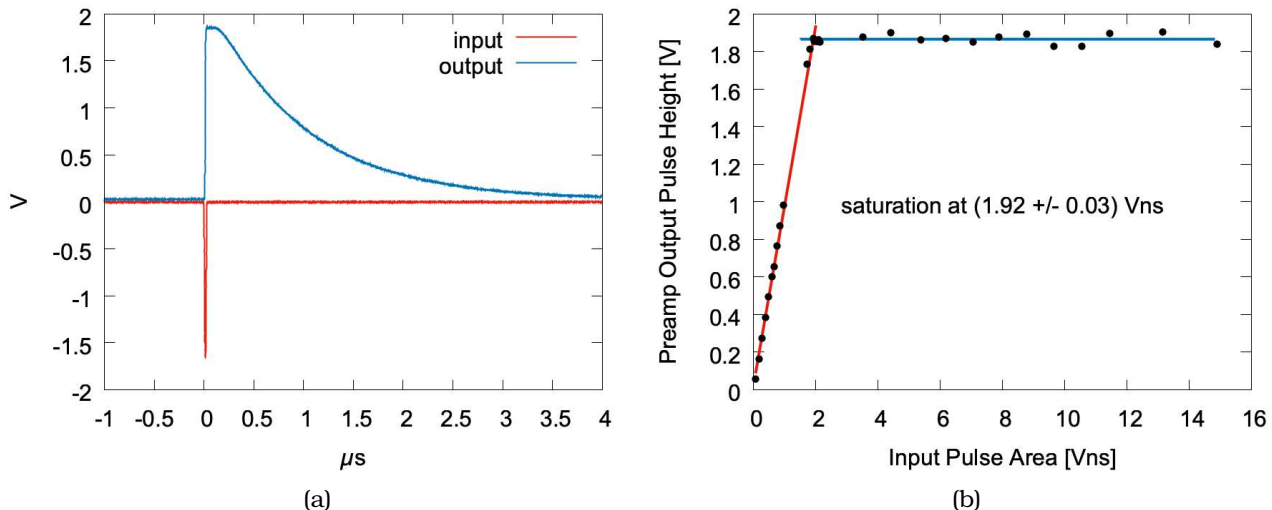


Figure 10-7 Finding the saturation point of the LTC6268-based charge integrating preamplifier with termination resistance of 82Ω and input resistance 124Ω . (a) Agilent 33522B input pulse and amplifier response (b) Amplifier pulse height against input pulse area.

D.3. Temperatures Inside GRIFFIN Vacuum Chamber During Operation with PACES

D.3.1. Introduction

The temperature inside the central vacuum chamber of the Gamma-Ray Infrastructure For Fundamental Investigations of Nuclei (GRIFFIN) was monitored during preparation and operation of the Pentagonal Array of Conversion Electron Spectrometers (PACES) in the upstream position. Two Omega PT100 Resistance Temperature Detectors (RTDs) were calibrated using liquid nitrogen as a fixed point and connected to the GRIFFIN State of Health (GRIFFIN SOH / GRIFSOH) logging system for data collection. The temperature behaviour inside PACES has never been measured and this data will be used to update estimates on cooling and warming times of the detector, as well as to obtain an estimate of radiative cooling effects on downstream detectors, when used in conjunction with PACES.

D.3.2. Calibration of RTD's

The resistance of PT100 sensors has a highly linear dependence on temperature and the devices are designed to have a resistance of 100Ω at zero degrees Celsius. To take measurements inside the vacuum chamber, different connectors were soldered onto the RTD cables so that the signal could be passed through a vacuum feed-through flange. The connectors, as well as the 70 foot cables going to the GRIFFIN shack, added an unknown resistance offset to the sensors which had to be accounted for in calibration.

To obtain a calibration data point the sensors were dunked into a flask containing liquid nitrogen. As the boiling point of nitrogen is well below room temperature it can be assumed that the liquid nitrogen was at exactly its boiling temperature. This provides a known fixed point that can be used to calibrate the RTD's.

Figure 10-8 shows the temperature reading as the sensors were dunked in LN_2 twice. Equations of the form $y = c$ where c is a constant were fitted to the sections of stable temperature the dunks. The values from the two dunks were then averaged:

$$\text{POS2} : (-195.810 \pm 0.008)^\circ\text{C}$$

$$\text{POS3} : (-194.006 \pm 0.009)^\circ\text{C}$$

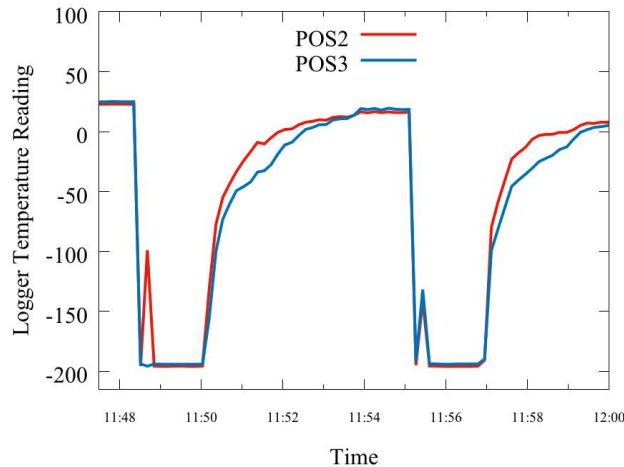
The boiling temperature of liquid nitrogen at atmosphere is known to be -195.79°C . We can thus calculate constant offsets that should be used when interpreting readings from the logger:

$$\text{POS2} : (0.026 \pm 0.008)^\circ\text{C}$$

$$\text{POS3} : (-1.784 \pm 0.009)^\circ\text{C}$$

At room temperature the difference between the calibrated sensor readings is now effectively zero:

Figure 10-8 LN_2 Dunks



$$\Delta = (0.00 \pm 0.02)^\circ C$$

D.3.3. Mounting RTD's inside vacuum chamber

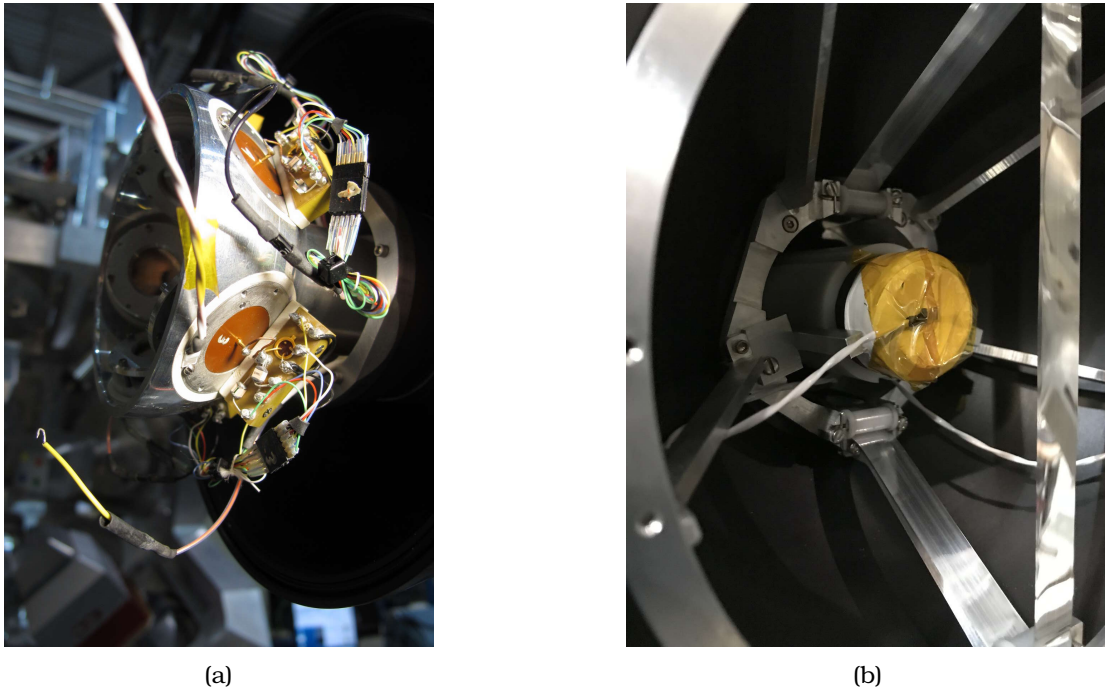


Figure 10-9 Positioning of RTD's inside GRIFFIN central vacuum chamber (a) Positioning of POS2 RTD on PACES coldfinger (b) Positioning of POS3 RTD on ZDS

Figure 10-9 shows the positions that the two temperature sensors were mounted in. The position 2 RTD is mounted on the PACES coldfinger, and secured using a screw that is used to attach a grounding connection during normal operation. The sensor in position 2 was used to monitor the temperate of the PACES coldfinger, and hence the Silicon detectors. The coldfinger is also the largest source of radiative cooling. For position 3 the sensor was secured onto the front of the Zero Degree Scintillator (ZDS) using Kapton tape, and was used to measure the effect of radiative cooling on a downstream ancillary detector during PACES operation.

D.3.4. Results

Overview

Figure 10-10 shows the temperature and pressure inside the vacuum chamber during various stages of preparation, operation and post-operation PACES procedures. The individual stages will be discussed in following sections.

Preparing PACES

Before PACES operation the vacuum chamber must first be pumped down to high-vacuum using turbo-pumps and then cooled by filling the PACES dewar with liquid nitrogen.

Figure 10-11a shows the pressure and temperature behaviour while pumping down the vacuum chamber.

During the initial pumping process a sharp drop in pressure is achieved, following this the pressure seems to reach an equilibrium. During the pumping the temperature changes slightly, with a general downwards trend after the pressure reaches equilibrium.

From Figure 10-11b we can determine that it takes just over three and a half hours for the pressure to reach an equilibrium of $(9.460 \pm 0.007) \times 10^{-7}$ Torr with PACES in the upstream position and the ZDS in the downstream position.

Following the chamber evacuation the PACES dewar can now be filled with liquid nitrogen.

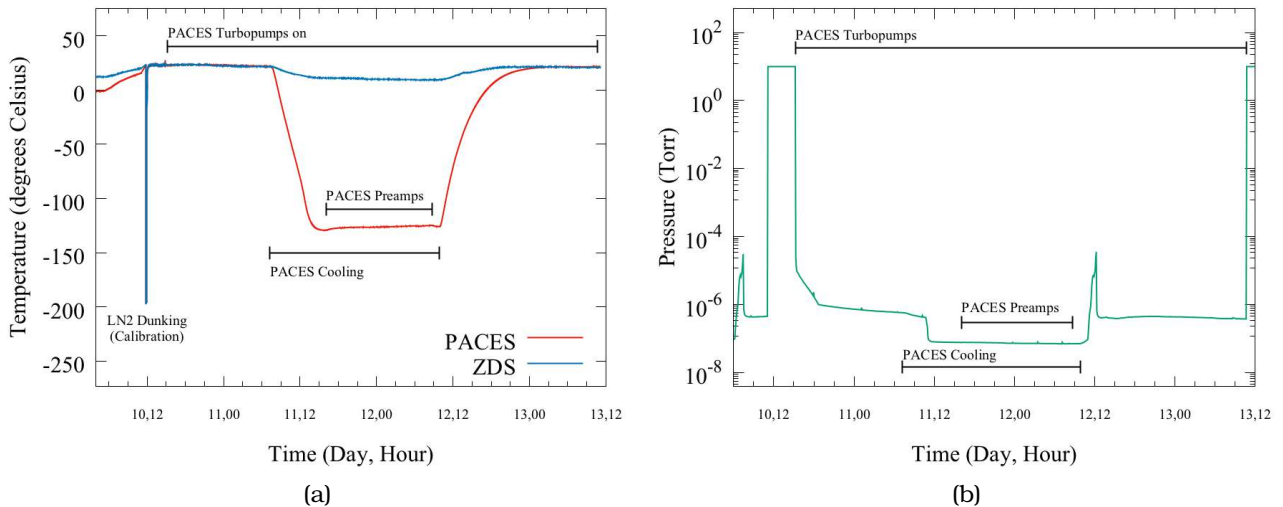


Figure 10-10 Overview (a) Temperature overview (b) Pressure overview

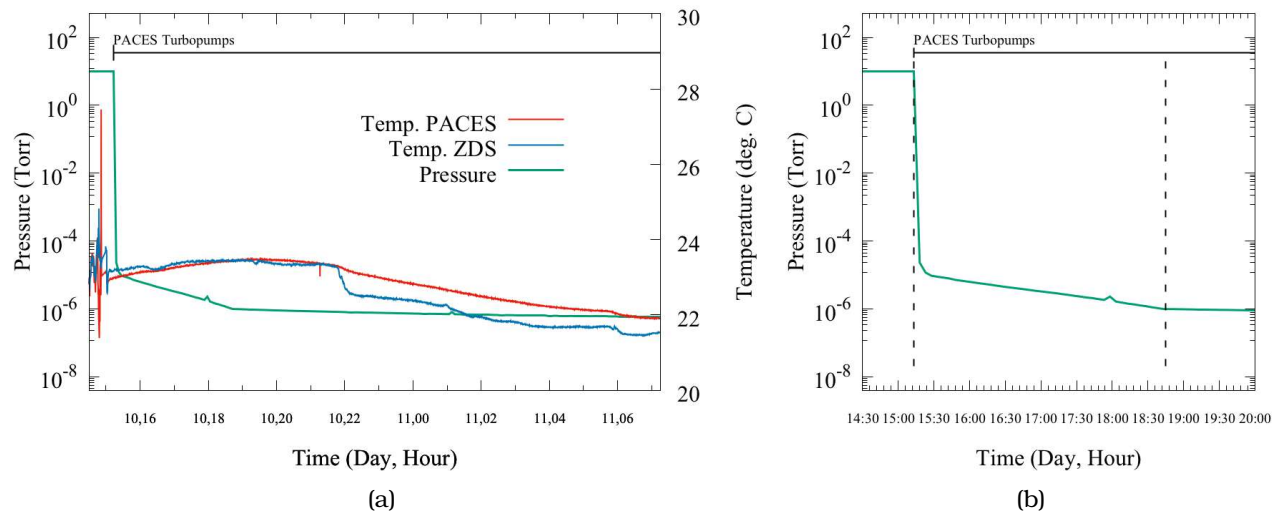


Figure 10-11 Pumping down PACES (a) Pressure and temperature overview (b) Pressure equilibrium

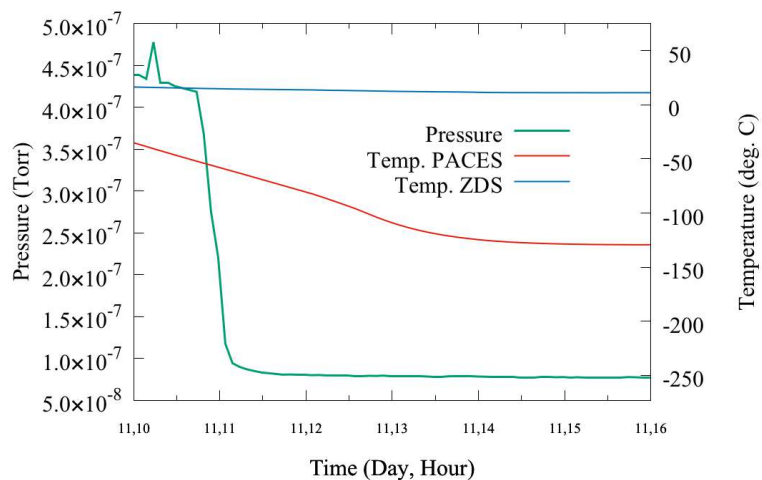


Figure 10-12 Cooling PACES

From Figure 10-12 we can see that the time taken to reach equilibrium is different for pressure and temperature. Pressure reaches an equilibrium of $(7.826 \pm 0.001) \times 10^{-7}$ Torr within about four and a half hours, while the temperature of the coldfinger takes longer at about seven and a half hours to reach a stable value of

(-129.40 ± 0.02) degrees Celsius. The temperature at the ZDS continued decreasing even as the pressure and temperature of the coldfinger stabilised. This is the result of radiative cooling occurring.

Effect of powering PACES preamps

Following a temperature stabilisation of the PACES coldfinger, the PACES preamps were switched on. These high-voltage electronics emit a significant amount of heat, raising the temperature of the coldfinger.

In Figure 10-13, it can be seen that there is a clear increase in the temperature of the PACES coldfinger during operation of the preamps. Following a non-linear increase the temperature increases at a steady rate, interrupted only by drops in ambient temperature due to filling of the GRIFFIN High-Purity Germanium detector's liquid nitrogen dewars.

The initial non-linear increase of about 2.7 degrees Celsius occurs over a time period of approximately three hours. Following this, the average rate of heating (ignoring the dips due to the LN₂ filling) is (0.2151 ± 0.0005) degrees Celsius per hour.

For each GRIFFIN LN₂ fill the temperature drops 0.1 ± 0.2 degrees in 1.22 ± 0.07 hours, before continuing to warm up at the usual rate.

Warming curves

After PACES operation, the preamps were turned off and after the liquid nitrogen in the dewar evaporated PACES returned to room temperature. Figure 10-14 shows this warming curve. It took about 20 hours for the PACES coldfinger to return to room temperature, with dry nitrogen blowing into the dewar.

Radiative cooling

The ZDS, which is significantly warmer than the PACES coldfinger loses heat through radiation. Following an initial drop of about ten degrees in under seven hours, the rate of cooling stabilises to (-0.0748 ± 0.0006) degrees per hour. This behaviour can be seen in Figure 10-15.

Downstream ancillary detectors that have a temperature dependence to their operation will need to have their signals adjusted if they are to be used in conjunction with PACES.

D.3.5. Conclusion

The temperature inside GRIFFIN's central vacuum chamber was measured during various stages of PACES operation. The time taken to cool and warm up the PACES coldfinger was obtained. Additionally, the heating rate of the preamps and the radiative cooling rate inside a downstream chamber were determined.

It was found that while certain processes effect both the temperature and pressure, this does not necessarily mean they will reach equilibria at the same time. Changes to protocol for pre- and post- operation procedures for PACES can be informed by the results presented earlier.

In order to determine the points at which radiative cooling, as well as the heating effect of the PACES preamps stabilise, experiments over a longer timespan would be needed.

Figure 10-13 Preamp heating

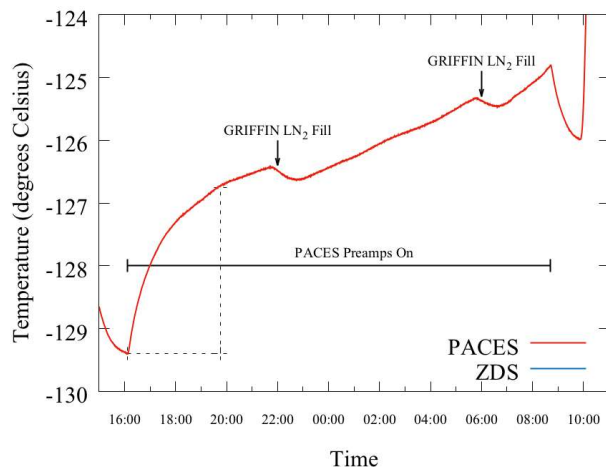


Figure 10-14 Return to room temperature

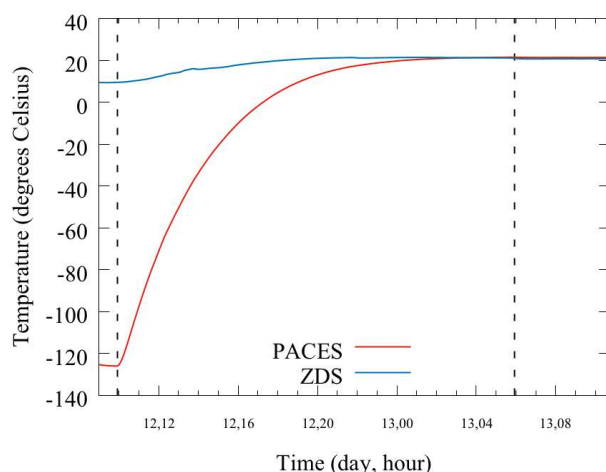
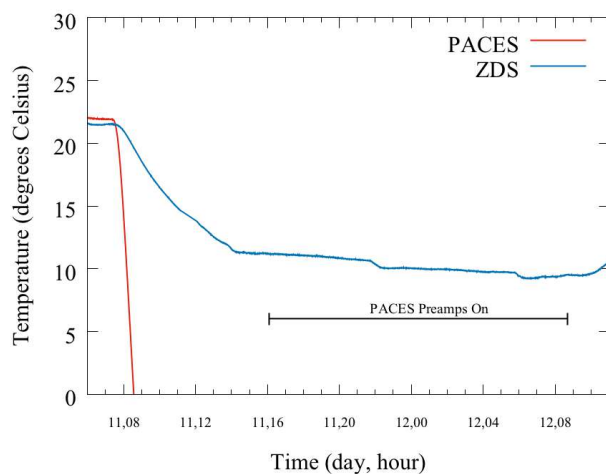


Figure 10-15 ZDS Radiative cooling



E. Literature Review and Interim Report

This final appendix contains the entire Literature Review and Interim Report as submitted to the module PHY3058 in late July 2018. The report has not been modified since submission and comprises 34 pages beginning overleaf.

Design and Construction of a New Scintillator Array for β -Tagging in GRIFFIN

Literature Review and Interim Report (PHY3058)

M.S.C. Winokan^{*1,2}

¹*TRIUMF, 4004 Wesbrook Mall, Vancouver, British Columbia, Canada V6T 2A3*

²*Department of Physics, University of Surrey, Guildford, Surrey GU2 7XH, United Kingdom*

30th July 2018

***E-mail address:** mw00368@surrey.ac.uk, University Registration Number: 6352420

Abstract

The SCintillating Electron Position Tagging ARray (SCEPTAR) is an array of twenty plastic scintillators for the detection of beta particles originally developed for use with the 8π spectrometer and now used with the Gamma-Ray Infrastructure For Fundamental Investigations of Nuclei (GRIFFIN) array at TRIUMF-ISAC (Isotope Separator and ACcelerator). As a β -tagging array, SCEPTAR allows for coincidence gating and vetoing of punch through electrons of data taken within the GRIFFIN spectrometer. The β - γ -coincidence gating greatly reduces the room background and thus improves the signal-to-background ratio of GRIFFIN spectra, while a geometric-vetoing can suppress the background in HPGe spectra from punch-through electrons and Bremsstrahlung photons. SCEPTAR remains GRIFFIN's primary ancillary detector system and together these produce high-precision measurements of complex β -decay schemes near stability and detailed spectroscopic studies of stopped radioactive beams.

The current intent for SCEPTAR's replacement is to construct an array of 1.6 mm thick plastic scintillators (Saint Gobain BC404) arranged in a geometry colinearly matching GRIFFIN's Germanium crystals, as well as the triangular ancillary positions. Contrary to the original SCEPTAR design, SCEPTAR II will replace the light guides, optical feedthrough flange, and external photomultiplier tubes (PMT's) with silicon photomultiplier sensors (SiPM's) mounted directly onto the scintillator material.

To make informed component choices; the sources, interactions in matter, and detection mechanisms of β - and γ -radiation are discussed. Following this, descriptions of scintillation detectors, silicon photodiodes, and Germanium γ -rays are provided with details on how their performance can be quantified through experimental and simulated methods. The past research capabilities of SCEPTAR in 8π and the current performance in GRIFFIN is reported, along with expected improvements resulting from the updated design. Finally, two examples of alternative solutions to a scintillator tagging array are presented.

Contents

1	Introduction and Overview of Facilities	4
1.1	The 8π spectrometer	4
1.2	TRIUMF's ISAC Facility	4
1.3	SCEPTAR, a β -tagging array	5
1.4	The GRIFFIN spectrometer	5
1.5	SCEPTAR II, a successor to SCEPTAR	6
2	Background Physics	7
2.1	Radioactive Decay	7
2.1.1	Beta decay	7
2.1.2	Gamma-ray producing processes	8
2.2	Radiation interaction in matter	9
2.2.1	Interaction of fast electrons in matter	9
2.2.2	Interactions of photons in matter	11
3	Radiation Detectors	14
3.1	Scintillation detectors	14
3.2	Photosensors	16
3.2.1	Vacuum photomultiplier tubes	16
3.2.2	Silicon photodiodes and photomultipliers	16
3.3	Germanium γ -Ray Detectors	18
4	Quantifying Radiation Detector Performance	21
4.1	Scintillation detectors	21
4.1.1	Scintillator light output	21
4.1.2	Detection efficiency	21
4.2	γ -ray spectrometers	22
4.2.1	γ -ray spectrometer detection efficiency	22
4.2.2	γ -ray spectrometer energy resolution	22
4.2.3	Solid angle coverage	22
4.2.4	Photopeak to total ratio	22
4.3	Photomultipliers and photodiodes	23
4.3.1	Breakdown voltage and overvoltage	23
4.3.2	Gain	23
4.3.3	Photon Detection Efficiency and Responsivity	24
4.3.4	Noise	25
4.3.5	Temperature Dependency	25
5	Research Capabilities and Motivations	26
5.1	Current and past capabilities of SCEPTAR I	26
5.1.1	Gating on detected β particles	26
5.1.2	Vetoing punch through signals	26
5.2	Future capabilities of SCEPTAR II	28
5.2.1	Shortcomings of SCEPTAR I in GRIFFIN	28
5.2.2	Technological advances facilitating SCEPTAR II design	28
6	Alternative solutions	31
6.1	Scintillating Fibre Detectors	31
6.2	Parallel Plate Avalanche Counters	31
7	Conclusion and Outlook	32
Bibliography		33
Acknowledgements		35

1 Introduction and Overview of Facilities

The SCintillating Electron-Positron Tagging ARray (SCEPTAR) is a two-part ancillary detector first designed for use with the 8π High-Purity Germanium (HPGe) detector array[1]. 8π 's replacement, the γ -Ray Infrastructure For Fundamental Investigations of Nuclei (GRIFFIN), made many improvements with respect to its predecessor. The modular and backwards-compatible design of GRIFFIN's vacuum chamber and beampipe allowed for SCEPTAR and other 8π to be used[2]. A successor to SCEPTAR will improve upon the ageing original, by matching GRIFFIN's geometry and making use of technologies previously unavailable.

This report will discuss;

- the sources of radiation studied with 8π and GRIFFIN in Section 2.1;
- the interactions in matter of the radiation produced in Section 2.2;
- the detectors with which this radiation can be studied in Chapter 3;
- how these detectors can be characterised in Chapter 4;
- what kind of research has and can be performed with SCEPTAR and its successor in Chapter 5;
- and finally two alternative detector designs in Chapter 6.

The remainder of this section serves to give a brief introduction and context to the various facilities discussed in this report.

1.1 The 8π spectrometer

Proposed in 1984, the 8π spectrometer is an array of 20 high-purity Germanium γ -ray detectors initially operated at the Chalk River laboratory, in Canada from 1985 until 2000[3, 4]. 8π was built to investigate high-spin nuclear structure through in-beam reaction experiments. Following its tenure at Chalk River, the spectrometer was moved to the ISAC (see Section 1.2) Rare-Isotope Beam (RIB) facility at TRIUMF in 2000[4].

At ISAC, 8π was adapted for use with low-energy stopped RIBs and through the inclusion of several ancillary detectors has proved immensely useful in radioactive decay studies[4]. The 8π facility was involved in TRIUMF's research efforts across many fields, including nuclear structure, nuclear astrophysics, and fundamental symmetries[5, 6].

Radioactive decay measurements taken with the 8π spectrometer can be used to determine half-lives of parent nuclei, daughter decay schemes, properties of excited levels (such as spin assignments, transition rates and multipolarities), as well as Q and ft^1 values for β -decays[5, 6].

In 2013 the operation of 8π at ISAC was concluded and the spectrometer was moved to Simon Fraser University making way for the GRIFFIN facility[4, 5].

1.2 TRIUMF's ISAC Facility

TRIUMF's ISAC facility produces high-quality radioactive beams through the Isotope-Separation On-Line (ISOL) technique[8]. 500 MeV protons bombard targets with an intensity of up to 100 microamps. Resulting low energy 20-60 keV RIBs can be transported to several detector facilities such as GRIFFIN (See Section 1.4)[2, 8].

¹ $ft_{1/2}$ is the half-life scaled by the dimensionless theoretical integral factor ' f ' from Fermi's theory of β -decay, see reference [7]

1.3 SCEPTAR, a β -tagging array

SCEPTAR (SCintillating Electron-Positron Tagging ARray) is an array of in-vacuum plastic scintillators used to detect β -particles within a larger γ -ray spectrometer[4]. Made up of two hemispheres, one downstream and one upstream, SCEPTAR comprises 20 1.6 mm thick BC404 scintillators manufactured by Saint Gobain arranged in a 2" diameter geometry[1, 4]. The polyvinyl-toluene-based scintillator paddles are arranged in two rings, one with square scintillators, the other with trapezoidal scintillators[4]. The angular positions of the scintillators are determined by the locations of the 8π HPGe detectors, such that each Germanium detector position has an associated scintillator paddle. In this arrangement SCEPTAR's scintillators subtend nearly 4π of the solid angle, facilitating an 80% β -particle detection efficiency[2].

For nuclear structure research in neutron rich nuclei, demand for high precision branching ratio measurements and super-allowed β -decay transition rates motivated the development of SCEPTAR. By meeting these aims the 8π spectrometer and SCEPTAR array became the facilities of choice for β -decay and isomer studies at ISAC[1]. As a β -tagging array, SCEPTAR also provides the capability to gate and veto based on detected parent nuclear decays, which can significantly reduce the impact of room background radiation, and suppress unwanted Bremsstrahlung signals[2, 4]. SCEPTAR's experimental remit will be discussed in more detail in Chapter 5.

SCEPTAR's scintillators are incorporated into the vacuum chamber, with Ultra-Violet Transmitting (UVT) acrylic light guides carrying the produced fluorescence to out-of-vacuum 13 mm diameter Hamamatsu H3165-10 Photo-Multiplier Tubes (PMTs) through an optical feedthrough flange located 40 cm from the array's centre[4]. The mechanisms of scintillator detectors and photomultipliers are discussed in Section 3.1 and Section 3.2.1, respectively.

1.4 The GRIFFIN spectrometer

GRIFFIN (Gamma-Ray Infrastructure For Fundamental Investigations of Nuclei) is a state-of-the-art γ -ray spectrometer that replaces the previous 8π facility, taking over as TRIUMF's main detector system for stopped radioactive beam research into nuclear structure, nuclear astrophysics and fundamental symmetries[2, 9]. Similar in its geometry and apparatus to the TIGRESS spectrometer[10, 11], GRIFFIN is made up of 16 clover-type Germanium semiconductor particle detectors in a close-packed formation with detector faces at 11 cm from the implantation point[2]. Through their high volume, large solid angle coverage, and advanced suppression techniques GRIFFIN's HPGe detectors greatly improve upon 8π 's performance with very high-efficiency and precision γ -ray spectrometry. The GRIFFIN detector array provides energy resolutions around 1.9 keV FWHM for a γ -ray energy of 1.33 MeV[5, 9]. Each of GRIFFIN's Germanium clovers is made up of four 90 mm long n-type crystals in a shared liquid-nitrogen cooled cryostat[2].

The GRIFFIN array can be used to great effect in many types of experiments, while greatly improving efficiency when compared to the 8π array it replaces. GRIFFIN's efficiency is factors of 17-70 times better for summed neighbour and clover modes and a up to 500 times increase in $\gamma - \gamma$ -coincidence efficiency - of which the latter is the most common experimental mode[2, 5, 9]. This enormous increase in efficiency revolutionized the decay spectroscopy research program at ISAC. Rare isotopes produced in ISAC, and in the future ARIEL, can be studied using GRIFFIN to produce high-precision measurements of complex β -decay schemes near stability and detailed spectroscopic studies[12].

To improve and extend GRIFFIN's capabilities, TRIUMF has developed an arsenal of ancillary detectors which can either occupy part of the beampipe at the focus point of the array's geometry or fill one of eight triangular ancillary positions in GRIFFIN's rhombicuboctahedral geometry. Included in the suite of ancillary detectors are several scintillator-based detectors - SCEPTAR and the Zero Degree Scintillator (ZDS) - as well as PACES[13], the Pentagonal Array of Conversion Electron Spectrometers. These detector halves can be mixed and matched for various applications.

In its first year of operation alone, GRIFFIN has been used; to examine the competition between the rapid and slow neutron capture processes in the astrophysical production of ^{116}Cd ; to perform high-statistics β -decay studies of ^{46}Ca and ^{47}Ca ; and to make spin-parity assignments of γ s occurring in ^{32}Mg following a β -decay from ^{32}Na [2, 8]. In 2018, Compton suppression shields were installed in the GRIFFIN array, similar to the style of the TIGRESS suppressors[14] these will improve the peak to total ratio of collected data.

1.5 SCEPTAR II, a successor to SCEPTAR

Due to GRIFFIN's backwards compatible design, SCEPTAR can still be used to great effect out of 8π . Far from being decommissioned, SCEPTAR remains the primary ancillary system in use in the GRIFFIN facility[2]. See Section 5.2.1 for details.

However, changing to GRIFFIN's geometry and the resulting one-to-one correspondence to the Germanium crystals will improve the ability to veto signals caused by punch through β particles, which proved to be very useful in the 8π array[5]. Use of modern technologies such as compact Silicon PhotoMultipliers (SiPM's) will make moving to GRIFFIN's geometry feasible. See Section 3.2.2

While the possible addition of an array of PIN diodes that can be used for α -particle tagging in the upstream hemisphere of the new detector will also be explored, the details of such detectors as well as their characterisation will be omitted from this report for the sake of brevity. Should the PIN diodes make it into the final SCEPTAR design the details of their acceptance testing, and characterisation will be included in the thesis. A relevant reference for PIN diode use for alpha tagging can be seen in [13].

2 Background Physics

To create a successful radiation detector design, the nature of the radiation must be understood from its source to the properties of its interaction with matter.

2.1 Radioactive Decay

Radioactive decays occur in unstable nuclei. In the case of α and β -decays, the parent nuclei emit particles in order to approach a more stable isobar for their given mass number. In γ -decay the nuclear species remains unchanged[15].

Measurements of radioactive decay products provide access to excited states of nuclei in a controlled environment that removes many of the typical pitfalls of in-beam reaction experiments such as Doppler lineshape broadening, Coulomb-excitations of the chamber, and other secondary radiation such as X-rays and electrons (delta-rays)[5].

2.1.1 Beta decay

β -decay will be the main source of fast electrons that are detected in a β -tagging array at GRIFFIN. Rare-isotope beams (RIBs) are implanted on a metallic tape in the central vacuum chamber. Often unstable nuclei that decay through β -decay, these produce electrons and positrons that can be detected in SCEPTAR.

Fast electrons in radiation measurement most frequently come from a radioisotope that decays through β -minus emission[16]. β minus decay “provides a convenient way for an unstable nucleus to ‘slide down’ the mass parabola[15]”.



Equation 2.1 shows the process for β -minus decay schematically. X and Y are the parent and daughter nuclei, β^- denotes an electron, and $\bar{\nu}$ is an anti-neutrino[16–18].

β -decay is a result of the weak interaction, and unlike electromagnetic interactions does not conserve the number of protons and the number of neutrons[19]. β -minus involves a down quark changing flavour to an up quark, or the reverse for β -plus decay[17]. Hence equation 2.1 is often written in terms of quarks as in equation 2.2 or its nucleons as in equation 2.3.



The neutrinos produced by β -decay go mostly undetected due to their remarkably small interaction probability with matter[18, 20]. Combined with the fact that the recoil in nucleus Y is of a very small energy, the fast electron becomes the only significant radiation product. The recoil nucleus Y while carrying little kinetic energy, is in most cases in an excited state, releasing γ -rays following a relaxation to the ground state, see Section 2.1.2. The minority of β -decays producing an unexcited daughter nucleus are known as ‘pure β -decays.[16].

β -minus emitting radioisotopes can be reliably produced by neutron bombardment of stable materials, ranging in activity, half-lives and endpoint energy[16].

Properties of produced radiation

Equation 2.4 considers the conservation of energy in a β minus decay. With the rest mass energy of the parent nucleus on the LHS and the rest mass energies of the daughter nucleus, and electron, as well as the kinetic energy of the electron and energy of the neutrino on the RHS[7, 21]. While the nucleus Y must recoil to conserve momentum, its kinetic energy is essentially zero.

$$m_X^N c^2 = m_Y^N c^2 + m_e c^2 + T_e + E_\nu \quad (2.4)$$

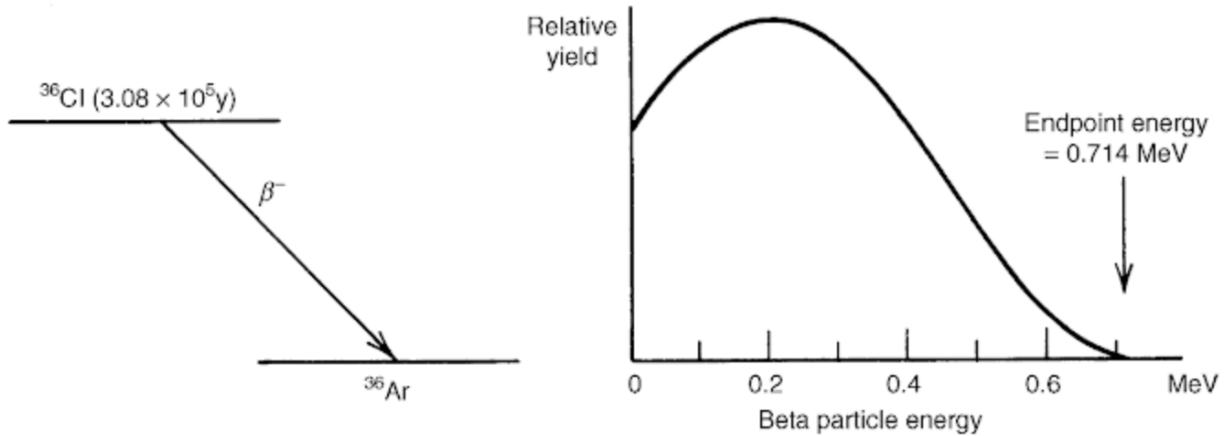


Figure 2.1: The decay scheme of ^{36}Cl and the electron resulting energy distribution. Figure taken from [16].

β -decays can be characterised by an invariant decay energy known as the Q -value. This energy value is equal to the difference in binding energy that can be released in the decay[15, 22]. See equation 2.5 for β^- decay.

$$Q_{\beta^-} = (m(X) - m(Y)) \times c^2 \quad (2.5)$$

Yet, even though the energy released in the decay is a fixed value the β -particles are produced with a continuous energy distribution[15, 16, 23]. Early explanations such as energy losses through scattering were disproved through calorimetry experiments, and it is now known that the “missing” energy is carried away by the undetected neutrino[7, 15].

An exemplary β -minus energy distribution is shown in Figure 2.1. This distribution is obtained through Fermi’s phase space theory that considers the product of the density of momentum states for the neutrino and electron. Producing a bell-shaped curve for the momentum that when squared produces distributions as in Figure 2.1[15, 18, 20, 21, 23].

The endpoint energy describes the maximally possible energy of the β -radiation, when the energy carried by the neutrino approaches zero[7, 16, 21].

The energy distribution in Figure 2.1 is characteristic of β -minus decays between two nuclei (X and Y) in their respective ground states. A decay to or from an excited state will change the endpoint energy, and as decays to and from several states of the same isotope are possible the final energy spectrum may consist of a superposition of several distributions[16].

Q -values vary in magnitude depending on the radioisotope in question and can range from tens of keV to thousands of keV for the most common ‘pure’ β -minus sources[16, 21, 22]. Other β -emitters come in a broad spectrum of half-lives ranging from thousands of years down to near-instant. Although the most common pure β radioisotopes have half-lives of tens of days[16].

2.1.2 Gamma-ray producing processes

Radioactive γ -emission is analogous to electromagnetic radiation emission as a result of optical or x-ray emissions. A decay from an excited state to a lower excited state conserves energy by emitting a γ -photon. γ -emission often follows an α - or β -decay as those processes frequently result in the production of excited daughter nuclei[15].

Gamma-rays following β -decay

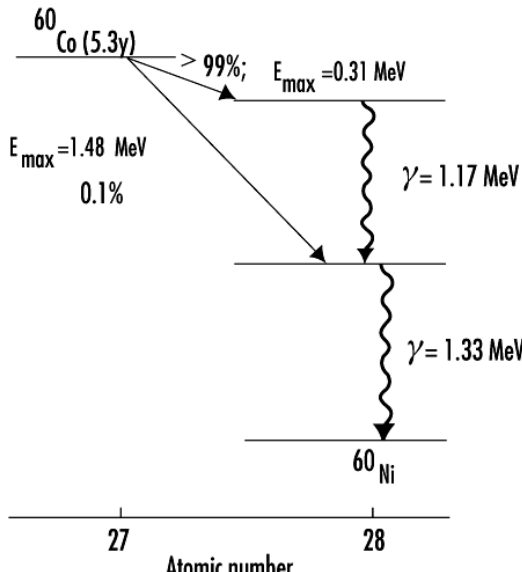
Non-pure β -decays produce daughter nuclei which are in an excited nuclear state. Similar to optical transitions in atoms, the excited nucleons will reconfigure to reduce the overall energy of the quantum state[16]. When this occurs, γ -rays carry off the excess energy. The de-excitation can be directly to the ground state or to an intermediate state which will also decay by γ -emission. See Figure 2.2a.

In the absence of Doppler shifting, the produced photons are nearly mono-energetic, with state-to-state transitions having very specific energies, a decay’s γ spectrum can be used to make deductions about the level and decay schemes involved[16]. In complicated decay schemes, γ -ray spectrometry can be crucial to determining which decays occurred in actuality.

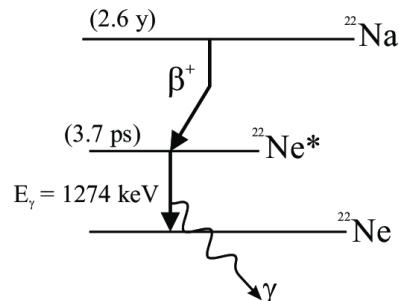
γ -decays usually have half-lives of order 10^{-9} s, and while exceptions exist, these are rare and are denoted as 'isomers' or metastable states. Metastable states are indicated by a superscript 'm', e.g. ^{110m}Ag [15].

Annihilation Radiation

Decays through β^+ -emission, produce annihilation photons when the positron encounters an electron. Two electromagnetic annihilation photons are produced, each at 511 keV and travelling in opposite directions due to momentum conservation. For example, in the decay of ^{22}Na to ^{22}Ne , a positron is emitted in the β^+ decay producing two 511 keV γ -rays, as well as the 1274 keV single γ -ray from the decay of $^{22}\text{Na}^* \rightarrow ^{22}\text{Na}$ [16]. See Figure 2.2b.



(a) β^- decay of ^{60}Co . From [24].



(b) β^+ decay of ^{22}Na . From [25].

Figure 2.2: Exemplar decay schemes of common laboratory β radioisotopes.

Gamma-rays as secondary radiation

Fast electrons travelling through matter can also produce γ -rays when scattering, this is known as 'Bremsstrahlung' and is covered in Section 2.2.1.

2.2 Radiation interaction in matter

When radiation, whether high-energy electrons, heavy charged particles, or photons pass through matter it transfers some of its energy to the molecules of the material. This results in excitations and/or ionisations that can be experimentally observed[16, 17]. An understanding of radiation interactions in matter is crucial to the development of radiation detectors.

The relevant particles and materials for the development of the SCEPTAR II array are electrons in scintillator materials, photons in silicon photodiodes and Germanium detectors. The following subsections will describe the mechanisms with which fast electrons (from β -decays), and photons (gamma-rays and ultraviolet) interact with matter.

2.2.1 Interaction of fast electrons in matter

Electrons can lose energy through Coulomb interactions also known as "collisional" interactions (excitation, ionisation) as well as through radiative processes (Bremsstrahlung.[16, 17]. Electrons due to their low mass have a large angle of diffusion and can backscatter back out of the material. Hence, they do not necessarily deposit all their energy, even in an infinite amount of material[26, 27].

Coulombic interactions

“Collisional” losses occur when a fast electron interacts with and transfers energy to an orbital electron. Either exciting it or ionising it, depending on the energy deposited. When a fast electron interacts with an orbital electron, due to their equal masses very large angle deviations are possible[16, 28]. In 1930, Bethe proposed equation 2.6 for calculating the average stopping power of electrons due to Coulombic interactions.¹[28, 29].

$$-\left(\frac{dE}{dx}\right)_c = \frac{2\pi e^4 NZ}{m_0 v^2} \left(\ln \frac{m_0 v^2 E}{2I^2(1-\beta^2)} - (\ln 2) \left(2\sqrt{1-\beta^2} - 1 + \beta^2 \right) + (1-\beta^2) + \frac{1}{8} \left(1 - \sqrt{1-\beta^2} \right)^2 \right) \quad (2.6)$$

The quantity $(dE/dx)_c$ measures the differential loss in energy as the electron travels linearly in the material.

Radiative energy losses

Radiative energy losses can occur at any point of an electron’s passage through matter and can take the form of “Bremsstrahlung” or electromagnetic radiation[16, 28]. Bremsstrahlung is a result of an interaction with the nuclear Coulomb field as shown in 2.7 which is a process forbidden in vacuum.



Through quantum mechanics, the probability of emitting radiation in the form of a photon is proportional to acceleration squared. As a result, it is much more likely to occur close to a nucleus than an atomic electron, as the nuclear forces are greater and hence contribute to the particle’s acceleration more at closer distances[17].

For radiative energy losses an equivalent equation to equation 2.6 exists in equation 2.8, using the same units and symbol assignment[16, 28].

$$-\left(\frac{dE}{dx}\right)_r = \frac{NEZ(Z+1)e^4}{137m_0^2c^4} \left(4 \ln \frac{2E}{m_0 c^2} - \frac{4}{3} \right) \quad (2.8)$$

Combining collisional and radiative stopping powers

The contributions from Coulombic and radiative energy losses can be combined trivially by addition, as seen in equation 2.9:

$$\frac{dE}{dx} = \left(\frac{dE}{dx}\right)_c + \left(\frac{dE}{dx}\right)_r \quad (2.9)$$

A convenient approximation for the ratio between radiative and collisional losses is given in equation 2.10:

$$\frac{(dE/dx)_r}{(dE/dx)_c} \approx \frac{EZ}{700} \quad (2.10)$$

The energy domains in which ionisation and bremsstrahlung dominate are illustrated in Figure 2.3.

Databases of stopping powers and CSDA ranges

Analytical equations combined with experimental results, such as from the work of Al-Ahmad and Watt in [30] were used by the National Institute of Standards and Technology (NIST) to develop the eSTAR database. NIST’s eSTAR provides an online tool for calculating stopping powers and ranges of electrons in matter[31]. This tool provides access to stopping power tables for a large database of common target materials including pure elements up to Californium and common compounds, as well as providing the ability to define new materials by its constituents. The eSTAR database sets

¹In equation 2.6, v and ZE are the velocity and charge of the primary particle, N and Z are the number density and atomic number of the absorber atoms, m_0 is the electron rest mass, and e is the electronic charge. The parameter I represents the average excitation and ionization potential of the absorber and is normally treated as an experimentally determined parameter for each element[16]

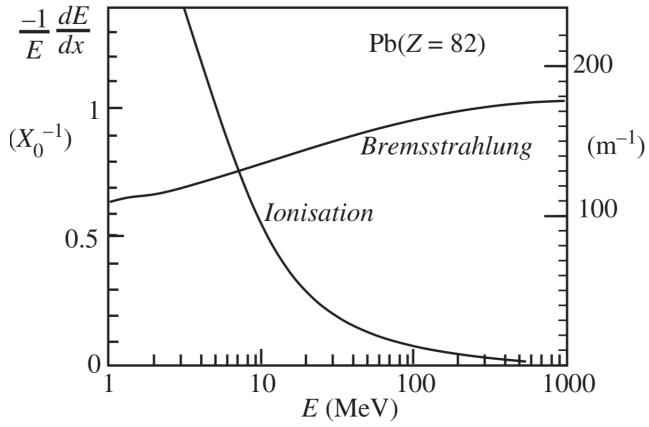


Figure 2.3: Relative contributions of ionisation and bremsstrahlung energy losses of electrons in lead. Figure taken from [17].

the standard for electronic energy loss calculations and is the basis for many numerical and Monte Carlo simulations.

Figure 2.4a and Figure 2.4b show the stopping power and CSDA ranges of electrons in a polyvinyltoluene based (PVT-based) plastic scintillator.

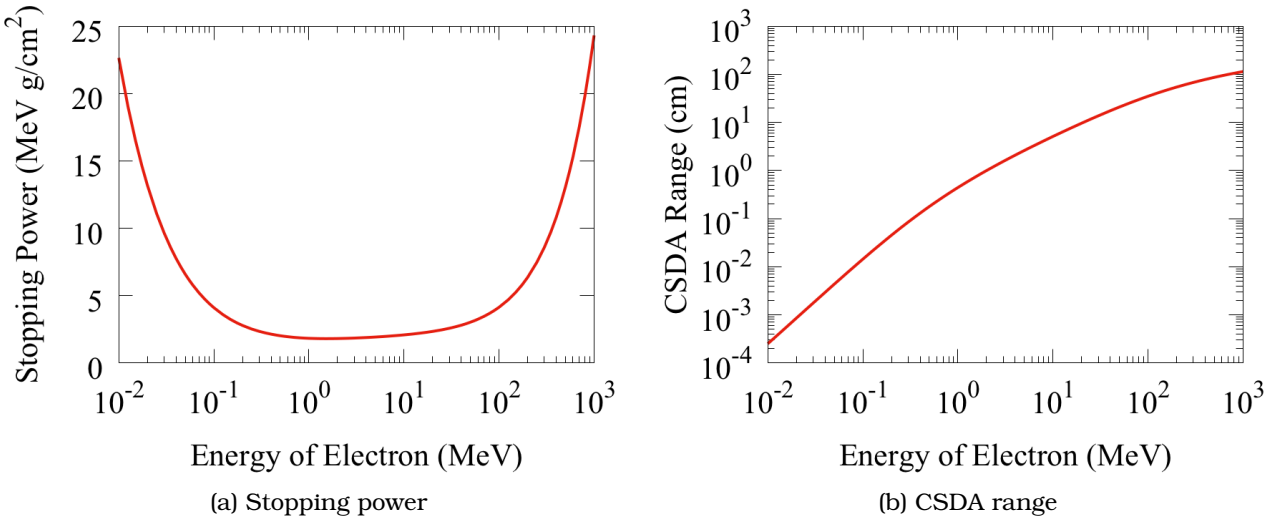


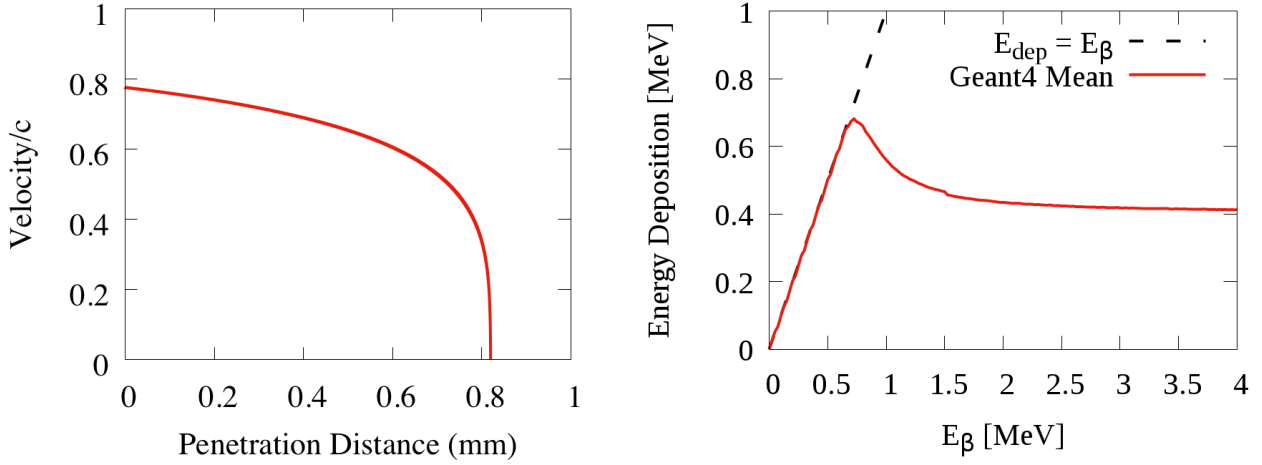
Figure 2.4: Stopping powers and ranges of electrons in PVT-based plastic scintillator. Figures produced with data from eSTAR.

The data in Figure 2.4a can be employed in finite element analyses to simulate the energy deposition and range of electrons in scintillator materials. Figure 2.5a shows the average velocity of an electron as it travels through PVT. The electron begins by gradually losing energy and hence velocity, however, the more energy deposits the greater the stopping power of the material, leading to a sharp drop-off and eventual stop.

The average fraction of energy that a fast electron will deposit in a material is dependent on its initial velocity. The main categories of behaviours are; electrons which lose all their energy within a material are known as 'captured'; those which leave through the other side of the material with non-zero energy are known as having *punched-through* the material; and electrons which scatter within the material and eventually leave through the front face of the scintillator are known as *backscattered*. A typical energy deposition curve is shown in Figure 2.5b.

2.2.2 Interactions of photons in matter

Photons emitted in nuclear decays and their products' interactions are energetic enough to alter the state of atoms and nuclei they encounter. Above energies of several keV, photons are classified as γ -rays. Of the large variety of mechanisms through which γ -rays interact in matter, only three prove to be relevant for radiation detection. These are photoelectric absorption, Compton scattering, and



(a) Simulated average velocity as a 300 keV electron loses energy. From finite element analysis using eS-TAR data.
(b) Geant4 simulated energy deposition of fast electrons.

Figure 2.5: Simulations of electron interactions in BC404 scintillator.

pair production[17]. Unlike the interaction of charged particles, γ -rays typically deposit almost all their energy in single “catastrophic” events. In such an event, a sudden and abrupt change occurs in the incident photon.

As energy increases the interaction probabilities (cross sections) vary between the three main interaction mechanisms. The relative contributions of the photoelectric effect, Compton scattering and pair production are shown in Figure 2.6.

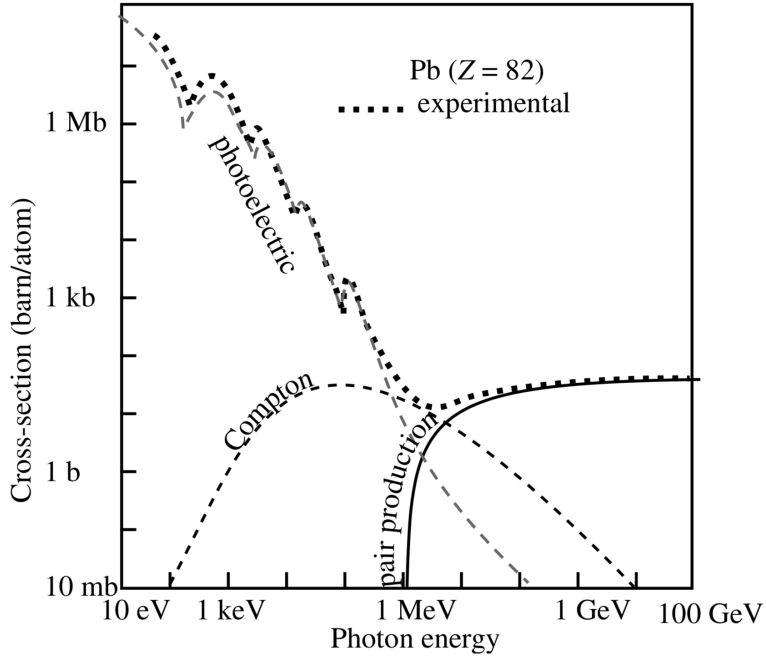


Figure 2.6: Photon interaction cross sections in lead. Figure taken from [17].

Photoelectric absorption

At energies below 1 MeV the photoelectric effect is the most probable mechanism of interaction for γ -rays[17]. High Z absorber materials also enhance the probability of this process[32]. In the photoelectric absorption, the γ -photon’s energy is completely deposited into the absorber atom. This is facilitated by an electron which is released from the bulk material. These energetic electrons are known as “photoelectrons” and can only occur with whole atom interactions (not with free electrons). K shell electrons - the most tightly bound - are the most likely to be the ejected. Given that the

γ -ray has sufficient energy[16]. The energy of the photoelectron is given in equation 2.11 where E_b denotes the binding energy of the electron, in its original shell, which is also known as the work function of the material[16, 33].

$$E_{e^-} = h\nu - E_b \quad (2.11)$$

In addition to the photoelectron, an ionized atom is also left behind. Its electronic vacancy can be filled resulting in an x-ray or Auger electron emission[16, 33].

Compton scattering

Compton scattering is frequently the dominant process in γ -ray energies ordinarily produced from radioactive decay. Compton scattering involves the deflection of a photon by an angle θ relative to its incident direction. The electron, assumed to be initially at rest, absorbs some of the photon's energy and becomes known as a *recoil electron*. The fraction of energy transferred in the interaction depends on the recoil angle, producing a continuous spectrum of deposited energies[16, 17, 32]. See equation 2.12.

$$h\nu' = \frac{h\nu}{1 + \frac{h\nu}{m_0c^2}(1 - \cos\theta)} \quad (2.12)$$

The angular probability distribution of the resulting γ -ray is given as a differential of solid angle by the "Klein-Nishina formula" in equation 2.13² and is shown in Figure 2.7[16].

$$\frac{d\sigma}{d\Omega} = Zr_0^2 \left(\frac{1}{1 + \alpha(1 - \cos\theta)} \right)^2 \left(\frac{1 + \cos^2\theta}{2} \right) \left(1 + \frac{\alpha^2(1 - \cos\theta)^2}{(1 + \cos^2\theta)(1 + \alpha(1 - \cos\theta))} \right) \quad (2.13)$$

As the energy of the incident γ -ray increases the probability of large angle deflections decreases[32].

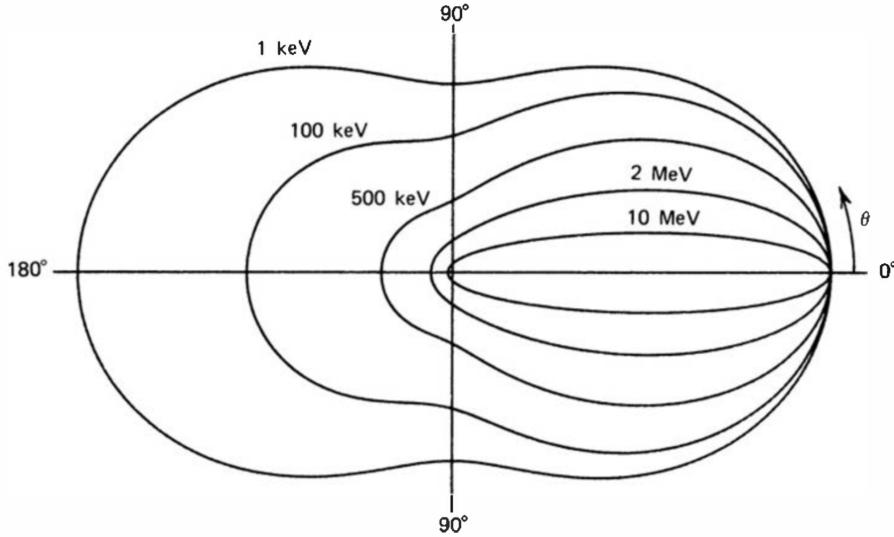


Figure 2.7: Angular distribution following Compton scattering predicted by Klein-Nishina formula.

Pair production

If the energy of the γ -ray is greater than the rest-mass of two electrons, then the photon may spontaneously produce a matter-antimatter pair in an electron and positron which is shown in equation 2.14[16].



As seen in Figure 2.6 above 1.022 MeV the pair-production interaction channel rapidly becomes dominant. Excess energy above 1.022 MeV is carried away as kinetic energy, split evenly between the two particles[16, 28]. The positron soon meets an electron and producing two secondary annihilation photons, see Section 2.1.2.

²Where $\alpha \equiv h\nu/m_0c^2$ and r_0 is the classical electron radius

3 Radiation Detectors

Radiation detectors offer nuclear physicists insights into nuclear reactions through observations of their products, as direct measurement is almost always impossible[34].

3.1 Scintillation detectors

Detection of scintillation light has been one of the oldest methods for ionising radiation detection. Energy deposition (dE/dx) through radiation interactions discussed in Section 2.2 cause transitions to excited states of the detector molecules, that emit light when they decay. When combined with a photoreceptor, scintillators can be used for a variety of purposes such as calorimetry, time-of-flight measurement, tracking, tagging and vetoing. Scintillators remain an integral detector type in the fields of nuclear, particle, and medical physics[16, 35, 36].

While the specifics of the energy level schemes differ for various materials, the behaviour of scintillation materials can be summarised by two groups - inorganic and organic scintillators.

Organic scintillators

The fluorescence from organic scintillation materials occurs through transitions of individual molecules (as opposed to crystalline excitations in inorganic scintillators). A common level structure shared by many organic scintillation materials is known as the π electron structure as shown in Figure 3.1a.

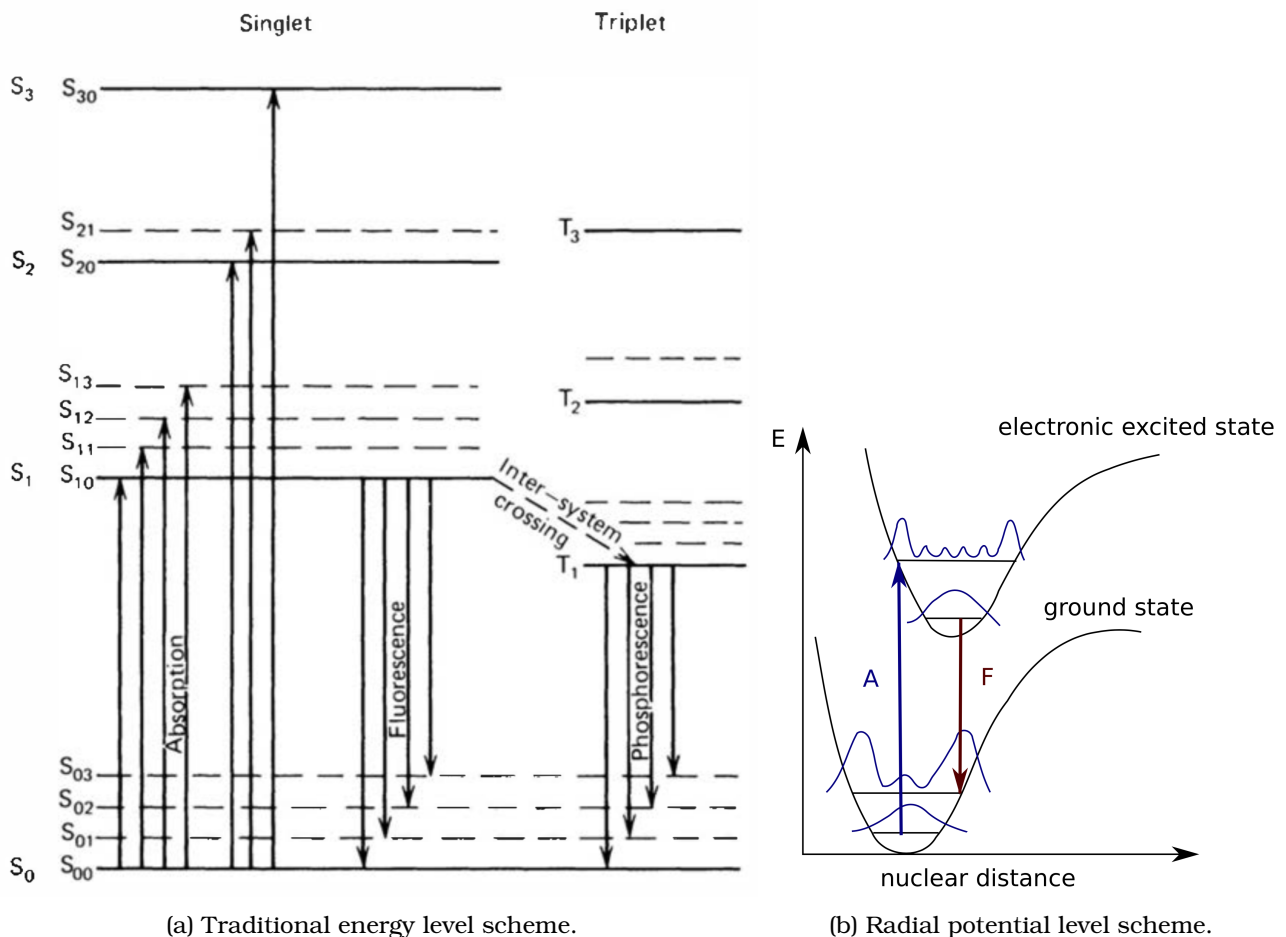


Figure 3.1: π electron structure energy level scheme common to organic scintillators. Figures adapted from [16]

Three categories of light emission following a de-excitation commonly occur in organic scintillators - prompt fluorescence, delayed fluorescence and phosphorescence. Prompt fluorescence is the de-excitation mode relied on for radiation detection, due to its relatively fast decay times. Prompt fluorescence is also referred to as *principal scintillation light*, and occurs between the vibrational singlet states and the ground states ($S_{1x} \rightarrow S_{0x}$ in Figure 3.1a). Phosphorescence results in emission of lower energy photons, with a slower decay time. Finally, delayed fluorescence has a far longer emission time compared to prompt fluorescence but emits light with the same energy spectrum[16].

The typical energy spacing between S_1 and S_0 is 3 or 4 eV, and typical vibrational state spacing is of the order of 0.15 eV. As average thermal energies are about 0.025 eV, at room temperature practically all molecules are in the S_{00} state.

De-excitations from states higher than S_1 occur through radiationless internal conversion, and occur very quickly. Thus, following a deposition of energy in the scintillator, a population of molecules in the S_{10} state is created, which then decays to the various vibrational ground states releasing fluorescence. The intensity of fluorescence at time t follows equation 3.1[16].

$$I = I_0 e^{-t/\tau} \quad (3.1)$$

τ the fluorescence decay constant is usually of the order of a few nanoseconds. The triplet states (T_{xx}) are much longer-lived and are accessed through transitions known as *intersystem crossing*, which involve an ionisation and a recombination[35]. The decay constant for the T_1 state may be anything up to 10^{-3} s, thus phosphorescence is delayed relative to the scintillation light. It is possible for molecules in T_1 to be excited back to the S_{1x} states, in which case they will decay through the principal fluorescence mode, thereby giving rise to delayed fluorescence[16].

A property of the π electron structure that makes it especially useful as a scintillator material is its transparency to its own fluorescence. As the absorption transitions are of higher energy than all but the $S_{10} \rightarrow S_{00}$ fluorescent decays. This lack of self-absorption is illustrated in Figure 3.2 which shows an example of optical absorption and emission spectra.

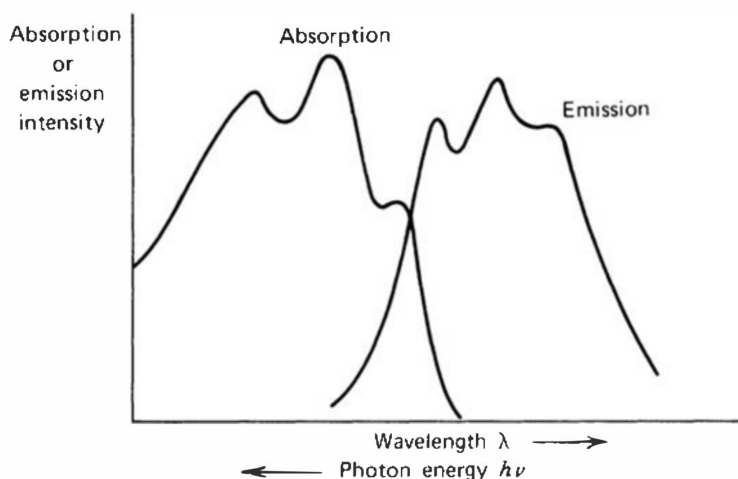


Figure 3.2: Typical optical emission and absorption spectra of an organic scintillator.

Plastic and liquid organic scintillators

One markable advantage of organic scintillators is that scintillator molecules can be suspended in a transparent polymer or liquid and can be engineered to best fit their specific function[16].

Plastic scintillators are formed by taking a polymer (e.g. polystyrene, lucite/plexiglass, polyvinyl-toluene) and doping with a scintillator (e.g. p-Terphenyl, PDB)[35]. Plastic scintillators also have a far lower 'retro-diffusion'¹ rate of the order 8% compared to 80-90% of sodium iodide[27].

Liquid scintillators replace the polymer with a liquid such as benzene, toluene or mineral oil[35].

Inorganic scintillators

Inorganic scintillators require a crystalline lattice structure in order to scintillate. Inorganic crystal scintillators are made up of a crystal (dielectric) doped with an activator, for example NaI(Tl), CsI(Tl),

¹the rate of *retro-diffusion* is the probability that incident radiation will scatter back out through the front face of a thin detector

and BGO (bismuth germanate). Energy losses promote electrons from the band gap into the conduction band. When doped with an activator, which provides more activator energy levels within the band gap, the photon emission likelihood can be increased[16, 35].

While popular in the field of radiation detection, and having a higher light output compared to organic scintillation materials, the inexpensive cost and flexibility of plastic scintillators leads to these being favoured in the SCEPTAR ancillary detectors.

3.2 Photosensors

To complete a scintillator radiation detector, a photoreceptor is required to produce an electronic signal from the fluorescence. Traditionally vacuum photomultiplier tubes (PMT's) have been employed. Recently, the advent of photodiode arrays, also known as silicon photomultipliers (SiPM's) have become increasingly comparable to vacuum PMTs in performance, and may prove to be more reliable and cost-effective[37].

3.2.1 Vacuum photomultiplier tubes

A vacuum photomultiplier tube consists of a photocathode, a focussing electrode, several stages of dynodes, and finally an anode. These are housed within a glass vacuum tube and surrounded by a high-permeability (μ -metal) cylinder[35].

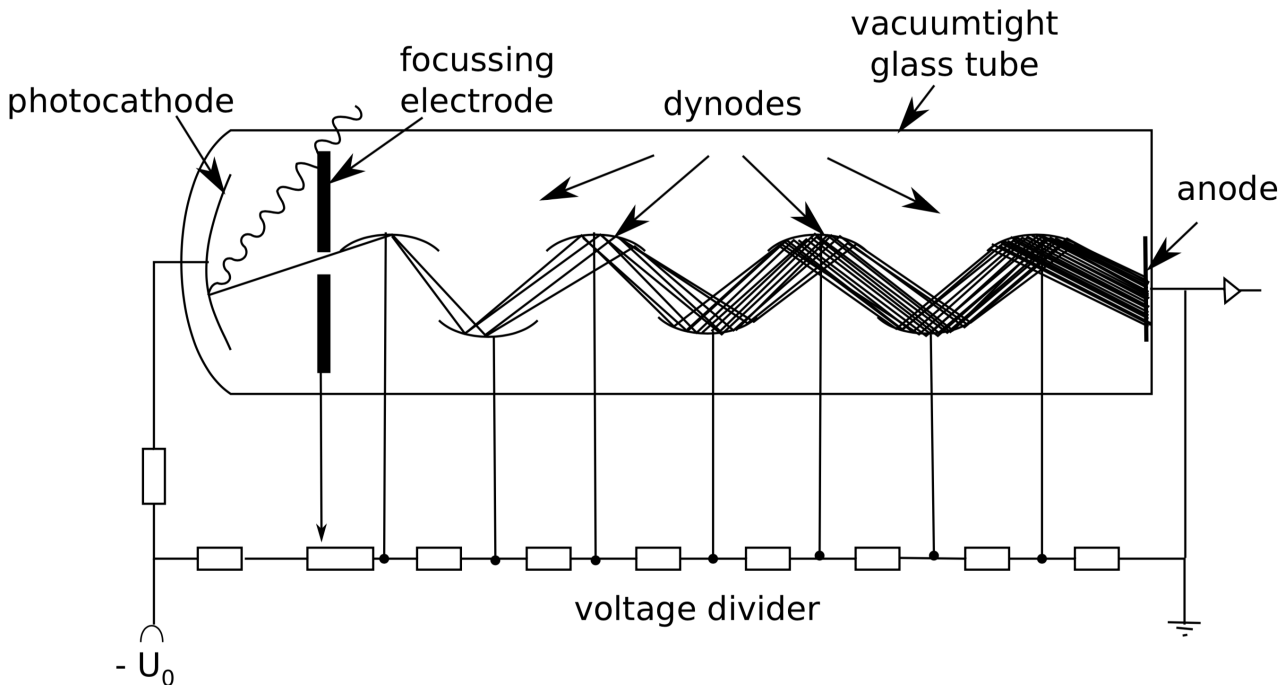


Figure 3.3: Typical layout of a vacuum photomultiplier tube. Figure taken from [35].

Figure 3.3 shows the main components of a vacuum PMT. The photocathode makes use of the photoelectric effect to produce electrons from incident electromagnetic radiation.

The reaction that occurs in the photocathode involves a photon which interacts with an atom, freeing an electron and leaving behind an ion[33].

$$T_{e^-} = h\nu - W \quad (3.2)$$

The energy is given in equation 3.2, where W is the work function of the material. For PMT applications involving detection of scintillation light, specially developed alloys such as bialkali or multialkali have been developed as these have a small enough work function 1.5-2.0 eV, compared to the energy of fluorescence (3-4 eV.[35]).

3.2.2 Silicon photodiodes and photomultipliers

Photodiodes are solid-state semiconductor photon detectors. When operated in Geiger-mode and configured into large arrays, they are capable of amplifying single-photon energy depositions into

pulses suitable for digitisation.

Silicon photodiodes

In order to work as a photodiode, Silicon must be doped to create regions with unbalanced negative (electrons) and positive (holes) charge-carriers. Intrinsic silicon crystal's resistance is high, and a *pn*-junction must be formed for efficient charge collection. By doping a region with atoms of group V elements (electron donors such as phosphorous or arsenic) and an adjacent region with group III elements (electron acceptors such as boron or aluminium). These *extrinsic* regions are known as *n*-doped and *p*-doped, respectively, and allow either negatively-charged electrons or positively-charged holes to become the majority charge carriers. As the conduction and valence band energy levels are shared by all atoms in the lattice, an electric field can easily cause the charge-carrier to drift through the crystal. At the *pn*-junction a depletion layer is formed, which is free of mobile charge carriers, as these are attracted across the junction to recombine with their opposite charge partners. It is in this region that an incident photon will create an electron-hole pair that can be accelerated by a reverse-bias to produce a current.[23, 38–40]

Figure 3.4 shows the typical layered structure of a *pn* photodiode.

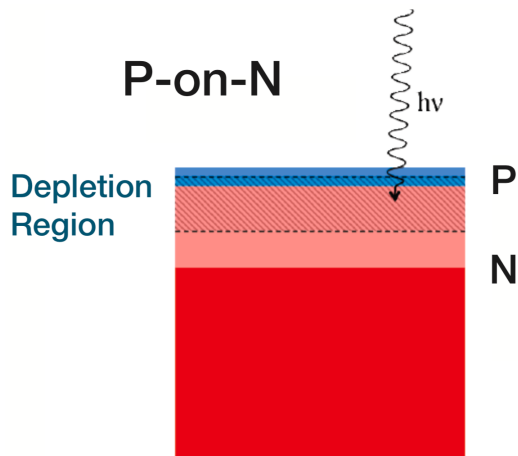


Figure 3.4: Typical structure of an avalanche photodiode. Figure adapted from [39].

The avalanche photodiode

Avalanche photodiodes exploit the photoelectric effect to convert light to electricity. Increasing the bias voltage across a *pn*-junction increases the acceleration of charge-carriers, meaning that they gain more kinetic energy in between scattering events[38, 39].

Usually such collisions produce *phonon vibrations*, however above a bias known as the *breakdown voltage* the mean energy of the carriers will be sufficient to exceed the silicon band gap energy[38]. This results in *impact ionisations* producing further electron-hole pairs and thus carrier multiplication. This rapid increase in charge-carriers is known as an avalanche.

This process is called Geiger discharge, and allows for a single allowed photon to trigger a self-perpetuating cascade of ionisation through the silicon which has now broken down and become conductive. The current flow created must be halted by means of a quenching resistor, which effectively lowers the voltage and stops the avalanche. Following a recharge period, the diode is once again susceptible to a photon-induced breakdown. This cycle can be seen in Figure 3.5.

Silicon photomultipliers compared to vacuum PMTs

A Silicon photomultiplier (SiPM) is an array of avalanche photodiodes connected in parallel. Each microcell is operated in Geiger mode and can produce gains of the order of 10^5 to 10^6 charge-carriers per signal[38, 39, 41]. These signals last up to tens of nanoseconds. Silicon photomultipliers provide an excellent alternative to vacuum photomultiplier tubes.

While a mere decade ago SiPM performance was less favourable compared to vacuum PMTs[42, 43] the technology has come a long way, and now silicon photomultipliers are in routine operation for many of the world's greatest detector facilities, for fast-timing, and single-photon counting purposes[41]. Silicon photomultipliers have quickly become staple detectors in the fields of high-energy

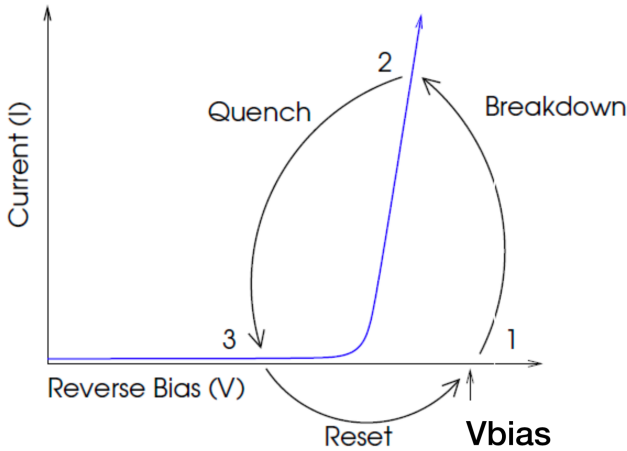


Figure 3.5: Breakdown, quench, and recharge cycle of an APD operating in Geiger mode. Figure taken from [39].

physics, astroparticle physics and medical imaging and have been used extensively on projects at CERN[44], for CMS[45], and for CTA[37].

The lower cost, reliability of solid-state components, insensitivity to magnetic fields, and far smaller footprints make SiPM's excellent alternatives to vacuum PMTs[35]. Additionally, modern silicon photomultipliers have high photon-detection efficiencies (PDE), are mechanically and electrically robust, and require far less power and lower bias voltages during operation[41].

3.3 Germanium γ -Ray Detectors

For over 30 years the state of the art for γ -ray spectroscopy relies on high-purity Germanium crystals. The reason for this is that in order to capture γ -rays large detector active areas are required. The active area in a semiconductor radiation detector is defined by the depletion region, the size of which is given by equation 3.3[16, 23].

$$d = \left(\frac{2\epsilon V}{eN} \right)^{1/2} \quad (3.3)$$

Where ϵ is the dielectric constant, V is the reverse bias voltage, e is the electronic charge, N is the net impurity concentration. Hence, we can see that for a given bias voltage the size of the depletion region depends on the number of impurities. Due to Germanium's lower melting point, refining techniques such as zone refining can be applied to bulk germanium to produce large crystals with impurity levels as low as 10^9 atoms/cm³.[16].

The crystals used in the GRIFFIN spectrometer are coaxial, meaning that their core is removed and made into an electrical contact. Coaxial crystals allow for larger volumes. See Figure 3.6 for schematics of coaxial HPGe crystals. GRIFFIN's crystals are closed-ended and are tapered on two sides[2, 16].

HPGe detectors have very small bandgaps (around 0.7 eV). At room temperature the dominance of thermally-induced leakage current makes it impossible to use germanium detectors. By cooling with liquid nitrogen to temperatures below 130 K (which are deemed acceptable for spectroscopy performance[46–48]) the detectors can be operated to achieve the gold standard in γ -ray spectroscopy[16].

Features of a γ -ray energy spectrum

In Section 2.2.2 the main interaction mechanisms by which γ -rays lose energy in matter were discussed. Figure 3.7 shows a typical γ -ray spectrum detected in a simulated GRIFFIN HPGe detector. In the Geant4 simulation mono-energetic photons pass through various structural and ancillary detector materials before depositing their energy in the Germanium crystal. By considering these interaction modes, the features of the γ spectrum can be explained.

The most prominent feature is the photopeak in the highest energy occupied histogram bin. The photopeak is a result of a photoelectric absorption event, by which all the photon's energy

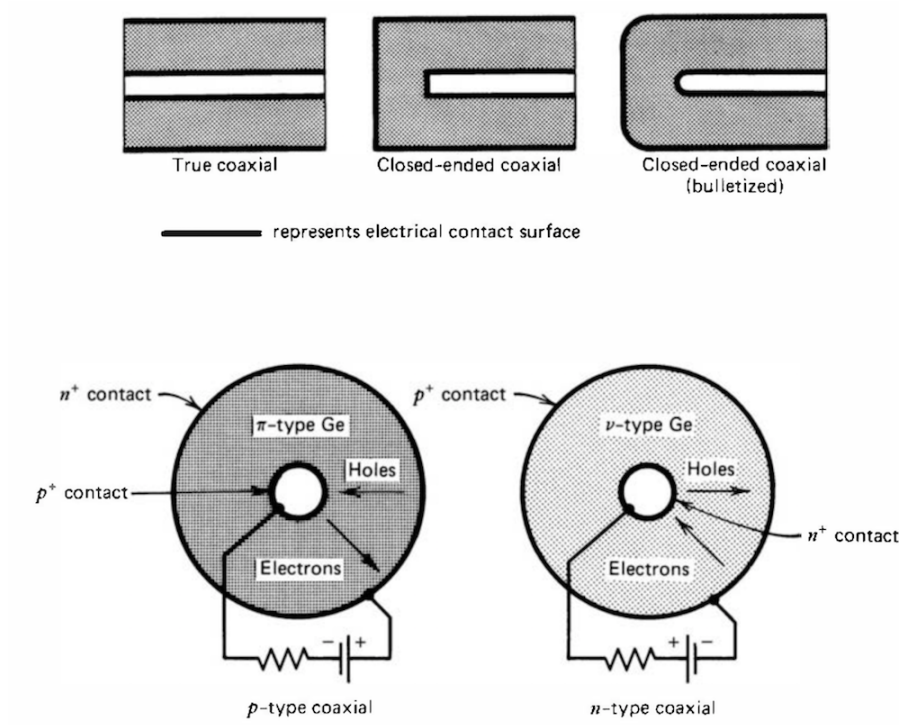


Figure 3.6: Common coaxial geometries for high-purity Germanium crystals. Figure taken from [16].

is deposited in the active area of the detector. This can be formed through a single photoelectric absorption or by a series of scattering events within the depletion region of the **same** crystal and concluded with a photoelectric absorption[16, 32].

Compton scattering is responsible for the continuum of energies below the photopeak, where the γ -ray only loses part of its energy in the active volume of the detector[32]. The Compton edge is found at the maximum possible energy deposition through a *single* scattering event.

The backscatter peak is formed when the photon undergoes a large angle ($\theta = 180^\circ$) backscatter in surrounding material *before* the secondary photon is absorbed in the detector. The energy of the backscatter peak can be found by minimising equation 2.12. The energy of the photopeak and hence the energy of the incident γ -ray is given by the sum of the backscatter and Compton edge energies[16, 32].

In addition to the features of the continuous spectrum, there are three peaks attributed to pair production. With sufficiently large photon energies, the γ -ray can produce an electron-positron pair which deposit their kinetic energies, and eventually the positron can annihilate with an electron in the material to produce 511 keV photons which contribute to the annihilation peak in Figure 3.7. If near the edge of the Germanium crystal, the annihilation energy may escape detection, if one photon escapes what's known as the *single escape* peak (SE in Figure 3.7), located at $h\nu - m_0c^2$. In *double escape* only the kinetic energy is captured forming a peak at $h\nu - 2m_0c^2$ [16].

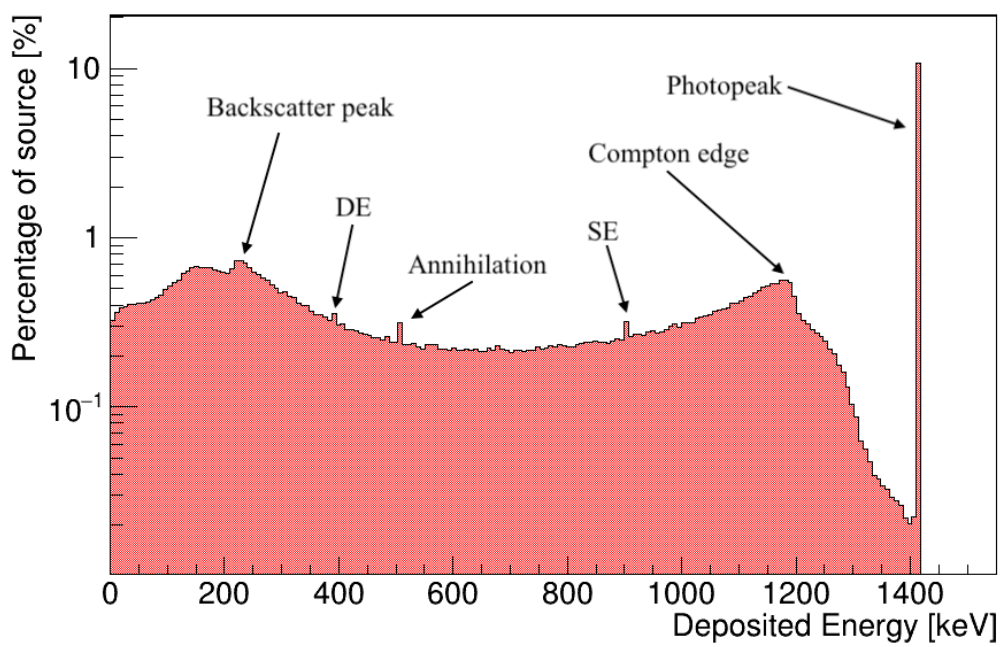


Figure 3.7: A typical γ -ray spectrum in a Germanium detector. Mono-energetic 1.4 MeV γ -rays are simulated in Geant4, passing through absorber materials before detection.

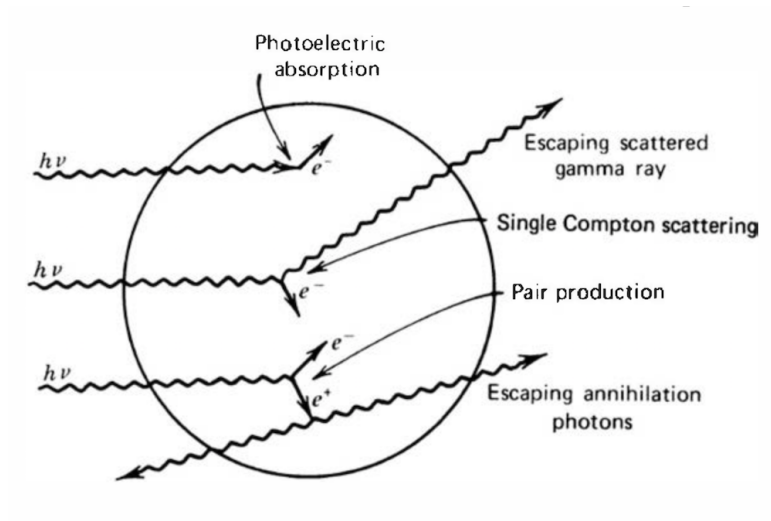


Figure 3.8: Gamma-ray interaction mechanisms.

4 Quantifying Radiation Detector Performance

When designing a radiation detector determining metrics by which performance can be summarised and compared is vital.

4.1 Scintillation detectors

4.1.1 Scintillator light output

Organic scintillation light output is often quantified relative to the output of Anthracene, one of the oldest organic scintillators in use. Anthracene also has the highest light output in its class[16].

Anthracene has been widely studied for its β -particle detection capabilities (see references [49–51]) and its light output is dependent on electron energy and detector geometry. The electron to photon energy conversion efficiency is of the order of one or two percent, and the amount of energy deposited per produced photon is of the order of several keV[50].

To determine the light yield from a scintillator a calibrated photomultiplier or photodiode can be used, alternatively a standard scintillator (such as bismuth germanate) can be used in a comparative calibration with an uncalibrated photosensor[52, 53]. To calibrate a photosensor, an integrating sphere and known light source (such as a laser pulser) can be used (See also Section 4.3)[41].

The collection of scintillation light is also of significant importance when designing detectors. With modern scintillation materials (except for very large scintillator volumes) self-absorption light losses are negligible, and the main difficulties arise from the scintillator's interfaces. Standard practice in scintillation arrays is to use light guides to direct the scintillation light to photodetectors[16].

4.1.2 Detection efficiency

Any radiation detector can be characterised by the efficiency at which it detects radiation. For scintillation detectors not only are there geometrical factors, limitations in physical material, but also considerations must be made into light detection.

Solid angle coverage

The main geometric factor involved in a β -tagging array such as SCEPTAR is the solid angle coverage. Solid angle is a measure of the surface area of a unit sphere covered by a projection of a certain object and can be calculated by performing a surface integral projection onto a unit sphere for every surface:

$$\Omega = \iint_S \frac{\hat{n} \cdot d\mathbf{a}}{r^2} \quad (4.1)$$

Where \hat{n} is a unit vector from the origin, $d\mathbf{a}$ is the differential patch of area, r is the distance from the origin to the patch. Written in spherical coordinates this integral becomes:

$$\Omega = \iint_S \sin \phi d\theta d\phi \quad (4.2)$$

SCEPTAR's scintillator paddles cover about 80% of 4π [4].

Light detection

Another factor determining overall detection efficiency in scintillation detectors will arise through the light detection mechanisms. Photons can be lost at interfaces, in light guides, and are not guaranteed to be detected in the photodetectors.

Detection thresholds

Theoretically, any energy deposition above the 3-4 keV spacing between the fluorescent and ground state of the scintillator will result in the emission of scintillation light. At this minimum energy, however, single photons will be produced which may not be detected in the photosensors. In reality this leads to higher minimum energy thresholds for electron detection in scintillators.

Other considerations are aspects such as the electronic noise level in the circuit, and the dark current of the photodetector (which may not be distinguishable from low amplitude pulses generated by low energy electrons).

4.2 γ -ray spectrometers

4.2.1 γ -ray spectrometer detection efficiency

The efficiency of Germanium detectors for use in spectrometers can be defined relative to a standard detector, or absolutely. The relative efficiency for the HPGe in use at 8π and GRIFFIN are given relative to the efficiency of a 3-inch square sodium iodide scintillator at a 25 cm source-to-detector distance.

The absolute γ -ray detection efficiency for a large γ -ray spectrometer the probability that a γ -ray emitted from the origin of the vacuum chamber has its energy fully captured in a Germanium crystal. This is calculated by taking the ratio of photons in the photopeak to the total emitted photons. The absolute γ -ray efficiency will include the intrinsic efficiency of the Germanium detectors (measured also by the relative efficiency) and include geometric factors such as the solid angle coverage of the crystals.

An effective way to obtain this absolute efficiency is to run simulations in Geant4[54]. Geant4 simulations include definitions of the HPGe detectors, that have been validated against experimental results[55].

The absolute efficiency of the 8π array is about 1% at 1.3 MeV, whereas the GRIFFIN array has an efficiency of about 11% at the same energy[2, 4]. This large improvement can largely be attributed to the improved solid angle coverage and add-back¹ capabilities of GRIFFIN[56].

4.2.2 γ -ray spectrometer energy resolution

The energy resolution of a γ -ray spectrometer is given through the combination of several factors: the statistical spread in the number of charge carriers, electronic noise and variations in the charge collection efficiency. The energy resolution is measured by the full width at half maximum (FWHM) of a Dirac delta-function, such as an ideal measurement of a monoenergetic γ -ray from a nuclear level transition[16].

The resolution of the HPGe detectors used in the 8π and GRIFFIN arrays are similar achieving peak FWHM around 2 keV for 1.3 MeV γ -rays[4, 57].

4.2.3 Solid angle coverage

As with any spectrometer, γ -ray spectrometers benefit from large solid angle coverage to maximise detection efficiency. See Section 4.1.2 for general details on solid angles. Each of 8π 's Germanium crystals cover approximately 0.25% of the 4π total solid angle resulting in about a 5% coverage for the full array of 20 detectors. GRIFFIN greatly improves on this with over 40% of solid angle coverage, and largely being responsible for GRIFFIN's efficiency improvement over the 8π facility[5, 9].

4.2.4 Photopeak to total ratio

A measure of γ -ray spectrometer's performance that is not greatly affected by geometric factors is the photopeak to total ratio. This ratio is calculated by comparing the population of the full-energy/photopeak and the total captured energy spectrum. As only detected γ -rays are considered (ignoring those which do not deposit energy in the Germanium) this is a useful method for taking away geometric factors and improves the signal-to-noise ratio at a cost of efficiency[32]. The GRIFFIN facility can operate up to 48% photopeak-to-total ratio at 1 MeV in summed neighbour mode[9]. The GRIFFIN array can be operated in optimised-peak-to-total mode where Compton suppression shields are used to improve this performance with lower efficiencies.

¹add-back considers γ -rays that deposit energy in neighbouring crystals of the same detector in multiple scattering events.

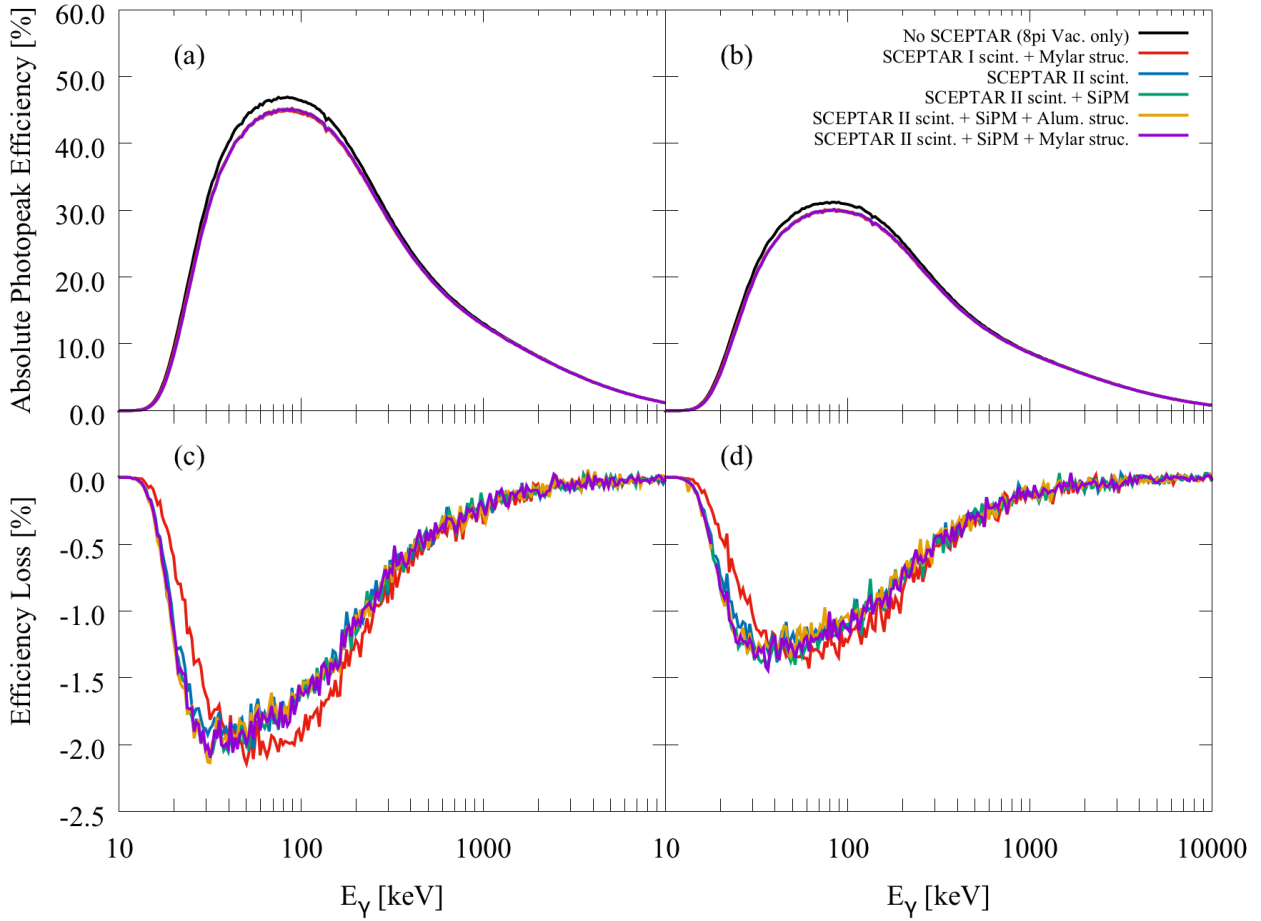


Figure 4.1: Simulated absolute γ -ray detection efficiency of GRIFFIN in various configurations. The top two quadrants show the absolute γ -ray efficiencies with the other quadrants showing the difference in efficiency between the vacuum chamber only and other configurations. The left two quadrants are with GRIFFIN in unsuppressed mode with the others showing optimised peak to total suppressed mode.

4.3 Photomultipliers and photodiodes

Silicon photomultiplier sensors are characterised by the following parameters: breakdown voltage, photon detection efficiency, optical crosstalk, afterpulsing and temperature dependency. These parameters which will be briefly outlined in the following section, as well as basic descriptions of how they can be measured[39].

4.3.1 Breakdown voltage and overvoltage

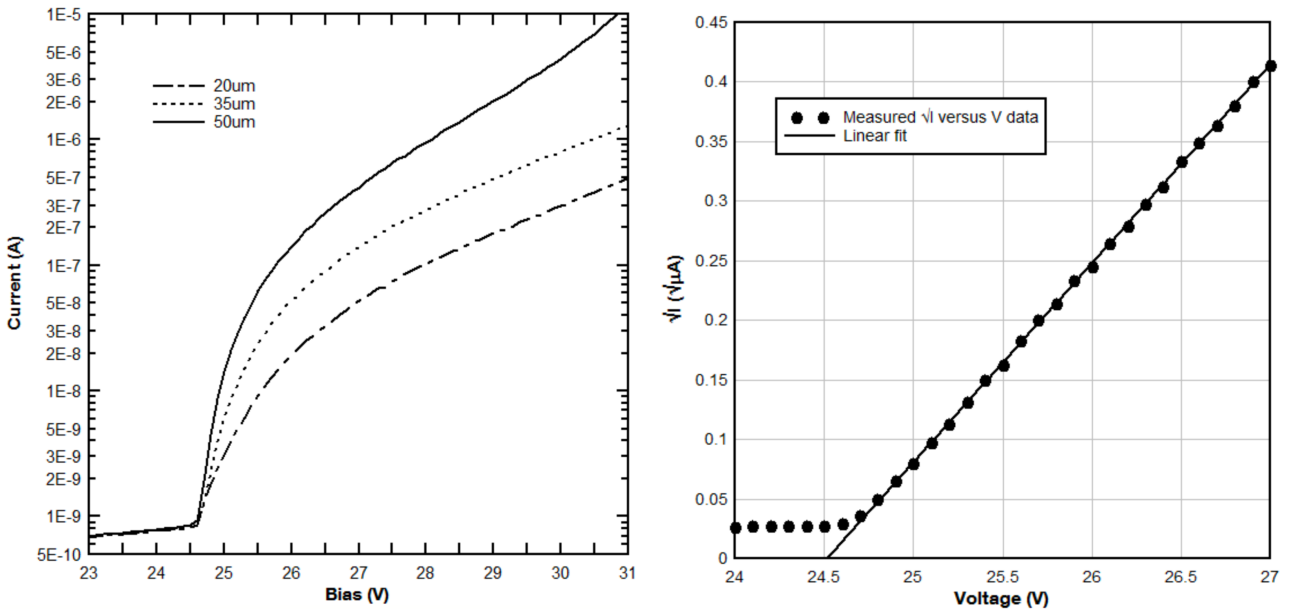
The breakdown voltage is the bias potential at which the APD's in the SiPM array operate in Geiger-mode. The breakdown voltage can be measured by observing the sudden increase in current in an IV plot (see Figure 4.2a), or for more precise determination by taking a linear fit to the voltage intercept of a \sqrt{I} versus V plot (see Figure 4.2b[39]).

Many, if not all other parameters of a SiPM are determined by the overvoltage. Defined as the difference between the biasing voltage and the breakdown voltage (as seen in equation 4.3), the overvoltage affects gain, PDE, dark performance, crosstalk, and afterpulsing[40].

$$\Delta V = V_{bias} - V_{br} \quad (4.3)$$

4.3.2 Gain

The gain of a SiPM sensor is defined as the charge produced for each detected photon. The gain is given as a function of overvoltage (ΔV), the microcell capacitance (C , itself a function of microcell



(a) Dark current vs voltage plots for 3 mm C-series sensors with 20, 30, and 50 μm microcells.
(b) Determining breakdown voltage from a \sqrt{I} vs V plot.

Figure 4.2: Figures taken from [39].

size), and the electronic charge (e).

$$G = \frac{C \cdot \Delta V}{e} \quad (4.4)$$

The gain can be measured by finding the distance between adjacent photoelectron peaks in a SiPM photoelectron spectrum such as in Figure 4.3. Such a spectrum is generated by performing charge integration on a signal produced by a SiPM while being exposed to low-level pulses[58].

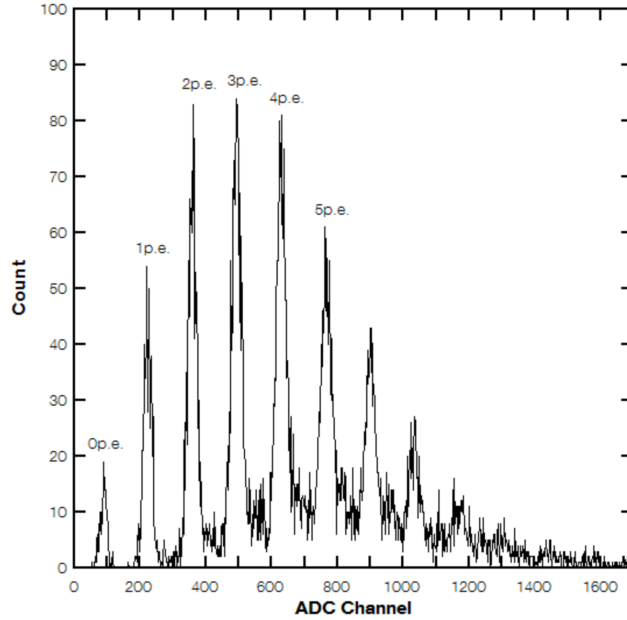


Figure 4.3: Photoelectron spectrum of a SiPM, achieved using low-level light pulses. Figure taken from [39].

4.3.3 Photon Detection Efficiency and Responsivity

The photon detection efficiency (PDE) while slightly different from the quantum efficiency often quoted for PMTs and APDs, is a measure of the sensitivity of a SiPM. The PDE is a function of wavelength, overvoltage and microcell fill factor[39, 41].

Rigorously, the PDE is the statistical probability that an incident photon interacts with a microcell producing an avalanche and is defined in equation 4.5.

$$PDE(\lambda, V) = \nu(\lambda) \cdot \epsilon(V) \cdot F \quad (4.5)$$

Where ν is the quantum efficiency of silicon, ϵ is the avalanche initiation probability, and F is the fill factor of the device. To calculate the PDE the responsivity R of the sensor is used. Defined as the average photocurrent per incident optical power, $R = I_p/P_{op}$. The PDE can now be written as follows:

$$PDE = \frac{R \cdot hc}{\lambda Ge(1 + P_{AP})(1 + P_{XT})} \cdot 100\% \quad (4.6)$$

where h is the Planck constant, c is the speed of light, λ is the wavelength of incident light, G is the gain and e is the elementary charge. P_{AP} and P_{XT} are the afterpulsing and crosstalk probabilities, respectively[39].

Using an integrating sphere with a known light-splitting ratio and a calibrated photodiode the PDE of a specific SiPM can also be determined[59, 60].

4.3.4 Noise

Dark Count Rate / Dark Current

The main source of noise in a silicon photomultiplier is the dark count rate (DCR) which primarily originates from thermal electrons generated in the active volume. These electrons initiate an avalanche producing breakdown signals that are identical to photon-generated signals[39]. Thermally-generated electrons form noise at single-photon amplitudes, which can be reduced by setting a sufficiently large threshold. Often quoted in kHz as the dark count rate is comprised of a series of pulses, for continuous applications the dark count rate is often considered as a *dark current*.

The DCR can be measured using a counting system with a threshold set at the half-photon level. The DCR increases with bias and temperature and scales with the size of the active area[40].

Optical Crosstalk

Optical crosstalk is an additional component of SiPM noise that is a result of Bremsstrahlung photons that initiate secondary avalanches in adjacent microcells. Crosstalk is defined as the probability that an avalanching microcell will cause an avalanche in a second microcell. The process happens instantaneously and thus single-photons can generate signals equivalent to multiple photons[39, 61].

The optical crosstalk can be estimated by taking the ratio of the dark count rates for thresholds where single-photon events are excluded against all higher than half-photon events[59]. Crosstalk increases with overvoltage.

Afterpulsing

Due to defects in the silicon, charge carriers can become trapped during a breakdown. These are released with a delay up to several nanoseconds, potentially triggering another avalanche known as an afterpulse[39]. Afterpulsing is negligible if the delay is short (and the microcell has not recharged yet)[61]. The afterpulse probability can be determined by measuring the statistical distribution of consecutive pairs of dark counts[59].

4.3.5 Temperature Dependency

The breakdown voltage of a SiPM varies linearly with temperature. Increases in temperature result in a higher breakdown voltage, which in turn determines many of the important characteristics of a photomultiplier such as the gain and PDE[39]. SensL C-Series SiPM's are notably stable in response to temperature changes with a breakdown voltage temperature dependency of $dV_{br}/dT \approx 20mV/K$ [40]. The dark count rate - resulting from thermal electrons - is also affected by temperature fluctuations, such that higher temperatures produce more frequent dark signals (higher DCR).

5 Research Capabilities and Motivations

5.1 Current and past capabilities of SCEPTAR I

Sensitive to electrons and positrons created in radioactive decays, SCEPTAR has been used extensively in 8π and GRIFFIN to improve the spectrometers' performance in β -decay studies, as well as in nuclear structure investigations.

5.1.1 Gating on detected β particles

One of SCEPTAR's most important functions - and indeed its primary function in the GRIFFIN array - is to allow for β - γ coincidence gating[2]. By taking only γ -detection events where a β particle was also detected in SCEPTAR - and hence a β -decay occurred - a large portion of the background spectrum can be removed.

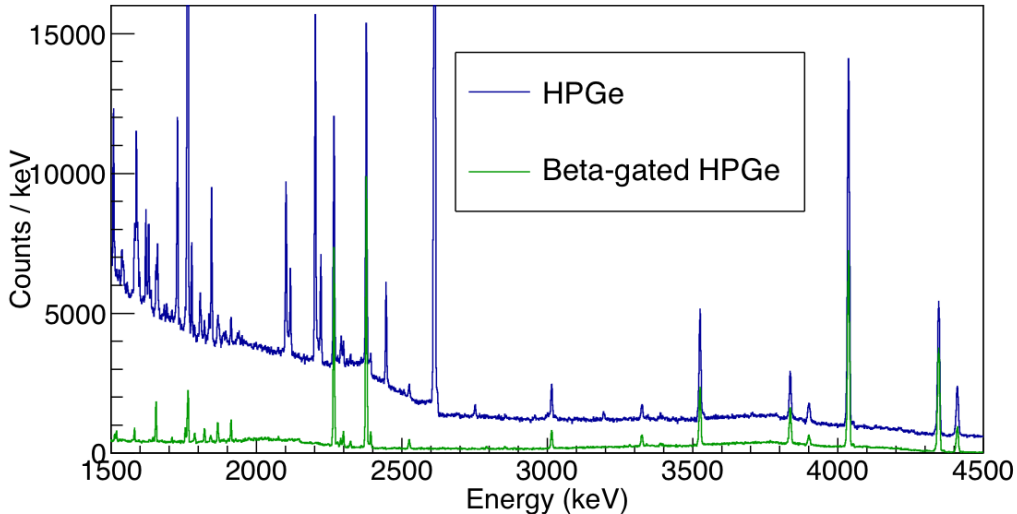


Figure 5.1: GRIFFIN HPGe signal versus β -gated HPGe signal for the ^{132}In to ^{132}Sn β^- decay. From experimental data gathered at TRIUMF in July 2016 (S1519). Figure adapted from [62].

Figure 5.1 provides an example of how effective β -gating with SCEPTAR can be. In this particular case, where SCEPTAR was used in GRIFFIN, many prominent background peaks were removed through the gating method. Notably, the uncorrelated 2614.51 keV peak from the β^- -decay of ^{208}Tl was excluded successfully.

When used in coincidence with 8π , SCEPTAR's gating allowed for such an improvement to the signal-to-background ratio that beams delivered at 2-3 ions/s could be studied[5, 63].

SCEPTAR also considerably improves the signal-to-background ratio in γ - γ coincidence spectra through β - γ - γ coincidence gating, see Figure 5.2.

5.1.2 Vetoing punch through signals

Plastic scintillators are ΔE detectors, this means that at sufficiently high energies, they will only measure a fraction of the electrons energy (See Section 2.2.1). Such electrons are said to punch through the scintillator and can prove to be very problematic for the signals from surrounding γ -ray detectors. Fast electrons entering Germanium crystals create unwanted signals, contributing to the noise level and reducing the peak to total ratio. Additionally, during radiative scattering events within the scintillator the fast electrons will produce Bremsstrahlung which further increases background signals in the HPGe detectors located coaxially to the scintillator volume.

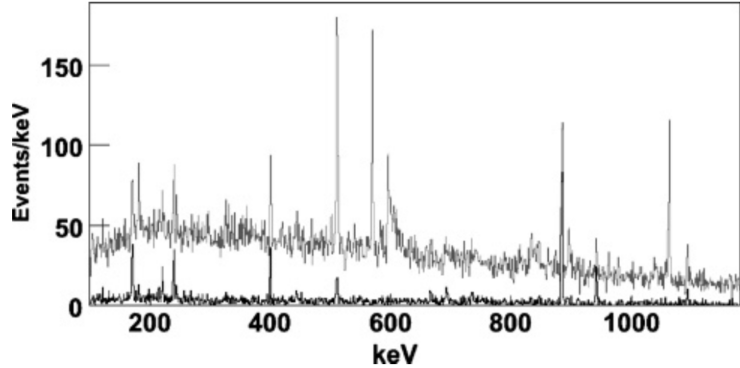


Figure 5.2: $\gamma\text{-}\gamma$ (light) and $\beta\text{-}\gamma\text{-}\gamma$ (dark) coincidence projections. Figure taken from [63].

Hence, the 8π and GRIFFIN facilities include optional Delrin domes (up to 20 mm) that can be placed between the central vacuum chamber and the Germanium crystals[2, 5]. As low-Z absorbers, these do not greatly affect the γ -ray detection efficiency, while slowing down and stopping all but the most energetic β -particles. The issue associated with this method of removing undesired β -signals is that of Bremsstrahlung produced when stopping the electrons. Bremsstrahlung - as electromagnetic radiation - will also interact with the Germanium producing noise[32].

SCEPTAR offers an alternative to low-Z shielding, through vetoing. When a β -particle is detected, the γ -ray signals from the Germanium crystals covered by that scintillator paddle can be ignored (vetoed). SCEPTAR's 1:1 geometry correspondence to the 8π HPGe detectors makes this particularly effective, as only the bare minimum of sensitive volume is ignored. In 8π vetoing $\beta\text{-}\gamma$ coincidence signals in the colinear HPGe detector effectively reduced the background in the spectrum at a small cost of 5% loss in overall coincidence events. β -decays with sufficiently low Q-values can be discriminated against and not excluded, as the electrons are stopped instead of slowed down in SCEPTAR[63].

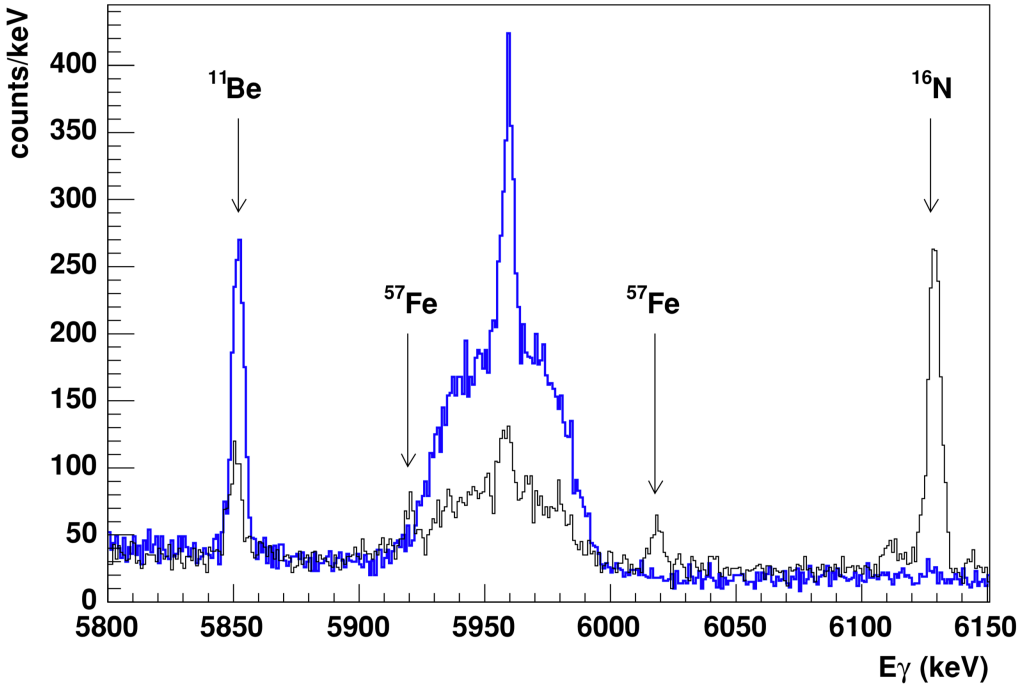


Figure 5.3: Portion of γ -ray spectrum from β -delayed neutron decay of ^{11}Li taken with SCEPTAR, PACES and 8π . This compares well to the previously obtained γ -singles data from [64]. Figure taken from [6].

Figure 5.3 shows an example of SCEPTAR's β -tagging and vetoing capabilities when studying β -delayed neutron decay of ^{11}Li . The improved signal-to-noise ratio of the $\beta\text{-}\gamma$ coincident data more clearly shows the unresolved 5960 keV doublet in ^{10}Be and 5957 keV narrow peak of the indirect feeding of the 1^-_1 level from the ground state of ^{10}Be , as well as removing the iron and nitrogen

background peaks[6].

5.2 Future capabilities of SCEPTAR II

While SCEPTAR remains a key system facilitating experiments even in the GRIFFIN array it was not designed for - it has been in use for over a decade and is beginning to show signs of age. This is most notable in the photon detection efficiencies of individual PMTs, some of which are registering lower signals than at the time of their commission. Additionally, new technologies will allow for a change to GRIFFIN's geometry.

5.2.1 Shortcomings of SCEPTAR I in GRIFFIN

As SCEPTAR scintillator paddles are arranged to match 8π 's geometry, each scintillator has more than one Germanium crystal in its 'shadow' when SCEPTAR is used in GRIFFIN. As a consequence, using SCEPTAR coincidences to reduce Bremsstrahlung signals in GRIFFIN causes a higher loss in data than necessary. Changing to square scintillator paddles that will match GRIFFIN's rhombicuboctahedral geometry will reinstate one-to-one scintillator to Germanium crystal correspondence.

Figure 5.4 shows the approximate geometry of the scintillator paddles in SCEPTAR II. Each square face will be covered by four scintillator volumes in a two by two grid.

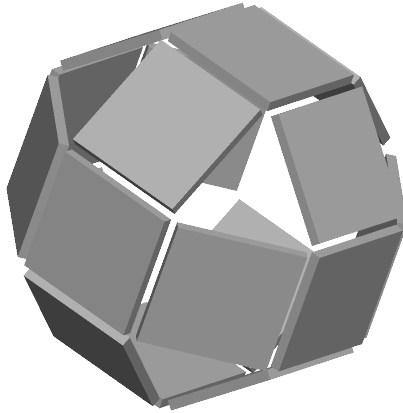


Figure 5.4: Proposed geometry of scintillator paddles for SCEPTAR II.

5.2.2 Technological advances facilitating SCEPTAR II design

Silicon Photomultipliers

Silicon photomultipliers are much more compact, inexpensive, and require lower biasing voltage when compared to vacuum photomultiplier tubes. The original SCEPTAR vacuum chamber design is very mechanically challenging due to the light guides, optical feedthrough flange, and PMT all having to fit within their respective parts of the beampipe and chamber. This is can be seen in the design schematics shown in Figure 5.5.

The smaller dimensions of SiPM's will allow for direct mounting onto the scintillators, removing the need for light-guides and feedthroughs.

An important consideration is the compatibility of the photodetector to the scintillation light. Figure 5.6 shows the compatibility of the chosen SensL C-series SiPM's to the BC404 and BC422Q scintillators, used in SCEPTAR and ZDS (Zero-Degree Scintillator) respectively.

3D printing

The proposed geometry for SCEPTAR II's scintillators will require a support structure that would incur significant cost if machined. The complex structure lends itself very well to 3D printing solutions. Figure 5.7 shows what a low-cost and fast turnover print of the prototype structure looks when printed in ABS.

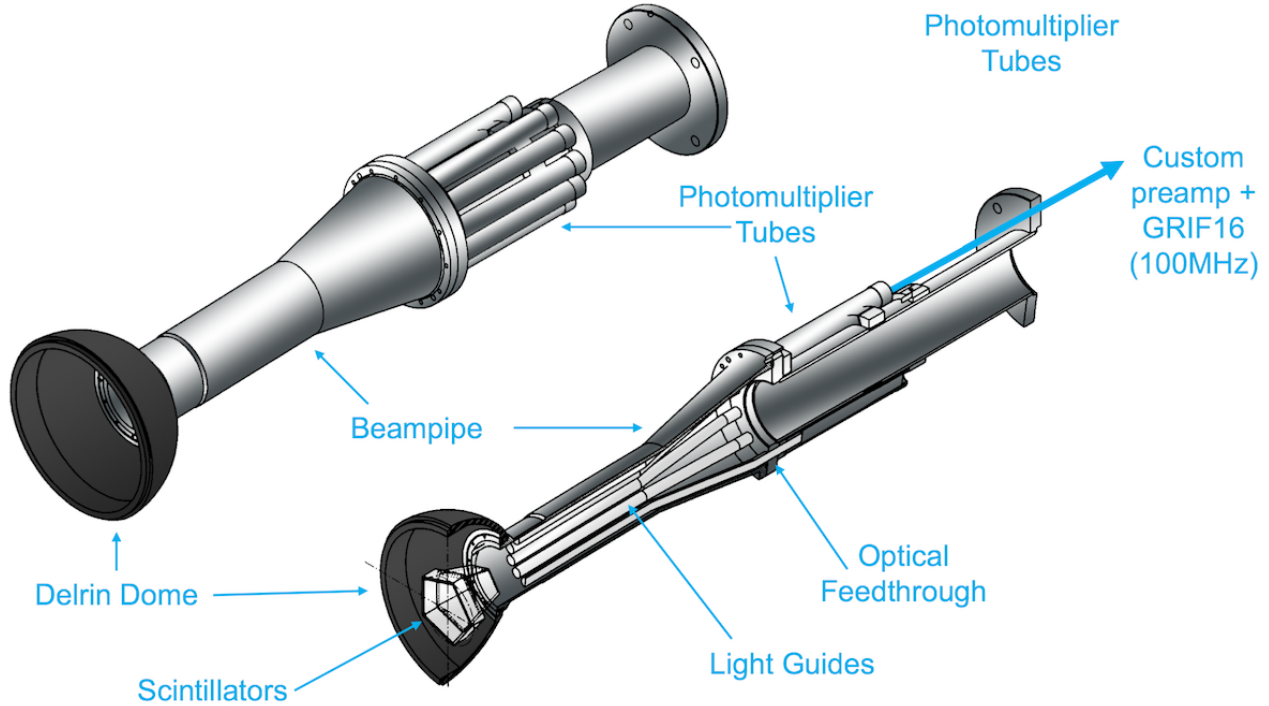


Figure 5.5: CAD schematics of SCEPTAR detector.

For additional rigidity, and vacuum properties (outgassing reduction) a material such as aluminium would be favourable. Nowadays aluminium 3D printing is available through Direct Metal Laser Sintering (DMLS).

Flexible printed circuit boards

While mounting SiPM's directly onto the scintillators in the vacuum chamber removes the need for optical feedthroughs and light guides, there will be a significant number of signal cables that need to be routed out through a flange and into the data acquisition system. To reduce the number of parts, and improve the ease of construction, flexible printed circuit boards (fPCB's) present an opportunity to combine a part of the support structure with the signal cables. Often manufactured from Kapton, and thin copper sheets these fPCB's cause very little γ -ray attenuation and have excellent vacuum properties.

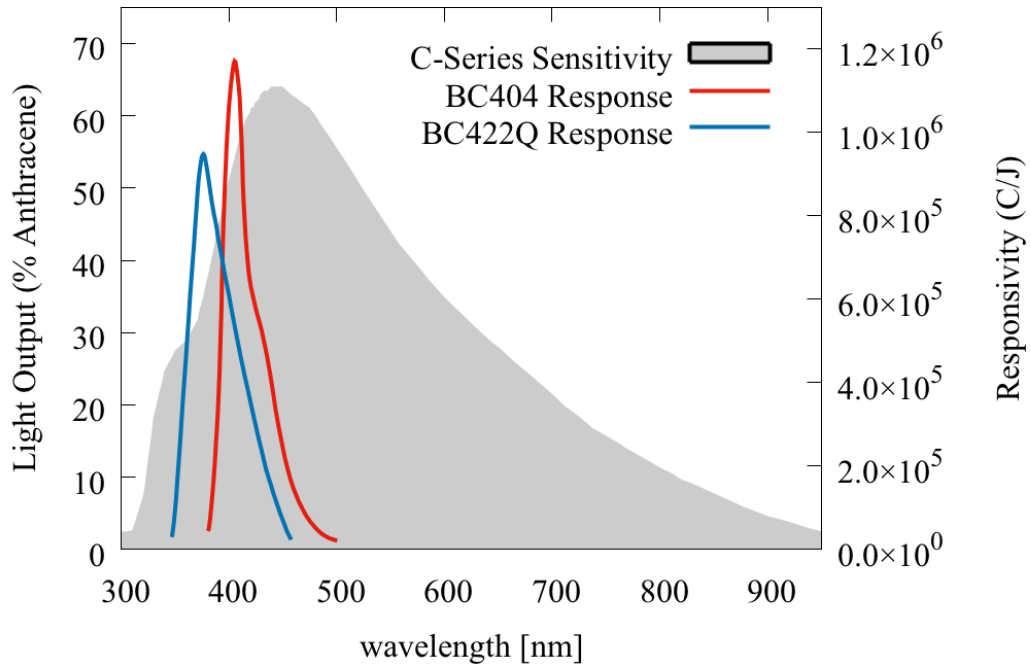


Figure 5.6: SensL C-Series SiPM responsivity vs St. Gobain BC404 and BC422Q scintillator light output.

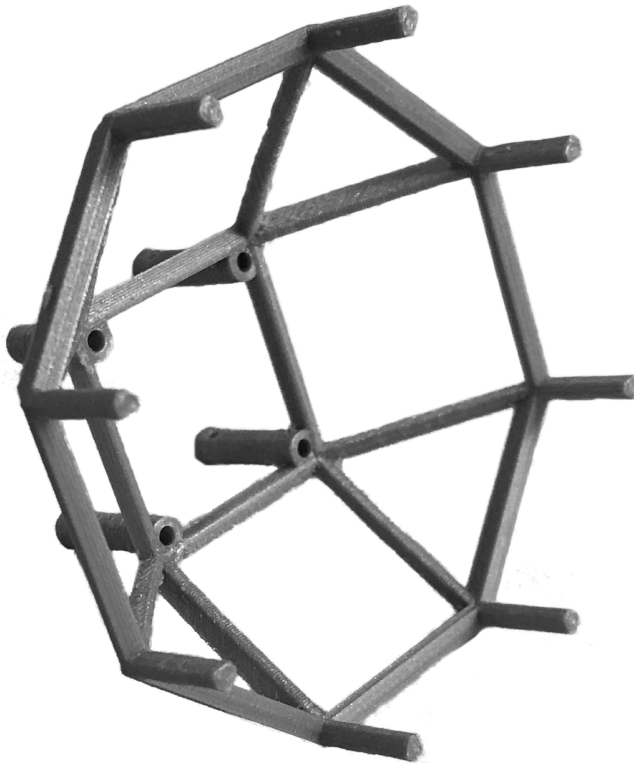


Figure 5.7: Prototype of one hemisphere of SCEPTAR II's support structure 3D printed in acrylonitrile butadiene styrene (ABS).

6 Alternative solutions

There exist a large number of potential alternative solutions to the problem of β -particle-tagging in GRIFFIN. This section will provide two examples, one employing similar technology (scintillators and silicon photomultipliers) and another non-solid-state gas-filled alternative.

6.1 Scintillating Fibre Detectors

Plastic scintillation fibres provide an alternative method for tracking the positions of charged particles. Identical in mechanism to the plastic scintillators used in the original SCEPTAR, scintillating fibre detectors (SFD's) differ in their geometry such that bundles of long rods are wrapped around the origin of radiation. At each end of the fibres photosensors are placed and the photons from energy deposition events can be correlated by the two signals to obtain positional information along the fibres which can be transformed to the lab coordinate system.

Available from manufacturers such as St. Gobain[65], plastic scintillator fibres are often formed from a polystyrene active core, with an acrylic cladding. Producing less light output per incident MeV of energy compare $\bar{\gamma}$ 8000 photons/MeV of BCF12 to $\bar{\gamma}$ 12000 photons/MeV of BC404, as well as having less favourable timing performance (2.7 versus 1.8 ns decay time), scintillator fibres compensate by allowing for superior geometry possibilities especially useful in barrel and pipe detectors[66]. One such barrel-shaped detector is in the UA2 detector at CERN (see reference [67]), another example being the crystal barrel detector at ELSA in Germany[68].

While it is possible to imagine geometries such that would cover all of the 4π solid angle in fibres, this would pose quite some difficulty to incorporate into the current two-hemisphere ancillary detector template for GRIFFIN. Further drawbacks arise through the worse timing and light output performance of scintillator fibres compares to scintillator sheets, as well as through the higher demand for analysis.

6.2 Parallel Plate Avalanche Counters

Parallel plate avalanche counters (PPAC's) are a variant of proportional counters that rely on the phenomenon of gas multiplication. Gas multiplication amplifies the charge represented by the original ion pairs formed within the gas. Similar to how avalanches are formed at a *pn*-junction in silicon (see Section 3.2.2) a sufficiently powerful electric field will raise the mean kinetic energy of free electrons to above the ionization threshold[16, 69].

PPACs have steadily gained attention since the 1970's in applications where fast timing is a higher priority than energy resolution, and in the study of heavy ions where the associated radiation damage would rule out the use of solid-state detectors. PPACs are now stable detectors at world-leading experimental facilities such as CHICO[70] and BigRIPS[71]. PPACs, as their name suggests, use two parallel electrodes within a volume of proportional gas. Incident radiation creates electron tracks which are accelerated and multiplied by the constant electric field. The number of ions formed is proportional to the energy deposited by the radiative particle, hence PPACs are another ΔE detector that could be employed in an application such as β -tagging in GRIFFIN[16, 72].

Drawbacks to using parallel plate detectors as a successor to SCEPTAR are; that the geometry of the detectors would not be in correspondence to the Germanium detectors requiring further manipulation of the data to provide vetoing and gating functionality; that the difficulty of discriminating between different particles; as well as the various support systems required to reliably operate a gas-filled detector system and the associated costs.

7 Conclusion and Outlook

The SCEPTAR (SCintillating Electron Positron Tagging ARray) detector array remains the primary ancillary in use at the GRIFFIN (Gamma-Ray Infrastructure For Fundamental Investigations of Nuclei) spectrometer. By providing β -particle tagging data for use in coincidence gating and vetoing, SCEPTAR improves GRIFFIN's performance and empowers the state-of-the-art facility to pursue a wide program of stopped radioactive beam research into nuclear structure, nuclear astrophysics and fundamental symmetries.

SCEPTAR is over a decade old and its geometry - determined by the positions of the 8π Germanium detector - is suboptimal when operated within the GRIFFIN array. The once high-end vacuum photomultiplier tubes are now ageing, and modern equivalents can be found in the smaller, solid-state silicon photomultiplier sensors. With a new scintillator geometry mimicking that of the GRIFFIN high-purity Germanium detectors, SCEPTAR's successor SCEPTAR II will harness advancements in radiation detection technology to improve performance and expand its capabilities.

From the sources of β - and γ -radiation studied with SCEPTAR and GRIFFIN, to the interactions of said particles and thus the mechanisms by which they can be detected, this report has detailed the considerable underlying physics involved in radiation detection in Chapter 2. Proceeding then to the descriptions of β -particle and photon detectors, and the methods by which these can be characterised and compared in Chapter 3 and Chapter 4. In Chapter 5 we have seen how SCEPTAR and in the future SCEPTAR II will support GRIFFIN in its experimental capabilities through β - γ -coincidence gating and vetoing. Two notable alternative solutions to a square scintillator tagging array were presented in Chapter 6 as well as a discussion of their benefits and limitations.

This project will continue to be pursued with the aim of constructing the new detector by the end of 2018. The next stage will involve acceptance and feasibility testing of the scintillator and silicon photomultiplier components in the dark as well as with radioactive sources. Should these measurements yield satisfactory results the support structure and vacuum chamber designs will be finalised, and construction of the final detector can begin. Time permitting, calibrations of the real array as well investigations into the most suitable pre-amplification and digitisation of the signals will be conducted.

Bibliography

- [1] E. Cunningham in APS Division of Nuclear Physics Meeting Abstracts, **2003**.
- [2] A. Garnsworthy, *Acta Phys. Pol. B* **2016**, 47, 713.
- [3] H. Andrews et al., Proposal for a national facility-the 8π spectrometer, tech. rep., Atomic Energy of Canada Ltd., **1984**.
- [4] A. Garnsworthy in EPJ Web of Conferences, Vol. 93, EDP Sciences, **2015**, p. 01032.
- [5] A. B. Garnsworthy et al., *Hyperfine Interact.* **2014**, 225, 121–125.
- [6] G. C. Ball et al. in Journal of Physics: Conference Series, Vol. 387, IOP Publishing, **2012**, p. 012014.
- [7] A. F. Bielajew, Elements of Nuclear Engineering and Radiological Sciences II, β decay, Nuclear Engineering and Radiological Sciences, The University of Michigan, **2012**.
- [8] J. Dilling et al., *Hyperfine Interact.* **2014**, 225, 1–8.
- [9] C. Svensson et al., *Hyperfine Interact.* **2014**, 225, 127–132.
- [10] C. E. Svensson et al., *J Phys G Nucl Part Phys* **2005**, 31, S1663.
- [11] G. Hackman et al., *Hyperfine Interact.* **2014**, 225, 241–251.
- [12] J. Dilling et al. in *ISAC and ARIEL: The TRIUMF Radioactive Beam Facilities and the Scientific Program*, Springer, **2013**, pp. 253–262.
- [13] E. O’Sullivan, “Designing and Building SPICEy PDA (PIN Diode Array)”, Internal report, **2016**.
- [14] M. Schumaker et al., *Nucl Instrum Methods Phys Res A* **2007**, 575, 421–432.
- [15] K. S. Krane et al., *Introductory nuclear physics*, Vol. 465, Wiley New York, **1988**.
- [16] G. F. Knoll, *Radiation detection and measurement*, John Wiley & Sons, **2010**.
- [17] A. Bettini, *Introduction to Elementary Particle Physics*, Cambridge University Press, **2008**.
- [18] L. Nanni, *arXiv preprint* **2018**.
- [19] M. S. Jean-Louis Basdevant, James Rich, *Fundamentals in nuclear physics: from nuclear structure to cosmology*, 1st ed., Springer, **2005**.
- [20] E. Fermi, *Nuovo Cimento* **1934**, 11, 1.
- [21] W. N. Catford, Lectures in Nuclear and Particle Physics, Faculty of Engineering and Physical Sciences, University of Surrey, **2017**.
- [22] E. Roeckl et al., *Int J Mass Spectrom* **2013**, 349-350, 100 years of Mass Spectrometry, 47–56.
- [23] K. S. Krane, *Modern Physics*, 3rd ed., Wiley, **2012**.
- [24] J. M. Stellman, *Encyclopaedia of occupational health and safety*, Vol. 1, International Labour Organization, **1998**.
- [25] C. Palacio, “Some effects on polymers of low-energy implanted positrons”, **2008**.
- [26] K. Siegbahn, *Alpha-, Beta-, and Gamma-Ray Spectroscopy*, Vol. 1, 2nd ed., North-Holland Publishing Company, **1966**.
- [27] L. Miramonti, *Radiat Meas* **2002**, 35, 347–354.
- [28] E. Segrè, *Nuclei And Particles An Introduction To Nuclear And Subnuclear Physics 2nd.Ed*, W. A. Benjamin, **1977**.
- [29] Bethe H., *Ann Phys*, 397, 325–400.
- [30] K. Al-Ahmad et al., *J Phys D Appl Phys* **1983**, 16, 2257.
- [31] National Institute of Standards and Technology, ESTAR: Stopping Powers and Ranges of Electrons, (Available at: <https://physics.nist.gov/PhysRefData/Star/Text/method.html>).
- [32] G. Nelson et al., *Passive nondestructive analysis of nuclear materials* **1991**, 27–42.
- [33] A. Einstein, *Am J Phys* **1965**, 33, 367.

- [34] National Research Council Staff, *Nuclear Physics*, National Academies Press, Washington, United States, **1986**.
- [35] J. Stachel, Detectors in Nuclear and Particle Physics, Scintillation counters, Department of Physics and Astronomy, University of Heidelberg, **2015**.
- [36] Y. Yu et al., *Astropart Phys* **2017**, 94, 1–10.
- [37] A. Otte et al., *Nucl Instrum Methods Phys Res A* **2015**, 787, New Developments in Photodetection NDIP14, 85–88.
- [38] A Ghassemi and K Sata and K Kobayashi, “Multi-Pixel Photon Counter”, Hamamatsu technical note, **2016**.
- [39] SensL, “An Introduction to the Silicon Photomultiplier”, Manufacturer’s technical note, **2011**.
- [40] SensL, “How to Evaluate and Compare Silicon Photomultiplier Sensors”, Manufacturer’s technical note, **2015**.
- [41] A. N. Otte et al., *Nucl Instrum Methods Phys Res A* **2017**, 846, 106–125.
- [42] B. Dolgoshein et al., *Nucl Instrum Methods Phys Res A* **2006**, 563, TRDs for the Third Millennium, 368–376.
- [43] D. Renker et al., *J Instrum* **2009**, 4, P04004.
- [44] A. Benaglia et al., *Nucl Instrum Methods Phys Res A* **2016**, 830, 30–35.
- [45] B. Lutz et al., *J Phys Conf Ser* **2012**, 404, 012018.
- [46] G. A. Armantrout, *IEEE Trans Nucl Sci* **1972**, 19, 289–298.
- [47] G. Nakano et al., *IEEE Trans Nucl Sci* **1977**, 24, 68–72.
- [48] R. H. Pehl et al., *IEEE Trans Nucl Sci* **1973**, 20, 494–499.
- [49] E. Gatti et al. in Nuclear Electronics II. Proceedings of the Conference on Nuclear Electronics. V. II, **1962**.
- [50] J. Hopkins, *Rev Sci Instrum* **1951**, 22, 29–33.
- [51] L. W. Johnston et al., *Rev Sci Instrum* **1957**, 28, 765–767.
- [52] M. Moszynski et al., *IEEE Trans Nucl Sci* **1997**, 44, 1052–1061.
- [53] I. Holl et al., *IEEE Trans Nucl Sci* **1988**, 35, 105–109.
- [54] S. Agostinelli et al., *Nucl Instrum Methods Phys Res A* **2003**, 506, 250–303.
- [55] M. Schumaker et al., *Nucl Instrum Methods Phys Res A* **2007**, 570, 437–445.
- [56] U. Rizwan, PhD thesis, Simon Fraser University, **2015**.
- [57] U. Rizwan et al., *Nucl Instrum Methods Phys Res A* **2016**, 820, 126–131.
- [58] V. Chmill et al., *Nucl Instrum Methods Phys Res A* **2017**, 854, 70–81.
- [59] P. Eckert et al., *Nucl Instrum Methods Phys Res A* **2010**, 620, 217–226.
- [60] W. Gebauer et al., *Nucl Instrum Methods Phys Res A* **2017**.
- [61] Y. Du et al., *Nucl Instrum Methods Phys Res A* **2008**, 596, 396–401.
- [62] A. Garnsworthy, Experience with GRIFFIN, TRIUMF FRIB Decay Station Workshop, **2018**.
- [63] C. Mattoon et al., *Phys Rev C* **2007**, 75, 017302.
- [64] F. Sarazin et al., *Phys. Rev. C* **2004**, 70, 031302.
- [65] Saint-Gobain, <https://www.crystals.saint-gobain.com/>.
- [66] S.-G. Ceramics et al., “Organic Scintillation Materials and Assemblies”, **2018**.
- [67] J. Alitti et al., *Nucl. Instrum. Methods Phys. Res., A* **1988**, 279, 364–375.
- [68] G. Suft et al., *Nuclear Instruments and Methods in Physics Research Section A: Accelerators, Spectrometers, Detectors and Associated Equipment* **2005**, 538, 416–424.
- [69] A. Breskin et al., Timing properties of parallel plate avalanche counters with light particles, tech. rep., Weizmann Inst. of Science, **1977**.
- [70] M. Simon et al., *Nucl Instrum Methods Phys Res A* **2000**, 452, 205–222.
- [71] H. Kumagai et al., *Nucl Instrum Methods Phys Res B* **2013**, 317, 717–727.
- [72] H. Stelzer, *Nucl Instrum Methods* **1976**, 133, 409–413.

Acknowledgements

I would like to thank Dr. Adam Garnsworthy for the opportunity to pursue this exciting project at TRIUMF as part of my MPhys degree, as well as his valuable expertise and guidance. In addition, I would like to thank Shaun Georges, James Smallcombe, Mike Bowry, and Paddy Regan for their assistance to the progress of the work and their contributions to my understanding of the relevant physics and methodology.